Thermal characterization, multi-scale thermal modeling and experimental validation of lithium-ion batteries for automobile application

Von der Fakultät Energie-,Verfahrens- und Biotechnik
der Universität Stuttgart zur Erlangung der Würde
eines Doktor-Ingenieurs (Dr.-Ing.)
genehmigte Abhandlung

vorgelegt von

Muhammad Wasim Tahir
geboren in Kasur, Pakistan

Hauptberichter:	Prof. Dr.-Ing. habil. Clemens Merten
Mitberichter:	Prof. Dr. rer. nat. habil. Wolfgang Bessler

Tag der mündlichen Prüfung: 19.01.2016

Institut für Chemische Verfahrenstechnik
der Universität Stuttgart
2016

Affectionately dedicated to

my parents

Fazeelat Begum (RIP) and Muhammad Amin

Preface

The present thesis is the outcome of my Ph.D. research work carried out mainly at the Institute of Chemical Process Engineering (ICVT), University of Stuttgart and partly at the Institute of Technical Thermodynamics (ITT), German Aerospace Center (DLR), Stuttgart. This work focuses on studying the thermal aspects of automotive battery systems that includes developing a detailed thermal model for lithium-ion battery systems comprising an electrochemical heat generation model and a heat transfer model dynamically coupled together to form a full 3D thermal model and validating the model by experimental findings.

I am highly indebted and grateful to my Ph.D. advisor (Doktorvater) Professor Clemens Merten for his able guidance and support throughout the course of this work. I always found him helpful and supportive not only professionally but socially too. Being a foreigner I always found him welcoming in rendering extra support on different matters which I acknowledge with a great sense of gratitude. I am especially thankful to my co-supervisor Professor Wolfgang Bessler and gratefully acknowledge his able and valuable guidance on the electrochemical aspects of this work and support in conducting the experimental work at the German Aerospace Center (DLR), Stuttgart.

I thankfully acknowledge valuable inputs from Christian Löw and Andreas Freund in designing and construction of experimental setup and developing finite element model for thermal parameter evaluation of lithium-ion cells at ICVT. I greatly appreciate help from Christian Hellwig in continuously improving the electrochemical heat generation model developed at ITT, DLR, Stuttgart. Moreover help from Seniz Sörgel in carrying out battery cycling experiments at ITT, DLR is also greatly acknowledged. Additionally I thank Mr. Thomas Lorenz and his team from the ICVT technical workshop and Holger Aschenbrenner for their support in the design and construction of experimental setups.

My special thanks to all the staff members and faculty at ICVT whom I always found friendly, supportive, and welcoming. Ines Lauerwald, Christian Spengler, Philipp Günther, Manuel Huber, Michaela Auerbach, Katrin Hungerbühler are few to mention. I also want to thank members of the computational electrochemistry group at ITT, DLR for being gracious and friendly during my stay there.

In the end I wish to express my greatest regards to my friend Robert Fettig and appreciate his help and support throughout my stay at ICVT. Moreover I highly appreciate Hannes Meinhold for sparing his valuable time to help.

I really feel short of words in expressing my feelings of love, affection, and gratitude for my family back home who always gave me energy to move on no matter how hard the times were. I wish them to stay around always.

Stuttgart, January 2016 Muhammad Wasim Tahir

Table of contents

Symbol Lists

Abbreviations

26650m1A®	2.3 Ah LFP cell from A123 Systems
1D	One dimensional
2D	Two dimensional
3D	Three dimensional
A123®	A123 Systems GmbH (Battery manufacturing)
ANSYS®	Finite element software package
APDL®	ANSYS parametric design language
ASTM	American Society for Testing and Materials
BEV	Battery electric vehicle
BLAS	Basic linear algebra subprogram
CAD	Computer assisted design
CATIA®	CAD software package
CC	Constant current
CC	Current collector
CCCV	Constant current constant volt
CoV	Cut off voltage
CT	Computer tomography
CV	Constant voltage
CW	Cell wall
DAE	Differential algebraic equation
DC	Direct current
DENIS©	Detailed electrochemistry and numerical impedance solver

Symbols

DETCHEM	Detailed chemistry software package
Disch.	Discharge
DLR	German Aerospace Center (Deutsches Zentrum für Luft- und Raumfahrt)
DOD	Depth of discharge
DOF	Degrees of freedom
EC	Ethylene carbonate
ECD	Equivalent circuit diagram
EC-T	Electrochemical-thermal
EpoSS	European Technology Platform on Smart Systems Integration
EV	Electric vehicle
FE	Finite element
FEA	Finite element analysis
GHG	Greenhouse gas
HEV	Hybrid electric vehicle
HG	Heat generation
HPPC	Hybrid Pulse Power Characterization
HT	Heat transfer
IC	Initial conditions
BC	Boundary conditions
ICE	Internal combustion engine
IEA	International Environmental Agency
IHL	Inner Helmholtz layer
JR	Jellyroll
LAPACK	Linear algebra PACK
LFP	Lithium-iron-phosphate
LMO	Lithium-manganese-oxide
LTO	Lithium-titanate-oxide
M	Metal
MSMD	Multi-scale multi-domain/dimension
NCA	Lithium-nickel-cobalt-aluminium-oxide
NMC	Lithium-nickel-manganese-cobalt
OHL	Outer Helmholtz layer

PCM	Phase change material
PHEV	Plugin hybrid electric vehicle
PNGV	Partnership for New Generation of Vehicles
PROE®	CAD software package
Regen	Regeneration
SAFT®	SAFT Inc. (Battery manufacturing)
SEI	Solid electrolyte interface
SOC; SOC_i	State of charge; state of charge at start of discharge
SOD	State of discharge
SHE	Standard hydrogen electrode
VL 7P®	7 Ah NCA cell from SAFT Inc.

Chemical formulae

C_6	Graphite
CoO_2	Cobalt(II)-oxide
CO_2	Carbon dioxide
$FePO_4$	Iron phosphate
H_2	Hydrogen
H_2O	Water
H_2SO_4	Sulphuric acid
KOH	Potassium hydroxide
LiC_6	Lithium-graphite (lithiated graphite)
$LiCoO_2$	Lithium-cobalt-oxide or LCO
$LiFePO_4$	Lithium-iron-phosphate or LFP
$LiPF_6$	Lithium hexafluorophosphate
$LiMn_2O_4$	Lithium-manganese-oxide or LMO
$LiNi_{0.8}Co_{0.15}Al_{0.05}O_2$	Lithium-nickel-cobalt-aluminum-oxide or NCA
$LiNiMnCoO_2$	Lithium-nickel-manganese-cobalt-oxide or NMC
MH	Metal hydride
NiCd	Nickel-cadmium

NiMH	Nickel-metal-hydride
NiOOH	Nickel oxyhydroxide
$Ni(OH)_2$	Nickel(II)-hydroxide
Pb	Lead metal
PbO_2	Lead oxide
$PbSO_4$	Lead sulphate

Latin symbols

1, 2	(-)	Radiating surfaces 1 and 2
A	(m^2)	Area
A_1	(m^2)	Area of radiating surface 1
A_2	(m^2)	Area of radiating surface 2
A_a; A_b	(m^2)	Areas of radiating surface *a* and *b*
a	(-)	Radiating surfaces *a*
a_i	(-)	Activity of species *i*
B	(-)	Bruggeman exponent
b	(-)	Radiating surfaces *b*
C	(F); (Ah)	Capacitance; Capacity
c	($J/(m^3 \cdot K)$)	Volume specific heat capacity
c_P	($J/(kg \cdot K)$)	Specific heat capacity
c_0	(kg/m^3)	Concentration of ionic species at the electrode surface
c_B	(kg/m^3)	Concentration of the bulk solution
c_i	(kg/m^3)	Concentration of species *i*
∇c_i	(kg/m^3)	Species *i* concentration gradient
D	(m^2/s)	Diffusivity or diffusion coefficient
D_e	(m^2/s)	Electrolyte diffusivity
D^{eff}	(m^2/s)	Effective diffusion coefficient
$\not{D}_{\pm}^{eff}$	($mol/(C \cdot \Omega \cdot m)$)	Migration coefficient of the positive and negative ions
D_i	(m^2/s)	Diffusion coefficient of species *i*
$\not{D}_i^{eff}$	($mol/(C \cdot \Omega \cdot m)$)	Effective migration coefficient of species *i*

$d(A_1)$, $d(A_2)$	(-)	Differential patches on radiating surfaces 1 and 2
E^0	(V)	Standard half-cell potential
E	(J/mol); (%)	Capacitor stored energy; cumulative error
E; E_{cell}	(V)	Electrochemical cell potential
E_a	(J/(mol·K))	Activation energy
E_{an}	(V)	Anode potential
E_{ca}	(V)	Cathode potential
E_{eq}	(V)	Equilibrium cell potential
e_0	(V)	Standard electrode potential
e_{0a}	(V)	Standard anodic potential
e_{0c}	(V)	Standard cathodic potential
e_a	(V)	Anodic potential
e_c	(V)	Cathodic potential
F	(C/mol)	Faraday's constant = 96487
$\dot{F}$	(-)	Form factor or view factor between radiating surfaces
$\dot{F}_{12}$	(-)	Radiant energy fraction from surface 1 to surface 2
$\dot{F}_{21}$	(-)	Radiant energy fraction from surface 2 to surface 1
$\dot{F}_{ab}$	(-)	View factor between radiating surfaces *a* and *b*
$F_{s\text{-}w}$	(-)	View factor between cell surface and climate chamber components
$f_{\pm}$	(-)	Activity coefficient
G	(J)	Gibb's energy
ΔG	(J)	Free energy change
ΔG_M	(J/mol)	Molar free energy of reaction
ΔG^0	(J/mol)	Standard free energy
h_c	(W/(m^2·K))	Film coefficient for cooling
h_f	(W/(m^2·K))	Heat transfer or film coefficient
ΔH	(J/mol)	Enthalpy change
I	(A)	Applied current
i_0	(A/m^3)	Exchange current density
i_{0a}	(A/m^2)	Anodic exchange current density
i_{0c}	(A/m^2)	Cathodic exchange current density

Symbols

i_{00}	(A/m^3)	Pre-exponential factor for exchange current density
i	(A/m^2)	Current density
i_a	(A/m^2)	Anodic current density
i_c	(A/m^2)	Cathodic current density; Cathodic current
i_L	(A/m^2)	Limiting current density
i^V	(A/m^3)	Volumetric current density
j_-	(mol/(m^3·s))	Rate of reaction of the anion per unit volume
k	(W/(m·K))	Thermal conductivity
$[k]$	(W/(m·K))	Thermal conductivity tensor
k_r	(W/(m·K))	Thermal conductivity in radial direction
k_{ref}	(W/(m·K))	Thermal conductivity of reference material
k_S	(W/(m·K))	Thermal conductivity of specimen material
k_{xx}, k_{yy}, k_{zz}	(W/(m·K))	Anisotropic components of thermal conductivity
k_z	(W/(m·K))	Thermal conductivity in axial direction
L	(m)	Length
l	(m)	Length (of conducting path)
M_i	(kg/mol)	Mean molar mass of phase i
m	(kg)	Mass
N	(mol)	Overall molar mass
N	(-)	Number of radiating surfaces
N	(kg/(m^2·s))	Diffusion flux
N_i	(kg/(m^2·s))	Diffusional flux of species i
n	(-)	Number of electron moles
$\mathbf{n}$	(-)	Unit vector, normal to the surface
$\mathbf{n}_1$, $\mathbf{n}_2$	(-)	Surface normal vectors of differential patch d(A_1) and d(A_2)
P	(Pa)	Pressure
Pr	(-)	Prandtl number
Q	(C)	Charge
$\dot{Q}$	(J/s)	Heat flow rate
$\dot{Q}_{12}$	(J/s)	Radiative heat exchange between surface 1 and surface 2
$\dot{Q}_a$	(J/s)	Radiative heat emitted or received by surface a
$\dot{Q}_{ab}$	(J/s)	Radiative energy exchanged between surfaces a and b

$\dot{Q}_{gen}$	(J/s)	Overall heat generation rate
$\dot{Q}_{irr}$	(J/s)	Irreversible heat generation rate
$\dot{Q}_{joul}$	(J/s)	Heat generation rate due to joule effects
$\dot{Q}_{pol}$	(J/s)	Heat generation rate due to polarization
$\dot{Q}_{r}$	(J/s)	Heat flow in radial direction
$\dot{Q}_{rej}$	(J/s)	Overall heat dissipation rate
$\dot{Q}_{rej,\ con}$	(J/s)	Convective heat dissipation rate
$\dot{Q}_{rej,\ rad}$	(J/s)	Radiative heat dissipation rate
$\dot{Q}_{rev}$	(J/s)	Reversible heat generation rate
$\dot{Q}_{V}$	(J/(s·m^3))	Volumetric heat generation rate
$\dot{Q}_{z}$	(J/s)	Heat flow in axial direction
q	(J/(s·m^2))	Heat flux
[**q**]	(J/(s·m^2))	Heat flux vector
$\mathbf{q}_{con}$	(J/(s·m^2))	Convective heat flux
$\mathbf{q}_{rad}$	(J/(s·m^2))	Radiative heat flux
q_x, q_y, q_z	(J/(s·m^2))	Heat flux in x, y, and z directions
R	(J/(mol·K))	Ideal gas constant = 8.3145
R	(Ω)	Ionic species flow resistance
R_{el}	(Ωm^2)	Electrolyte resistance
r	(m)	Radius
r_{12}	(m)	Distance between differential area patches d(A_1) and d(A_2)
$R_{i,gen}$	(mol/(m^3·s))	Net generation rate of species i (reaction source term)
R_{ohm}	(Ω)	Ohmic resistance of electronic conductor
S	(J/K)	Entropy
ΔS	(J/(mol·K))	Entropy change of entropy reaction
T	(K)	Absolute temperature
T_a, T_b	(K)	Absolute temperatures at radiating surface a and b
T_{amb}	(K)	Ambient or operating temperature
T_B	(K)	Bulk temperature
T_c	(K)	Coolant temperature
T_{ini}	(K)	Initial temperature at the beginning of simulation
T_{max}	(K)	Maximum temperature

Symbols

T_{min}	(K)	Minimum temperature
T_{ref}	(K)	Temperature of reference material
T_s	(K)	Solid surface temperature
T_{sur}	(K)	Cell surface temperature
T_w	(K)	Climate chamber walls temperature
ΔT_{eff}	(K)	Effective temperature gradient = ($T_{max} - T_{min}$)
t	(s)	Time
t/t_{th}	(-)	Normalized time
$t_{+/-}$	(-)	Transference number for cations and anions
u_i	((m^2·mol)/(J·s))	Mobility of species *i*
U	(V)	Applied voltage
V	(m^3)	Volume
v	(m^2/s)	Kinematic viscosity
$[v]$	(m/s)	Velocity vector for bulk (mass) transport of fluid
v_i	(-)	Number of equivalents of species *i* taking part in reaction
v_i	(m/s)	Velocity of species *i* in the electrolyte phase
W	(W)	Electric work
x, y, z	(m)	X, Y, and Z coordinates of space
z	(-)	Charge or valence number
z_i	(-)	Valence number of species *i*

Greek symbols

α	(m^2/s)	Thermal diffusivity
α	(-)	Dimensionless charge transfer coefficient
∇	(-)	Vector (divergence) operator
$\nabla\phi$	(V)	Potential gradient
δ	(m)	Thickness of the concentration gradient
δ_T	(m)	Thermal boundary layer Thickness
δ_v	(m)	Velocity boundary layer Thickness
ε	(-)	Pore volume fraction or porosity

ε	(-)	Emissivity
ε_a	(-)	Emissivity of radiating surface *a*
ε_s	(-)	Emissivity of cell outer surface
κ	(S/m)	Ionic conductivity
κ^{eff}	(S/m)	Effective ionic conductivity (corrected by porosity)
κ_D^{eff}	(S/m)	Effective diffusional ionic conductivity
κ_{el}	(S/m)	Electrolyte specific conductivity
η	(V)	Overpotential
η_{act}	(V)	Activation overpotential
η_{con}	(V)	Concentration overpotential
η_{el}	(V)	Electrolyte polarization
η_{ohm}	(V)	Ohmic polarization
ρ	(Ωm)	Material specific resistance or resistivity
ρ	(kg/m^3)	Density
ρ_{el}	(Ωm)	Resistivity of the electrolyte
σ	(W/(m^2·K^4))	Stefan-Boltzmann constant, = 5.676 × 10^{-8}
τ	(-)	Tortuosity of porous media
φ	(-)	Circumferential angle of cylindrical cell
ϕ	(V)	Solution or electrolyte potential
$\Delta\phi_{an}$	(V)	Potential gradient at anode-electrolyte interface
$\Delta\phi_{ca}$	(V)	Potential gradient at cathode-electrolyte interface
ϕ_{el}	(V)	Electrolyte potential
$\phi_{el,an}$	(V)	Electrolyte potentials at the anode-electrolyte interfaces
$\phi_{el,ca}$	(V)	Electrolyte potentials at the cathode-electrolyte interfaces
θ_1	(°)	Angle corresponding to differential patch d(A_1)
θ_2	(°)	Angle corresponding to differential patch d(A_2)

Subscripts

0	Initial, standard, and/or equilibrium state
00	Pre-exponential factor

Symbols

±	Anionic and cationic
Al	Aluminium
a	Anodic
act	Activation
amb	Ambient
an	Anode
B, *b*	Bulk
Cu	Copper
c	Cathodic
ca	Cathode
cell	Cell
con	Convective
conc	Concentration
D	Diffusional
e	Electrode
el	Electrolyte
el, *an*	Electrolyte-anode
el, *ca*	Electrolyte-cathode
eq	Equilibrium
f	Film coefficient
gen	Heat generation
i, gen	Net generation rate of species *i*
ij	Ionic species *i* and *j*
ini	Initial
irr	Irreversible
joul	Joule
L	Limiting
M	Molar
max	Maximum
min	Minimum
ohm	Ohmic
P	Specific heat

pol	Polarization
rad	Radiative; radiant
rej	Rejected or dissipated
rej, con	Dissipation through convection
rej, rad	Dissipation through Radiation
rev	Reversible
ru	Repeat unit
s; *sur*	Solid surface; cell surface
sep	Separator
s-w	Surface to wall
T	Thermal
th	Theoretical
V	Volumetric
v	Velocity
w	Wall
x, y, z	Spatial coordinates
xx, *yy*, *zz*	Anisotropic components

Superscripts

0	Standard
©	Copyright
eff	Effective
®	Trade mark
V	Volumetric

Abstract

Present day civilization has become addicted to the energy which is proving hard to harvest as days go by due to scarcity of conventional energy sources. Many efforts are being invested to produce cheap, abound, and clean energy from nuclear fusion which to the experts is still decades away. This makes us to stay on conventional energy sources the major of which comes from fossil fuels. Transportation sector is the largest consumer of oil and a major contributor to air pollution and greenhouse gases (GHG). Researchers suggest that global oil production could reach its maximum any time from now on to 2030 after which it would enter terminal decline. To delay this point of maximum production (peak oil) and control GHG emissions, oil consumption especially in ICE vehicles needs to be economized. Electrification and electric hybridization of vehicles could serve the purpose to some extent.

Recent advancements in the battery technologies have brought the energy and power ratings of electric vehicles to scales comparable to that of the ICE vehicles. Amongst the present day battery technologies used in electric vehicles (EVs) and hybrid electric vehicles (HEVs), lithium-ion stands superior due to high energy density, low self-discharge, and higher current output. Almost all of the automotive battery technologies require effective cooling system to avoid thermal runaway that could be caused by excessive release of energy due to high loads, short circuits, or accidents. Comprehensive thermal analysis of individual cell types used to power automotive has seldom been realized.

This study is aimed at developing an understanding of thermal responses of different types of EV lithium-ion battery technologies under variable loads and environmental conditions using cycling experiments combined with detailed simulations. The ultimate goal is to develop and validate a detailed multi-scale multi-domain (MSMD) model which can be used as an adequate tool for design and optimization of thermal management systems of EV battery packs and modules.

Abstract

Thermal modelling is an effective tool for predicting thermal behaviour of individual cells and packs. A complete thermal model of a battery system consists of two parts; an electrochemical (EC) heat generation model and a heat transport (HT) model. A coupled electrochemical-thermal (EC-T) model can form the basis for devising an effective thermal management and cooling system for EVs and HEVs.

A MSMD model has been developed to simulate thermal variations taking place in the selected lithium-ion cells under different loads and environmental conditions. 3D heat transfer model and 1D electrochemical heat generation model have been coupled using different coupling methods. To predict thermal behavior of a battery using a thermal model, accurate knowledge of model parameters is a prerequisite. In this work different methods based on experiments and computer simulations have been worked out to find thermal and physical properties of lithium-ion cells.

A nanophosphate based LFP cell 26650 has been used for experimental thermal response study. Effect of ambient temperature (T_{amb}) and applied current on cell surface temperature (T_{sur}) and cell discharge behaviour has been probed. Moreover open circuit voltage (OCV) varying as a function of T_{amb} has also been investigated. Outcomes of these investigations have been used partially to validate MSMD EC-T model mentioned above. The above mentioned experiments have been simulated under similar conditions using the thermal model. Furthermore, additional parameters and loading conditions have also been investigated through detailed simulations.

An ideal battery module for EV power delivery system should be compact and low weight. Cooling systems have to be designed in such a way not burden the module with extra weight and dimensions. Higher power demand in EVs puts an extra thermal load on batteries and requires an effective cooling strategy to avert thermal runaway. It is important to identify areas on the cell exterior where heat could effectively be rejected from. In addition, thermally efficient cell designs are required. Such designs should be aimed at dissipating the generated heat with minimum of external efforts and resources involved. A thorough numerical investigation into the thermal response of VL 7P cell under the influence of changes in geometrical design parameters and cooling conditions has been conducted. Additionally, impact of cell configurations on thermal behavior of the cells has also been investigated.

After validation, the model has then been used to carry out detailed simulations. Dynamic thermal behavior of 26650 cell has been studied under constant current loads at different operating

temperatures. In addition to constant current loads, high current pulses for short intervals have also been simulated as per HPPC test. Moreover, thermal response of the cell at high operating temperatures due to side reactions taking place at SEI has also been simulated.

Experimental findings lead to the conclusions that lower operating temperature and higher applied currrents erode cell capacity causing reduction in power output efficiency of the cell. Optimum operating temperature window for 26650 cell has been found to be between 10 °C and 50 °C. Simulation results have been found in good agreement with the experimental findings. At higher operating temperatures and lower currents, a less rigorous vertical coupling method that accounts only for temporal variations can be employed. A more rigorous horizontal coupling method can be used costing higher computation time and resources.

Improvement in thermal efficiency of the cell caused by thicker cell wall and current collectors has been observed to be too small to compensate for the added weight and cost. Flat cell configuration has been found to be thermally more efficient than cylindrical and prismatic cells. Simulation results suggest that 26650 cell can function over a wider useable energy and operating temperature windows without significantly compromising its power deliverance capabilities. It has also been found that the temperature surge caused by **SEI** side reactions in 26650 cell while in idle mode dies down spontaneously thus causing no harm to the cell.

The model has been found fully capable of handling spatial as well as temporal variations in parallel making it suitable to predict dynamic thermal behavior of the cells. Though model has shown promise in predicting thermal behavior of the selected cells, results suggested that at high currents and subzero temperatures, model has a room for further improvement. It is suggested to improve model by further refining model parameters. It is proposed to further investigate the parasitic side reactions and SEI mechanisms at elevated temperatures. Extension of 3D EC-T model to a module level with actual flow simulations using CFD tools and investigating module cooling strategies using cooling fluids and phase change materials (PCM) is proposed too.

Abstract

Zusammenfassung

Die heutige Zivilisation ist von Energie abhängig geworden, die sich, aufgrund der Knappheit der konventionellen Energiequellen, als immer schwerer zu gewinnen erweist. Viele Anstrengungen werden unternommen, um kostengünstige, nahezu unbegrenzte saubere Energie aus Kernfusion zu gewinnen, wobei bis dahin nach Meinung der Experten noch Jahrzehnte vergehen. Das zwingt uns weiterhin auf konventionelle Energieträger zu setzen, wobei die wichtigsten davon die fossilen Brennstoffe sind. Der Transport-Sektor ist der größte Verbraucher von Öl und der größte Produzent von Umweltverschmutzung und Treibhausgasen (GHG). Forscher prophezeien, dass die weltweite Ölförderung ihr Maximum jederzeit von heute an bis 2030 erreichen könnte und sich diese anschließend unumkehrbar verringert. Um das Erreichen dieses Punktes der maximalen Ölproduktion (Oil-Peak) zeitlich zu verzögern und zur Kontrolle der Treibhausgas-Emissionen, muss der Öl-Verbrauch vor allem von Verbrennungsmotoren sparsamer werden. Die Elektrifizierung und die elektrische Hybridisierung von Fahrzeugen können in gewisser Weise dazu dienen.

Neue Entwicklungen in der Batterie-Technologie haben dazu geführt, dass die Leistung von Elektrofahrzeugen heutzutage mit denen von herkömmlichen Kraftfahrzeugen vergleichbar ist. Die aktuell verwendete Batterie-Technik in Elektrofahrzeugen (EVs) und Hybridfahrzeugen (HEVs) basiert auf Lithium-Verbindungen und zeichnet sich aus durch eine hohe Energiedichte, eine geringe Selbstentladung und höhere Ausgangsstromstärken. Fast alle der Kfz-Batterie-Techniken erfordern effektive Kühlsysteme um thermische Instabilität zu vermeiden, welche durch übermäßige Freisetzung von Energie durch hohe Lasten, Kurzschlüsse oder Unfälle verursacht werden können. Umfassende thermische Analysen von einzelnen Zelltypen, die zur Versorgung von Fahrzeugen verwendet werden, wurden nur selten realisiert.

Abstract (German)

Diese Arbeit verfolgt das Ziel der Entwicklung eines besseren Verständnisses des thermischen Verhaltens der verschiedenen Arten von EV Lithium-Ionen-Akkumulatoren unter veränderlichen Lasten und Umweltbedingungen durch Verwendung zyklischer Experimente in Kombination mit detaillierten Simulationen. Ziel ist die Entwicklung und Validierung eines detaillierten Multiskalen Multi-Domain (MSMD) Modells, das als geeignetes Werkzeug für die Auslegung und Optimierung von Wärmemanagementsystemen der EV Akkupacks und Module verwendet werden kann. Die thermische Modellierung ist ein effektives Werkzeug für die Vorhersage des thermischen Verhaltens der einzelnen Zellen und Packs. Ein vollständiges thermisches Modell eines Batteriesystems besteht aus zwei Teilen: einem Modell für die elektrochemische Wärmeerzeugung (EC) und einem Modell für den Wärmetransport (HT). Ein gekoppeltes elektrochemisch-thermisches (EC-T) Modell kann die Grundlage für die Ausarbeitung eines effektiven Wärmemanagement- und Kühlsystems für EVs und HEVs bilden.

Ein MSMD-Modell wurde entwickelt, um Temperaturschwankungen in den ausgewählten Lithium-Ionen-Zellen unter verschiedenen Lasten und Umgebungsbedingungen zu simulieren. Ein 3D Wärmetransportmodell und ein 1D Modell für die elektrochemische Wärmeerzeugung wurden in Verbindung mit verschiedenen Kopplungsmethoden verwendet. Um das thermische Verhalten einer Batterie mit einem thermischen Modell vorherzusagen, ist die genaue Kenntnis der Modellparameter Voraussetzung. In dieser Arbeit wurden verschiedene Methoden basierend auf Experimenten und Computersimulationen erarbeitet, um thermische und physikalische Eigenschaften von Lithium-Ionen-Zellen zu bestimmen.

Eine Nanophosphate-basierte LFP Zelle 26650 wurde für die experimentelle Untersuchung des thermischen Verhaltens verwendet. Der Einfluss der Umgebungstemperatur (T_{amb}) und des anliegenden Stroms auf die Zelloberflächentemperatur (T_{sur}), sowie das Entladungsverhalten der Zelle wurden überprüft. Darüber hinaus wurde die Leerlaufspannung (OCV) als Funktion der Umgebungstemperatur T_{amb} untersucht. Die Ergebnisse dieser Untersuchungen wurden teilweise eingesetzt, um das oben genannte MSMD EC-T-Modell zu validieren. Die oben genannten Experimente sind unter ähnlichen Bedingungen mit dem thermischen Modell simuliert worden. Darüber hinaus wurden zusätzliche Parameter und Belastungsbedingungen durch detaillierte Simulationen untersucht.

Ein ideales Batteriemodul für EV Leistungsversorgungssysteme sollte kompakt sein und ein geringes Gewicht haben. Die Kühlsysteme müssen so entworfen werden, dass sie das Gewicht

und die Abmessungen der Module nicht erhöhen. Der hohe Leistungsbedarf der EVs stellt eine zusätzliche thermische Belastung der Batterien dar und erfordert eine effektive Kühlstrategie, um thermisches Durchgehen zu verhindern. Es ist wichtig, die Bereiche an der Zellaußenseite zu identifizieren, an denen die Wärme effektiv abgeleitet werden kann. Zusätzlich sind thermisch effiziente Zellkonstruktionen erforderlich. Solche Konstruktionen sollten das Abführen der erzeugten Wärme mit einem Minimum an externem Aufwand und Ressourcen bewerkstelligen. Eine gründliche numerische Untersuchung des thermischen Verhaltens der Zelle VL 7P bei Änderungen der geometrischen Entwurfsparameter und der Kühlbedingungen wurde durchgeführt. Zusätzlich wurde der Einfluss des Zellaufbaus auf das thermische Verhalten der Zellen untersucht.

Nach der Validierung wurde das Modell eingesetzt, um detaillierte Simulationen durchzuführen. Das dynamische, thermische Verhalten der 26650 Zelle wurde unter Konstantstromlasten bei verschiedenen Betriebstemperaturen untersucht. Neben Konstantstromlasten wurden hohe Stromimpulse für kurze Intervalle nach dem HPPC (Hybrid Pulse Power Characterisation) Test simuliert. Darüber hinaus wurde das thermische Verhalten der Zelle bei hohen Betriebstemperaturen aufgrund von stattfindenden Nebenreaktionen in der SEI (Solid Electrolyte Interface) Schicht simuliert.

Experimentelle Untersuchungen führen zu der Schlussfolgerung, dass eine niedrigere Betriebstemperatur und eine höhere Stromlast den Leistungs-Wirkungsgrad der Zelle reduzieren. Als optimales Betriebstemperaturfenster für die 26650 Zelle wurde der Bereich zwischen 10 °C und 50 °C gefunden. Die Simulationsergebnisse stehen in guter Übereinstimmung mit den experimentellen Resultaten. Bei höheren Betriebstemperaturen und geringeren Strömen kann eine weniger rigorose vertikale Kopplungs-Methode für zeitliche Variationsrechnungen eingesetzt werden. Eine rigorosere horizontale Kopplungs-Methode kann angewendet werden, welche jedoch eine höhere Rechenzeit und mehr Ressourcen benötigt.

Eine Verbesserung der thermischen Effizienz der Zelle konnte bei Erhöhung der Dicken von Zellenwand und Stromabnehmer beobachtet werden, die jedoch zu gering war, um das zusätzliche Gewicht und die Kosten zu kompensieren. Ein flacher Zellenaufbau ist thermisch effizienter als zylindrische und prismatische Zellen. Die Simulationsergebnisse zeigen, dass die 26650 Zelle über einen größeren Bereich nutzbarer Energie und ein größeres Betriebstemperaturfenster ohne signifikante Einbuße bei der Leistungsversorgung. Ebenfalls

wurde festgestellt, dass der Temperatur-Anstieg durch SEI Nebenreaktionen in der 26650 Zelle während des Leerlauf-Modus abklingt, wodurch kein Schaden an der Zelle auftrat.

Das Modell ist in der Lage, parallel räumliche und zeitliche Veränderungen abzubilden und das dynamische thermische Verhalten der Zellen vorherzusagen. Obwohl das Modell das thermische Verhalten der ausgewählten Zellen bei hohen Stromlasten und Minus-Temperaturen beschreibt, bestehen weitere Verbesserungsansätze. Es wird vorgeschlagen, das Modell durch präzisierte Parameter zu verbessern. Es wird empfohlen, die parasitären Nebenreaktionen und die SEI Mechanismen bei erhöhten Temperaturen näher zu untersuchen. Die Erweiterung des EC-T 3D-Modells auf Modul-Niveau durch Strömungssimulationen mit CFD-Tools und Untersuchungen zu Modul-Kühlungsstrategien mit Kühlflüssigkeiten und Phasenwechselmaterialen (PCM) werden ebenfalls vorgeschlagen.

Chapter1

Introduction

Fairly cheap and abound energy is the bloodline of modern world. Owing to the fact that mass is highly condensed form of energy, according to Einstein's $E = mC^2$, we humans are supposed to have ample supply of energy. But unfortunately, at the time, no straight forward mechanism is available to put this abundant energy into use. Nuclear fusion is the most efficient and clean method to convert mass into energy. Many efforts have been made to fuse hydrogen atoms in laboratory and different types of reactors to obtain fusion energy but to the disappointment, watt balance turned out to be negative every time. That means the system consumes more energy than what it produces. Even if the output energy exceeds the input it remains so small that it is not viable commercially. According to experts, we are still 30 - 40 years away from making fusion a workable energy source and by the time we get to that point we have to stay on conventional energy sources the major of which comes from fossil fuels [1].

The main energy consuming sectors are transportation, residential, commercial, and industrial. Transportation sector is the major consumer of oil and contributor to air pollution and greenhouse gases (GHG). This sector has observed the largest growth in demand in recent decades which has largely come from new demand for personal–use–vehicles powered by internal combustion engines (ICE). Transportation sector also has the highest oil consumption rates, accounting for approximately 68.9 % of the oil used in the United States in 2006, and 55 % used worldwide as reported in Peaking of World Oil Production created for the US Department of Energy in 2005[2, 3].

Peak oil is the point in time when the maximum rate of global petroleum extraction is reached, after which the rate of production enters terminal decline (Figure 1.1). Peak in the global oil production could reach any time from now on to 2030, researchers suggest. To delay peak oil and control GHG production, at least to the point when an alternate reliable and clean source of energy gets established, some strategy has to be devised to economize the use of oil especially in ICE vehicles. Electrification and electric hybridization of vehicles could retrench the oil consumption and GHG production by tremendous amounts [2, 3].

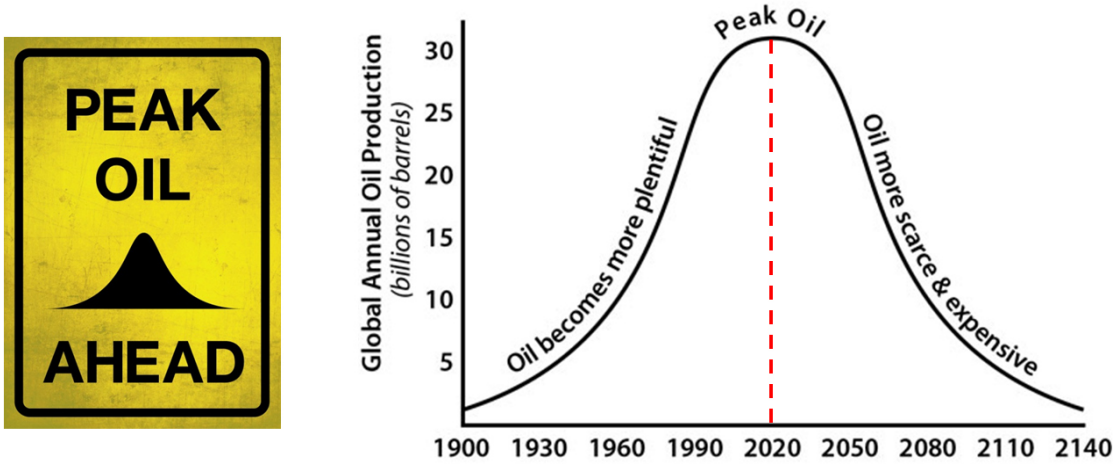

Figure 1.1: Bell curve for current global oil production. This curve is mere an approximation and indicator of the current and future oil production scenarios [18].

Despite many efforts made in the past to use electrical energy to power vehicles, electric propulsion proved to be a wild goose chase due to short ranges and low power offered by the existing energy storage systems as compared to ICE vehicles. But recent advancements in the battery technologies have brought the energy and power ratings of electric vehicles to scales comparable to that of ICE vehicles. Amongst the present day battery technologies used in electric and hybrid electric vehicles, lithium-ion stands superior due to high energy density, low self-discharge, and higher current output. Based on the combination of different electrode chemistries, lithium-ion batteries are divided into different types. The most dominant of these technologies specifically for automotive application are lithium-manganese-oxide (LMO), lithium-nickel-cobalt-aluminium-oxide (NCA), lithium-nickel-manganese-cobalt (NMC), lithium-titanate-oxide (LTO), and lithium-iron-phosphate (LFP) [51].

1.1 Motivation

Rates of chemical reactions are significantly influenced by temperature due to dependence of kinetic parameters on temperature. It has been approximated that the rate of chemical reaction doubles for every 10 °C rise in temperature. In case of electrochemical reactions that means the amount of equivalent current gets doubled. In other words higher the current drawn from a battery higher will be the rise in its temperature. This strong dependence of current on temperature becomes even more significant in case of electric propulsion where sudden draw of higher currents during acceleration could cause the temperature of the cells to rise sharply [19].

Comprehensive thermal analysis of individual cell types used to power automobiles has seldom been realized specifically for the new battery technologies emerging from intensive research in the field of lithium-ion batteries. Amongst these new technologies LFP and NCA are the most sought-after technologies as compared to the rest. Thus two different types of high-power lithium-ion cells based on the above mentioned cathode chemistries have been selected for this work. These cells include VL P7 from SAFT consisting of NCA cathode and ANR26650M1A (referred to as 26650 in this text) from A123 Systems consisting of LFP cathode. The choice has been made based on individual merits on vehicle application and growing demand of these cells in the vehicle market. Hence a detailed investigation into the thermal behavior of selected cell types is rational.

Almost all of the automotive battery technologies require elaborate monitoring and effective cooling system to avoid thermal runaway that could be caused by excessive release of energy due to high loads, short circuits, or accidents [51]. Moreover calendar and cycle life as well as performance of the battery is greatly influenced by temperature. A high temperature can cause fire or explosion in lithium-ion battery packs, therefore controlling the temperature is essential not only for performance but also for safety purposes. Thus it is important to fully understand how a typical battery responds thermally to the applied loads and environmental conditions which can effectively be achieved using different experimental and modelling techniques.

Thermal modelling is an effective tool for predicting thermal behaviour of individual cell and packs. A complete thermal model of a battery system consists of two parts; an electrochemical heat generation model and a heat transport model. Both the heat generation and heat transfer

models are part and parcels as far as accurate prediction of thermal behaviour of a cell is concerned. Hence it is essential to comprehend the coupled behavior of these two mechanisms. A coupled electrochemical-thermal (EC-T) model can form the basis for devising an effective thermal management and cooling system for electric and hybrid electric vehicles (EVs and HEVs).

Different strategies have been adopted by the researchers to develop EC-T coupled models for lithium-ion batteries. Due to inconsistent geometry of cells, complex nature of electrochemical and transport processes, and difficulties involved in dynamic coupling, most of the EC-T coupled models have been restricted to a 2D level [5, 6, 7, 8, 9] or assumed a spatially uniform temperature [10]. Some researchers used temperature dependent physiochemical properties like diffusion coefficient and electrolyte ionic conductivity to couple electrochemical and thermal models through Arrhenius equation [9, 10, 11, 12]. Others used equivalent-circuit-diagram (ECD) approach to simulate electrical response of an electrochemical system and a lumped thermal model to simulate heat transport inside and out of the cell [13, 14, 15, 16].

Because of high complexity and nonlinearities involved in electrochemical systems, ECDs always remain an approximation [13]. Lumped model does not account for the inner details of the battery geometry [16]. 2D models are not capable of fully predicting the anisotropic nature of thermal responses of individual lithium-ion cells especially in automobile application where higher thermal gradients are expected due to the involvement of higher currents. An innovative coupling strategy has been applied in this study to model thermal behavior of the selected cell types.

1.2 Goals and objectives

This study is aimed firstly at developing an understanding of thermal responses of two different types of lithium-ion battery technologies under variable loads and environmental conditions using cycling experiments. And secondly to study the effect of different parameters on temperature distribution and heat flow patterns in the cell using simulation techniques. The ultimate goal is to develop and validate a detailed multi-scale multi-domain (MSMD) EC-T model which can be used as an adequate tool for design and optimization of thermal management systems of EV battery packs and modules.

To predict thermal behavior of a battery using a thermal model, accurate knowledge of model parameters is a prerequisite. Model parameters can either be derived from the previous findings or determined experimentally as well as using different simulation methods. The more accurate model parameters are the more reliable model is. A great deal of innovation takes place in an effort to improve energy and power ratings of lithium-ion batteries. New materials are being developed at such a pace that it is almost impossible to have a complete knowledge of electrochemical and thermal parameters of the individual cell types present in the market. It is always a challenge to find accurate parameters for a thermal model of a particular cell type. Therefore it is also intended to explore different methods based on experiments and computer simulations to find thermal and physical properties of different types of lithium-ion cells.

1.3 Scope of the work

An introduction to the EV systems is presented in chapter 2 which includes historic developments and future prospects of EVs as well as different types and technologies being developed. Additionally an introduction to different energy storage systems with a brief description and comparison of existing battery technologies is presented. Merits and demerits of battery technologies are discussed in view of the basic criterion required to be fulfilled for automotive application. Moreover risks associated with thermal abuse scenarios and the basic mechanisms driving thermal runaway are described in chapter 2. Finally a brief account on the recent history of lithium-ion battery related accidents is given.

In chapter 3, basic heat transfer mechanisms like conduction, convection, and radiation have been elaborated. In addition, heat generation in electrochemical systems along with the processes driving electrochemical reaction as well as electrochemical reaction parameters have been discussed in detail.

Thermal modelling is an economical and convenient way to predict thermal behaviour of lithium-ion batteries and design effective thermal management system for automobile battery systems. A 3D thermal model for VL 7P cell and a multi-scale dynamic thermal model for 26650 cell have been developed and presented in chapter 4. In multi-scale model, a 1D electrochemical model is made to interact with a 3D finite element (FE) heat transfer model. Mathematical details of the

two models and parameters used are included. A coupling strategy has been devised to make interaction between electrochemical and thermal models more efficient and dynamic preserving much of the geometrical details and electrochemical complexities. Vertical (indirect) and horizontal (direct) coupling methods have been used for the interaction between the two models. Moreover, a review of the previously developed electrochemical heat generation (HG) and heat transfer (HT) models has also been included in chapter 4.

Safety and performance of lithium-ion battery is strictly tied to the operating temperature and loading conditions. Therefore it is important to know how a typical cell responds thermally to the variations in operating temperature and loading conditions especially in automobile application where sudden higher draw of current during the acceleration could make the cell temperature to rise sharply. Detailed experiments have been carried out to understand thermal behaviour of a 26650 cell under the influence of environmental temperature and applied current. Results and description of experimental procedure used have been described and discussed in chapter 5.

Gradients in temperature across the cell and heat flow patterns in and out of the cell body are greatly influenced by geometrical design variations and cell shapes. Chapter 6 deals with studying the effect of geometrical design variations, like cell-wall and current-collector thickness, on thermal behaviour of VL 7P cell. A 3D heat transfer model have been used for different arbitrary cell geometries like cylindrical, prismatic, and flat assuming steady state conditions and uniform heat generation rates amounting to 8-10 watts per cell. Detailed simulation results are presented and discussed.

To run simulations for carrying out detailed thermal analysis of 26650 cell using the model developed in chapter 4, a prior validation of the model is required in order to prove its authenticity. Hence thermal and electrochemical aspects of the model have been validated against measured cell surface temperature and cell potential (presented in chapter 5) respectively. Validation results have been included in the first part of chapter 7. Once the model is validated, it has been used to conduct thermal analysis of 26650 cell at different ambient temperatures as well as applied currents. Simulations have been carried out using constant current as well as pulse current profile adopted from *FreedomCAR Battery Test Manual for Power-Assist Hybrid Electric Vehicles* [126]. Moreover effect of reactions, taking place at the solid electrolyte interface (SEI),

on thermal behaviour of 26650 cell have also been simulated. Simulation results are presented and discussed in the second part of chapter 7.

Finally, in view of the results obtained from experiments and detailed simulations, some important conclusions have been made and presented at the end of chapter 7. Future possibilities and prospects to extend this work have also been explored towards the end of chapter 7.

Chapter 2

Electric propulsion and energy storage systems

Before moving on to the main body of this work, it would be handy to get introductory background knowledge about electric propulsion and energy storage systems. This chapter covers two major themes: an introduction to the electrically powered vehicle systems which includes historic development and future prospects of electric vehicles as well as different types and technologies of electric vehicles being developed; and a description of construction, working principles, and applications of different types of energy storage technologies. Moreover, an account of performance and safety issues as well as risks associated with thermal abuse of automobile battery systems and control strategies have also been given.

2.1 Electric propulsion

With ever increasing concern about environmental deterioration and GHG emissions caused by gas-fueled road transport, electric vehicles seem quite promising in view of being less hostile towards environment as compared to the traditional ICE technology. In recent years, support for such vehicles to play an important role in reducing environmental burden by controlling CO_2 emission and noise pollution, especially in light vehicles and cars, has tremendously increased.

In HEVs and PHEVs combustion engine runs periodically to assist in making up the power requirements thus indirectly contributing to the GHG emissions. Therefore electric hybridization and electrification of vehicles with the existing battery technologies does not offer complete

solution. Remedy lies in the development of highly efficient battery technologies that could provide sufficient power without engine combined with derivation of electricity from renewable sources. In USA, reduction in GHG emissions by EVs was 20 % in case of coal derived electricity and near 100 percent in case of electric energy derived from hydro or renewable sources. Similar results were found in case of Germany, China, and Japan with the exception that higher reduction was observed with coal derived electricity in case of Germany and Japan due to higher efficiency of coal power plants in these two countries. HEVs and PHEVs are described in the following sections of this chapter [20, 105].

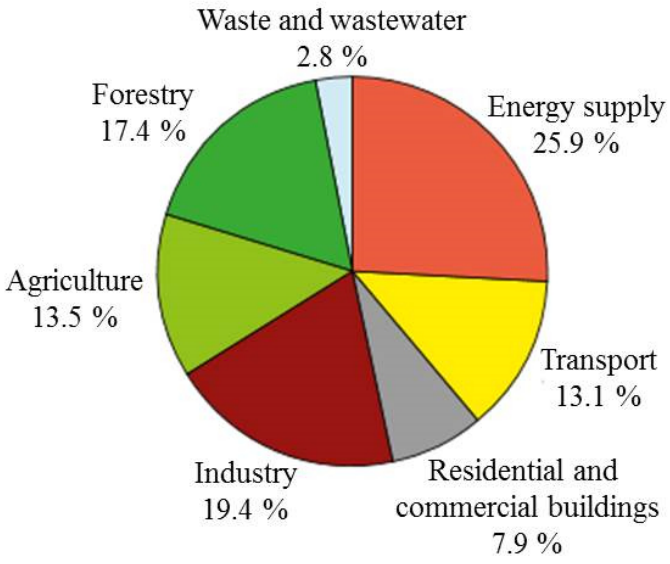

Figure 2.1: Contributions to global GHG emissions by different sectors in 2004. Source: Climate Change 2007 [106].

2.1.1 Evolution of electric vehicles

When and where the very first electric vehicle had been developed is not certain but history could be traced back to the early 19th century. Present day electric vehicle has been evolved over the years. In 1800 AD, invention of Volta pile by Alessandro Volta and discovery of electromagnetic induction by Faraday, in 1831 AD, made the inventors to think about using Volta pile to power electric motor to drive the wheels of a light vehicle. But no significant development took place in the field of electric propulsion until 1859 when the lead-acid battery was invented by Gaston

Planté. Zenobe Theophile Gramme, a Belgian inventor, constructed the first direct current (DC) motor in 1869 producing 746 watts of power which could also be used as generator when rotated mechanically. The availability and capability of both storage batteries and electric motors made it possible to provide sufficient power to drive a road vehicle [22].

During the following years many inventors invented and tried their own versions of electric vehicles and established many speed and distance records prior to the prominence of internal combustion engines (ICEs). At the beginning of 20th century, large number of electric vehicles had been produced to be used as cars, vans, taxis, and buses. However despite the promise of the early electric vehicles, internal combustion engine proved to be more attractive powering option for vehicles once cheap oil had become widely available and the self-starter for the IC engine had been invented in 1911.

a) ***b)***

Figure 2.2: EV examples: *a)* Tesla Roadster; *b)* Tesla Premier Sedan Model-S [28, 29].

Although electric car could not take hold of the automobile market due to easy availability of gasoline, lower speed and range, and higher charging times, nevertheless energy crisis in 1970s and 1980s and fluctuations in the hydrocarbon energy market brought about renewed interest in electric vehicles. Some other factors that contributed to the shift in interest towards electric propulsion systems included environmental damage caused by GHG emissions.

Technological advances in energy storage as well as drive systems gave a further boost to the idea of electrically driven vehicles. Toyota and Honda lead the way in hybrid electric vehicle production. Toyota dominates all the others when it comes to hybrid cars. They have produced hybrid versions of many of their existing models. The first European commercial electric car was

Audi Duo produced in 1997. But now Tesla Motors is marketing a two-seater all-electric sports car with 400 km range topping over at 210 km/h. It has just 4 seconds of transition time for 0 km/h to 96 km/h. Tesla has already delivered more than 2000 Roadsters (Figure 2.2*a*) to its worldwide customers. Built from the scratch Premium Sedan model S (Figure 2.2*b*) has already been introduced in the market. A prolific future of electric cars is already predicted by the auto producers, policy makers, and analysts [23-31].

2.1.2 Future of electric vehicles

Many European countries along with Japan, China, United States, and others have made significant announcements regarding their plans for the introduction of electric vehicles. On the other hand, car manufacturers, battery producers, and academics are joining hands on initiatives like *EUROELECTRIC* Task Force on Electric Vehicles and EpoSS (European Technology Platform on Smart Systems Integration). The European Commission, together with European Investment Bank, has launched the European Green Cars Initiative, with Euro 5 billion dedicated partly to the development and manufacturing of electric cars and batteries and to research.

Although in the past decades, attempts to reintroduce electric vehicles in the market have not been successful, the future looks brighter today owing to the great progress in battery technology. It is expected that by 2050, electric vehicles could capture more than 60 % of new sales and constitute up to 25 % of the global car fleet. An estimate of worldwide future production of all hybrids is shown in Figure 2.3. An ascending trend in all types of HEVs manufacture from 2010 onwards is obvious. But future estimates vary greatly because there still exists an uncertainty regarding the development of technology and consumer behavior [32].

It is indicated, in a recently updated Electric Vehicle Roadmap report by the International Energy Agency (IEA) that future production plans of major EV/PHEV manufacturers are well below the sales targets set by countries. Industry and governments should collaborate closely to achieve the roadmap's vision. Talking specifically of Germany, Gartener Inc. recommends German government must closely examine and reconsider its current efforts regarding e-mobility and expand its funding of research and development programs for battery technology to achieve its goal of substantial EV sales. According to the German government's National Electro-mobility

Development Plan, more than a million electric vehicles are expected to be on the roads by 2020 [34, 35].

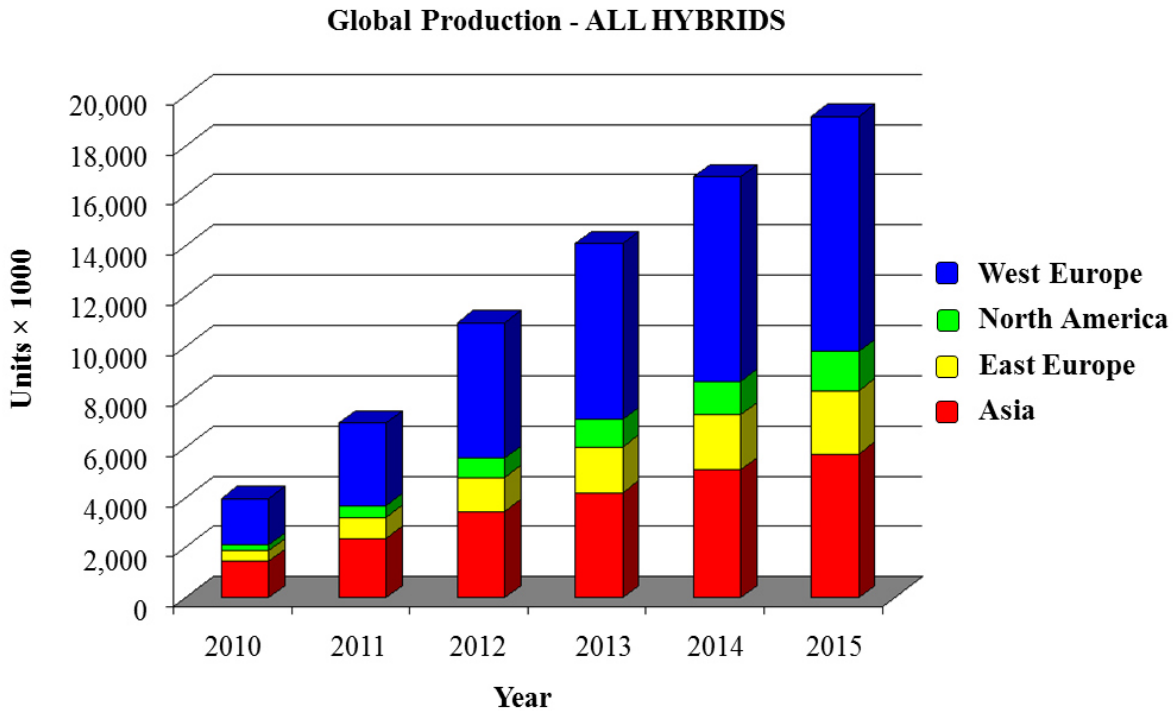

Figure 2.3: An overall worldwide hybrid vehicle production trend [33].

The most important factor to achieve the above mentioned goals is the availability of basic infrastructure to support e-mobility on a mass level that includes efficient charging points and smart grid technology [27, 31].

2.2 Electric vehicle configurations

As mentioned before the early attempts to replace the gasoline-powered vehicles by electrically-powered vehicles failed due to higher costs, short ranges, and poor performance. But thanks to the advances in the automotive and battery technologies during the recent years, a new generation of high performance, low cost electric cars seem to hit the market very soon. In the meantime efforts have been made to combine electric and gasoline power together in a single vehicle. A

number of designs are available in the market or under the development phase. Based on these designs, electric vehicle are broadly classified into three categories namely electric vehicles (EVs), hybrid electric vehicles (HEVs), and plug-in hybrid electric vehicles (PHEVs) [36].

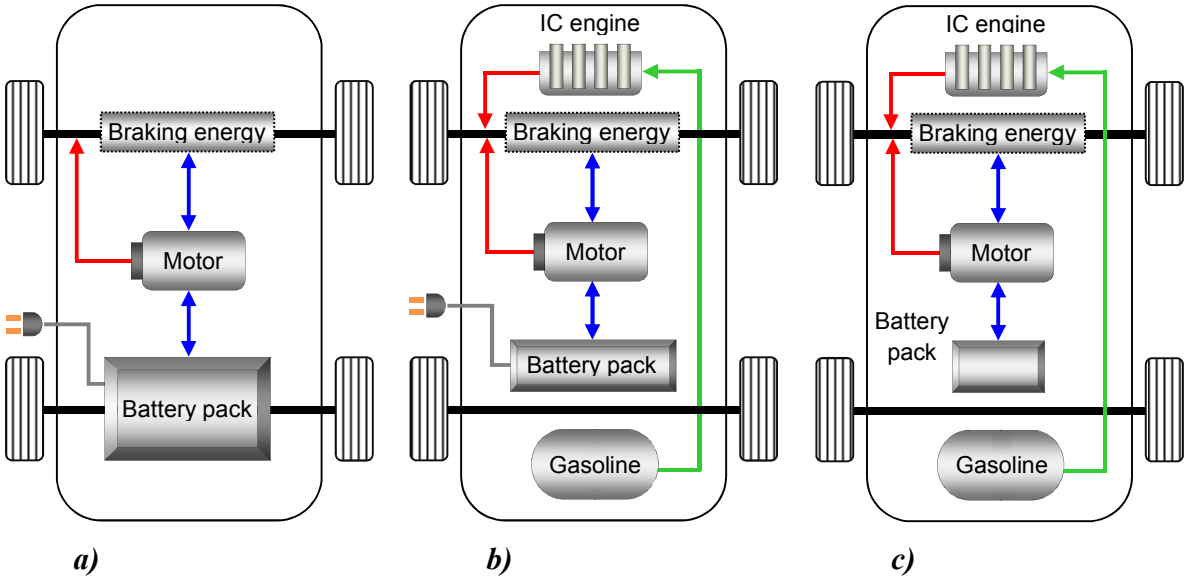

Figure 2.4: Schematic of different types of EVs: *a)* All Electric Vehicle (EV), *b)* Plug-in Hybrid Electric Vehicle (PHEV), *c)* Hybrid Electric Vehicle (HEV) [37].

2.2.1 Electric Vehicle (EV)

Electric vehicle also called all electric or battery electric vehicle (BEV) is powered by the onboard battery system alone. It does not use any other power source for propulsion. Charging in EVs is achieved by connecting specially designed connecter to the electric grid. Part of energy is recovered by the electric motor being switched to function as a generator during regenerative braking and deceleration mode. An EV can recover up to 5 % to 15 % of its propulsion energy used prior to braking. Schematic of a typical EV is shown in Figure 2.4*a*. Since EV depends solely on electric power, the battery system has to be efficient enough to meet the power requirements. *Nissan* LEAF and *Tesla* Roadster are examples of EVs [31].

2.2.2 Hybrid Electric Vehicle (HEV)

Electric cars have certain limitations regarding range and power. Improved energy storage can extend the range only to some extent. To solve these problems, a conventional gas propulsion system is combined with electric propulsion system to produce a hybrid version of EV. In HEV, an electric motor/generator is used to power the wheels at low speeds and low power demand. At high speed and high power demand, ICE takes over which in addition to powering the wheels charges the batteries. During braking, energy is used to turn the motor-cum-generator which charges the batteries thus saving the otherwise wasted energy. Though hybrid technology improves gas mileage by reducing fuel consumption, it does not offer a complete solution. A typical HEV is shown in Figure 2.4*c*. [36]. Based on the powertrain used, HEVs are further classified as follows:

I) Series Hybrid Electric Vehicle

Schematic of a series HEV is shown in Figure 2.5*c*. A fuel tank supplies fuel to the engine coupled to a generator. Engine delivers power to the generator which charges the battery system to supply electrical energy to the motor-cum-generator which in turn transmits power to the wheels through transmission box. Thus from engine to the wheels a single power transmission route is followed in Series HEV. During braking and deceleration, motor-cum-generator is used to charge the batteries.

II) Parallel Hybrid Electric Vehicle

In parallel HEV, two parallel power transmission routes are followed: an electric route and an engine route as shown in Figure 2.5*b*. Engine and motor-cum-generator are coupled through gear box or transmission which allows either of the two or both to power the wheels. In Parallel HEV efficient coupling between engine and motor-cum-generator is required to maintain performance and drivability [38].

III) Series-parallel Hybrid Electric Vehicle

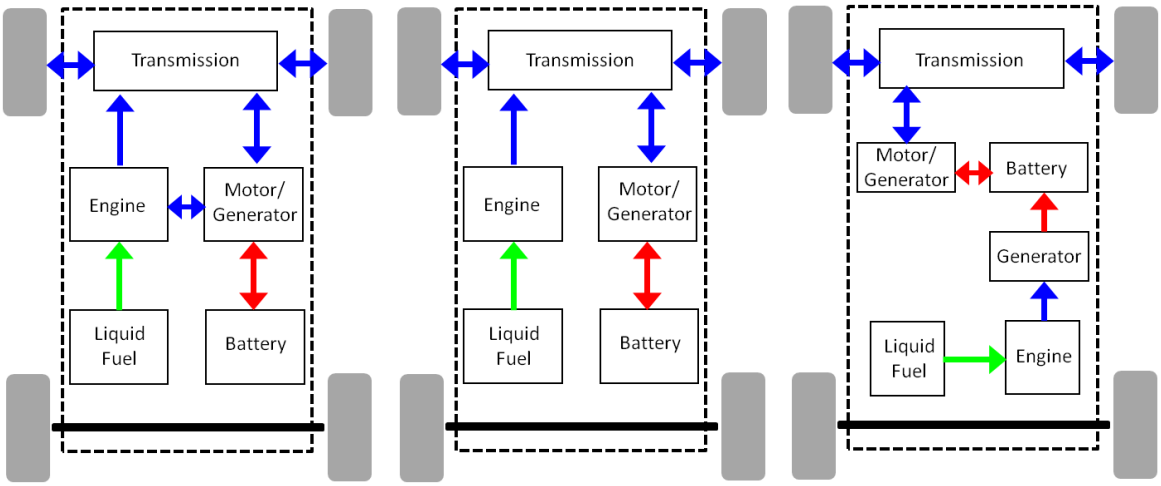

a) ***b)*** ***c)***

Figure 2.5: *a)* Series-parallel hybrid powertrain; *b)* Parallel hybrid powertrain; *c)* Series hybrid powertrain [38].

In Series-parallel HEV shown in Figure 2.5*a*, both parallel and series power transmission routes are followed. Engine can either drive transmission gears directly like in parallel HEV or be disconnected from it like in series HEV. At lower speed, it functions as a series HEV whereas at higher speed, where series HEV is less efficient, it functions as a parallel HEV. Series-parallel HEV performs better than the other two but at a higher cost because of complex power flow and larger storage systems involved. Depending on the degree of hybridization, HEVs can broadly be classified as Full and Mild hybrids. ***Full hybrid*** has the ability to run on the electric motor or the engine alone, or the combination of the two whereas ***Mild hybrid*** cannot be driven by electric motor alone [21, 39].

2.2.3 Plug-in Hybrid Electric Vehicle (PHEV)

Plug-in hybrid is a hybrid vehicle installed with the battery system that can be recharged by an external power source in addition to the onboard generator and that is why it is also called rechargeable hybrid vehicle. A sketch of a typical PHEV is shown in Figure 2.4*b*. The all-electric

driving range of PHEV is 30-65 km higher than that of standard HEV. PHEV is capable of driving through longer distances. PHEVs can be driven in full electric or full hybrid mode. Because of significantly improving fuel economy and reducing emissions, PHEV is expected to revolutionize auto industry during the years to come. Chevrolet Volt from General Motors is a typical example of PHEV. It can be driven up to about 1000 km on a single tank fuel without external charging [36].

2.3 Energy storage mechanisms

Capacitors and batteries are the two competing energy storage mechanisms especially for high-power applications. Capacitors use electrostatic mechanism for charge storage while batteries use electrochemical method for storage of energy. As present study is concerned mainly with the latter, we will discuss the former only briefly. A comparison between the two energy storage mechanisms is presented herein. Energy stored in a capacitor is given by:

$$E = \frac{1}{2} C U^2 \tag{2.1}$$

Where, E is the stored energy, U is the applied voltage, and C is called the capacitance and is given by:

$$C = \varepsilon \left(\frac{A}{d} \right) \tag{2.2}$$

Where d is the separation between charged surfaces, ε is the absolute permittivity of dielectric, and A is the area of charged surfaces. Two parallel metal plates separated by a thin insulating sheet called dielectric form a capacitor known as parallel plate capacitor. Separation between the plates is of the order of 1000 nm or higher. Electric charge can be stored by applying voltage across the plates. If solid dielectric is replaced by liquid electrolyte in the parallel plate capacitor, it forms electric double layer at the plate surfaces significantly enhancing the energy storage capacity of the capacitor. This enhanced energy storage version is called the ultracapacitor. Double layer formed in ultracapacitor is less than 1 nm thick which is 1000 times thinner than that of the parallel plate capacitor. It means energy storage capacity of ultracapacitor is thousand times higher than the parallel plate capacitor.

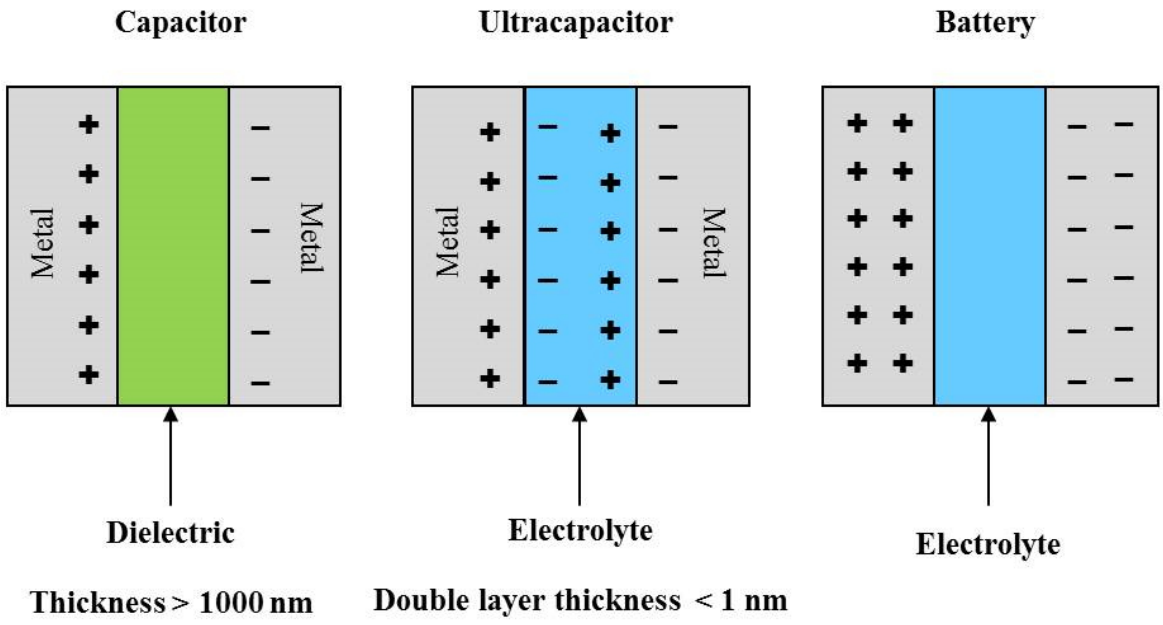

Figure 2.6: Schematic comparison of different energy storage systems using different mechanisms to store energy [40].

Schematic of parallel plate capacitor, ultracapacitor, and battery is shown in Figure 2.6. In ultracapacitors the two adjacent double layers formed at the metal surfaces act as the capacitors connected in series. The key difference between batteries and capacitors is that the latter use surface energy storage while the former use bulk energy storage mechanism. For that reason capacitors can provide sudden higher bursts of power but only for a short time which is due to limited energy storage capability of capacitors. Batteries on the other hand can store more energy within the active electrode materials but due to the fact that interaction between the charged particles and its surroundings is far greater than that in the capacitors, charged particles suffer higher resistance in flow thus minimizing the power delivering capability of batteries. Power and energy delivering capability of different devices is shown in Figure 2.11 [40].

2.4 Electrochemical energy storage

Battery is one of the most remarkable inventions in the history of science. Since its invention battery has become a common power source for many domestic and industrial applications

especially for portable electrical devices. As mentioned in 2.1.1 that many efforts have been made in the past to use batteries as a substitute for gasoline engine but with rare success. Nonetheless in recent years batteries have drawn a lot of attention to be used as automotive power source thanks to the advancements in the battery technology during the last two decades thereby reinventing interest in the electric power-train systems. A number of different types of batteries are used in automobile and transportation industry. These include lead-acid, nickel-metal-hydride, and lithium-ion batteries. Before discussing different battery types in detail, it will be useful to define some of the terms often used to estimate battery performance and state.

2.4.1 Battery characteristics and state estimators

Capacity of a battery is given by the product of current and time:

$$C = I \cdot t \tag{2.3}$$

Where C is capacity measured generally in ampere hours (Ah), I the amount of current drawn or applied in amperes (A) during discharging or charging, and t the total time in hours (h) required to fully discharge or charge the battery operating at its nominal voltage. Charge or discharge current as a multiple of capacity is known as C rate. For example if we use 4 A current to charge or discharge a battery having 2 Ah capacity it is called 2C rate because 4 is simply double to 2. Similarly 1 A current will be equal to C/2 rate. Higher the C rate faster will be the charge or discharge process and vice versa. If capacity is given per unit weight or volume it is known as specific capacity with the former being termed as gravimetric specific capacity in Ah/kg and the latter as volumetric specific capacity in Ah/l.

Drop in battery capacity with the number of charge-discharge cycles due to deterioration of the active materials is called capacity fading.

Energy density is the amount of energy that can be stored per unit mass or volume of battery. Normally dead weights are excluded and only active materials are used to refer energy density. Actual energy obtained is always lower than that predicted theoretically due to side reactions and other limitations. Energy density is measured in Wh/kg or Wh/l.

Power of a battery is the amount of energy a battery can deliver per unit time. It is the product of current and electric potential and is measured in watts.

Power density like energy density can be mentioned in W/kg or W/l.

Cycle life is the number of repeated charge-discharge cycles a battery can attain before losing its capacity to a point where it can no longer provide required energy and power. Typical cycle life of batteries used in portable electronics is about 300 cycles and that in the vehicles is on the order of 3000 cycles. Quality of a cell to maintain its capacity even after going through a number of cycles is called capacity retention [42].

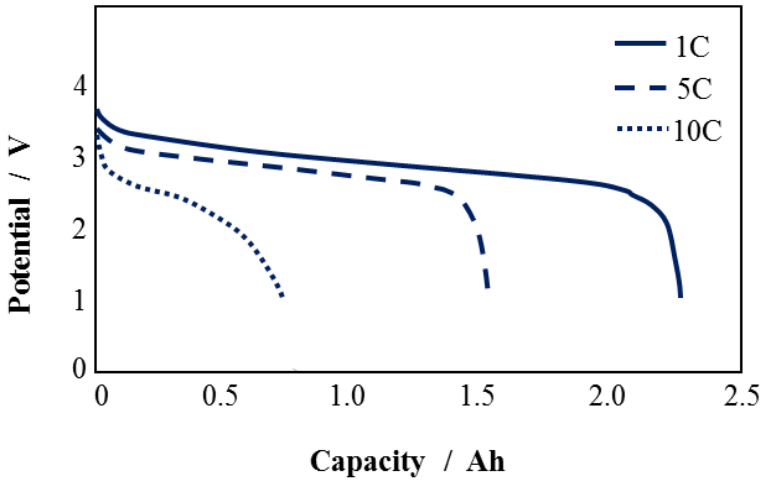

Figure 2.7: Hypothetical discharge curves of a 3.6 V and 2.5 Ah cell, under different applied currents.

Discharge behavior of batteries is studied using discharge curves. Discharge curve is obtained by plotting the discharge voltage versus capacity. Shape of discharge curve determines how well battery is performing. A flatter discharge curve indicates a low or almost no loss in capacity and hence power. If on the other hand curve drops short, it indicates a loss in capacity and power. Amount of discharge current or applied load significantly affects the discharge performance of a battery. Most batteries suffer loss in effective capacity when subjected to a high discharge current as shown in Figure 2.7. On the contrary, if battery is discharged slowly (at low rate) loss in capacity diminishes. An automotive battery should ideally exhibit a smooth and flat discharge curve to deliver required power until and unless required otherwise [41].

State of charge (SOC) indicates how much charge left in a battery at a given time. SOC is the percentage of charge available for use at a particular point in time. SOC of a fully charged battery is taken as 100 %, that of the fully discharged (empty) as 0 %, and the half empty as 50 %. Most batteries are recommended not to be discharged to 0 % to avoid irreversible damage.

Depth of discharge (DOD) or state of discharge (SOD) is a converse term used for SOC. In other words SOC of 80 % can conversely be expressed as 20 % DOD [42].

2.4.2 Lead-acid battery

Since its invention, lead-acid battery has been a battery of choice throughout the world for quite a long time. It is popular for being simple, less expensive, and based on an easy to follow and duplicable technology. Durability, relatively small size, and dependability have made it world's most widely used battery. In addition to automotive application, it has several other uses like powering emergency lighting, communication devices, and tools.

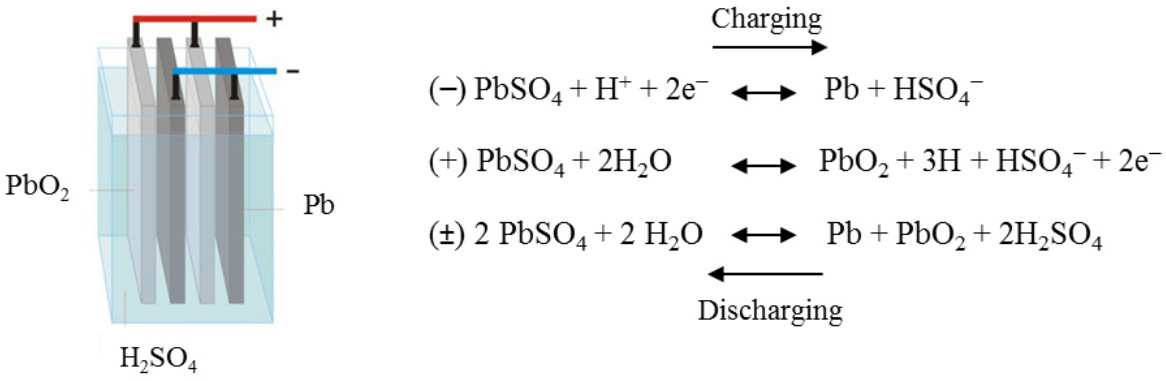

Figure 2.8: Basic construction scheme of lead acid battery and reactions involved. (-) and (+) represent anode and cathode respectively while (±) represents full cell [43].

A typical automotive lead-acid battery consists of six cells enclosed in interconnected compartments. Each cell is made up of 16 metal plates suspended in an electrolyte solution, typically 65 % water and 35 % sulfuric acid contained in a durable plastic casing. Each plate consists of a positive electrode (cathode) coated with lead oxide, a negative electrode (anode)

coated with lead, and a separator (e.g. micro porous glass fiber). Cells are connected in series and generate 2 volts each thus making up 12 volts across the battery terminals (Figure 2.8). Current is drawn by the vehicle to start its engine and for other applications. Once the vehicle starts moving, a reverse current is supplied to the battery through an alternator thus recharging the battery using the engine power.

At the beginning of 20^{th} century the improved design of rechargeable lead-acid battery was widely used to develop new types of electric vehicles. But it was soon realized that it better suited igniting the internal combustion engines rather than powering it. Although lead–acid batteries are still used to power forklifts, airport ground support equipment, and likes in a cost effective manner yet due to lower energy density and limitations on repeated charge-discharge cycles, it does not show any promise to high speed vehicle application [31, 44].

2.4.3 Nickel-metal-hydride (NiMH) battery

Before nickel-metal-hydride (NiMH) entered the market in the early 1990's, Nickel-cadmium (NiCd) was the dominating battery technology to which NiMH battery shares many commonalities. NiMH technology has edge over NiCd in having higher energy density and being less harmful to the environment. Since its invention, NiMH battery has gone through many improvements and significantly advanced in energy rating. The latest NiMH battery offers almost double the energy density of NiCd battery. The demerits of NiMH technology include its lower durability and service life as compared to the NiCd. Moreover its self-discharge rate is also comparatively higher than that of the NiCd [41].

Basic reactions and charge transport process taking place in NiMH cell are shown in Figure 2.9. The key feature of the NiMH cells is the capability of absorbing, releasing, and transporting hydrogen between the electrodes. Hydrogen absorbing alloys, used in the negative electrode, contribute to the high energy density of NiMH negative electrode resulting in the increased volume for the positive electrode.

During charge, positive electrode releases hydrogen into the electrolyte which in turn gets absorbed and stored by the negative electrode. When OH^- from the electrolyte and $Ni(OH)_2$ in the positive electrode react together, NiOOH (nickel oxyhydroxide) is produced within the positive

electrode, H_2O in the electrolyte and one free electron (e^-) is given away. The metal M in the negative electrode, H_2O from the electrolyte, and an electron (e^-) react to form MH (metal hydride) in the negative electrode and OH^- in the electrolyte. During discharge, the mechanism occurring during charge process gets reversed [45].

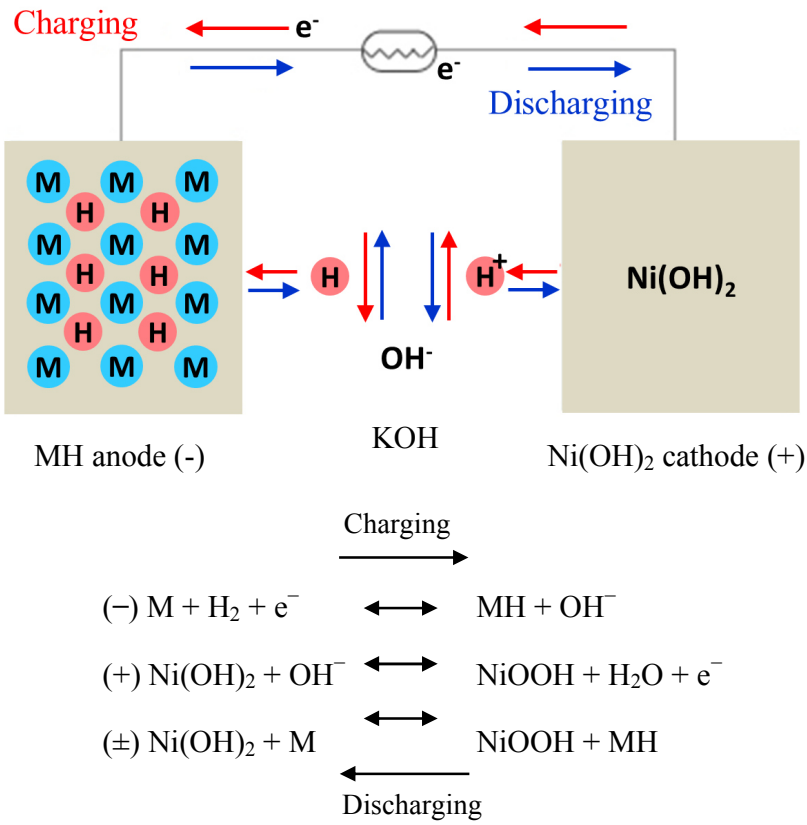

Figure 2.9: Basic reactions and transport mechanism taking place in nickel-metal-hydride cell [46].

Like most of batteries, temperature and discharge current significantly influence the discharge voltage of NiMH battery. Ideally potential should stay at 1.2 V (nominal voltage) throughout the discharge process but in reality discharge voltage decreases as current increases or temperature decreases thus decreasing the discharge efficiency. Cycling the battery repeatedly under high discharge cut-off voltage (> 1.1 V) causes the discharge voltage to drop which sometimes causes a simultaneous drop in capacity. This is crucial especially for EVs and HEVs because a drop in discharge voltage gives rise to a drop in power [47].

2.4.4 Lithium-ion (Li-ion) battery

The first commercial lithium-ion battery was introduced by Sony Corporation in 1991. Lithium-ion batteries offer double the energy density of that of the standard nickel based batteries. Voltage of lithium-ion battery (3.6 V) is three times higher than that of the NiMH battery (1.2 V) that suits high-power applications. Other pluses of Lithium-ion batteries include low toxicity, comparatively low self-discharge, higher energy efficiency, and low maintenance [48].

When lithium was first started being used in batteries in the early seventies, lithium metal was used as anode material. In lithium rechargeable batteries, use of metallic lithium as anode material proved to be problematic due to its high reactivity and unsafe operating characteristics. Many substitute materials for lithium anode have been reported during the last decade amongst which graphite appeared to be the most promising.

Typically lithium-ion batteries are composed of positive and negative electrodes separated by an electrically insulating but ionically conducting separator all soaked in electrolyte which is typically a lithium salt e.g. $LiPF_6$ dissolved in an organic electrolyte. Most commonly a mixture of ethylene carbonate and diethyl carbonate is used. Anode and cathode are prepared by pasting graphite and lithium-metal-oxides onto copper and aluminium current collecting foils respectively. Many types of cathode chemistries are being used in today's lithium-ion batteries (see section 2.6) but the transport mechanism is more or less the same in all types [63].

Charge transfer mechanism in typical lithium-iron-phosphate ($LiFePO_4$) battery along with anodic and cathodic reactions is shown in Figure 2.10. During charging, lithium ions move into the perfectly layered structure of graphite (anode) while during discharge lithium ions follow the reverse path and move through the electrolyte into the micro channels of cathode intercalation material i.e. iron-phosphate ($FePO_4$) as shown in Figure 2.10. Ability of lithium electrodes to absorb and release ions and electrons without undergoing changes in their structures is called intercalation or lithiation. When ions move into the channels of the electrode host material, the process is called intercalation while deintercalation when ions move out. During the intercalation process, electrons move from anode to cathode during discharge and vice versa. In a lithium-ion cell, lithium ions carry current from cathode to the anode during charging and from anode to the cathode during discharging [50].

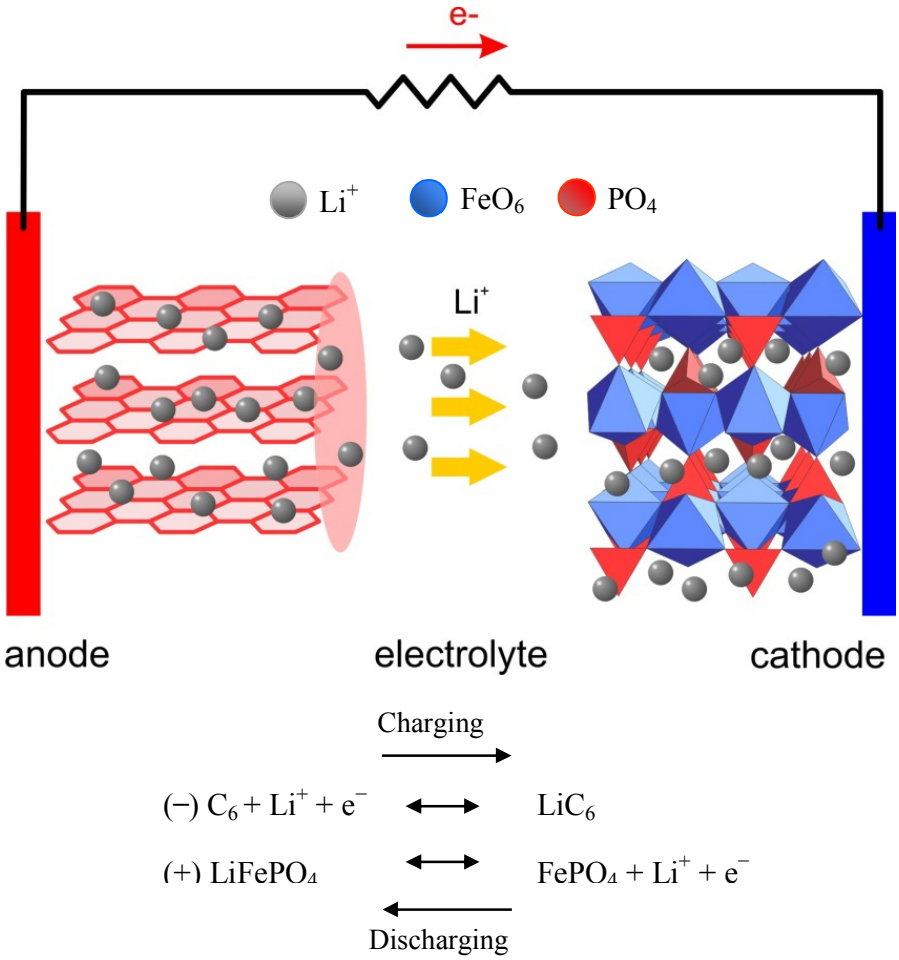

Figure 2.10: Transport mechanism in lithium-iron-phosphate battery during discharge [48, 49].

2.5 Automotive battery criterion

Batteries perform in much more aggressive environment in EVs than that in the portable electronics and other applications. Therefore automotive batteries are supposed to meet much higher standards regarding power and energy deliverance, safety, cycle stability etc. A battery used for electric propulsion should ideally be capable of delivering high power along with high energy in order to compete with the energy and power ratings of gasoline engines [44].

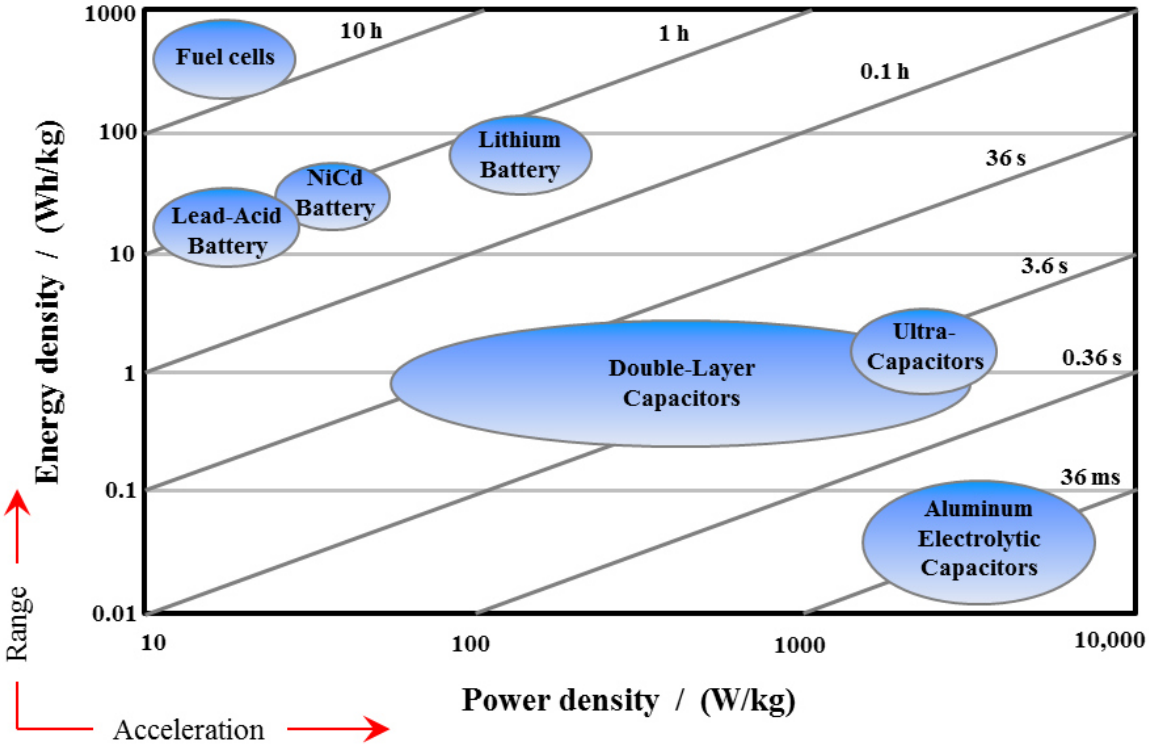

Figure 2.11: Ragone plot showing tradeoffs between power and energy ratings of different energy storage devices [41].

A useful way to counterpoise energy and power rating of a particular energy storage device is to use Ragone diagram shown in Figure 2.11 in which energy densities of different energy storage devices is plotted against their power densities. Parallel lines in Figure 2.11 represent the relative time required to draw the charge into or out of the device. It can be seen that capacitors need just seconds to get charged or recharged making them ideal for recovering braking energy in electric and hybrid electric vehicles. Lithium-ion batteries can be seen to stand somewhere at an optimum place in the chart indicating a reasonable compromise between power and energy delivering capabilities. It is not ideal but appears superior to the competing battery technologies [41].

Table 2.1: Comparison amongst existing automotive battery technologies [52, 53]

	LA	**NMH**	**Li-ion**	**Li-ion P**
Energy density, (Wh/kg)	30 – 50	60 – 120	110 – 160	100 – 130
Power density, (W/kg)	1880	250 – 1000	1800	-
Charge/discharge efficiency, (%)	70 – 92	66	99.9	-
Cycle life, (cycles) (80 % of initial capacity)	200 – 300	300 – 500	300 – 500	300 – 500
Life, (years)	3	-	2 – 3	-
Fast charging time, (h)	8 – 16	2 – 4	2 – 4	2 – 4
Overcharge tolerance	High	Low	Very low	Low
Self-discharge/month, (%) (at room temperature)	5	30	10	~ 10
Nominal voltage, (V)	2	1.25	3.6	3.6
Peak load current (in C rates)	5	5	> 2	> 2
Best load current (in C rates)	0.2	≤ 0.5	≤ 1	≤ 1
Discharge temperature, (°C)	-20 – 60	-20 – 60	-20 – 60	0 – 60
Maintenance (after days)	90 – 180	60 – 90	NA	NA
Typical cost in US$	25(*)	60(**)	100(**)	100(**)
Cost per cycle in US$	0.10	0.12	0.14	0.29
Toxicity	High	Relatively low	Low	Low

LA: Lead Acid; **NMH:** Nickel Metal Hydride; **Li-ion:** Lithium-ion; **Li-ion P:** Lithium-ion Polymer
(*) 6 Volt cell; (**) 7.2 Volt cell

In addition to energy and power rating of a particular battery to be used for electric propulsion, there are some other factors that need to be thought of carefully. An automotive battery system should meet the selection criteria based on five key target goals shown in Figure 2.12. It can be high-energy or high-power battery depending on the application and should be cost effective, long lasting, and abuse resistant. In view of the target characteristics highlighted in Figure 2.12, a

comparison among some of the major contender battery technologies in the automotive industry is presented in Table 2.1. It is obvious that Lithium-ion technology stands superior to the others with a clear margin as far as energy, power, and efficiency is concerned. Cost and thermal stability are the areas where lithium-ion battery technology needs improvement [33].

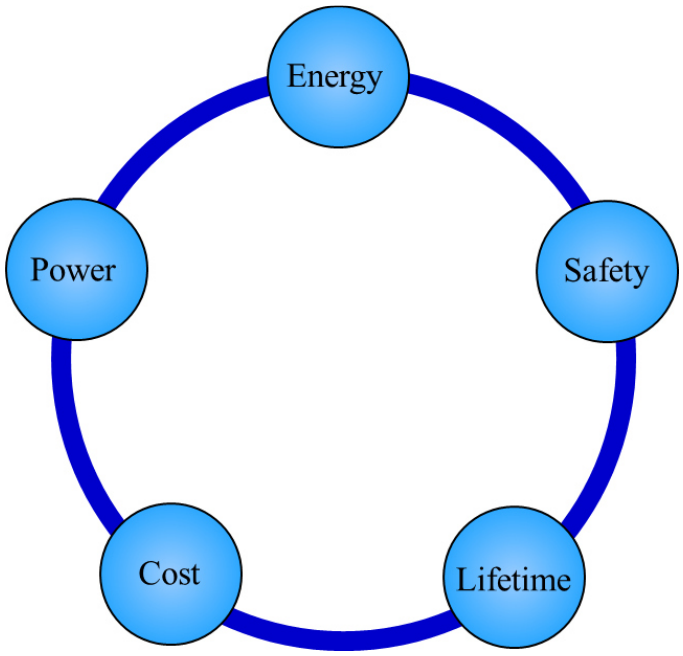

Figure 2.12: Target characteristics to be considered for automotive battery selection [33].

2.6 Lithium-ion battery technologies

A variety of combinations of anode and cathode materials are used to improve performance and efficiency of lithium-ion batteries. Each of these combinations has certain merits and demerits based on certain critical parameters like cost, safety, and performance. Based on the combination of different electrode chemistries, lithium-ion batteries are categorized into different types. The most dominant of these technologies specifically for automotive application are lithium-manganese-oxide (LMO), lithium-nickel-cobalt-aluminium-oxide (NCA), lithium-nickel-manganese-cobalt (NMC), lithium-titanate-oxide (LTO), and lithium-iron-phosphate (LFP). LMO, NCA, NMC, and LFP are cathode materials whereas LTO is used in the anodes. None of

the five lithium-ion battery chemistries mentioned above stands superior to the other in terms of meeting the six target dimensions shown in Figure 2.13.

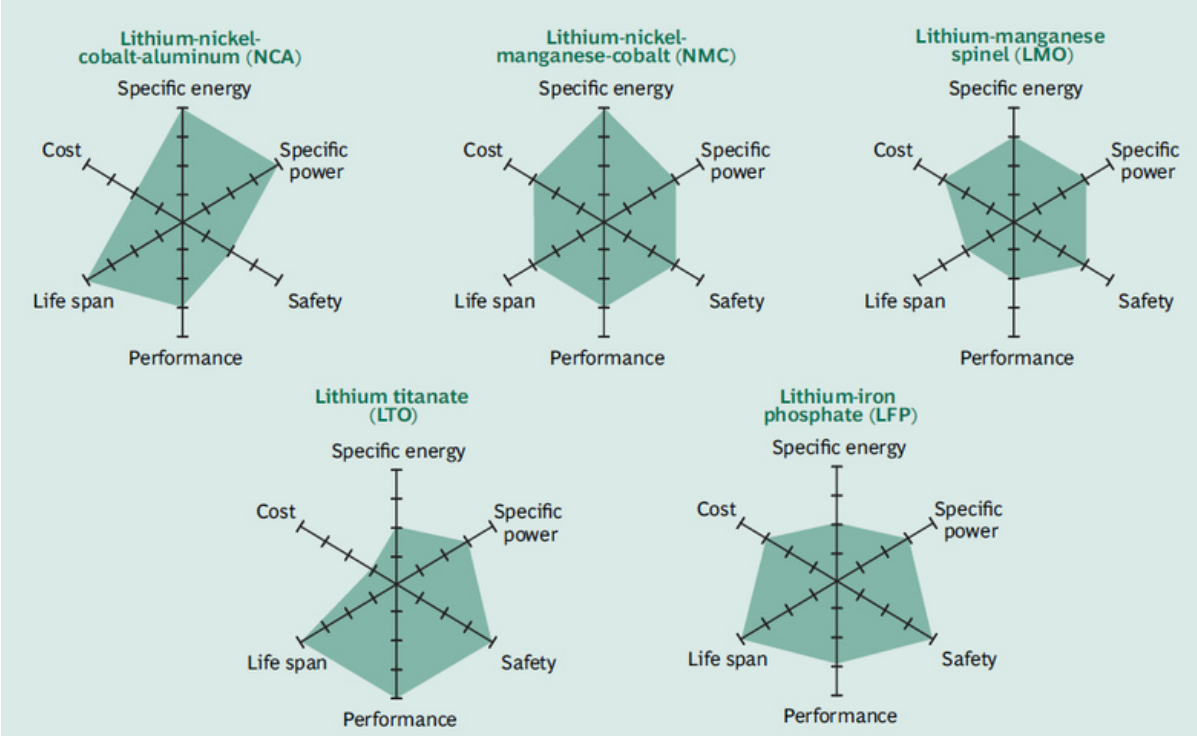

Figure 2.13: Trade-offs amongst the existing lithium-ion battery technologies, the further the dark green colour extends along specific dimension, the better the performance along that dimension and vice versa **[**51, 54**]**.

A technology superior in one dimension lacks in the other. For example, NCA technology is superior in performance but poor in safety. Similarly LFP technology is safer but offers low specific energy. So until some new technology emerges that satisfies all the six dimensions, consumers are forced to compromise on some of the dimensions depending on the specific application and need [51].

At the moment lithium-ion batteries offer 10 - 15 times lower energy density than that of the gasoline. Although molar energy densities of gasoline and lithium-ion batteries are not hugely apart, difference arises due to higher density of materials used in lithium-ion batteries. Future success of EV systems depends on the development of new lightweight materials offering low

resistance to the charge transport. Despite many shortcomings like higher costs, safety issues etc. and a lot of room for improvements, lithium-ion battery technology appears to be the most favoured candidate to meet the energy storage and power supply demands of the future automotive industry.

New high power lithium-ion batteries have been developed that make use of advanced nanostructured materials which are low cost and safe. For example, titanium oxide and nanostructured alloys having lithium insertion potential higher than graphite are used to make anodes. For cathodes, nanostructured lithium-iron-phosphate ($LiFePO_4$) and lithium-manganese-oxide ($LiMn_2O_4$) are used that are low cost and environment friendly.

New range of non-volatile and non-flammable electrolytes are developed using lithium salts in ionic liquids. LFP technology has become the focus of innovative research. The patent activity focusing LFP technology is at least double to the LTO technology and quadruple to the NMC technology. It can only be justified by LFP's higher effective capacity and promising safety features [51, 55].

2.7 Safety and performance

Almost all of the automotive battery technologies require elaborate monitoring and effective cooling system to operate within a certain temperature window for better performance and to avoid fire or explosion that could be caused by excessive release of energy due to higher loads, short circuits, accidents, or some other abuse event. High temperature can cause thermal runaway in lithium-ion battery packs. Thermal runaway is a state when heat generation rate inside battery increases exponentially which cannot be removed efficiently hence temperature in the cell rises abruptly causing the cell to catch fire or explode. Thermal runaway is discussed in detail in 2.7.2. Hence controlling cell temperature is essential not only for the battery to perform well but also for safety purposes [51, 56].

2.7.1 Temperature dependence of reaction parameters

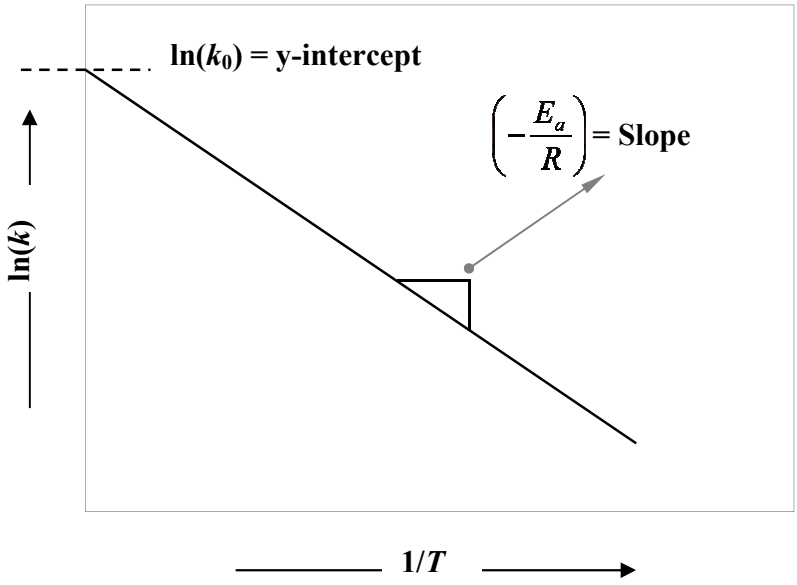

Figure 2.14: Arrhenius plot showing linear trend between natural log (ln) of reaction rate constant k and inverse of temperature T [19]. Units of k and k_0 (pre-exponential or frequency factor) depend on the order of reaction.

Rates of chemical reactions and the reaction kinetic parameters are strong functions of temperature. This temperature dependence of kinetic parameters and reaction rates can be expressed by Arrhenius equation (Equation 2.4).

$$k = k_0 e^{-\frac{E_a}{RT}} \tag{2.4}$$

If ln(k) is plotted along y-axis and (1/T) along x-axis, a plot of the sort shown in Figure 2.14 is obtained. This plot is called the Arrhenius plot and it indicates that the rate of reaction approximately doubles with every 10 °C increase in temperature. Since rate of electrochemical reaction is expressed in terms of current density i in A/m^2, for every 10 °C rise in temperature the amount of current flowing across the electrode surface gets doubled. This implies a strong temperature dependence of current [19].

2.7.2 Thermal runaway

Under normal operation, heat generated in the cell is too small that it easily gets dissipated to the environment. There remains a balance between the heat generated and that dissipated until some abusive event causes the heat generation in cell to surpass heat dissipation by tremendous amounts. In such a case, cell temperature rises exponentially until a point is reached where fire or explosion becomes inevitable. That particularly is the possible scenario in automobile battery packs and modules where multiple cells are so closely packed that temperature surge in a single cell could trigger cell-to-cell chain reaction.

When lithium-ion battery is charged initially, a negative change in potential takes place at the anode surface which causes the electrolyte in contact with the surface to reduce or decompose. The decomposition products form a passive layer at the anode surface which being electronically nonconductive inhibits the transfer of electrons to the bulk thus preventing the further reduction of electrolyte. This layer is called the solid electrolyte interface or SEI. SEI conveniently allows the positive ions to pass through to the electrolyte during the charge-discharge processes. There are many factors that impart instability to this protective layer. Although potential significantly influences the thickness of SEI, higher temperature has more pronounced effect on the changes taking place in SEI due to increased rate of side reactions at higher temperatures. At high temperatures, reaction between the active electrode material and the SEI or electrolyte and SEI starts taking place. At about 120 °C, SEI starts conducting electrons to the electrolyte and permits lithium from the carbon of the anode to pass through and react with the electrolyte. As temperature increases further, more complex exothermic reactions start which could lead to thermal runaway [57].

At 90 - 120 °C, the metastable components in SEI decompose exothermically. As mentioned above that SEI acts as a barrier between lithiated carbon and electrolyte by stopping them to react with each other. Also at about 100 °C and in the absence of SEI, anode active material starts reacting exothermically with the electrolyte further increasing temperature to about 200 °C. At the cathode side, not only the possibility of reaction between cathode active material and electrolyte exists but also the oxygen released by cathode is likely to react with electrolyte as well. This is highly exothermic reaction that could occur at about 180 °C or above. At this temperature melting of separator can take place which can short circuit the cell creating more

heat. As electrolyte used in lithium-ion batteries are organic in nature they can readily catch fire when in vapour form.

Graphite in the anode is likely to react at 330 °C releasing further heat. At this stage the amount of heat generated in the cell increases exponentially and reaches a level where it cannot be removed through normal means. A state of thermal runaway exists at this stage that could lead to fire or explosion. This is the main concern towards wide application of lithium-ion batteries in EVs, HEVs.

Thermal modelling can provide a useful insight into how battery design can impact the onset of thermal runaway. Temperature at which thermal runaway can occur depends on SOC, cell chemistry, and abuse conditions. Design of batteries and packs has to be carefully carried out so as to minimize the chances of thermal runaway in case of abusive event or high temperatures [58].

Effect of overcharging

Let us consider an example of a lithium-ion cell consisting of a graphite anode and a lithium-cobalt-oxide ($LiCoO_2$) cathode soaked in an electrolyte solution composed of $LiPF_6$ (lithium hexafluorophosphate) dissolved in a mixture of organic solvents (e. g. ethylene carbonate, diethyl carbonate). Anode and cathode potentials are referred to lithium metal reference electrode as shown in Figure 2.15.

As charging starts, potential starts dropping at the anode side until it reaches ~1 volt. At this point lithium starts reacting with the electrolyte thus forming SEI. As potential drops further, more and more lithium moves into the carbon and once it reaches zero volts, lithium starts to plate on to the carbon anode (electro-deposition). In an uncontrolled deposition, metal grows into spikes or filaments which can damage the separator. Damaged separator can cause shorting of the electric circuit which can lead to fire. In case of fast charging, a lot of current is driven to the anode making the kinetics to control the surface reaction at the anode surface hence contributing to an increased over-potential. This makes the anode potential to drop until it reaches lithium plating voltage.

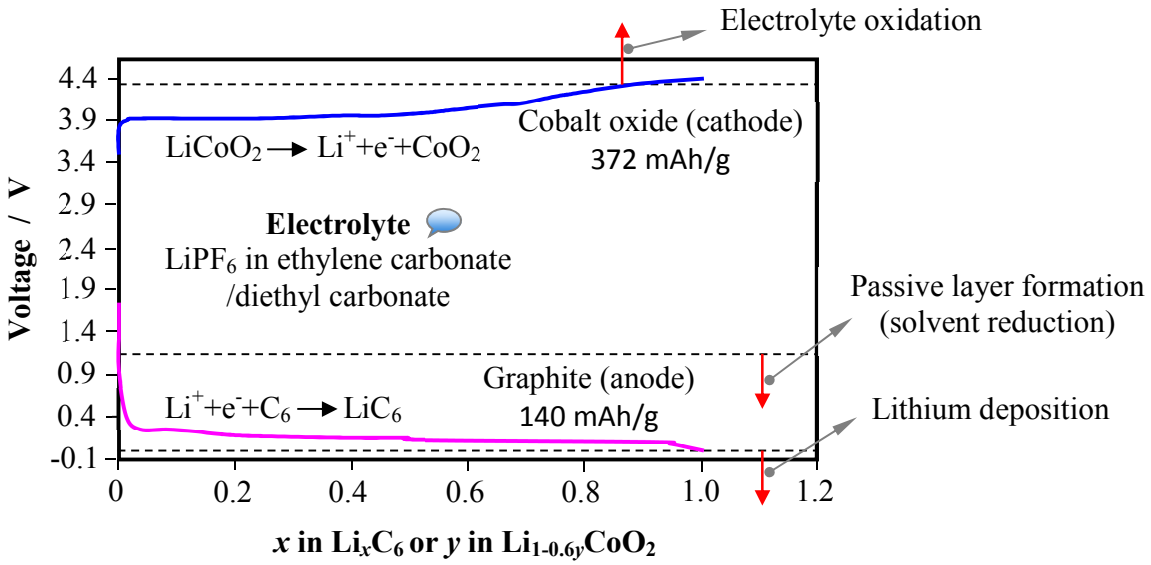

Figure 2.15: Steady state charge curve of a graphite-$LiCoO_2$ cell showing half-cell potentials along with and thermodynamic potentials of different side reactions [63].

On the other hand at the cathode side, a deficiency of lithium makes the cathode potential to increase. At about 4.2 volt, cobalt oxide starts to oxidize. Oxidation being exothermic reaction it gives off heat causing the cell temperature to rise. At about 250 °C, cobalt oxide stars decomposing giving off oxygen which in turn reacts with the organic electrolyte. Released oxygen further oxidizes the organic electrolyte that generates more heat. Excess heat in presence of oxygen makes a perfect recipe for thermal runaway or disaster. In view of the above mentioned facts operating voltage window has to be carefully chosen so as to avoid any untoward incidents and the battery to perform well and longer [63].

2.7.3 Performance

At sub-zero temperatures, charge transport in electrolyte and reaction at the electrode surfaces in lithium-ion batteries significantly slow down due to which the battery suffers a drop in performance. At higher temperatures (> 60 °C), due to increased diffusion rate, reaction at the electrode-electrolyte interface becomes very fast which can cause mechanical failure or deterioration of the electrode active material. Moreover at higher temperatures, possibility of parasitic side reactions increases that could catastrophically kill the cell capacity. The temperature

range over which a lithium-ion battery should be charged is typically 0 – 45 °C. But due to the development of new electrode and electrolyte materials that temperature range is widening. Higher temperature could increase temperature inside the battery making the battery to swell in case of pouch configuration. Higher pressure could also cause mechanical damage to the cell. Thus temperature affects not only the performance of the battery in the short run, but also calendar and cycle life of battery in the long run [59].

2.7.4 Lithium-ion battery related mishaps

Lithium-ion battery related events of fire and explosion have been reported throughout the world some of which are listed in Table 2.2 [58]. Detailed list of battery related events involving smoke, fire or explosion took place in the air transport industry during March, 1991 and October 2012 can be found in U.S. Federal Aviation Administration (FAA) published document [60].

One typical example is that of Chevrolet Volt fire that took place about three weeks after a crash test was conducted on May 12, 2011 in United States. A Chevrolet Volt after being gone through crash test was stored on a dumping site where it caught fire and turned into ash along with other four vehicles that were parked alongside. Investigation revealed that a metal part located under the driving seat pierced through the battery compartment rupturing the liquid cooling system of the battery module followed by short circuit causing the fire to start [134].

Figure 2.16: Boeing 787 Dreamliner (left) and battery pack removed from ANA flight for inspection (right) [61].

At the beginning of 2013, all the in service Boeing 787 Dreamliner, new state of the art planes, have been grounded due to safety concerns related to the on-board lithium-ion battery systems. In January, 2013 two Japanese airlines were faced with lithium-ion battery related fire incidents. Fire detected on Japan Airline (JAL) flight from Tokyo to Boston shortly after it landed in Boston. In another event an All Nippon Airways (ANA) flight was forced to make an emergency landing due to fire smoke caused by lithium-ion batteries in one of its electrical compartments (Figure 2.16). These events raised alarm over safety issues related to the wider use of lithium-ion battery technology [61].

Table 2.2: Lithium-ion battery related fire or explosion events during past years [62]

No.	Date	Event	Cause
1	July 18, 2011	EV bus catches fire, Shanghai, China	Overheated LFP batteries
2	April 11, 2011	EV taxi caught fire, Hangzhou, China	LFP battery (16 Ah)
3	September 3, 2010	Fire on a Boeing 747 cargo plane, Dubai	Overheated Li-ion batteries
4	April 26, 2010	Dell, Apple, Toshiba, Lenovo, Acer, and Sony recalled laptop batteries	Potential fire hazards
5	March, 2010	Two iPod music players caught fire in Japan	Overheated Li-ion batteries
6	January, 2010	Two EV buses caught fire, Urumqi, China	Overheated LiFePO4 batteries
7	July, 2009	Pre-flight fire on cargo plane, Shenzhen, China	Spontaneous combustion of li-ion batteries
8	June 21, 2008	Laptop fire during conference, Japan	Overheated batteries
10	2006 on	Thousands of mobile phone fires or explosions	Short-circuit, overheating etc.

In view of the above mentioned incidents and risks associated with the use of lithium-ion batteries, it is very important to design an efficient thermal management and cooling system that could effectively neutralize any unexpected heat surge caused by some abusive event. To design an effective cooling system for the battery packs to be used in automobiles it is essential to fully understand how an individual cell responds to different environmental and loading conditions.

One way to get information about the thermal behaviour of a cell is to carry out extensive experimental work which could not only be proved tedious but sometimes also falls short of serving the desired purpose. For example to measure the interior temperature of a cell, a thermocouple has to be inserted into the cell which can damage the cell leaving it unusable. To save the efforts, time, and resources, and to obtain the information, which otherwise can be hard to obtain, is to make use of mathematical models. Modelling is an effective tool in designing and optimization of automotive thermal management system.

In this work a detailed 3D coupled electrochemical-thermal model has been developed and validated against experimental findings. The model was used to perform thermal analysis of two distinct types of high-power lithium-ion cells i.e. LFP and NCA. The choice has been made on the basis of future scope of these cell types in the automotive market and individual merits on automobile application. The model developed in this work could not only contribute to the designing efforts of new thermal management system for automobiles but also optimization of the existing systems.

In the next chapter, heat transfer and electrochemical heat generation mechanisms will be discussed in detail prior to moving on to the model development. The purpose is to have a better understanding of the basic principles and theory working behind the model equations. Heat transfer and heat generation mechanisms are treated as the two distinct mechanisms that complement each other to constitute a complete cell model.

Chapter 3

Heat transfer and electrochemical heat generation mechanisms

Complete thermal model of a battery is constituted by an electrochemical heat generation model and a heat transfer model. This chapter includes the basic description of these two mechanisms in a little elaborative manner. The intention is to get equipped with the basic knowledge and theory required to fully appreciate the model equations presented in chapter 4 without being burdened with extra details. Basic heat transfer mechanisms like conduction, convection, and radiation that transport heat in batteries are discussed in the first section of this chapter. Heat generation in electrochemical systems is a complex mechanism which needs to be described in bit of a further detail. Hence rest of the sections are devoted to electrochemical reaction mechanisms and how these mechanisms contribute to heat generation in the cells.

3.1 Heat transfer mechanisms

Temperature of a given system is measure of thermal energy of the constituent particles. Thermal energy is the energy associated with the motion of particles [16]. Heat generated inside a system tends to move from a region of higher temperature to that of the lower. Heat transfer takes place either by the actual movement of particles having higher energy within the system thus transporting energy from one place to the other or by the vibrational movement of particles with higher energy oscillating along their mean position and transferring energy to the neighboring

particles by colliding with them. The former is termed as convective while the latter as conductive transport of energy. There is yet another mechanism in which energy is transported by means of electromagnetic waves and is called radiative transport. In some cases energy is transported through diffusion of two or more interdiffusing mixtures and is called diffusive energy transport [64].

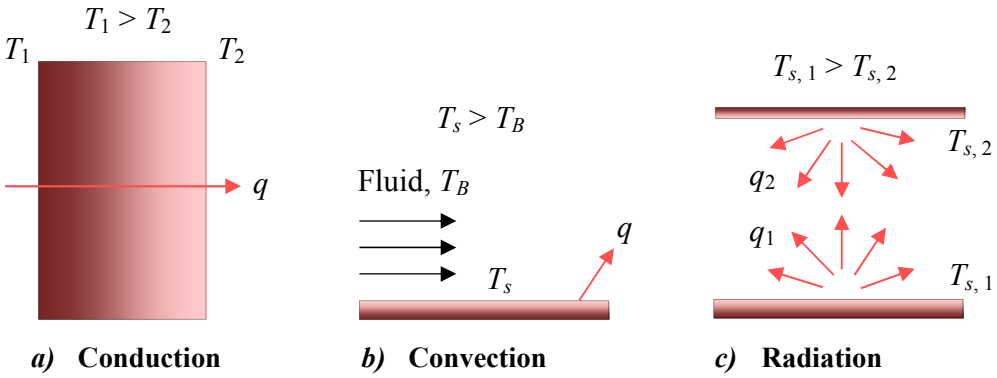

Figure 3.1: Different mechanisms of heat transfer from one location to the other [65].

In solids or stagnant fluids, due to the absence of bulk motion, heat transfers from a point of higher temperature to that of the lower temperature by conduction. On the other hand when a moving fluid comes into contact with a surface at higher temperature, heat dissipates from surface to the adjacent fluid particles by conduction and to the bulk of fluid by convection. In radiation two or more surfaces at different temperatures exchange heat through electromagnetic waves giving rise to a net transfer of heat between the surfaces. Radiation heat requires no medium to get through. These three modes of heat transport are elucidated in Figure 3.1. Each of the three heat transfer modes are discussed below in further detail.

3.1.1 Conduction

In gases, in the absence of bulk or macroscopic movement of particles, thermal energy is associated with the rotational or vibrational energy of the particles. Particles (atoms or molecules) at higher energies vibrate and collide with the neighboring particles having lower energy thus

transferring part of their energy to them. This way heat gets transferred from one part to the other without the actual movement of particles.

Situation in liquids is more or less the same with only difference that in liquids, particles are more closely packed and collisions are more frequent. In solids conduction is associated with the atomic activity in form of crystal lattice vibrations. A modern view is that the lattice waves are formed due to atomic motions and energy transferred from one part to the other through these lattice waves [65].

To further elaborate let us consider that a constant amount of heat is flowing through a rectangular specimen of a solid material of thickness X having a cross-sectional area A (Figure 3.2). At steady state, a constant temperature gradient ΔT exists between the opposite faces of the specimen and the heat transfer rate required to maintain this temperature gradient is given by:

$$\frac{\dot{Q}}{A} = -k\frac{\Delta T}{X} \tag{3.1}$$

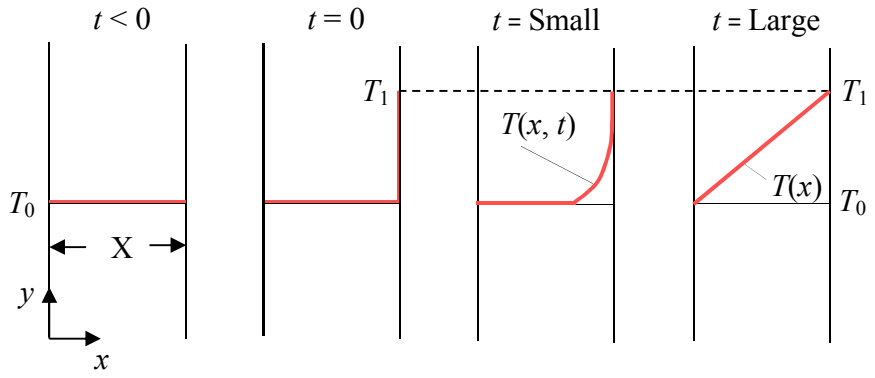

Figure 3.2: Steady state temperature profile progression between the two faces of a solid specimen [16, 65].

Equation (3.1) states that the rate of heat transfer per unit area of a solid material is proportional to the temperature gradient existing between the two points X distance apart. The proportionality constant k is the thermal conductivity of material through which heat is being transferred. In the SI system of units thermal conductivity is represented by watts per meter per Kelvin W/(m·K).

Equation (3.1) holds true also for the materials in liquid or gaseous state until enough care is exercised to counter the convection and radiation effects.

In its differential form Equation (3.1) is written as:

$$q_x = -k\frac{dT}{dx} \tag{3.2}$$

Similarly for temperature gradient in *y* and *z* directions:

$$q_y = -k\frac{dT}{dy} \tag{3.3}$$

$$q_z = -k\frac{dT}{dz} \tag{3.4}$$

Adding Equations (3.2), (3.3), and (3.4) after multiplying each by a suitable unit vector, we end up in a 3D form of Fourier`s law of thermal conduction represented by Equation (3.5).

$$[\mathbf{q}] = -k\nabla T \tag{3.5}$$

Equation (3.5) is valid for isotropic materials which has the same thermal conductivity in all directions. For anisotropic materials, Equation (3.5) becomes:

$$[\mathbf{q}] = -[\boldsymbol{k}]\cdot\nabla T \tag{3.6}$$

Where, [$\boldsymbol{k}$] is a second order symmetric tensor known as thermal conductivity tensor. Besides thermal conductivity *k*, thermal diffusivity α is another important quantity used in heat conduction problems and is defined as:

$$\alpha = \frac{k}{\rho c_P} \tag{3.7}$$

In Equation (3.7), c_P is the heat capacity or specific heat which in SI system is the amount of heat in joules (J) required to raise the temperature of one kilogram (kg) of a material by one Kelvin (K) thus having units of J/(kg·K). From Equation (3.7), it can also be seen that thermal diffusivity α has units of m^2/s which are similar to that of the kinematic viscosity *v*. For a system with

constant physical properties, the ratio ν/α represents a dimensionless parameter called the Prandtl number denoted by *Pr* and gives a measure of the ease of energy and momentum transport in a flow system [64].

$$P_r = \frac{\nu}{\alpha} \tag{3.8}$$

3.1.2 Convection

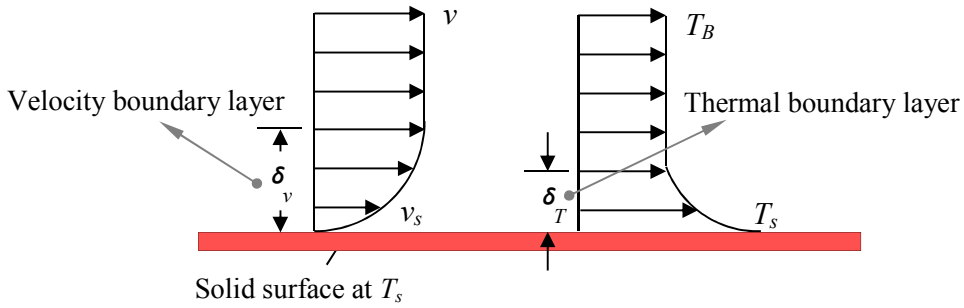

Figure 3.3: Development of velocity and thermal boundary layers at the solid heat transfer surface [65].

As mentioned above that on a macroscopic level convective heat transfer takes place due to the bulk motion of the fluid where molecules form clusters or aggregates which move from one place to the other as a whole thereby transporting heat. But in some inter-diffusing fluids when individual particles move randomly, inter-particle diffusion takes place causing the heat to move from one place to the other. It should be noted that temperature gradient is the key driving factor for the heat transfer to take place. During the bulk movement of fluids, particles still move randomly inside the clusters thus making the two phenomena to coexist. Generally the combined effect of these two phenomena of heat transfer is referred to as convection. Taking into account the only bulk motion of fluid, the phenomenon is referred to as advection [65].

The main concern of this work is heat transfer taking place between a solid surface and a stagnant or moving fluid. In case of stationary fluid heat transfer takes place only due to the random motion of particles. On the other hand when the fluid in contact with the solid surface is in

motion, both the random and bulk motions contribute to the transportation of heat. In case of moving fluid, velocity varies from zero at the solid surface to that of the flow velocity of fluid in the bulk. This region of varying velocity profile is referred to as the velocity boundary layer. In addition, temperature also varies from solid surface temperature (T_s) to that of the temperature of fluid bulk (T_B) provided both are at different temperatures. This region is referred to as the thermal boundary layer. Formation of velocity and thermal boundary layers are illustrated in Figure 3.3. Thermal boundary layer can be smaller, larger, or equal to the velocity boundary layer. Near the solid surface, diffusive or random particle motion is dominant while as we move away from the surface heat transfer due to bulk motion of fluid takes over.

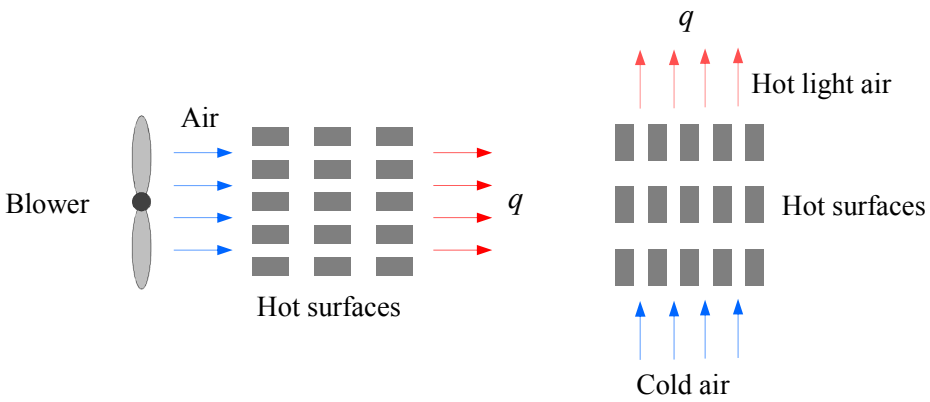

Figure 3.4: Forced convection (left) and natural convection (right) mechanism of heat transport [65].

According to Newton's law of cooling, convective heat flux from a surface to its surroundings is directly proportional to the temperature difference between the surface and its surroundings. General equation describing Newton's law of cooling is:

$$q = h_f \cdot \Delta T \tag{3.9}$$

Where, h_f is a proportionality constant called heat transfer coefficient. Quantitatively h_f is the amount of heat in J/s dissipating from a cross-sectional area of a meter square causing one degree change in temperature and thus has units of W/(m^2·K) in SI system. Referencing Figure 3.3, ΔT is given by:

$$\Delta T = T_s - T_B \tag{3.10}$$

Depending on the nature of flow, convection heat transfer can be divided into two subtypes

I) Natural convection

Heat transfer that occurs spontaneously without doing extra work or using external force is called natural or free convection. When fluid contacts with the hot surfaces its temperature gets increased near the surface which makes its density to drop thus making it comparatively lighter. This heated air being lighter moves upwards making the higher density cold air to replace it. Natural and forced convection phenomena are shown in Figure 3.4.

II) Forced convection

When air is made to flow over the hot surfaces using external sources like air blower, pumps etc. to remove heat the process is called forced convection. In addition to the above mentioned convection types, convection may occur due to combined action of natural and forced convection. An example is boiling and condensation of water.

3.1.3 Radiation

Thermal radiation is the energy emitted by a hot body to its surroundings in the form of electromagnetic waves in all directions. When this radiant energy crosses another body, part of it can be absorbed, reflected or emitted back depending on its temperature. When two bodies at different temperatures radiate energy, a net exchange of radiant energy takes place with the hotter body emitting more energy than it absorbs and vice versa. Even after reaching thermal equilibrium, radiation energy continues to be exchanged [66].

Radiant energy emitted by a body comprises of waves of different wave-lengths moving in all directions. A surface that could ideally absorb all the radiant energy falling on it is called a black body. According to Stefan-Boltzmann law of thermal radiation, the amount of radiant heat energy emitted by a black body per unit time per unit area at temperature T is given by:

$$q = \sigma T^4 \tag{3.11}$$

Where, σ is the proportionality constant called Stefan-Boltzmann constant having a value of 5.676×10^{-8} W/(m^2·K^4). There is yet another property of surface besides temperature which determines the amount of heat emitted by a surface. This property is called emissivity ε and is the fraction of radiant energy emitted by a body [67]. Taking into account the emissivity, equation (3.11) becomes:

$$q = \varepsilon \sigma T^4 \tag{3.12}$$

Where, $0 < \varepsilon < 1$

In case of more than one radiating surface, each surface exchanges radiation with the other rendering the radiation analysis less simple. As mentioned above that part of the radiant energy falling on to body is also reflected. Inclusion of reflection adds complexity to the radiation analysis especially in case of multiple surfaces. This complexity can be remedied by assuming all the surfaces as black bodies which implies that there is no reflection involved and hence emissivity approaches unity ($\varepsilon \rightarrow 1$). Let us now consider two surfaces (1 and 2) radiate to each other. Net radiation between the two is given by:

$\dot{Q}_{12}$ = [heat radiated by 1 intercepted by 2] – [heat radiated by 2 intercepted by 1]

Making use of reciprocity, we arrive at:

$$\dot{Q}_{12} = A_1 \dot{F}_{12} \sigma \left(T_1^4 - T_2^4 \right) \tag{3.13}$$

$\dot{F}$ is called the view factor or form factor and it depends on the mutual angles of the radiating surfaces. Reciprocity principle states that the two radiating surfaces cannot have the same view factor unless they have equal areas. $\dot{F}_{12}$ in Equation (3.13) is the fraction of radiant energy emitted by surface 1 intercepted by surface 2. Hence;

$$A_1 \dot{F}_{12} = A_2 \dot{F}_{21} \tag{3.14}$$

In radiation problem, an open or closed system in which a set of surfaces radiate to each other is called enclosure. We can have more than one enclosure with each having its own space

temperature. Let us consider an enclosure consisting of N number of surfaces with each having specific temperature and emissivity. Radiant heat energy given off by each surface a is given by:

$$\dot{Q}_a = \sum_{b=1}^{N} \dot{Q}_{ab} = \sum_{b=1}^{N} A_a \dot{F}_{ab} \boldsymbol{\sigma} \left(T_a^4 - T_b^4 \right) \tag{3.15}$$

Where, N is the number of radiating surfaces, T_a and T_b are absolute temperatures at surface a and b respectively, A_a the area of surface a, $\dot{Q}_{ab}$ the energy exchanged between surfaces a and b, ε_a the emissivity of surface a, and $\dot{F}_{ab}$ the view factor. Negative value q_a indicates radiation heat is received by surface a.

View factor calculation

Let us consider two surfaces are radiating to each other as shown in Figure (3.5). View factor $\dot{F}_{12}$ is the fraction of total radiant energy leaving surface 1 being intercepted by surface 2. It can be expressed mathematically as:

$$\dot{F}_{12} = \frac{1}{\Pi A_1} \int\int \frac{\cos\theta_1 \cos\theta_2}{r_{12}^2} d\left(A_1\right) d\left(A_2\right) \tag{3.16}$$

Similarly $\dot{F}_{21}$ is the radiant energy leaving surface 2 and intercepted by surface 1:

$$\dot{F}_{21} = \frac{1}{\Pi A_2} \int\int \frac{\cos\theta_1 \cos\theta_2}{r_{12}^2} d\left(A_1\right) d\left(A_2\right) \tag{3.17}$$

$\dot{F}_{12}$ and $\dot{F}_{21}$ are related by Equation (3.14).

Where A_1 and A_2 are surface areas of surface 1 and 2 respectively; $\mathbf{n}_1$ and $\mathbf{n}_2$ are Surface normal vectors of d(A_1) and d(A_2) respectively; θ_1 is the angle between $\mathbf{n}_1$ and radius line to differential patch d(A_1) and θ_2 is the angle between $\mathbf{n}_2$ and radius line to differential patch d(A_2); r_{12} is the distance between differential area patches d(A_1) and d(A_2) [64, 68, 69].

Till now the main mechanisms by which heat transfer takes place in different systems including batteries has been discussed. Following sections include electrochemical mechanisms that cause the heat to generate within the battery systems and the parameters that influence such mechanisms.

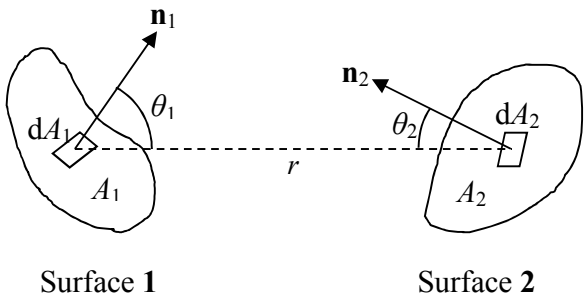

Figure 3.5: Geometric configuration to determine view factor between radiating surfaces 1 and 2 [68].

3.2 Electrochemical processes

As chemical reactions involve exchange of electrons between the reacting substances which are in direct contact with each other. If we place the reactants apart with an ion conducting medium between them and somehow make the electrons to be transferred via an external path, the process would be termed as electrochemical process.

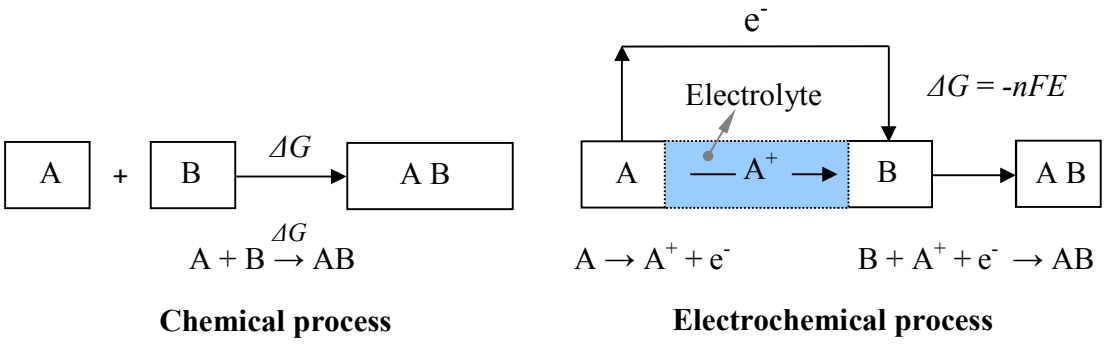

Figure 3.6: Difference between chemical and electrochemical processes. *F* is the Faraday's constant, *E* the voltage, and *n* the number of electron moles involved [40].

Referring to Figure 3.6, let us consider two reactants A and B reacting chemically to form product AB. Free energy change ΔG involved in chemical reaction converts to heat. Now if the two reactants react electrochemically, A converts to A^+ which reaches B moving through the electrolyte while electron given off by A takes the external route as shown in Figure 3.6 (right). Free energy of electrochemical reaction converts to electricity [40].

Thus the flow of current in an electrochemical cell can be used to do electrical work. The maximum work W that could be done at standard state equals the Gibb's free energy change ΔG associated with the overall cell reaction.

$$\Delta G = W \tag{3.18}$$

Now electrical work is also given by the cell potential (E_{cell}) times the total charge on the charged species involved. For n mole of electrons involved in the reaction, work done would be given as:

$$W = -\, n\, F\, E_{cell} \tag{3.19}$$

Where, n is the number of electron moles and F is the Faraday's constant that represents charge on one mole of electrons and is equal to 96487 Coulomb (C). From Equations (3.18) and (3.19), we can establish a relation between the cell reaction thermodynamics and its potential as [125]:

$$\Delta G = -\, n\, F\, E_{cell} \tag{3.20}$$

3.2.1 Electrochemical cell

Electrochemical processes involve conversion of chemical energy into electrical energy by the redox (oxidation-reduction) reactions taking place at the electrode-electrolyte interface. Addition of electrons is called reduction whereas loss of electrons is called oxidation. Redox reactions taking place at the electrodes cause the electrons to move through external circuit and the ions through electrolyte. An electrochemical cell is the basic unit of an energy storage or conversion device that interconverts chemical and electrical energies. Multiple cells packed together form a battery of cells.

Basic construction of an electrochemical cell is shown in Figure 3.7. It can be formed by immersing two electrodes having different electric potentials in an electrolyte solution. When connected by a metal wire electrons start flowing from the electrode at lower potential (negative electrode) to that at the higher potential (positive electrode) through the wire while positive charges move through electrolyte. Electrons and ions keep on moving until state of electrochemical equilibrium is reached. Reaction taking place at each electrode is called the half-

cell reaction. During discharge, oxidation reaction takes place at the negative electrode while reduction at the positive electrode [42].

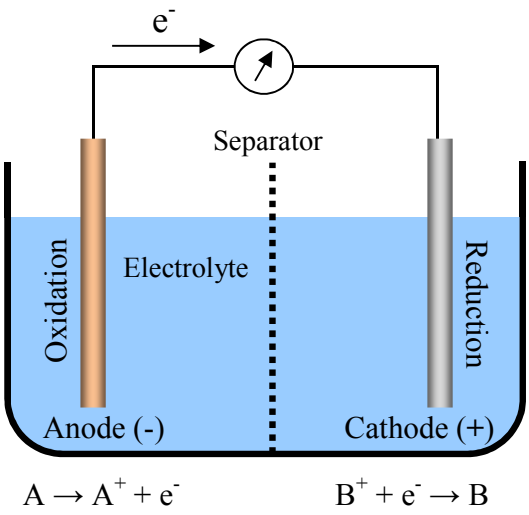

Figure 3.7: Schematic of an electrochemical cell showing oxidation-reduction reactions [40].

3.3 Electrochemical reaction parameters

In electrochemical modelling, two types of parameters are being considered; equilibrium or thermodynamic parameters and kinetic parameters. Thermodynamic equilibrium establishes when reaction reaches its final or limiting stage where rate in forward direction balances the rate in reverse direction. At this stage current stops flowing in any direction. Thus thermodynamic parameters correspond to the maximum or limiting values that could only be attained at equilibrium. Thermodynamic parameters give no clue of what happens when the reaction takes its course. Once the reaction starts, kinetic parameters take the charge. Kinetic parameters involve charge or mass transport by diffusion or migration to make the reacting species reach the electrode surfaces where reaction takes place. In addition, kinetic parameters also include potential changes caused by the flow of current in ionic or electronic conductors. Electrode design parameters like active material thickness, pore size and shape, and separation between the two electrodes significantly influence the kinetic parameters [70]. Each of these types of parameters is discussed separately in the following sections.

3.3.1 Electrochemical reaction thermodynamics

Electron activity in an electrochemical reaction causes a change in electrochemical potential which has profound effect on the rate of electrochemical reaction. Thermodynamics make us understand the energy changes involved in an electrochemical reaction. These energy changes act as a driving force and control the spontaneity of reaction in forward or reverse direction. As described in section 3.2 that a change of free energy ΔG is associated with every chemical reaction. The lower ΔG of products than the reactants would drive the reaction towards the product formation or in forward direction. Equation (3.20) can be used to give free energy change of an electrochemical reaction at equilibrium as:

$$\Delta G = -nFE_{eq} \tag{3.21}$$

Where E_{eq} is the equilibrium cell potential [71]. If electrochemical reaction involves charged species i, Equation (3.21) can be written as:

$$\Delta G = -z_i FE_{eq} \tag{3.22}$$

Where z_i is the valence number of charged species i. Equation (3.22) can be rewritten for equilibrium cell potential as:

$$E_{eq} = -\frac{\Delta G}{z_i F} \tag{3.23}$$

Enthalpy or heat of reaction ΔH is another thermodynamic parameter which is the amount of energy absorbed or released per mole of a substance during a chemical reaction. Positive ΔH indicates endothermic while negative ΔH indicates exothermic reaction. Difference between ΔH and ΔG is that the former is the energy consumed or released during reaction while latter is the free or excess energy that can be converted into electrical energy. In addition to enthalpy ΔH and Gibb's free energy change ΔG, there is a third important parameter called entropy of reaction ΔS that accounts for the reversible energy gains or losses involved in chemical or electrochemical processes. It represents the state of disorder of a system. We can also say that entropy represents the fraction of energy in a system that cannot be converted into useful work. In a chemical reaction if entropy of products is higher than that of the reactants, reaction will be favoured in

direction of product formation and vice versa. These three parameters are related through the following relation:

$$\Delta G = \Delta H - T \cdot \Delta S \tag{3.24}$$

$$\Delta H - \Delta G = T \cdot \Delta S \tag{3.25}$$

The right hand side of Equation (3.25) represents reversible heat effects. In a reversible process, this term represents heat exchange with the surroundings. A positive $T \cdot \Delta S$ means additional energy is generated by the cooling of surroundings [65, 70, 72]. Combining Equations (3.22) and (3.24) and rewriting in differential form gives:

$$\Delta S = -\left(\frac{\partial \Delta G_M}{\partial T}\right) = z_i F\left(\frac{\partial E_{eq}}{\partial T}\right) \tag{3.26}$$

From Equations (3.22), (3.25), and (3.26), we can write a relation for enthalpy change:

$$\Delta H = z_i F\left[T\left(\frac{\partial E_{eq}}{\partial T}\right) - E_{eq}\right] \tag{3.27}$$

Equation (3.26) is used to determine entropy of an electrochemical cell by measuring open circuit potentials as a function of temperature which subsequently is used to find enthalpy using Equation (3.27). Thermodynamic quantities like ΔH and ΔG are related to the activities or ionic concentrations of the reacting substances in the solution. This relation is demonstrated by Nernst's Equation.

$$\Delta G = \Delta G^0 + RT \ln\left[\prod_i (a_i)^{\nu_i}\right] \tag{3.28}$$

Where a_i is the activity of reacting species i, ν_i is the number of equivalents taking part in reaction, R is ideal gas constant and is equal to 8.3145 J/(mol·K), T is temperature in K, and ΔG^0 is standard value of Gibb's free energy at which all the activities are unity. Combining Equations (3.22) and (3.28) gives:

$$E_{eq} = E_{eq}^0 - \frac{RT}{z_i F} \ln\left[\prod_i (a_i)^{\nu_i}\right] \tag{3.29}$$

In electrochemical reactions a thin region of the order of 10 Å lies next to the electrode surfaces across which maximum potential changes take place. This region of maximum activity is called electric double layer [56].

I) Electric double layer

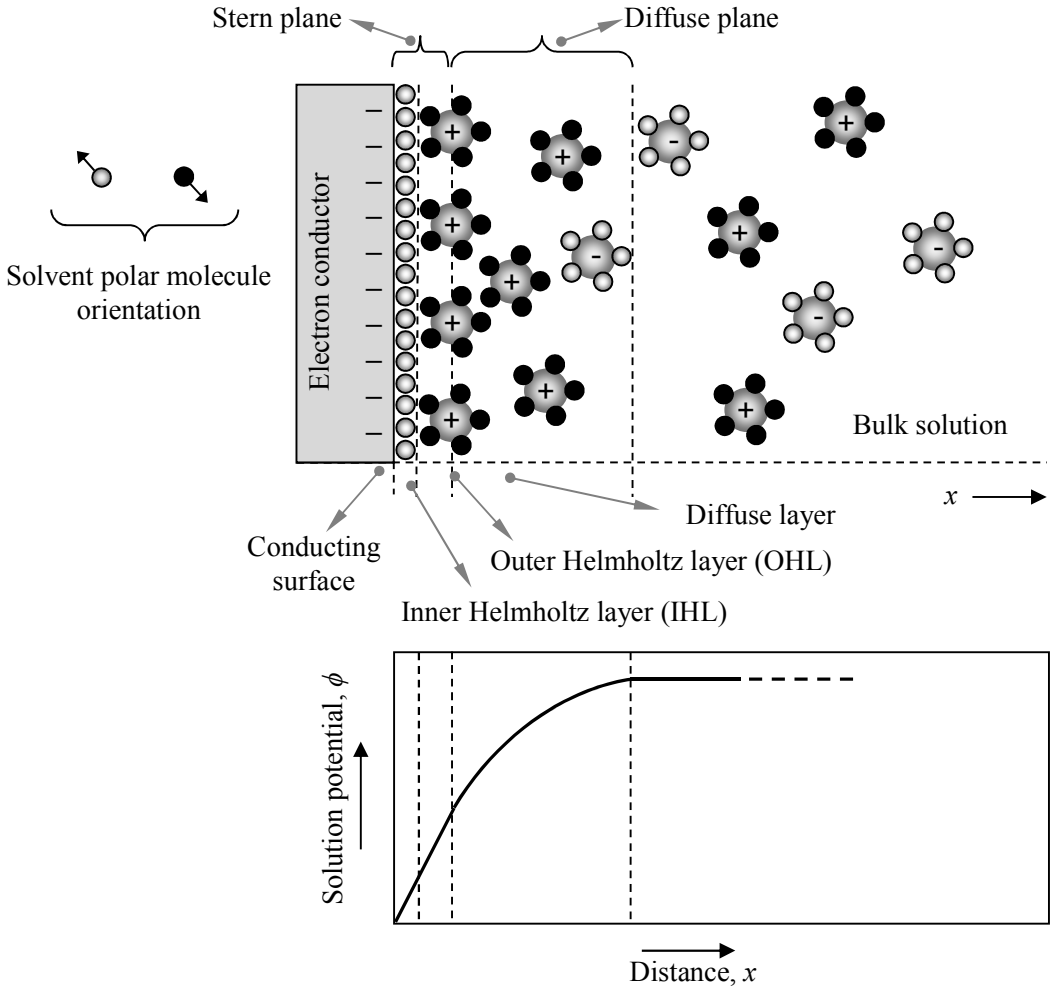

Figure 3.8: Electric double layer formation at the electrode-electrolyte interface and potential variation within the double layer [72, 73].

In an electrochemical cell, electron conducting surface forms a complex interface with ion conducting solution. Positively charged ions get attracted to the negatively charged surface thus forming a thin passive layer of solvent saturated with positively charged species (cations). This positively charged layer repels the following cations within the bulk solution thus restricting them to approach the conducting surface. This region of closest approach of positively charged cations to the negatively charged surface is called the outer Helmholtz plane. This plane of separated charges is referred to as electrical double layer or solid-electrolyte interface (SEI) which acts much like a charged capacitor [71].

Electric double layer is constituted by a single-molecule thick inner layer called the inner Helmholtz layer (IHL), an outer layer called the outer Helmholtz layer (OHL), and an outer most diffusive layer called Guoy-Chapman layer as shown in Figure 3.8. IHL consists of the absorbed solvent molecules (on conducting surface or electrode) in which potential varies linearly. OHL is occupied by solvated cations where potential again varies linearly with distance. Excess cations and anions are distributed in the outer most diffusion layer in which potential varies exponentially with distance in *x*-direction as can be seen in lower part of Figure 3.8 [73].

II) Electrode potential

Thermodynamic data is always obtained from a complete cell reaction. Therefore the derived voltage is actually the difference in voltages of the two electrodes. Potential difference between an electrode (electronic conductor) and electrolyte (electronic non-conductor) is hard to measure because potential difference could only accurately be measured between the two electronic conductors. To measure single electrode potential, one has to refer to another arbitrary voltage value which is given by a reference electrode called standard reference electrode. Many types of standard electrodes are used to measure single electrode potentials the most common of which is standard hydrogen electrode (SHE). In case of batteries, SHE is not used due to difficulties involved in handling and electrode contamination issues. In lithium-ion batteries which include organic electrolytes, special lithium electrodes are used as standard reference electrodes [70].

III) Potential distribution in the cell

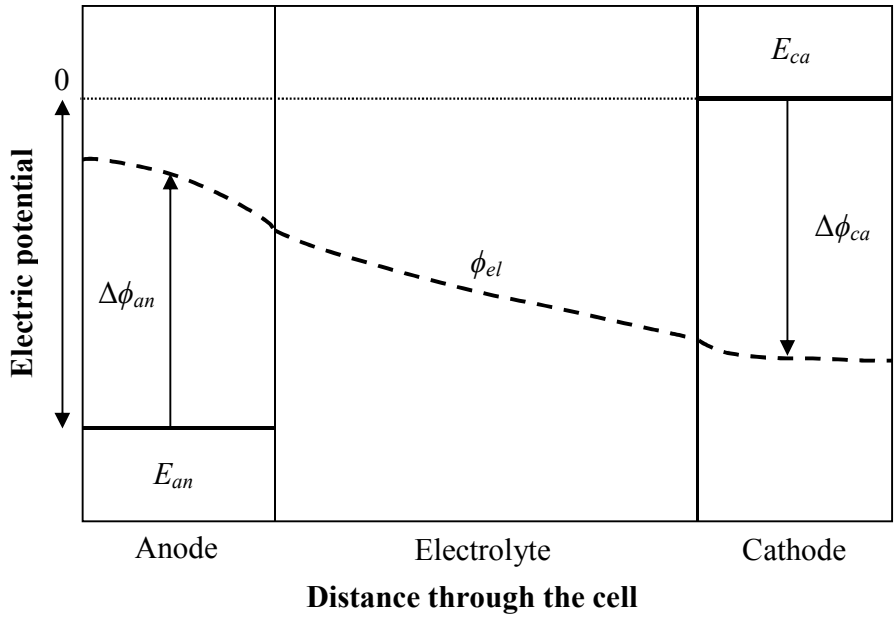

Figure 3.9: Electrolyte phase potential distribution in a composite electrode electrochemical cell in polarized state [74].

Potential distribution in a polarized (charged) cell with composite electrodes is schematically shown in Figure 3.9. Assuming electrodes and current collectors to have ideal conductivities, the cell voltage E is then given by the difference of cathode and anode potentials E_{ca} and E_{an} respectively. E_{ca} is used as a reference point and assumed to have a potential of zero volts.

$$E = E_{ca} - E_{an} \tag{3.30}$$

Change in potential within the electrodes is caused by the two potential steps $\Delta\phi_{an}$ and $\Delta\phi_{ca}$ formed in the double layers at the anode-electrolyte and cathode-electrolyte interfaces respectively. If ϕ_{el} is the electrolyte potential then $\Delta\phi_{an}$ and $\Delta\phi_{ca}$ are given by:

$$\phi_{an} = E_{an} - \phi_{el,an} \quad \text{and} \quad \phi_{ca} = E_{ca} - \phi_{el,ca} \tag{3.31}$$

Where $\phi_{el,an}$ and $\phi_{el,ca}$ represent the electrolyte potentials at the anode-electrolyte and the cathode-electrolyte interfaces respectively. Potential within the composite electrodes vary along the

thickness of electrode due to concentration variations of charged species. Potential change in the electrolyte is caused by the solution's ohmic resistance [74].

3.3.2 Electrochemical reaction kinetics

An understanding of fundamental laws governing the electrochemical reaction kinetics is essential to improve the performance of electrochemical cells. Study of the rates of electrochemical reactions is termed as kinetics. A key difference between electrochemical and non-electrochemical processes is the ability to exploit an additional driving-force variable called electric potential. Electrode kinetics is governed by the potential changes taking place across SEI. In the previous section electrochemical system at equilibrium has been discussed but as the system moves away from equilibrium, a net flow of current takes place. A different set of parameters are required to describe such a system [71].

I) Polarization

When current starts flowing, an electrochemical reaction takes place, at a finite rate, at the electrode surface. The simplest way to measure rate of reaction is by measuring the current flowing in the circuit ($I = dQ/dt$). As current is proportional to the surface area of electrode therefore current density ($i = I/A$) is used to characterize the rate of reaction. As electrode potential moves away from equilibrium, a potential difference establishes across the electrode surface which drives the electrochemical reaction. This shift of potential from equilibrium is called polarization [70, 75].

As mentioned above that electrochemical reactions occur only at finite rates. If electrons are made available to an electrode, potential at the electrode surface turns more negative. As the current flows, excess electrons with their negative charges start building up at the metal-electrolyte interface or solid-electrolyte interface (SEI). Since reaction is not fast enough to accommodate all the electrons waiting for the reaction. Due to this accumulation of negative charges at the SEI, electrode potential starts measuring more negative. This negative potential change is called cathodic polarization. Similarly a positive change in potential caused by a deficiency of electrons at the SEI is called anodic polarization.

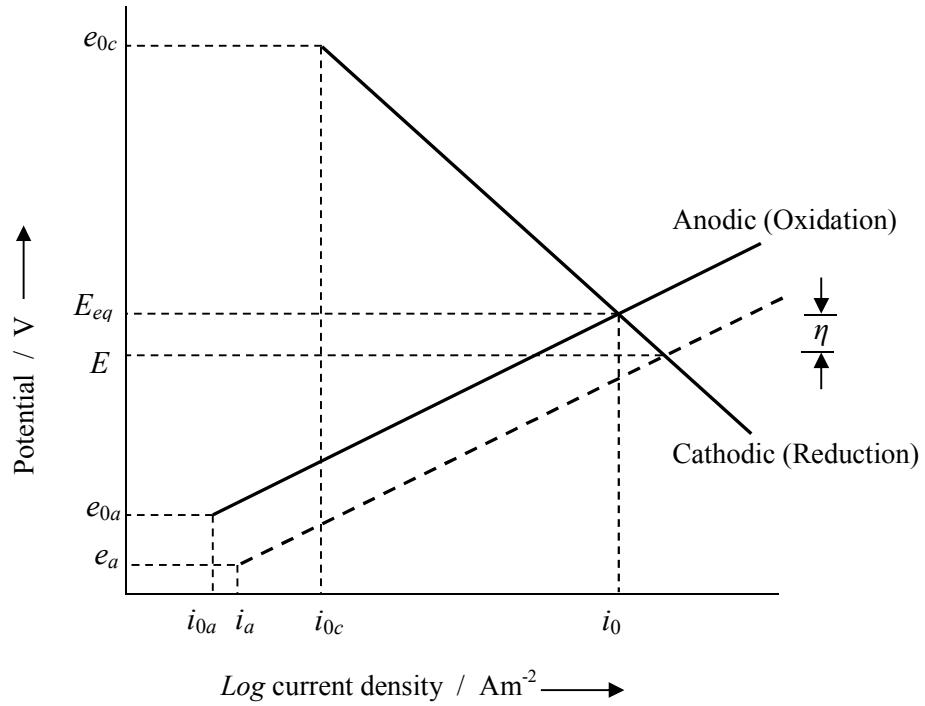

Figure 3.10: Hypothetical current-potential plot illustrating polarization at the metal electrode [71].

As an electrochemical cell consists of two half-cells with each going through a chemical reaction that corresponds to a characteristic potential in comparison to a standard reference electrode as mentioned above (section 3.3.1-II). One can demonstrate that each of the half-cell reactions has a potential-current relationship which can be plotted hypothetically as two straight lines representing anodic (oxidation) and cathodic (reduction) reactions on a semi-log graph as shown in Figure 3.10. The point the two lines cross at is the point of equilibrium. E_{eq} is the equilibrium half-cell potential while i_0 is the exchange current density that corresponds to equilibrium potential of the half-cell. e_{0a} and e_{0c} are the standard anodic and cathodic potentials respectively. i_{0a} and i_{0c} are the anodic and cathodic exchange current densities respectively. Electrochemical cell potential E_{cell} is the sum of two half-cell potentials.

$$E_{cell} = E_{an} + E_{ca} \tag{3.32}$$

Where, E_{an} and E_{ca} are anode and cathode potentials variously called electrode potentials.

$$\eta = E - E_{eq} \tag{3.33}$$

If excess electrons are made available to the electrode, potential at the electrode surface drops due to the inclusion of negatively charged electrons causing the half-cell potential to change from E_{eq} to E (Figure 3.10). This departure of potential from its equilibrium state is called polarization or over-potential. As electrochemical reaction shifts away from equilibrium, current starts to flow in one or the other direction. This flow of current always experiences some kind of resistance which impede the charge transfer process. Certain overpotential is required to deal with this resistance. Charges can face resistance at the electrode-electrolyte interfaces, within the electrode active material, in the bulk of electrolyte, or in the solid-state circuitry. Depending on the type of resistance, polarization can be of activation, concentration, or ohmic type [71].

Activation polarization

If the rate of electrochemical reaction is limited or controlled by the rate of electrochemical charge transfer process alone which is an activation controlled process, this gives rise to kinetics that is described by Butler-Volmer equation.

As at equilibrium oxidation and reduction reactions take place simultaneously at the electrode (anode and cathode) surface such that the rate of oxidation equals the rate of reduction. As we move away from equilibrium, one of the two reactions takes over the other. For example when we start discharging a cell, rate of oxidation or forward reaction is higher than that of the reduction or reverse reaction at the anode. The opposite is true at the cathode side. The first term in Equation (3.34) represents the forward reaction rate while second represents the reverse for each of the electrodes.

$$i = i_0\left(\exp\left(\frac{\alpha\, zF}{RT}\eta_{act}\right) - \exp\left(-\frac{(1-\alpha)zF}{RT}\eta_{act}\right)\right) \tag{3.34}$$

Where, i is current density (reaction rate) in A/m^2, i_0 is exchange current density in A/m^2 which corresponds to state of dynamic equilibrium (Figure 3.10), η is overpotential (= $E - E_{eq}$) in volts, n is number of electrons involved, α is dimensionless charge transfer or simply transfer coefficient.

Resistance against the reaction to take place at the electrode-electrolyte interface causes an energy barrier to develop across the interface which the ions have to surmount in order to react. That causes a change in potential across the interface and this potential change is called the activation polarization. Activation polarization depends profoundly on electrode characteristics and is strongly influenced by temperature because of being an inherent property of the electrode active materials [42, 76].

If potential shifts significantly far from equilibrium potential, the second term representing the reverse reaction in Equation (3.34) can be ignored. Thus simpler exponential relations between current (rate) and overpotential can be obtained. In other words, overpotential can be a logarithmic function of current density. This theory had been validated by the experimental findings of German physical chemist Julius Tafel in 1905. A plot between overpotential versus log of current density is called Tafel plot or Tafel lines the slope of which determines the value of transfer coefficients for the corresponding electrode reactions. Rewriting Equation (3.34):

$$\eta_{act} = b \log|i| - a \tag{3.35}$$

Where, $b = \dfrac{2.303\,RT}{\alpha\, zF}$ and $a = \dfrac{2.303\,RT}{\alpha\, zF} \log i_0$

Electrochemical reactions where high overvoltages are involved, Tafel lines are considered to be an effective approximation [70, 71].

Concentration polarization

At higher reaction rates, cathodic reduction reaction readily consumes the dissolved species from the adjacent solution. This creates a deficiency of charged species near the surface of the electrode creating a concentration gradient between the electrode surface and the solution bulk. Let us consider hydrogen reduction reaction.

$$2H^+ + 2e^- \rightarrow H_2$$

In Figure 3.11, concentration profile of H^+ is shown. c_0 is the concentration of H^+ at the surface of cathode, c_B is the concentration of the bulk solution, and δ is the thickness of the concentration gradient. The half-cell electrode potential of hydrogen reduction ($E_{H+/H2}$) is given by Nernst's equation (Equation 3.29).

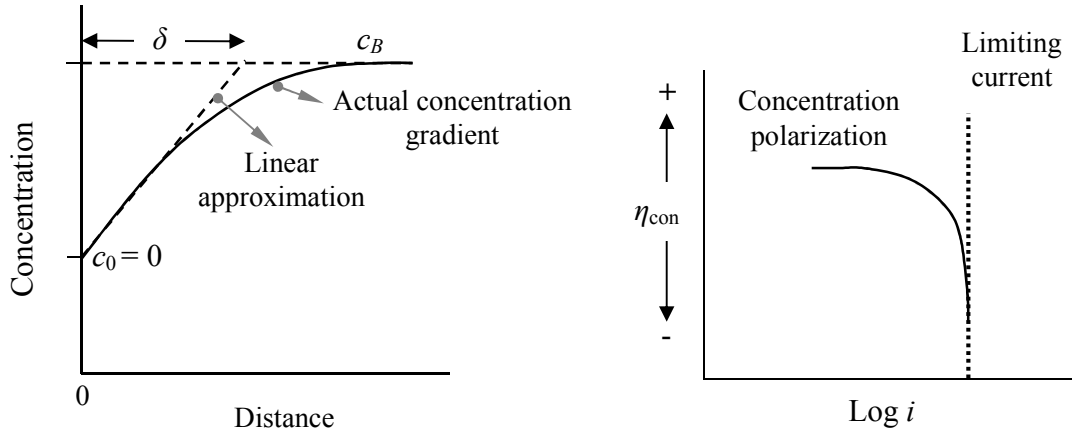

Figure 3.11: Concentration variation of charged species in electrolyte near electrode surface; cathodic concentration polarization plotted versus reaction rate or current density [71].

$$E_{H^+/H_2} = E^0_{H^+/H_2} + \frac{RT}{zF}\ln\frac{a^2_{H^+}}{a_{H_2}} \tag{3.36}$$

It is clear from Equation (3.36) that, $E_{H+/H2}$ decreases as H^+ is consumed at the surface. This decrease in potential gives rise to polarization called concentration polarization and can be written as a function of current density:

$$\eta_{conc} = \frac{RT}{zF}\ln\left[1 - \frac{i_c}{i_L}\right] \tag{3.37}$$

Using Equation (3.29) and Equation (3.33):

$$\eta_{conc} = \frac{RT}{zF}\ln\left(\frac{c_0}{c_B}\right) \tag{3.38}$$

It is obvious from Equation (3.37) that η_{conc} stays low until a point is reached where current density is reached its limiting value i_L. i_L can be defined as the maximum rate of reaction that cannot be exceeded due to limited H^+ diffusion rate in the electrolyte [56, 71].

Resistive and ohmic polarization

When charged particles move through a conducting material during current flow, they suffer a hindrance in their flow due to their interaction with oppositely charged particles. Charged particles tend to follow a straight path but due to the other particles (atoms or molecules) stack up on their way causing the moving particles to collide with them. During these collisions some of the energy contained by the moving particles gets converted into heat.

This hindrance can be in the ionic path if moving particles are ions or electronic path if particles are electrons. In electronic conductors (metals), resistance decreases at lower temperatures due to decrease in particle motion making the electrons to move with greater ease. Opposite is true with ionic conductors which exhibit lower resistance at higher temperatures due better ion mobility. This results in a higher ionic conductivity and low viscosity thereby reducing drag on particles. Material specific resistance or resistivity is measured in ohm meter Ωm and denoted by ρ. As resistivity varies inversely with the ionic conductivity of a material:

$$\rho_{el} = \frac{1}{\kappa_{el}} \tag{3.39}$$

Where, ρ_{el} is resistivity of the electrolyte and κ_{el} is electrolyte specific conductivity. If l is the length of conducting path in m, electrolyte resistance in Ωm^2 is given by:

$$R_{el} = \rho_{el} \cdot l \tag{3.40}$$

If i is the current density in A/m^2, then electrolyte polarization is given by:

$$\eta_{el} = R_{el} \cdot i \tag{3.41}$$

Resistance across electronic paths is given by Ohm's law which states that current flowing between two points in a conductor varies proportionally to the potential difference between the two points.

$$V = R \cdot i \tag{3.42}$$

Where, R is proportionality constant called resistance and has units of Ω in SI system. If R_{ohm} is the ohmic resistance of electronic conductor then ohmic polarization is given by [72]:

$$\eta_{ohm} = R_{ohm} \cdot i \tag{3.43}$$

Until this point, thermodynamics and kinetics of electrochemical processes have been discussed, but there remains yet another mechanism that has profound effect on electrochemical reactions taking place in batteries. This process is the transfer of charged particles through the electrolyte from one electrode to the other and is termed as mass transport in electrolyte or simply electrolyte transport. In composite electrodes mass transfer occurs not only in the electrolyte but also within the electrode active material particles called solid-state mass transport which has not been considered in this study.

3.3.3 Electrolyte transport

In an electrolyte solution mainly three processes contribute to the charge transfer between the electrodes: 1) convection; 2) electric migration; and 3) diffusion. Diffusion is the most significant of these three processes and described by the Fick's first law of diffusion which states that flux N of a material traversing a plane across distance x and time t is proportional to the concentration gradient and is given by:

$$N = -D\frac{\partial c}{\partial x} \tag{3.44}$$

Where, N is the diffusion flux in kg/(m^2·s), D the diffusion coefficient in m^2/s , c the concentration in kg/m^3, and x is the position in m. The rate of change in concentration is given by Fick's second law [77]:

$$\frac{\partial c}{\partial t} = D\frac{\partial^2 c}{\partial x^2} \tag{3.45}$$

In advanced battery systems composite porous electrodes are frequently used because they offer high surface areas for the reaction and short paths for the charged particles to move between the

electrodes. Transport through porous media is the whole of a subject that need elaborate description and is beyond the scope of this text. Here it is discussed only briefly with the standpoint of battery modeling.

I) Transport in porous electrodes

A porous electrode comprises of a porous matrix of electronic conductor and an electrolytic solution that fills the pores and voids in the matrix. One repeat unit of a lithium-ion battery consisting of porous cathode, anode, and separator is shown in Figure 3.12 (top). An image of porous NMC (lithium-nickel-manganese-cobalt-oxide, $LiNiMnCoO_2$) cathode and graphite anode produced by X-ray tomographic microscopy elucidating particle shape and size distribution in the micro-structured network is also shown in Figure 3.12 (middle, grey) [78].

Porous electrodes and separator are composed by a system of interconnected micro-channels of varying shapes and sizes posing a challenge to model transport mechanism in a 3D domain. Nonetheless the problem is remedied by assuming an adjustable parameter termed as tortuosity τ that is used to derive the effective transport parameters. τ depends on the material topology and gives a measure of the efficiency of permeation path. In porous electrode systems, higher τ values give rise to a decrease in energy and power densities because tortuous paths offer higher ohmic resistance to the transporting species. τ equals unity implies that the conductive path comprises of uniform cross-sectional channels parallel to the direction of flow further implying low resistance to flow and higher energy efficiency. Bruggeman relationship has widely been used though in modeling lithium-ion batteries which relate tortuosity to the pore volume fraction or porosity ε as:

$$\tau = \varepsilon^{1-B} \tag{3.46}$$

Where, B is called the Bruggeman exponent. A value of 1.5 is generally used for B in battery modeling, which has typically been derived for a system comprising uniformly sized non-conducting spherical particles mixed in a conductive electrolyte. Some have questioned the accuracy of this value but due to the lack of authentic measured data, $B = 1.5$ is still used in most of the battery models.

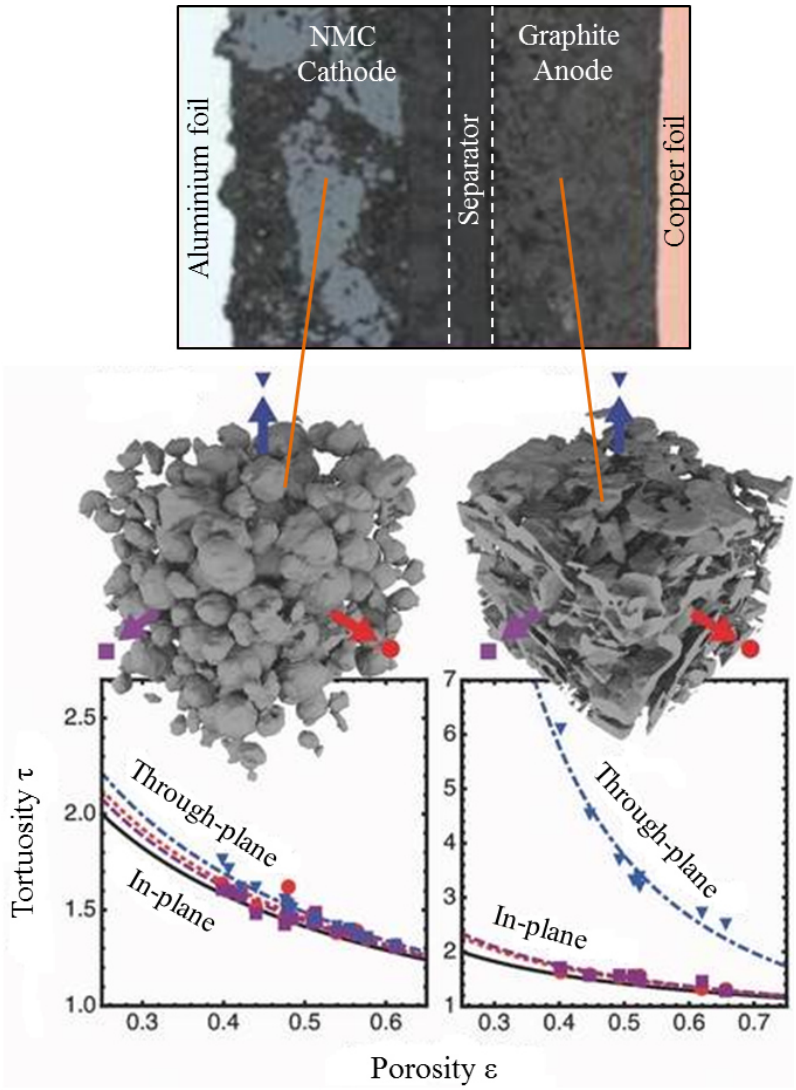

Figure 3.12: On top is shown one repeat unit of a lithium-ion battery consisting of porous NMC cathode, separator, and graphite anode along with current collecting foils; while below is the detailed image of porous electrodes created by X-ray tomographic microscopy with anisotropic tortuosities plotted versus corresponding porosities [119, 120].

Effective transport properties controlling the transfer of dissolved species (Li^+) through the electrolyte like ionic conductivity κ^{eff} and diffusion D^{eff} can be derived from the intrinsic properties of materials using tortuosity and porosity:

$$\kappa^{eff} = \frac{\varepsilon}{\tau}\kappa \quad \text{and} \quad D^{eff} = \frac{\varepsilon}{\tau}D \tag{3.47}$$

Due to the anisotropic nature of topology of new electrode materials and development of advanced measuring techniques, tortuosity can now be measured with more confidence like the one elucidated by the plots in Figure 3.12 (bottom). These plots depict anisotropic tortuosity values for NMC cathode and graphite anode plotted against corresponding porosities [121,122,123,124].

Generally two types of theories describe the electrolyte transport process: 1) dilute solution theory describes the simplest model of electrochemical systems that assumes ions interact only with solvent and not with any other species; 2) Concentrated solution theory assumes effective interaction among all the species present in the electrolyte. The two theories are discussed hereunder.

II) Dilute solution theory

This theory is seldom used in describing lithium-ion batteries for most of the electrolytes used in lithium-ion batteries demonstrate concentrated solution behaviour. But dilute electrolyte theory exhibit some utility in studying the side reactions because concentrated electrolyte theory is often proved tedious in describing the solutions involving more than three interacting species i.e. cations, anions, and solvent [79].

As current is attributed to the movement of charged particles, net current in the system can be given by the sum of fluxes of all the individual charged species :

$$i = F\sum_i z_i N_i \tag{3.48}$$

z_i is the charge number of each species. In dilute electrolytes charged particles can move around but the net current will be zero. Let us consider a small volume element within the porous electrode. Material balance of species *i* over the volume element is given by:

$$\frac{\partial \varepsilon c_i}{\partial t} = -\nabla \cdot N_i + R_{i,gen} \tag{3.49}$$

Where, $R_{i,gen}$ is the net production rate of species i. Overall this volume element exhibits an electrically neutral behavior because reaction frequently is restricted to the double layer region at the interface rendering this tiny region electrically partial. Since the interfacial region forms only a tiny fraction of the total volume of the element it is safe to assume electroneutrality within the volume element. Since we are considering only liquid phase transport, we write electroneutrality only for solution phase [71, 78].

$$\sum_i z_i c_i = 0 \tag{3.50}$$

Electrolyte ability to transport charge is associated with concentration and mobility of the charge carriers. We try to understand what actually drives the electrolyte transport. Concentration gradient causes the species to diffuse through the electrolyte hence moving from a place of higher concentration to that of the lower by diffusion. A potential gradient causes the species to move under the influence of an electric field by a physical process known as migration. Actual movement of the electrolyte bulk is another process that causes the species to move. Hence in dilute electrolyte solution, flux of each dissolved species within the pour is given by:

$$N_i/\varepsilon = \underbrace{-D_i^{eff} \cdot \nabla c_i}_{Diffusion} - \underbrace{z_i u_i F c_i \nabla \phi}_{Migration} + \underbrace{c_i v/\varepsilon}_{Convection} \tag{3.51}$$

Where, N_i is the flux of species i across the overall area of electrode, N_i/ε is flux in solution phase (pore area) only, v/ε can be approximated as the solution phase fluid velocity. ∇c_i is the concentration gradient, $\nabla\phi$ is the potential gradient negative of which is the electric field, and z_iF is the charge per mole on species i. u_i is called mobility of species i. Equation (3.51) includes some important transport parameters of an electrochemical system like diffusion coefficient, mobility, and velocity. This equation is valid for dilute electrolytes only. Combining equations (3.48) and (3.51) and neglecting diffusion and convection terms in view of the assumption that no concentration gradients exist and there is no movement of solution bulk gives:

$$i = -\varepsilon F^2 \left(\sum_i z_i^2 u_i c_i \right) \nabla \phi \tag{3.52}$$

$$\kappa^{eff} = \varepsilon F^2 \sum_i z_i^2 u_i c_i \tag{3.53}$$

Where, κ^{eff} is effective ionic conductivity of electrolyte in [$S \cdot m^{-1}$]. Also 1S (Siemens) = Ω^{-1}. Hence,

$$i = -\kappa^{eff} \nabla \phi \tag{3.54}$$

Equation (3.54) is the differential form of Ohm's law [Equation (3.42)]. Hence in electrolyte solutions, movement of charged species is governed by Equation (3.54) [80]. Nernst-Einstein equation further simplifies the dilute electrolyte theory by relating charge mobility to diffusion:

$$D_i^{eff} = RTu_i \tag{3.55}$$

Equation (3.55) implies that species that can readily be moved under the influence of electric field can also do the same under the influenced of concentration gradient.

If coefficient in the migration term of Equation (3.51) is termed as migration coefficient and denoted by $\not{D}_i^{eff}$ then:

$$\not{D}_i^{eff} = zu_i F c_i \tag{3.56}$$

Combining Equations (3.55) and (3.56), u_i can be eliminated to get:

$$\not{D}_i^{eff} = \frac{z_i F}{RT} c_i D_i^{eff} \tag{3.57}$$

III) Concentrated solution theory

Contrary to the dilute electrolyte theory that is restricted only to the ion-solvent interaction, concentrated electrolyte theory considers active interactions between all the species present in the solution and between species and the electrolyte itself. It is evident that in addition to polymer electrolytes used in lithium-ion batteries, liquid electrolytes also exhibit concentrated solution behaviour. The basis for concentrated electrolyte theory is the Stefan-Maxwell multicomponent diffusion equation.

$$c_i \nabla \mu_i = RT \sum_{\substack{j=1 \\ j \neq 1}} \frac{c_i c_j}{c_T D_{ij}} \left(v_j - v_i \right) \tag{3.58}$$

Where v_i is the velocity of species i in the electrolyte phase in relation to a reference velocity which we chose to be that of the solvent in this case. D_{ij} represents the pairwise friction interaction between species.

Considering the electrolyte to be a binary mixture for which flux relations can be obtained for both the constituting components (cations and anions). Considering electroneutrality [Equation (3.50)], representative mass balance equations for cations and anions should be identical. We can arrive at the flux equation for the anions by the inversion of Equation (3.50).

$$N_- = -\frac{v_- D_e}{vRT} \cdot \frac{c_T}{c_0} \varepsilon c \nabla \mu_e + \frac{i_2 t_-^0}{z_- F} + c_- v_0 \tag{3.59}$$

Where, $t_-^o = 1 - t_+^o = \dfrac{-z_- D_{o-}}{z_+ D_{o+} - z_- D_{o-}}$ and

$$D_e = \frac{D_{o+} D_{o-} \left(z_+ - z_-\right)}{z_+ D_{o+} - z_- D_{o-}}$$

From dilute solution theory, Equation (3.49):

$$\varepsilon \frac{\partial c_-}{\partial t} = -\nabla \cdot N_- + a j_- \tag{3.60}$$

Where, aj_- is the rate of reaction of the anion per unit volume. Substituting the flux equation,

$$\varepsilon \frac{\partial c}{\partial t} = \nabla \cdot \varepsilon D_e \left(1 - \frac{d \ln c_0}{d \ln c}\right) \nabla c + \frac{t_-^0 \nabla i_2 + i_2 \cdot \nabla t_-^0}{z_+ v_+ F} - \nabla \cdot c v_0 + a j_- \tag{3.61}$$

Where, $c = c_-/v_-$. Electrochemical potential in salt electrolyte and molality to concentration relations are:

$$\mu_e = v_+ \mu_+ + v_- \mu_- = \mu_e^0 + vRT \ln f_\pm m \tag{3.62}$$

Where, $m = \dfrac{c_e}{c_0 M_0}$

And charge balance for a binary electrolyte:

$$z_+ v_+ = -z_- v_- \tag{3.63}$$

Convection in electrolyte is usually negligible; hence term v_0 can be neglected. $z_+ v_+$ is 1 for most salts used in lithium-ion batteries. j is zero in absence of side reactions. If active material does not change in volume as it reacts and there is no side reactions that changes electrode porosity then no mass balance for solvent is needed.

The form of the mass balance presented in Equation (3.61) is the most convenient for treating multiple reaction pathways, such as encountered when treating side reactions, double layer capacitance or particle distribution. In these situations ∇i may have a complicated relationship to local reaction rates, but mass balance in form of Equation (3.61) remains unchanged [71, 78, 79].

In contrast to the dilute solution theory where effective diffusion coefficient D_{eff} is derived from porosity alone, additional parameters like electrolyte diffusivity D_e and ionic diffusional conductivity k_D^{eff} are required to derive effective diffusivity in case of concentrated electrolyte.

$$D_-^{eff} = \varepsilon_e^{B_-} D_e + \frac{t_- \kappa_D^{eff}}{z_- F c_-} \tag{3.64}$$

Effective diffusion coefficient also depends on transference number of positive ions in the solvent t_+ (where: t_- = 1- t_+). As different ions move at different speeds in the electrolyte, each of the ions contributes differently to the flow of current corresponding to the speed at which it moves represented by the quantity called transference number $t_\pm$. Where + and – subscripts indicate positively and negatively charged ions i.e. Li^+ and PF_6^- in this study. The effective diffusional ionic conductivity k_D^{eff} can indirectly be related to the chemical potential through the electrolyte concentration of the dissolved species [Equation (3.62)] and is given by:

$$\kappa_D^{eff} = \frac{2RT}{F} \kappa^{eff} (t_+ - 1)\left(1 + \frac{d \ln f_\pm}{d \ln c_e}\right) \tag{3.65}$$

The activity coefficient in Equation (3.58) compensates for the deviations of dissolved species from the ideal behavior where there is no interaction either between each of the dissolved species or between the species and electrolyte.

From Equations (3.54) and (3.59), migration coefficient of positive and negative ions can be obtained:

$$D_{\pm}^{eff} = \frac{t_{\pm}}{z \pm F} \kappa^{eff} \tag{3.66}$$

In case of concentrated solutions, the Bruggeman exponent used to get the corrected ionic conductivity κ^{eff} is different to that used to get the corrected diffusivity D^{eff} as can be seen from Equation (3.64). In addition to Bruggeman exponent parameters like electrolyte diffusivity D_e, ionic diffusional conductivity κ_D^{eff}, and transference number $t_{\pm}$ as well as activity coefficient $f_{\pm}$ is required to obtain D^{eff}. All the above mentioned parameters are temperature and concentration dependent and can be obtained from experimental measurements or fitting data from the published findings [72].

3.4 Heat generation in batteries

There are mainly three heat sources that contribute to the overall heat generation in electrochemical energy storage systems: 1) Reversible heating constituted by thermodynamic and entropic changes involved in the electrochemical reaction; 2) Irreversible heating constituted by activation and concentration polarization; and 3) Joule effects. Polarization effects include heat generation due the resistances induced by activation and concentration polarizations. Whereas Joule heating is caused by the electrolyte resistance and solid circuit resistance that include wires, connectors, terminals etc. Heat generation caused by electrolyte resistance is termed as resistive heating while that caused by the external circuit is called ohmic heating. Hence total heat generation rate in a cell is given by [72, 81]:

$$\dot{Q}_{gen} = \dot{Q}_{ent} + \dot{Q}_{pol,\,act} + \dot{Q}_{pol,\,conc} + \dot{Q}_{res} + \dot{Q}_{ohm} \tag{3.67}$$

Where,

Reversible heat $= \dot{Q}_{ent}$

Irreversible heat $= \dot{Q}_{pol,\,act} + \dot{Q}_{pol,\,conc}$

Joule heat $= \dot{Q}_{res} + \dot{Q}_{ohm}$

Starting from a basic electrochemical cell, it is learned how different complex mechanisms evolve into the heat generation process in electrochemical energy storage systems. Moreover important parameters required in building the model equations have also been defined. Mechanisms that help driving the generated heat off the cell have also been discussed. With reasonable background information provided in this chapter, the next stage is to build a comprehensive thermal model for the selected high-power lithium-ion battery systems which is presented in the next chapter.

Chapter 4

Model development

Thermal models help saving significant amounts of efforts and resources that otherwise are required for designing a robust thermal management system for automobile battery systems. In this chapter appropriate mathematical relations are developed that can be used to simulate thermal variations taking place in the selected lithium-ion cells under different loads and environmental conditions. The model is developed in three steps: 1) geometry construction; 2) heat transfer model; and 3) electrochemical heat generation model. Once heat transfer and heat generation models are developed, it is required to integrate them into a single model which is done by coupling of the two models using different coupling methods. A multi-scale and multi-dimensional (MSMD) dynamic coupling mechanism is presented at the end of this chapter that makes the two models act in a coordinated manner capturing all the variations in space and time. Priorly an overview of the previous thermal models and different coupling strategies is presented.

4.1 Review of lithium-ion battery thermal models

A complete thermal model of an electrochemical energy storage system comprises of two parts: an electrochemical heat generation model and a heat transfer model. These two models act in a coupled manner to give a complete and clear picture of thermal behavior of the cell. A brief review of the previous thermal models of lithium-ion batteries and coupling approaches used are presented hereunder.

Different strategies have been adopted by the researchers to develop coupled electrochemical-thermal (EC-T) models for lithium-ion batteries. Due to inconsistent geometry of cells, complex nature of electrochemical phenomena, and difficulties involved in coupling EC-T models dynamically, most of the EC-T coupled models are restricted to a 2D level [5, 6, 7, 8, 9] or assumed a spatially uniform temperature [10]. Some researchers used temperature dependent physicochemical properties like diffusion coefficient and electrolyte ionic conductivity to couple electrochemical and thermal models through Arrhenius equation [9, 10, 11, 12]. Others used equivalent-circuit-diagram (ECD) approach to simulate electrical response of an electrochemical system and a lumped thermal model to simulate heat transport inside and out of the cell [13, 14, 15, 16].

S. Chacko and Y.M. Chung developed a 3D fully coupled EC-T model to predict thermal behaviour of a Li-ion polymer pouch cell under dynamic loading conditions [85]. L. Kostetzer and others carried out system level electro-thermal simulations based on finite element (FE) model for an automotive lithium-ion battery pack [86]. Kyu-Jin Lee and associates developed a multi-scale multi-dimensional (MSMD) model to study thermal behaviour of a spirally wound large format automotive lithium-ion battery to look into the interactions between local electrochemical reactions and macro-scale heat transfer phenomena [87].

Because of high complexity and non-linearities involved in electrochemical systems, ECDs always remain an approximation [13]. Lumped model does not account for the inner details of the battery geometry [16]. 2D models are not capable of fully predicting the anisotropic nature of thermal responses of individual lithium-ion cells especially in cylindrical formats where higher gradients exist due to compact structure, smaller heat transfer areas, and restricted heat flow. Also in automobile application where higher thermal gradients are expected due to higher currents involved, 2D models stand short in serving the purpose.

Hence dynamically coupled, 3D transient model is required that incorporates both the complex electrochemical heat generation phenomena taking place on lower scales and the heat transport phenomena occurring on a cell level. A model is presented that comes up to aforementioned requirements. Before moving on to the main model, a brief description of the cell construction and electrode makeup is presented.

4.2 Cell construction and electrode chemistry

Detailed thermal analysis of individual cell technologies emanating from intensive research in the field of lithium-ion batteries has seldom been realized. Amongst these new technologies LFP and NCA are the most sought after technologies as compared to the rest used to propel vehicles. Hence for this work two high power cells based on NCA and LFP cathode chemistries have been selected that include VL 7P from SAFT and 26650 from A123 Systems respectively. The choice has been made based on individual merits on vehicle application and growing demand for these cells in the vehicle market.

New advanced nanostructured materials that are low cost and safe are being developed to be used as electrode active materials for high power lithium-ion batteries. For example, nanostructured lithium-iron-phosphate ($LiFePO_4$) and lithium-manganese-oxide ($LiMn_2O_4$) are used in the fabrication of cathodes are less expensive and friendly to the environment. On the other hand new anodes are being developed that use titanate-oxide and nanostructured alloys having potentials higher than graphite. New class of non-volatile and non-flammable electrolytes are developed using lithium salts in ionic liquids that are stable at higher temperatures and higher potentials and offer a better control of unwanted side reactions.

LFP technology has become the focus of innovative research. The patent activity focusing LFP technology is at least double than LTO and quadruple than NMC technologies [51, 55]. For that reason 26650 is opted to be used for multi-scale modelling incorporating both the electrochemical heat generation and heat transfer phenomena. While VL 7P due to its complex geometry is used to study the influence of geometrical parameters on thermal behaviour of the cell and heat flow patterns inside the cell. Such an analysis does not require micro level heat generation model since application of uniform heat generation rate as body load suffices. Additionally, to investigate the effect of cell configurations on thermal behaviour, arbitrary cell configurations e.g. cylindrical, prismatic, and pouch are modelled as well (chapter 6).

4.2.1 Lithium-iron-phosphate ($LiFePO_4$)

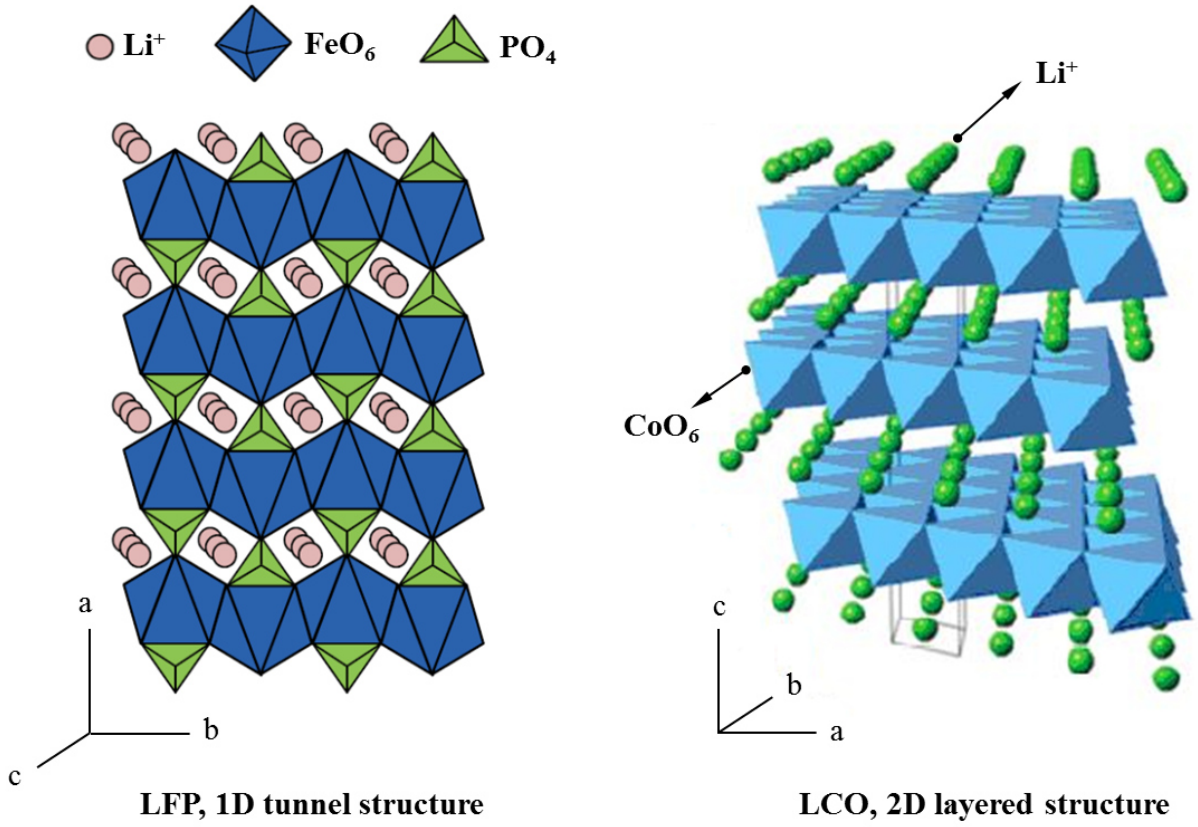

a) ***b)***

Figure 4.1: *a)* LFP olivine structure; *b)* LCO layered structure [83, 136, 137].

26650 cell is composed of a lithium-iron-phosphate ($LiFePO_4$) or LFP cathode and a graphite anode. Since 1997, when $LiFePO_4$ has been discovered, it has evolved as a winning candidate for cathode active material to be used in high power lithium-ion batteries. It possesses an olivine crystal structure as shown in Figure 4.1*a* in which Fe^{+3}/Fe^{+2} redox pair is stabilized through Fe-O-X inductive effect which incorporates high thermal stability thus making it to operate safely even at higher temperatures. Moreover it exhibits a flatter discharge potential behavior against Li/Li^+ [83, 4].

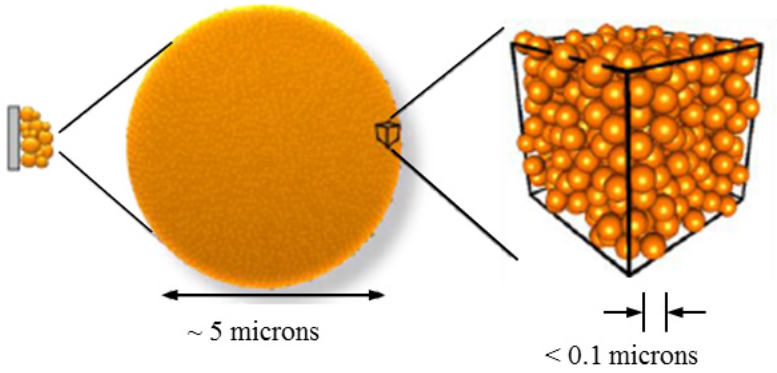

Figure 4.2: Schematic of LFP nanostructured cathode showing stepwise arrangement of active material particle size [84].

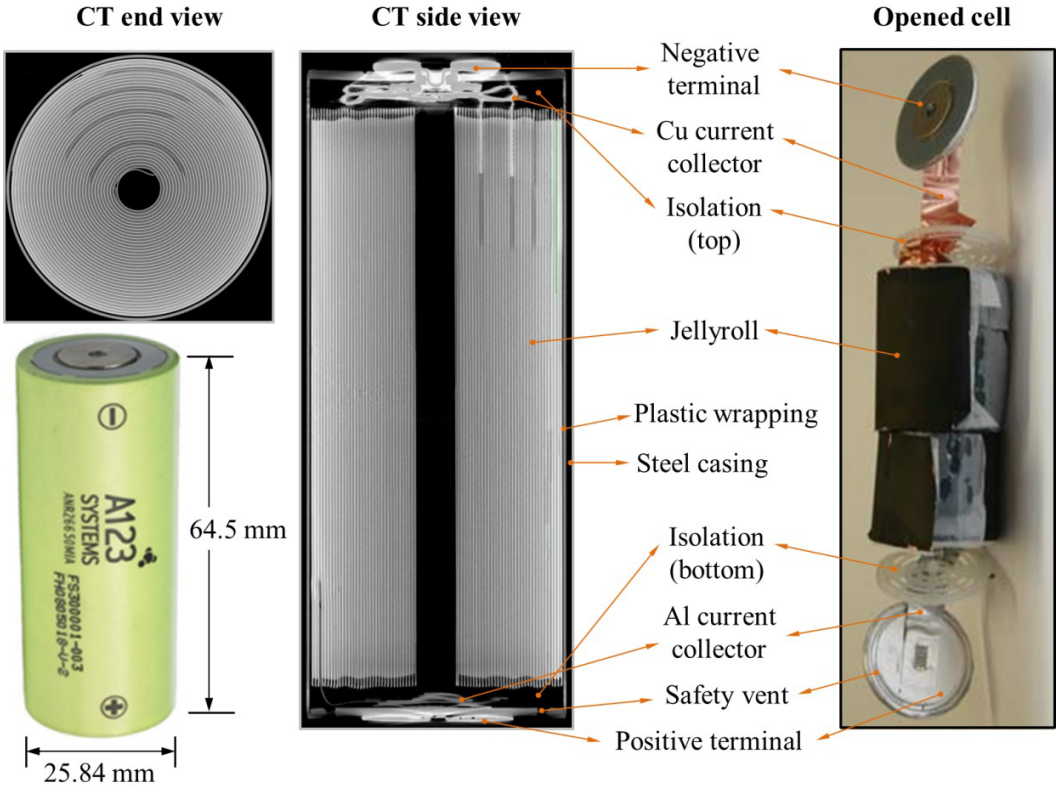

Figure 4.3: Geometrical details of 26650 cell and the constituting components obtained from computer tomographic (CT) scans and unpacking of the cell [49, 72, 88].

In recent years, employment of nanotechnology in the fabrication of $LiFePO_4$ based cathodes has further improved its electrochemical performance. Major drawback of LFP is its lower capacity

due to low electric conductivity. A lot of efforts are being made to overcome this problem which includes coating the particles with highly conductive material like carbon black powder [82].

Table 4.1: 26650 cell specifications [91]

Parameter	**Value**	**Units**
Cell diameter	25.85 ± 0.30	(mm)
Cell diameter (with sleeve)	26.62 ± 50	(mm)
Cell length	65.15 + 0.65/-0.00	(mm)
Cell weight	0.070	(kg)
Cell volume	0.034	(dm^3)
Cell capacity (nominal)	2.3	(Ah)
Cell capacity (minimum)	2.2	(Ah)
Cell voltage (nominal)	3.3	(V)
Internal impedance (1kHz AC)	8	(mΩ)
Standard charge method	3 A – 3.6 V (CCCV), 45 min	
Fast charge	10 A – 3.6 V (CCCV), 15 min	
Maximum contineous discharge	70	(A)
Maximum pulse discharge (10 sec)	120	(A)
Cycle life at 10C discharge, 100 % DOD	>1000	(cycles)
Operating temperature	-30 to 55	(°C)
Storage temperature	-40 to 60	(°C)

Chiang and his group [84] developed a new material called nanophosphate possessing olivine based crystal structure which showed a dramatic improvement in conductivity and rate capability

compared to normal lithium-iron-phosphates. This patented product had been adopted by A123 Systems for commercial application.

Nanophosphate due to specially designed structure and specific chemical properties impart lithium-ion batteries high performance capabilities. Stepwise particle size distribution in cathode active material increases the effective surface area by tremendous amounts. Figure 4.2 shows (left to right) nanophosphate particles in the range of 5 microns called secondary particles are applied on to aluminum current collecting foil. These secondary particles are composed of even smaller particles called primary particles of size less than one tenth of a micron. Nanophosphate technology offers a number of advantages like improved safety with high power and viable energy plus longer operation life [84].

In order to develop close to the real geometry model, the cell has been observed very closely and carefully using visual observations of the opened cell and images obtained from computer tomography (CT) of the cell. 26650 cell is shown in Figure 4.3 with details of the cell makeup components and CT scans (top and side views). Specification data of the cell is presented in Table 4.1. Geometrical data has been collected on two levels: 1) on cell level by visual observations and measurements; and 2) on electrode level using CT scans both carried out at the institute of technical thermodynamics (ITT) German Aerospace Center (DLR), Stuttgart, Germany.

Jellyroll is made by rolling over the anode-separator-cathode sequences and consists of 35.8 windings and 72 repeat units. A repeat unit with thicknesses of the constituting components is shown in Figure 4.4. Aluminum and copper current collectors are pasted with active material on both sides. Jellyroll makes 24.84 mm outer diameter and 4.4 mm inner diameter. Cathode (+) is connected to the outer casing while anode (-) is connected to the top terminal insulated from the casing by a thin insulating gasket. Cell is measured to have a length of 64.5 (~65) mm and outer diameter of 25.84 (~26) mm hence given the name 26650 [88]. Micro level dimensions of the electrodes, separator and current collecting foils are given below:

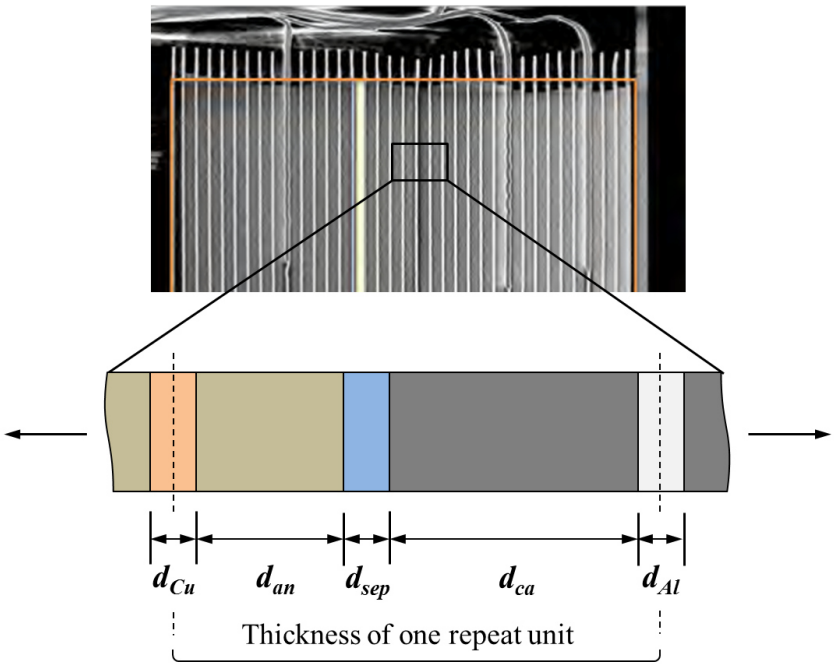

Figure 4.4: Schematic of micro-scale electrode structures zooming one repeat unit [72].

Thickness of copper current collector,	$d_{Cu} = 15.0 \times 10^{-6}$ m
Thickness of aluminum current collector,	$d_{Al} = 25.0 \times 10^{-6}$ m
Thickness of cathode active material,	$d_{ca} = 79.5 \times 10^{-6}$ m
Thickness of anode active material,	$d_{an} = 35.5 \times 10^{-6}$ m
Thickness of separator,	$d_{sep} = 20.0 \times 10^{-6}$ m

Thickness of one repeat unit, d_{ru} is the given by:

$$d_{ru} = d_{Cu}/2 + d_{Al}/2 + d_{ca} + d_{an} + d_{sep} = 155 \times 10^{-6} \text{ m} = 155\ \mu\text{m}$$

4.2.2 Lithium-nickel-cobalt-aluminum-oxide (NCA)

VL 7P consists of lithium-nickel-cobalt-aluminum-oxide or NCA ($LiNi_{0.8}Co_{0.15}Al_{0.05}O_2$) cathode and graphite anode. NCA belongs to a class of compounds having a closely packed lattice of anions (negatively charged ions e.g. O^{2-}). Each alternate layer in the anionic lattice is filled by redox-active transition metal (Co^{+2}/Co^{+3}, Fe^{+2}/Fe^{+3} etc.). Remaining unoccupied layers are then

inserted by lithium ions during intercalation process. This formation, elucidated in Figure 4.1*b*, enjoys advantage of storing more energy per unit of its volume due to compact layered structure [92].

Table 4.2: VL 7P cell specifications [93]

Parameter	**Value**	**Units**
Cell diameter	41	(mm)
Cell length	145	(mm)
Typical weight	0.37	(kg)
Volume	0.19	(dm^3)
Cell capacity (average)	7	(Ah)
Cell capacity (minimum)	6.5	(Ah)
Cell voltage (nominal)	3.6	(V)
Specific energy (after charge, 4.0 V)	67	(Wh/kg)
Energy density (after charge, 4.0 V)	131	(Wh/dm^3)
Specific power (10 s/50 % DOD)	1811	(W/kg)
Power density (10 s/50 % DOD)	3526	(Wh/dm^3)
Volt limit (charge)	4.0 (4.1 for peak)	(V)
Volt limit (discharge)	2.5 (2.0 for cold cranking)	(V)
Maximum contineous current)	100	(A)
Maximum peak current during 10 s	100	(A)

Since VL 7P is employed for heat transfer (macro level) modeling only, detailed electrochemistry (heat generation) model is not required for this cell. Details of cell construction with description of individual components obtained through visual observations of the opened cell are shown in Figure 4.5.

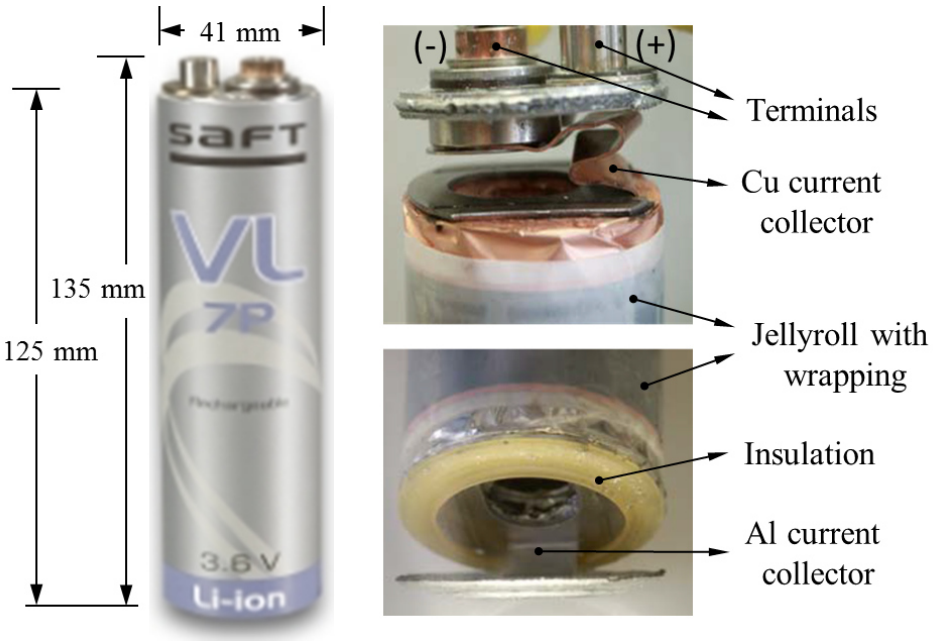

Figure 4.5: Inner and outer construction and constituting components of VL 7P cell [93].

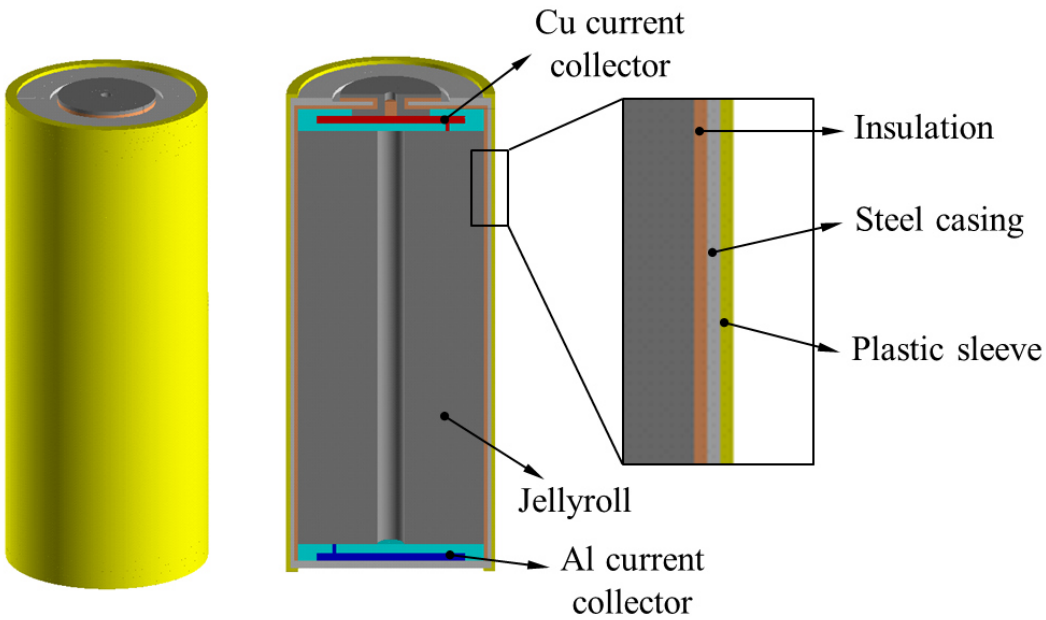

Figure 4.6: 3D geometry model presenting full and bisected view of 26650 cell.

4.3 Geometry model

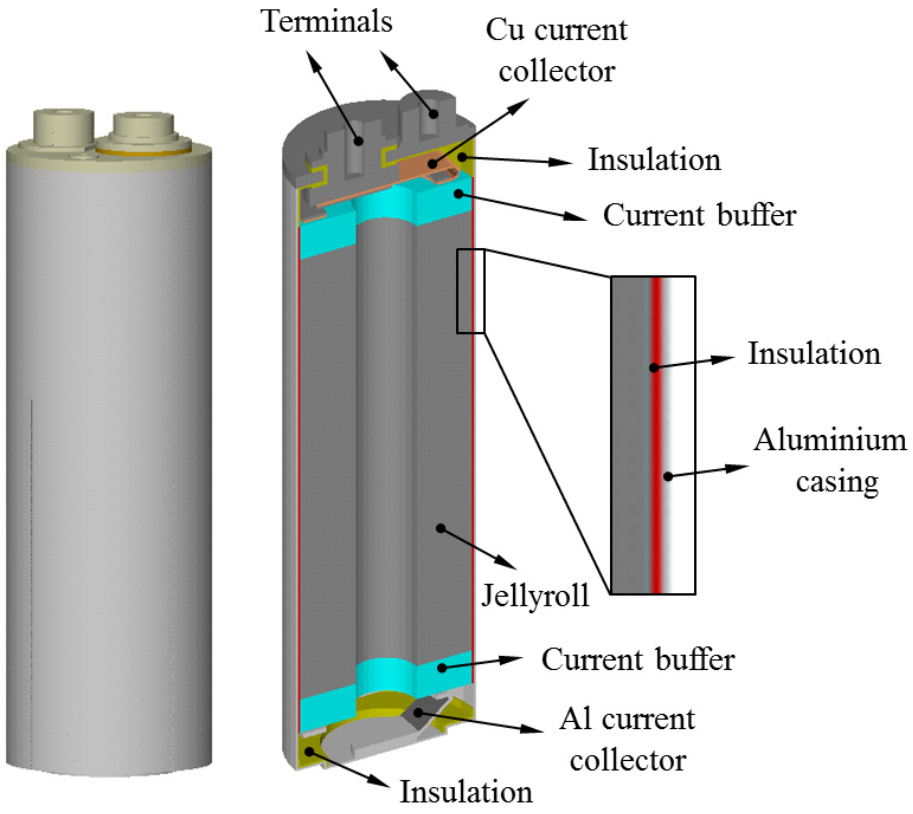

Figure 4.7: 3D geometry model presenting full and bisected view of VL 7P cell.

Variations in size and shape of a cell and components influence thermal efficiency of the cell as much as thermal and electrochemical reaction parameters do. Geometry model forms the basis for a mathematical model to make accurate predictions. While developing a geometry model the emphasis should be on capturing maximum topographical details without burdening the overall model with added complexities leading to extra computational efforts. Slight adjustments in actual geometry have to be made to accommodate for the domain discretization and software limitations.

Many computer aided design (CAD) based programs like CATIA, PROE, ANSYS etc. are available for creating 3D geometries. In present work, 3D geometry model has been developed

using ANSYS built in CAD tools. Geometry parameters for the two cells are presented in Table 4.1 and Table 4.2.

Detailed geometry model on a 3D level is proved somewhat expensive in terms of computation time and resources but offers more accurate predictions as compared to the lower dimension models. 1D or 2D geometry models can perform well in predicting temporal variations in parameters but they usually fall short in capturing spatial variations. 3D geometry models remedy this shortcoming by incorporating the hidden geometry details that are missed by 1D or 2D models. 3D visualization of gradients existing inside a battery provides important information about its thermal behavior.

In this section detailed 3D geometry models of the two cells are presented. The models incorporate most of the finer details of cell shape and construction. Jellyroll (JR) is assumed to be a composite material with distinct thermal and physical properties rather than a layered structure of electrodes. Geometry models of the two cells in their complete and bisected forms with description of the components are shown in Figure 4.6 and Figure 4.7. Minor adjustments are made in the models due mainly to the software limitations.

4.4 Heat transfer model

In this section equations governing heat transfer model derived from basic energy conservation laws are presented. In addition, initial and boundary conditions as well as assumptions made to simplify the model are also presented.

Due to the treatment of JR as a composite body, the dominating heat flow mechanism inside the cell restricted to conduction. Though convection dominates the heat dissipation process out of the cell, radiation cannot be ignored either. Input parameter for the heat transfer model is volumetric heat generation rate which can either be applied as a constant heat generation rate or derived through direct or indirect coupling with electrochemical heat generation model. Heat transfer model in this work is developed in a way to be used in combination with the electrochemical heat generation model or independent of the heat source. Temperature is the key output parameter obtained from heat transfer simulations.

For 3D heat transfer model, following assumptions have been made:

- Jellyroll (JR) is a single composite material with distinct thermal and physical properties e.g. thermal conductivity, heat capacity, and density
- Contacts between JR, insulation, and the outer can are perfect.
- No variations in heat generation rate in φ direction (Figure 4.12).
- Current collector perturbation effects are ignored.
- Spatial variations in heat generation rate between the coupling points are linearly interpolated in axial and radial directions.

4.4.1 Model parameters

Heat transfer transient simulations require thermal properties like specific heat (c_P), thermal conductivity (k), and density (ρ) for each of the cell components. For most of the cell components material properties are well established and can easily be found in published literature except for the jellyroll which is composed of variety of materials subject to manufactures confidentiality. Since overall weight and volume of most of the lithium-ion cells is occupied by the jellyroll, thermal parameters derived for the complete cell are often assumed for the jellyroll in heat transfer models.

As jellyroll is assumed to be a composite structure with distinct properties, thermal and physical parameters of jellyrolls of the two cells are presented in Table 4.3. Thermal parameters for rest of the cell component materials like copper, steel, aluminum, plastic etc. are derived from the literature. Volumetric heat capacities for the two cells presented in Table 4.3 are converted to specific heats by dividing by the cell densities. Due to comparative nature of simulations arbitrary values of heat transfer coefficient (h_f) have been used for VL 7P cell. For 26650 cell a value of 55 W/(m^2·K) adopted from [72] has been used to simulate heat dissipation from the cell surface inside the climate chamber.

Detailed description of different experimental and simulation methods used to determine thermal model parameters given in table 4.3 can be found in Appendix B.

Table 4.3: Thermal parameters used in 3D heat transfer model for the two cells

Parameter	Value	Units	Source
VL 7P jellyroll			
Thermal conductivity, k:			
Radial component, k_r	0.80	(W/(m·K))	[94]
Axial component, k_z	27	(W/(m·K))	[94]
Volumetric heat capacity, c	2.04×10^6	(J/(m^3·K))	[94]
Specific heat, c_P	1048	(J/(kg·K))	[c, e]*
Density, ρ	1947	(kg/m^3)	[93]
26650M1A jellyroll			
Thermal conductivity, k:			
Radial component, k_r	1.02	(W/(m·K))	[72]
Axial component, k_z	39.66	(W/(m·K))	[c, e]*
Volumetric heat capacity, c	1.85×10^6	(J/(m^3·K))	[72]
Specific heat, c_P	766.74	(W/(kg·K))	[c, e]*
Density, ρ	2412.80	(kg/m^3)	[c, e]*

[e]: Estimated; [c]: Calculated from [107, 108, 109, 110]

* Detailed calculations of parameter evaluation are presented in Appendix B.

4.4.2 Model development

Applying the energy conservation law across the differential element:

$$\dot{Q}_V = \rho c_P\left(\frac{\partial T}{\partial t} + [v]\nabla T\right) + \nabla\cdot[\mathbf{q}] \qquad (4.1)$$

Where,

$\dot{Q}_V$	= Volumetric heat generation rate,	(W/m^3)
ρ	= Density,	(kg/m^3)
c_P	= Specific heat,	(J/(kg·K))
T	= Temperature,	(K)
t	= time,	(s)
[**q**]	= Heat flux vector	(W/m^2)

∇ = Vector (divergence) operator (1/m)

$[v]$ = Velocity vector for bulk (mass) transport of fluid (m/s)

Substituting for heat flux vector [**q**] in Equation (4.1) from Equation (3.6):

$$\dot{Q}_V = \rho c_P \left(\frac{\partial T}{\partial t} + [v] \nabla T \right) - \nabla \cdot \left([k] \cdot \nabla T \right) \tag{4.2}$$

Where,

$$[k] = \begin{bmatrix} k_{xx} & 0 & 0 \\ 0 & k_{yy} & 0 \\ 0 & 0 & k_{zz} \end{bmatrix}$$ = Thermal conductivity matrix

k_{xx}, k_{yy}, k_{zz} = Thermal conductivity in 3D solid (differential) element in x, y, and z direction.

Since jellyroll is assumed to be a compact solid with no bulk movement, all the heat transfer inside the cell is supposed to take place by conduction alone. Hence ignoring velocity vector term in Equation (4.2) and expanding in its general form assuming global Cartesian system gives:

$$\rho c_P \frac{\partial T}{\partial t} = \dot{Q}_V + \frac{\partial}{\partial x}\left(k_x \frac{\partial T}{\partial x} \right) + \frac{\partial}{\partial y}\left(k_y \frac{\partial T}{\partial y} \right) + \frac{\partial}{\partial z}\left(k_z \frac{\partial T}{\partial z} \right) \tag{4.3}$$

Equation (4.3) in its compact form:

$$\rho c_P \frac{\partial T}{\partial t} = \dot{Q}_V + \nabla \cdot \left(k \nabla T \right) \tag{4.4}$$

In Equation (4.3), k_x, k_y, and k_z are x, y, and z components of thermal conductivity respectively. In case of cylindrical coordinates Equation (4.3) can be rewritten as:

$$\rho c_P \frac{\partial T}{\partial t} = \dot{Q}_V + \frac{1}{r} \cdot \frac{\partial}{\partial r}\left(k_r \frac{\partial T}{\partial r} \right) + \frac{1}{r^2} \cdot \frac{\partial}{\partial \varphi}\left(k_\varphi \frac{\partial T}{\partial \varphi} \right) + \frac{\partial}{\partial z}\left(k_z \frac{\partial T}{\partial z} \right) \tag{4.5}$$

Where, k_r and k_z are radial and axial components of thermal conductivity respectively whereas k_φ is the circumferential or angular component. Equation (4.4) is the main equation used to describe heat transfer within different configurations of lithium-ion batteries. For steady state analysis Equation (4.3) reduces to:

$$\dot{Q}_V = -\nabla \cdot (k \nabla T) \tag{4.6}$$

Quantity $\dot{Q}_V$ is the overall volumetric heat production rate which can either be applied as a uniform input as in case of VL 7P cell model or can be obtained through direct coupling with the electrochemical heat generation model as in case of 26650 cell. To describe heat transfer out of the cell, convection and radiation boundary conditions have been used at the cell exteriors.

4.4.3 Boundary and initial conditions

Two types of boundary conditions are applied at the cell exterior that is convection and radiation while adiabatic conditions are assumed at the cell interiors.

Heat dissipating from the cell outer surfaces to the ambient is the sum of the heats rejected due to convection and to radiation. Convective heat dissipating through the cell exteriors can be calculated using Equation (3.9):

$$\mathbf{q}_{con} \cdot \mathbf{n} = h_f (T_{sur} - T_{amb}) \tag{4.7}$$

Where $\mathbf{q}_{con}$ is heat transfer per unit area due to convection, $\mathbf{n}$ is the unit vector normal to the convective surface, and h_f is the heat transfer or film coefficient calculated at average of T_{sur} and T_{amb} [68].

Since in the experimental setup used to carry out battery cycling experiments for model validation, 26650 cell was placed inside the climate chamber, radiation heat flew from the cell exteriors to the climate chamber walls and components. Geometry model of climate chamber with cell and cell holder along with other components is shown in Figure 4.8. Since the surface area of the chamber walls and components is much larger than that of the cell, we considered the case of radiation heat exchange between a very small and very large surface. Hence the net radiation heat flux from the cell exterior is given by:

$$\mathbf{q}_{rad} \cdot \mathbf{n} = \frac{F_{s-w}\varepsilon_s}{F_{s-w}(1-\varepsilon_s)+\varepsilon_s} \sigma (T_{sur}^4 - T_w^4) \tag{4.8}$$

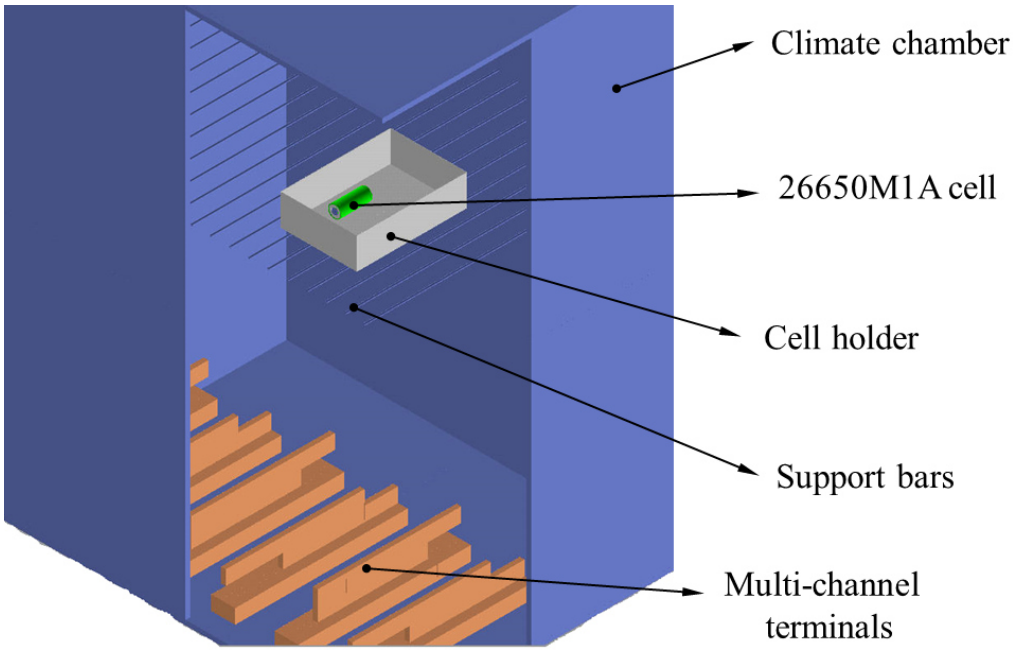

Figure 4.8: Geometry model showing inside view of climate chamber along with the cell. To simulate radiative heat exchange between cell and chamber interiors, approximate dimensions were used to create climate chamber geometry model.

Where $\mathbf{q}_{rad}$ is radiative heat flux from the cell and $\mathbf{n}$ is a unit vector. $F_{s\text{-}w}$ is the view factor between cell exteriors and climate chamber components, ε_s is the emissivity of radiating surfaces and T_{sur} and T_w are absolute temperatures at the cell surface and climate chamber walls or components respectively. Emissivity values of 0.90, 0.19, 0.60, and 0.65 have been used for cell sleeve (PVC), cell holder (aluminium), climate chamber walls (stainless steel), and electric terminals (copper) respectively. These values have been approximated from [140, 141].

Radiosity solution method has been used to find radiation heat flux which employs hemicube method for view factor calculations. In order to save computation effort, view factor calculations are done only at the first time step and used for the subsequent time steps. A default value of 10 is used to set the resolution of view factor calculations through HEMIOPT command. Higher value improves accuracy of view factor calculations. Detailed description of these methods and derivation of Equation (4.8) can be found in [128].

Following boundary conditions have been used at the cell interior:

$$\mathbf{q}_{con} \cdot \mathbf{n} = 0 \qquad \text{and} \qquad \mathbf{q}_{rad} \cdot \mathbf{n} = 0 \qquad (4.9)$$

At time, $t = 0$

$$T_{ini} = T_{amb}$$

Where, T_{ini} is the initial temperature at the beginning of simulation and T_{amb} is the ambient or operating or environment temperature.

4.4.4 Heat transfer simulations

Heat transfer model equations described above have been solved using ANSYS software package which is based on finite element method (FEM). It is a powerful numerical technique to solve complex engineering problems. In finite element analysis (FEA), domain is divided into a number of smaller regions of finite sizes called finite elements. Assemblage of these elements in a domain is called finite element mesh. Each finite element consists of two or more specific points called nodes [95, 96]. Each node in an element is assigned with a primary unknown e.g. temperature called degree of freedom (DOF) to be determined in the analysis. DOF in ANSYS are predefined for specific element types found in ANSYS element library [68]. All the elements in a mesh are connected by nodes with the neighboring elements sharing nodes on adjacent edges or faces depending on geometry (2D or 3D).

The major steps followed in ANSYS analysis include parameter definition followed by construction of geometry model using ANSYS built-in CAD tools. Once the geometry model is complete finite element mesh is generated using one of the appropriate predefined elements from ANSYS library. Free and mapped mesh patterns are used in ANSYS with mapped mesh requiring more efforts as compared to free mesh but offers advantages regarding the accuracy of final results. Elements exceeding the allowable limits of edge or face angles or aspect ratio give rise to poor quality mesh. In present work mapped meshing has been used throughout the domains. Bisected views of meshed geometries of the two selected cells are shown in Figure 4.9. Nodal temperature is calculated as key solution output which subsequently is used to obtain other thermal quantities like thermal fluxes, heat flow etc.

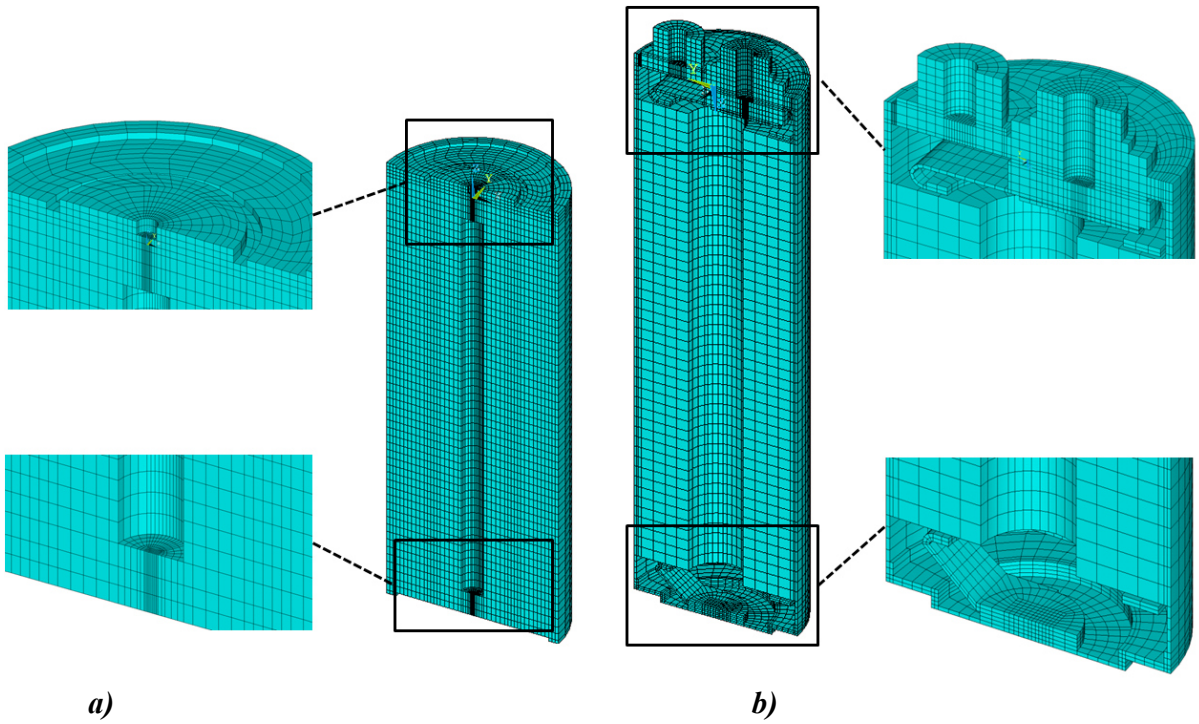

a) ***b)***

Figure 4.9: Bisections with enlarged views of 3D hexahedral element mesh on: *a)* 26650; *b)* VL 7P cells.

Different element types have been used in this analysis depending on the application. For example, plane areas have been meshed using 2D elements which have been extruded into 3D volumes. Exteriors of the meshed volumes have then been cladded with surface elements to find heat fluxes out of the cell exteriors.

A brief description of the specific element types selected for the simulations is given below:

1) **PLANE55:** a 2D, 4-node thermal element having 2D thermal conduction capabilities;
2) **SOLID70:** a 3D, 8-node thermal solid element with 3D thermal conduction capabilities;
3) **SURF152:** a 2D, 4-node element used for surface effect applications; and
4) **SURF252:** a thermal radiation surface effect element used with radiosity solution method to calculate radiative heat fluxes [68].

Detailed description of these elements and coordinate systems can be found in [129].

4.5 Electrochemical heat generation model

As mentioned before that a uniform heat generation rate is assumed in case of VL 7P cell model hence requires no direct coupling with electrochemical heat generation model. Therefore to develop electrochemical heat generation model, 26650 cell is considered alone. Electrochemical heat generation model is adopted from the previous work of C. Hellwig et al., J. P. Neidhardt et al., and W. G. Bessler et al. [97, 101, 103]. Parameters used in electrochemical heat generation model are presented in Table 4.4.

4.5.1 Thermodynamics

When lithium ions intercalate into the electrode active material, it undergoes thermodynamic changes causing the characteristic half-cell potential to change. This implies that the electrode half-cell potential varies as a function of lithium concentration within the electrode active material. Lithium ion concentration is used as a normalized quantity varying between 0 and 1. It is the ratio of lithium ion concentration at any given time to its maximum concentration.

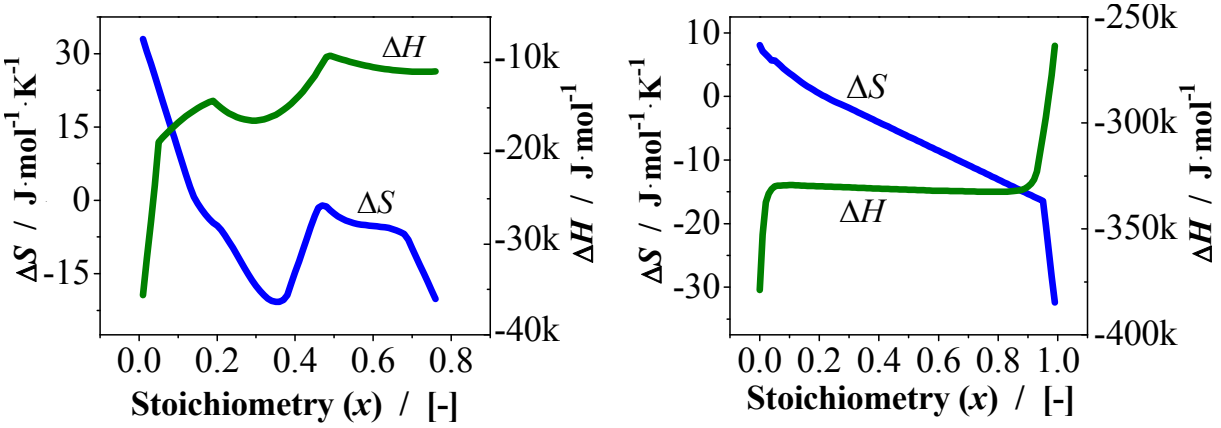

Figure 4.10: Thermodynamic parameters plotted as a function of normalized Li^+ concentration: *a)* Graphite (anode) enthalpy and entropy data derived from [130] and [131] respectively; and *b)* $LiFePO_4$ (cathode) enthalpy and entropy data derived from [49, 100].

Table 4.4: Electrochemical heat generation model Parameters

Parameter	Value	Units	Source
Geometry:			
Porosity / Tortuosity anode	0.33 / 1.2		[e]
Porosity / Tortuosity separator	0.50 / 1.2		[e]
Porosity / Tortuosity cathode	0.27 / 1.2		[e]
Density:			
Anode	2420.0	(kg/m³)	[f]
Cathode	1440.0	(kg/m³)	[f]
Electrolyte:			
Concentration $LiPF_6$	1.2	(mol/l)	[104]
Diffusion coefficient of lithium	Concentrated solution theory		[102]
Conductivity	Concentrated solution theory		[102]
Activity coefficient	Concentrated solution theory		[102]
Electron transfer reaction:			
i_{00} (an / ca)	$3.12 \cdot 10^{15}$ / $1.79017 \cdot 10^{12}$	(A/m²)	[f]
E_{act}	53411 / 41367	(J/mol)	[f]
α	0.5		[e]
Particle radius:			
Anode	3.58	(µm)	[e]
Cathode	37.0	(nm)	[e]
Double layer capacitance:			
Anode	$2.0 \cdot 10^{4}$	(F/m³)	[f]
Cathode	$1.0 \cdot 10^{5}$	(F/m³)	[f]
Serial resistance	$5.0 \cdot 10^{-4}$	(Ohm·m²)	[f]
Inductance	$1.5 \cdot 10^{-4}$	(Ohm·cm²·s)	[f]

[e]: Estimated data; [f]: Fitted data from [49, 72]

Since entropy contributes to the reversible heating of the electrode it is required to separate the entropy and enthalpy contributions in modeling heat generation in lithium-ion batteries. For that purpose we use Equation (3.20) and Equation (3.23) in terms of lithium ion concentration [97].

$$\Delta\phi_{eq}(c_{Li}) = -\frac{\Delta G}{zF} = -\frac{\Delta H(c_{Li}) - T\cdot\Delta S(c_{Li})}{zF} \tag{4.10}$$

Entropy and enthalpy data for $LiFePO_4$ and graphite have been derived from literature [49, 100, 130, 131]. Fitted entropy and enthalpy curves for both the anode and the cathode are shown in Figure 4.10. Parameters used in electrochemical heat generation model are presented in table 4.4.

4.5.2 Kinetics

On a nano-scale, electron transfer reaction taking place at the particle surface during the lithium ion intercalation into the active material is described by Butler-Volmer relation [Equation (3.30)] assuming the electron transfer process as a global single electron transfer.

$$i^V = i_0 \cdot \left(\exp\left(\frac{\alpha\, zF}{RT}\eta_{act} \right) - \exp\left(-\frac{(1-\alpha)zF}{RT}\eta_{act} \right) \right) \tag{4.11}$$

Where, i^V is volumetric current density that corresponds to unit volume of active material and is measured in A/m^3.

$$\eta_{act} = \Delta\phi - \Delta\phi_{eq}(c_{Li}) - \eta_{conc} \tag{4.12}$$

Where, $\Delta\phi$ and η_{conc} are given by Equation (3.27) and Equation (3.34) respectively:

$$\Delta\phi = E_{eld} - \phi_{ele} \tag{4.13}$$

$$\eta_{conc} = \frac{RT}{zF}\ln\left(\frac{c_0}{c(t)} \right) \tag{4.14}$$

Active material particles are assumed to be spherical with charge transfer reaction taking place all over the surface whereas lithium diffusion within the active material particle (solid phase) is neglected. i_0 is the exchange current density which depends on lithium ion concentration at

particle surface and electrolyte interface. This dependence in mathematical form is given by Equation (4.15).

$$i_0 = i_{00} \cdot \exp\left(\frac{E_{act}}{RT}\right) \cdot \left(c_{elyt}(Li^+)\right)^{0.5} \cdot \left(c_{surf}(Li)\right)^{0.1} \cdot \left(1 - c_{surf}(Li)\right)^{0.1} \tag{4.15}$$

4.5.3 Electrolyte transport

Lithium ion transportation mechanism in electrolyte solution is described by the dilute solution theory (section 3.3.3-II) [101] and parameters from [102]. Lithium ion transport is modeled on an electrode level where one repeat unit consisting of electrode active materials with current collectors and a separator (Figure 4.4) all submerged in electrolyte solution which is the lead salt of lithium hexafluorophosphate ($LiPF_6$) dissolved in ethylene carbonate (EC) solvent.

Change in the concentration of dissolved species over time depends on diffusion and migration and is given by:

$$\frac{\partial(\varepsilon c_i)}{\partial t} = \frac{\partial}{\partial y}\left(D_i \frac{\partial c_i}{\partial y}\right) + \frac{z_i F}{RT}\frac{\partial}{\partial y}\left(D_i c_i \frac{\partial \phi}{\partial y}\right) + M_i R_{i,gen} \tag{4.16}$$

4.5.4 Overall heat generation rate

Overall or total heat generation rate in lithium-ion batteries does not come from a single source but a number of different mechanisms contribute to that as mentioned in section 3.4. Using Equation (3.57), total heat generation rate is given by:

$$\dot{Q}_{gen} = \dot{Q}_{rev} + \dot{Q}_{pol} + \dot{Q}_{res} + \dot{Q}_{ohm} \tag{4.17}$$

Thermodynamic, kinetics, and Joule effects are the major contributors to the overall heat generation in lithium-ion cells given by $\dot{Q}_{rev}$, $\dot{Q}_{pol}$, and $\dot{Q}_{joul}$ respectively. Reversible heat $\dot{Q}_{rev}$ corresponds to the electrode active material entropy change which depends on the amount of lithium intercalated and is given by:

$$\dot{Q}_{rev} = \frac{i^V}{zF}\left[\sum_e -(T \cdot \Delta S_e)\right] \tag{4.18}$$

Subscript *e* in Equation 4.18 stands for electrode that includes anode and cathode. Kinetic contributions are attributed to the polarization resistances at the SEI caused by activation polarization and concentration polarization. Hence heat generation due to polarization effects $\dot{Q}_{pol}$ is given by:

$$\dot{Q}_{pol} = i^V\left[\sum(\eta_{act,e} + \eta_{conc,e})\right] \tag{4.19}$$

Joule heating is contributed by the heat due to resistance in the electronic circuit which includes current collectors, terminals, wires etc. and resistance across the ionic path which involves electrolyte. The former is called ohmic heat $\dot{Q}_{ohm}$ and the latter is called resistive heat $\dot{Q}_{res}$ and given by:

$$\dot{Q}_{ohm} = i^V\left[\sum_l \eta_{ohm,l}\right] \tag{4.20}$$

$$\dot{Q}_{res} = i^V\left[\sum_h \eta_{res,h}\right] \tag{4.21}$$

Electrolyte resistive polarization η_{res} and ohmic polarization η_{ohm} are given by Equation (3.37) and Equation (3.39) respectively and the sum of the two is termed as Joule heat ($\dot{Q}_{joul}$) as mentioned above.

4.5.5 Electrochemical simulations

DENIS, detailed electrochemistry and numerical impedance solver, is a multipurpose C-based code used to simulate fuel cells, batteries and other multiphase electrochemical systems. It is developed by W. G. Bessler and associates at the University of Heidelberg and the German Aerospace Center (DLR), Stuttgart, Germany [133]. DENIS employs finite volume method for the domain discretization. In DENIS *x*-coordinate is reserved for the gas phase, *y*- for the porous

electrodes, and *z*- for radial component within the spherical particle. Electrochemical model used in the present study (section 4.5) involves only reaction at electrode surface. In the absence of gas phase and diffusion inside the particle, only y-coordinate is taken into account for the simulations ignoring the other two.

Besides using the internal code DENIS also makes use of external program modules like DETCHEM developed by Deutschmann et al., Karlsruhe and LIMEX, a DAE system solver developed by Erig, Nowak, and Deuflhard. It employs LAPACK and BLAS [49, 135].

4.6 Multi-scale coupling

For efficient and safe operation of lithium-ion batteries there has to be a balance between heat generation and heat dissipation rates, that is, the amount of heat generated electrochemically inside the cell should not exceed the amount dissipated. Therefore it is essential to comprehend the coupled behavior of these two mechanisms. A coupled EC-T model can form the basis for devising an effective thermal management and cooling system for lithium-ion battery packs and modules used in automobiles.

4.6.1 Coupling methods

Total heat generation rate which is the key input parameter for heat transfer model is applied by three ways: 1) Direct input method that requires no input from electrochemical heat generation model and a constant value of heat generation is applied to the jellyroll as body load instead; 2) Heat generation derived from vertical coupling in which transient heat generation simulations run separately and the resulting heat generation profile is used as input for the heat transfer model; 3) Horizontal coupling method in which heat generation and heat transfer models run simultaneously in a dynamic way to exchange updated values of heat generation rate and temperature at the chosen time steps.

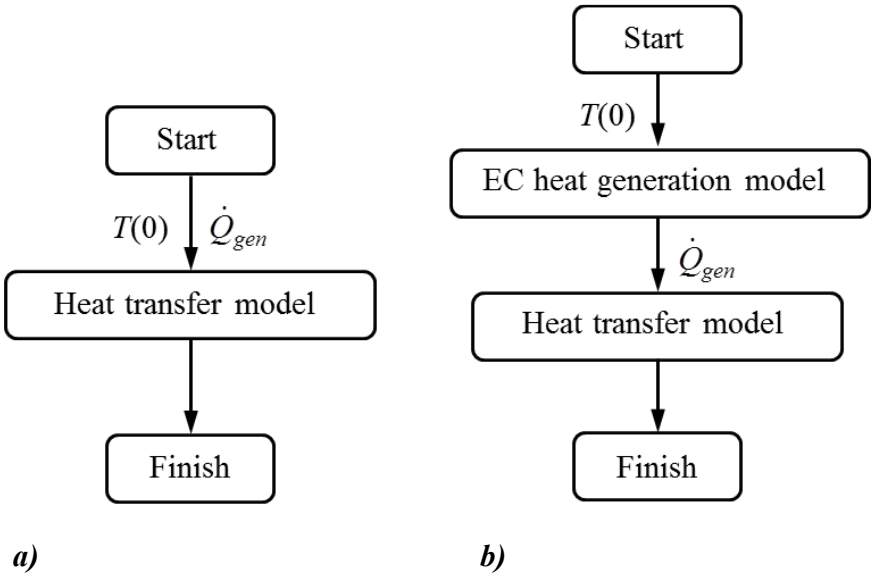

Figure 4.11: Simulation sequence of *a)* direct input method and *b)* vertical coupling.

I) Direct input method

In this method, spatial as well as temporal variations in heat generation rate have been ignored. This is an efficient and less time consuming way to look into the heat flow patterns in complex shaped cells like VL 7P shown in Figure 4.5. In this work direct input method has been used to study the effect of geometrical design variation on thermal behavior of VL 7P cell (see chapter 6). A constant volumetric heat generation rate is applied to the jellyroll to run static or transient simulations. Schematic flow diagram of direct input method is shown in Figure 4.11*a*.

II) Vertical coupling

Schematic of indirect or vertical coupling method is shown in Figure 4.11*b*. In this method temporal variations in heat generation rate have been taken into account while spatial variation ignored. Electrochemical heat generation model is used to run transient simulations separately to obtain transient heat generation profile which is applied as tabular or array input data to the heat transfer model.

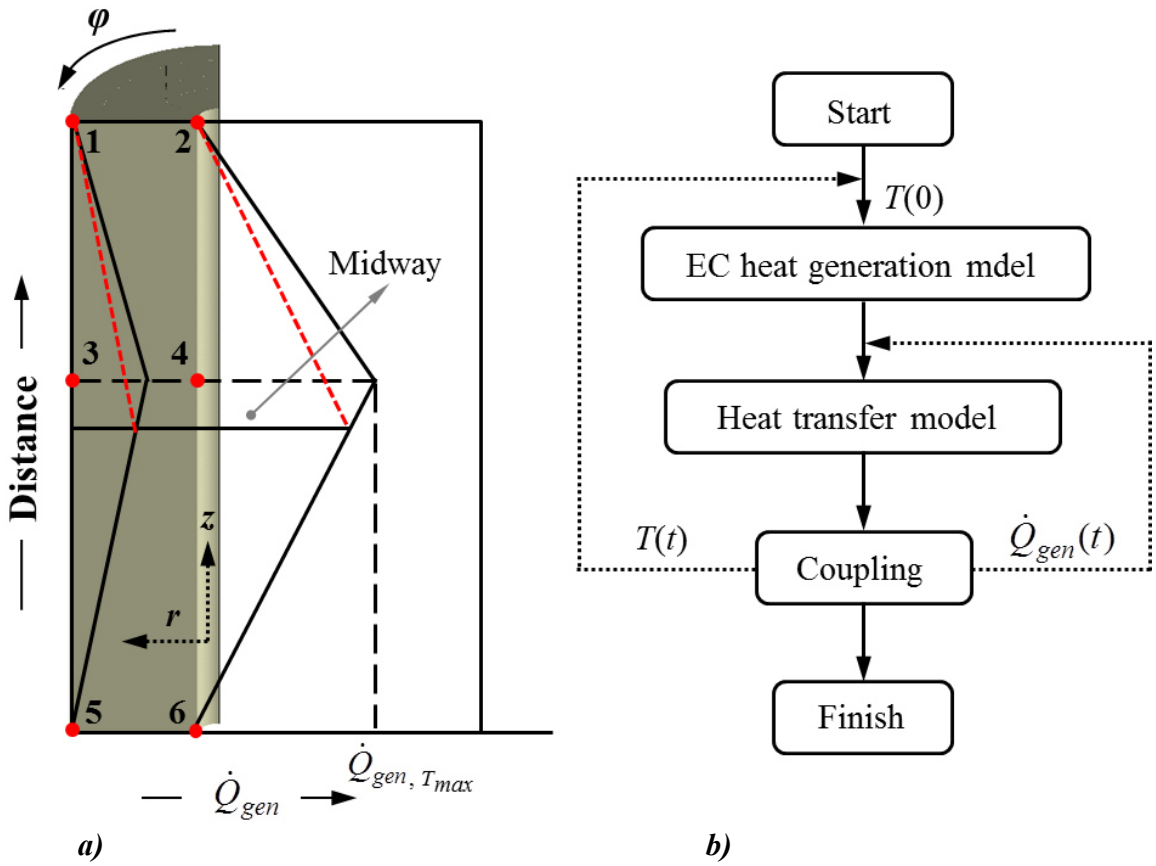

Figure 4.12: Horizontal coupling mechanism: *a)* coupling takes place at six representative locations shown in red dots on JR quarter-section; *b)* Schematic of horizontal coupling sequence.

III) Horizontal coupling

In horizontal or direct coupling, heat generation rate varies as a function of both space and time in a dynamic way. Flow diagram of horizontal coupling procedure is shown in Figure 4.12*b*. Six representative locations on JR, represented by red dots in Figure 4.12*a*, are selected at which coupling between the electrochemical and thermal models takes place. Temperatures for each of the six locations are fed to the electrochemical model which calculates the area specific heat generation rates (in W/m^2) for each location. Area specific heats from the electrochemical model are then converted to volumetric heat generation rates (W/m^3) by dividing the area specific heats by the thickness of one repeat unit (155 microns) for all the six temperatures.

Volumetric heat generation rates are then applied to the six elements corresponding to the six locations as body forces. Linear interpolation is used to apply heat generation rates to the elements falling in between the six selected elements in axial (z) as well as radial (r) directions. Elements along φ direction observe no divergence in heat generation rate since variations in φ direction have been ignored. Since batteries cycle faster at higher C-rates, smaller time steps are used for higher C-rates than those for lower C-rates. Time steps used for 1C-, 2C-, and 5C-rates are of the order of 100, 50, and 25 seconds respectively. At each time step the updated values of heat and temperature gets exchanged by the two models.

Referring to Figure 4.12*a*, points 1, 2 and 5, 6 are constrained while points 3 and 4 move up or down along z-axis at each time step corresponding to the T_{max} location as elucidated in Figure 4.12*a*. Fixing points 3 and 4, for example, at the middle of the jellyroll give rise to inaccurate heat profiles represented by red dashed lines in Figure 4.12*a*.

4.6.2 MSMD approach

A multi-scale multidimensional (MSMD) dynamic thermal model of 26650 cell is presented. 1D electrochemical model is worked out on two scales: a nanometer scale deals with lithium intercalation into the active material particles; and a micrometer scale where lithium ion transport takes place in the electrolyte. Lithium ion diffusion into the active material particle i.e. solid state diffusion is ignored in this study to reduce complexity and optimize simulation time.

1D electrochemical model is coupled to a 3D heat transfer model. Macro level model is based on heat transport across a single cell in which heat transfer takes place on a millimeter scale. Schematic of the multi-scale modelling approach adopted in this study is shown in Figure 4.13. Coordinate systems used in heat generation and heat transfer models are independent of each other. Heat transfer model presented in section 4.4 of this chapter has also been used in combination with different experimental measuring techniques to find lumped thermal parameters. These lumped parameters have been incorporated into the heat transfer model (macro level) used to carry out simulations. The procedure has been described in detail and can be found in Appendix B of this text.

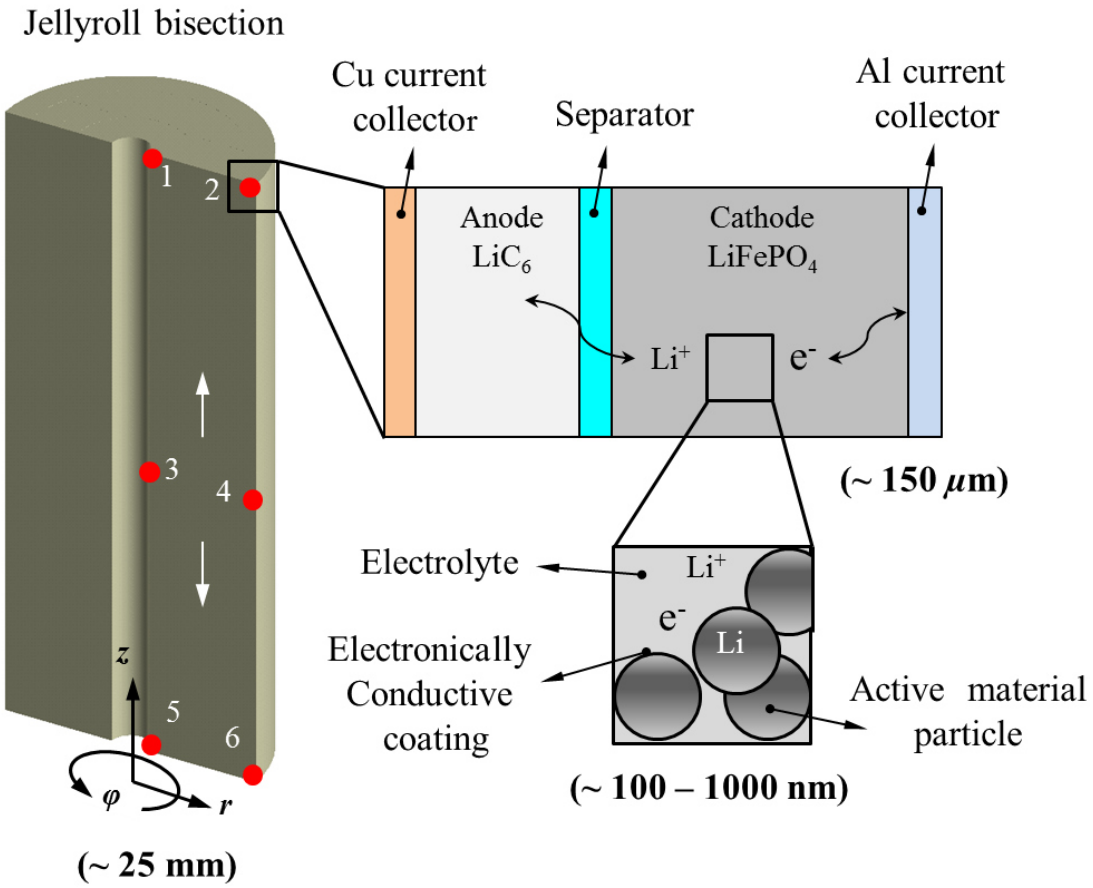

Figure 4.13: MSMD modeling approach involving nanometer, micrometer, and millimeter scales on 1D to 3D levels.

Having developed the model geometry, model equations, and coupling strategy, the next step is to implement the model into the simulations in order to investigate thermal behaviour of the selected cells. But it seems appropriate to validate the model in prior for which authentically measured data is required. Hence chapter 5 deals with the experimental thermal characterization of 26650 cell subjected to varying loads and environmental conditions. Results presented in chapter 5 have been used to validate the model.

Chapter 5

Experimental thermal response study of 266550 cell

As mentioned earlier that LFP battery technology has become preferred choice for high power applications like electric vehicles due to stable discharge potential, longer cycle life, lower cost, environmental merits, and wider operating temperature range. Hence, a nanophosphate based LFP cell 26650 has been selected for this experimental thermal response study. Effect of ambient temperature (T_{amb}) and applied current on cell surface temperature (T_{sur}) and cell discharge behaviour has been probed. Moreover open circuit voltage (OCV) varying as a function of T_{amb} has also been investigated. Outcomes of these investigations alongwith details of the experimental procedure and setup are presented in this chapter. Part of the results presented in this chapter are used to validate EC-T model presented in chapter 4. It should be noted that ambient temperature and operating temperature as well as current and applied load are used interchangeably in the discussions to follow.

5.1 Experimental

Owing to the susceptibility of lithium-ion batteries to temperature variations with regard to safety and performance, it is important to know how a typical cell responds to temperature changes especially in automobile applications where sudden higher draw of current during the acceleration could make the cell temperature to rise sharply. In present experimental study

thermal behaviour of 26650 cell in response to variations in T_{amb} and charge-discharge current is investigated. 26650 cell is shown in Figure 4.3 with technical data in Table 4.1.

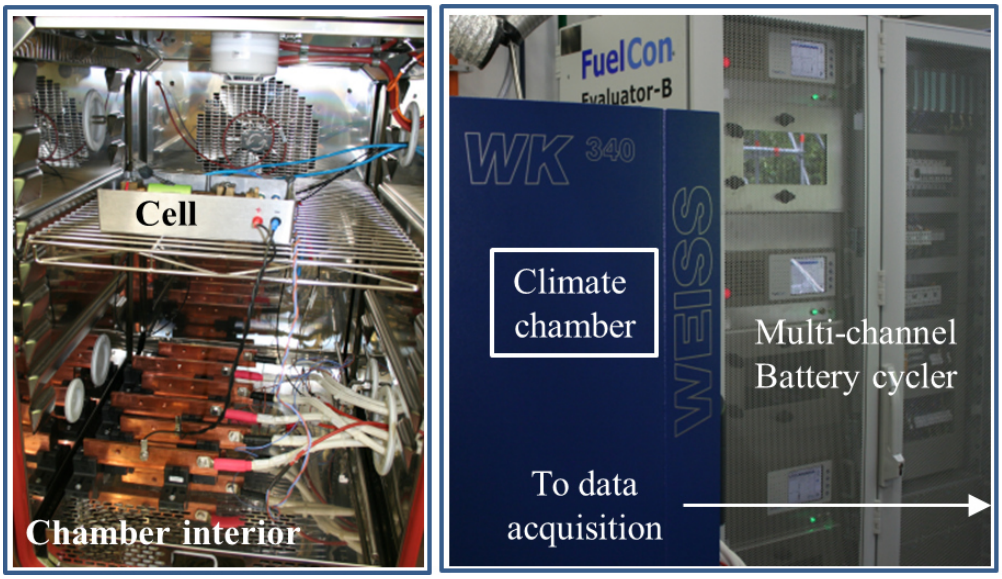

a) ***b)***

Figure 5.1: *a)* Interior view of climate chamber; *b)* climate chamber (blue) and FuelCon battery cycler (extreme right). Data acquisition system is not visible in the picture.

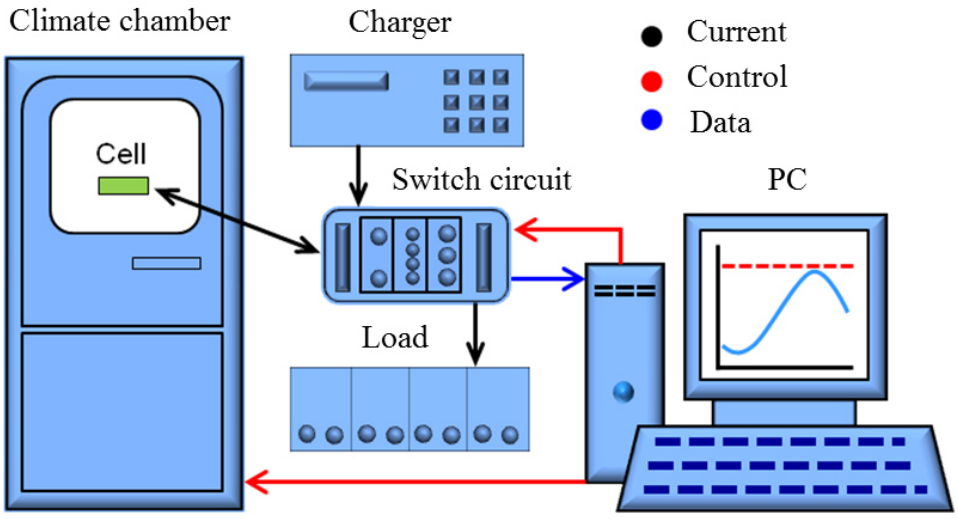

Figure 5.2: Schematic of experimental setup showing electric and control circuitry.

5.1.1 Experimental set up

Experimental set up shown in Figure 5.1 consists of Evaluator B, a multi-channel battery cycler from FuelCon fitted with WK-340/40/5 climate chamber from Weiss GallenKamp. Schematic of experimental setup elucidating electric and control circuits is shown in Figure 5.2. Test specimen (battery) was placed inside the climate chamber which was then adjusted to a specific operating temperature or set point. Once temperature inside the climate chamber was reached steady state, load was applied through the cycler. The cycler was connected to a data acquisition system where all the data was continuously acquired and retrieved later for further processing.

5.1.2 Experimental procedure

In a first set of experiments, measurements were carried out at 1C and 2C rate using a single discharge-charge cycle with constant current (CC) settings. Battery was charged to 100 % SOC before starting the cycle using constant current constant volt (CCCV) charging method. A value of 3.6 V was used as charge cut-off-voltage while 2 V as discharge cut-off-voltage. Operating temperature set points used for this study were -10 °C, 0 °C, 10 °C, 20 °C, 30 °C, and 50 °C. Conditions in the climate chamber and cycling loads were controlled using a computer code running on an attached machine. For each set of measurements, the above mentioned temperature values were set in the code running on the attached machine with 60 minute waiting steps between the two consecutive set points (e.g. -10 °C to 0 °C, 0 °C to 10 °C and so on) so that temperature inside the climate chamber should steadily change from the previous state to the next set point. Climate chamber was constantly kept under inert environment using nitrogen gas. If the cell was lying idle for more than 12 h, it needed to be first charged to 100 % SOC at room temperature using CCCV charging at 1C rate prior to start the specific set of measurements.

In a second set of experiments, five consecutive charge-discharge cycles were used employing 5C and 10C rate loads. The same procedure was followed as for single cycle profile described above. Operating temperature and time steps were also kept unchanged with the only exeption that the measurements corresponding to 30 °C and 50 °C operating temperatures were excluded for 10C rate due to the expected rise of temperature over 60 °C.

To study the effect of temperature on cell OCV, the cell was first charged at room temperature and 1C rate to 100 % SOC using CCCV charging method and then discharged to 50 % SOC at 1C rate followed by switching the load off. Two methods were adopted to study the effect of temperature on cell OCV at 50 % SOC: 1) Individual temperature steps i.e. -10 °C, 0 °C, 10 °C, 20 °C, 30 °C, and 50 °C were used seperately where for each temperature step the cell was brought to 50 % SOC using the above described method and allowed the cell to relax for half an hour and data acquired [Figure 5.10*a*, 5.10*b*]; 2) Cell was allowed to relax from 50 °C to -10 °C in steps of 10 °C each over a period of 14 hours [Figure 5.10*c*, 5.10*d*].

5.2 Results and discussions

Effect of T_{amb} on T_{sur}, cell discharge behavior, and OCV at different C rates was studied. Additionally the effect of applied current on the T_{sur} was also studied. Cell temperature was measured at the center of the cell surface along its length. A small patch from the cell sleeve was cut at the center to expose the metal surface. It was made sure that the thermocouple was in proper contact with the metal container as shown in Figure 5.3. Results obtained from the measurements are presented and discussed below. Equivalent temperature and potential scales are used in all the plots for individual data sets so that the comparative variations and effects can fully be appreciated.

Figure 5.3: Themocouple fixed at the center of 26650 cell surface. Patch of plastic cover was removed to measure temperature at the metal surface.

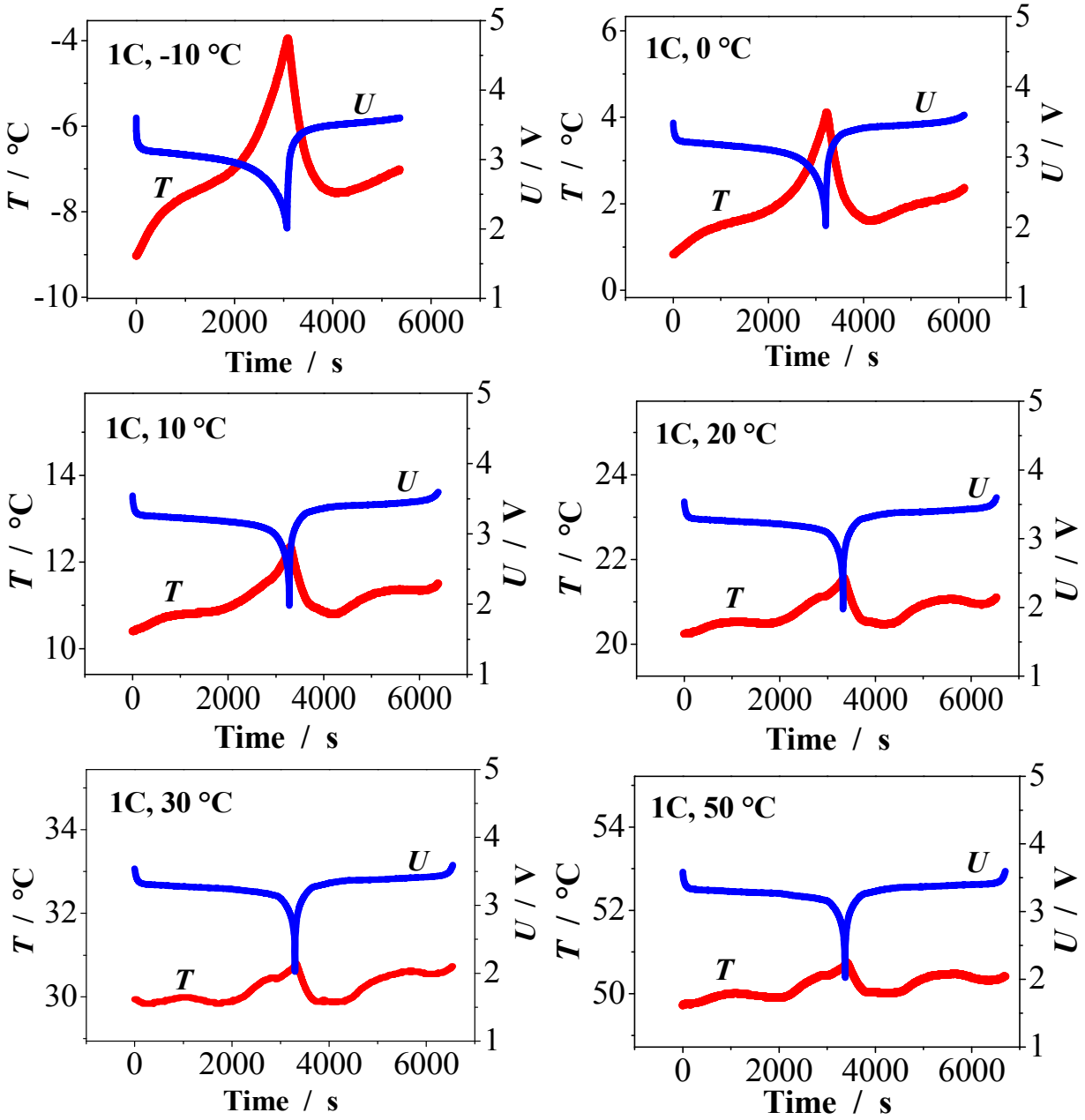

Figure 5.4: Single discharge-charge cycle at 1C rate. Variation in T_{sur} and U at T_{amb} = -10 °C; 0 °C; 10 °C; 20 °C; 30 °C; and 50 °C.

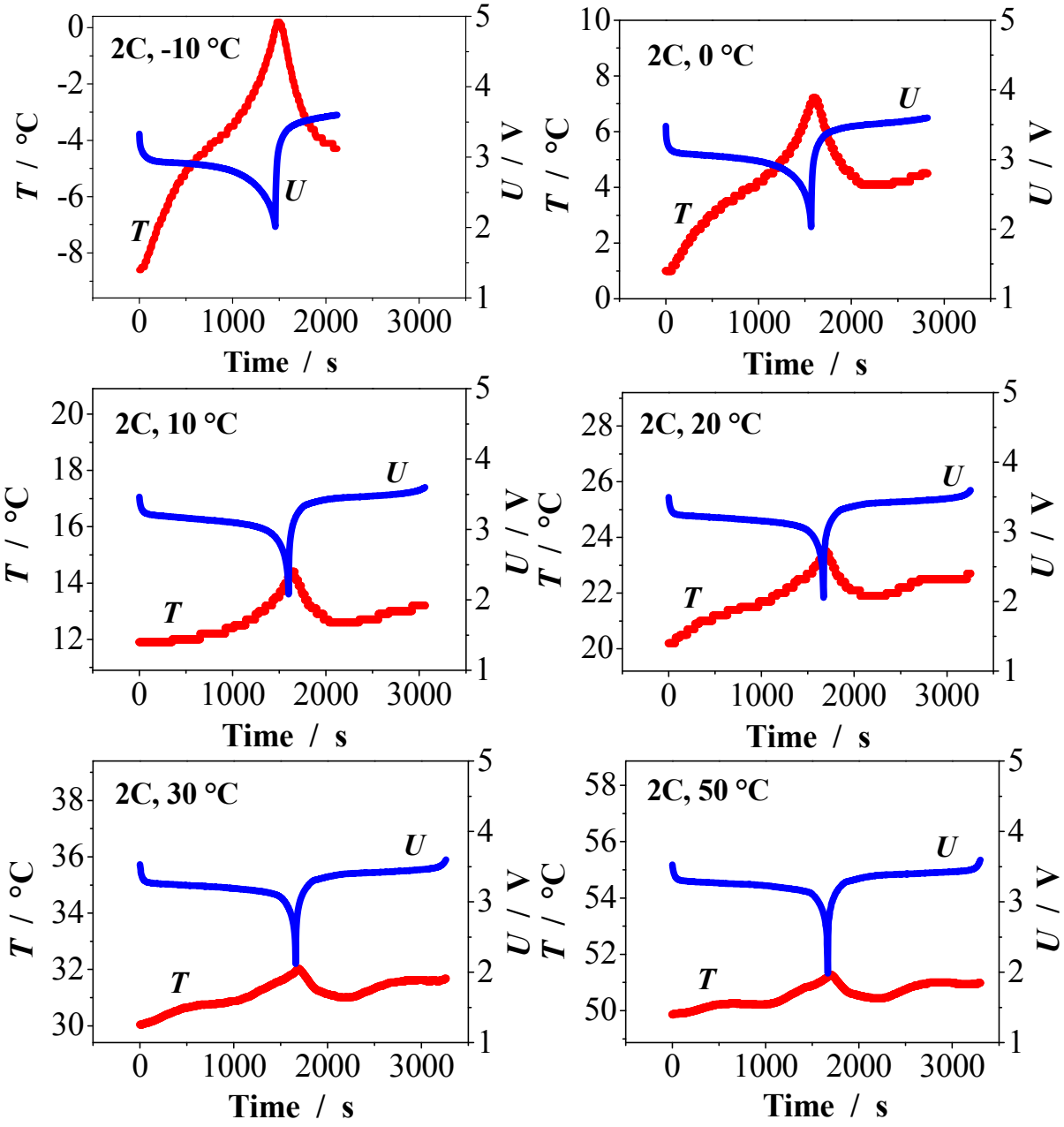

Figure 5.5: Single discharge-charge cycle at 2C rate. Variation in T_{sur} and U at T_{amb} = -10 °C; 0 °C; 10 °C; 20 °C; 30 °C; and 50 °C.

5.2.1 Effect of T_{amb} on T_{sur}

This section deals with investigating the effect of T_{amb} on T_{sur} at 1C and 2C rate using single cycle profile and at 5C and 10C rate using multiple cycle profile. Additionally, the effect of T_{amb} on potential of the cell have also been dealt. In Figure 5.4 through Figures 5.7, T_{sur} has been plotted

along with cell potential (U) as a function of time using equivalent scales along x (time) and y (T_{sur}, U) axes.

I) Single cycle at 1C and 2C rate

From Figure 5.4 and Figure 5.5, it can be seen that the maximum divergence in T_{sur} ranges from ~ 1 °C – 10 °C at 2C rate and ~ 1 °C – 5 °C at 1C rate with T_{amb} ranging from -10 °C to 50 °C. Also as we move from lower to the higher T_{amb}, variation over time in T_{sur} becomes smaller. This trend can be explained by the fact that at lower T_{amb}, diffusion and charge transfer processes slow down according to the Arrhenius relation (section 2.7.1) that manifests to an increased resistance across the electrolyte and at the electrode-electrolyte interfaces (SEI).

Additionally electrolyte viscosity decreases at lower T_{amb} giving rise again to an increased resistance to the flow of charged particles. These resistances causes the cell potential to drop due to polarization as described in section (3.2.2) [Equations (3.37), (3.38), (3.39)]. Also due to the restricted flow of charged particles, concentration garadients develop within the electrolyte and at the interface (SEI) causing the concentration polarization resistance to develop. These polarizations contribute to different heat generations thus causing the cell temperature to rise as described in section (4.5.4) [Equations (4.19) through (4.21)] . This is the reason for steeper and taller (along y axes) temperature curves at lower T_{amb} (Figure 5.4 and Figure 5.5) compared to that at higher T_{amb} where curves appear flatter and short.

Within the metallic parts i.e external circuit wires, current collectors, and terminals, electronic ohmic resistance decreases at lower T_{amb} but it does not have significant contribution to the overall heat generation. There is yet another type of heat that constitute significantly to the overall heat generation rate in the cell. In Equation (3.22), $T \cdot \Delta S$ represents thermal energy called the reversible heat which is associated with the entropy changes involved in the electrochemical reactions. It gets released and absorbed reversibly during intercalation and deintercalation processes. At higher reaction rates (or currents), entropic changes are not significant but at lower T_{amb} where reaction rate drops entropic changes become dominant thus making the reversible heat to contribute significantly.

It can be observed in Figure 5.4 and Figure 5.5 that at 1C and 2C rate, T_{sur} stays well between the safe operating temperature range at all T_{amb} set points (-10 °C through 50 °C). It is clear that above 0 °C, change in T_{sur} is reasonably small as compared to that at sub-zero temperatures at both 1C and 2C rates. In view of these observations, it can be concluded that the optimum operating temperature window for 26650 cell is from 10 °C to 50 °C.

II) Multiple cycles at 5C and 10C rate

As in case of 1C and 2C rate, 5C and 10C rate loads also exhibit steeper T_{sur} and U curves at lower T_{amb} as can be seen in Figure 5.6 and Figure 5.7. It is clear that at lower T_{amb}, divergence in T_{sur} is always higher than that at the higher T_{amb}. It can be seen that at the start of cycle, T_{sur} increases sharply and towards the subsequent cycles, divergence in T_{sur} tends to decrease. The cycling time decreases as we move towards higher cycle number indicating a decline in the capacity of the cell. This can be explained by the fact that due to steeper voltage curves towards the higher cycles, the set points for upper and lower cut-off voltage (CoV) of 3.8 V and 2 V respectively are reached thereby switching the load off without the cell being fully charged or discharged. That causes the DOD (during discharging) and SOC (during charging) to reduce significantly at higher currents and low T_{amb}.

It can be seen that at 10C rate and T_{amb} ranging from -10 °C – 50 °C, maximum divergence in the T_{sur} is ~ 10 °C – 35 °C, whereas at 5C rate the divergence is ~ 5 °C – 20 °C. Discharge time varies at every T_{amb} step because temperature has significant impact on the rate of reactions. As described in section 5.2.1-I that cell voltage drops sharply due to higher polarization at lower T_{amb} and hence it reaches the CoV of 2 V quicker than that at the higher T_{amb}. It can also be seen that at -10 °C and 0 °C, T_{sur} versus time curves follow a downward trend after the first cycle. That is because at lower T_{amb}, due to lower DOD and SOC during discharge and charge respectively, T_{sur} curves get interrupted while still not reached its final state therby exhibiting a narrower and steeper trend.

Figure 5.6 and Figure 5.7 also show that at lower T_{amb}, moving towards higher cycle number, cycle time keep on shrinking indicating a decrease in cell capacity. At higher T_{amb} on the other hand a sustained capacity is indicated by an almost constant cycle time as we moved from lower to higher cycle number. This implies that frequent cycling at lower operating temperatures and

higher currents deteriorates cell capacity. Figure 5.6 and Figure 5.7 also indicate that 26650 cell has reasonably good frequent or multiple cycling efficiency at $T_{amb} \geq 10$ °C at 5C rate and at $T_{amb} \geq 20$ °C at 10C rate.

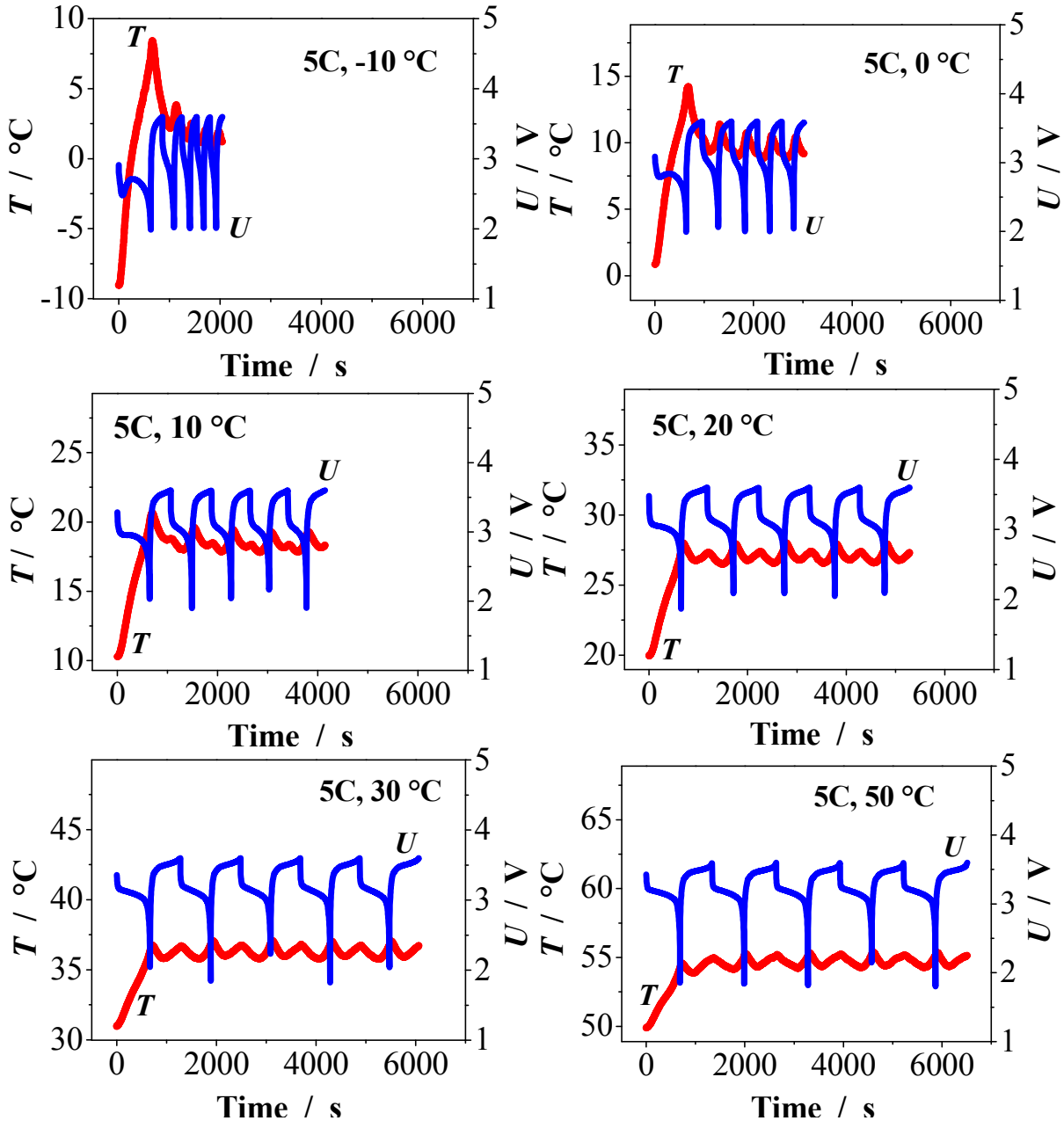

Figure 5.6: Multiple discharge-charge cycles at 5C rate. Variation in T_{sur} and U at T_{amb} = -10 °C; 0 °C; 10 °C; 20 °C; 30 °C; and 50 °C.

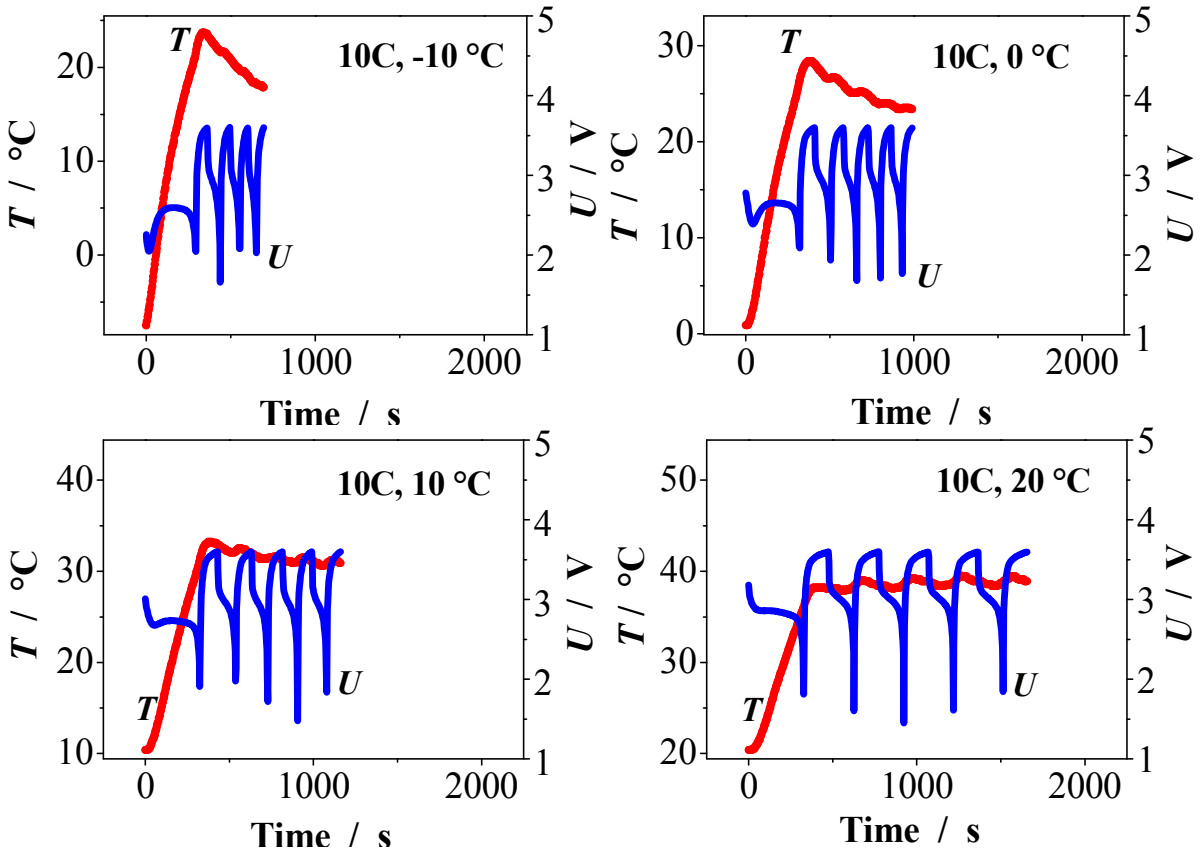

Figure 5.7: Multiple discharge-charge cycles at 10C rate. Variation in T_{sur} and U at T_{amb} = -10 °C; 0 °C; 10 °C; 20 °C; and 35 °C.

Discharging the cell at high but constant currents, T_{sur} increases significantly. But for short pulses of power drawn at intervals, as is the case with EVs and HEVs, cell temperature (T_{cell}) is expected to increase by only small amounts due to the interruption of discharge (intermittent charging) caused by deceleration or braking. Pulse power characterization analysis of 26650 cell has been presented in chapter 7 (section 7.2.3).

5.2.2 Effect of T_{amb} on discharge characteristics

Discharge curve of a typical cell is simply the cell potential plotted versus cell capacity. Since voltage drop in a typical lithium-ion cell suggests a loss of power, a steeper discharge curve indicates a drop in power deliverance capacity of the cell. A flat discharge curve, on the other

hand, implies that the power rating capability of the cell is very good. A modern cell used in automotive application should exhibit a flatter discharge curve trend [41].

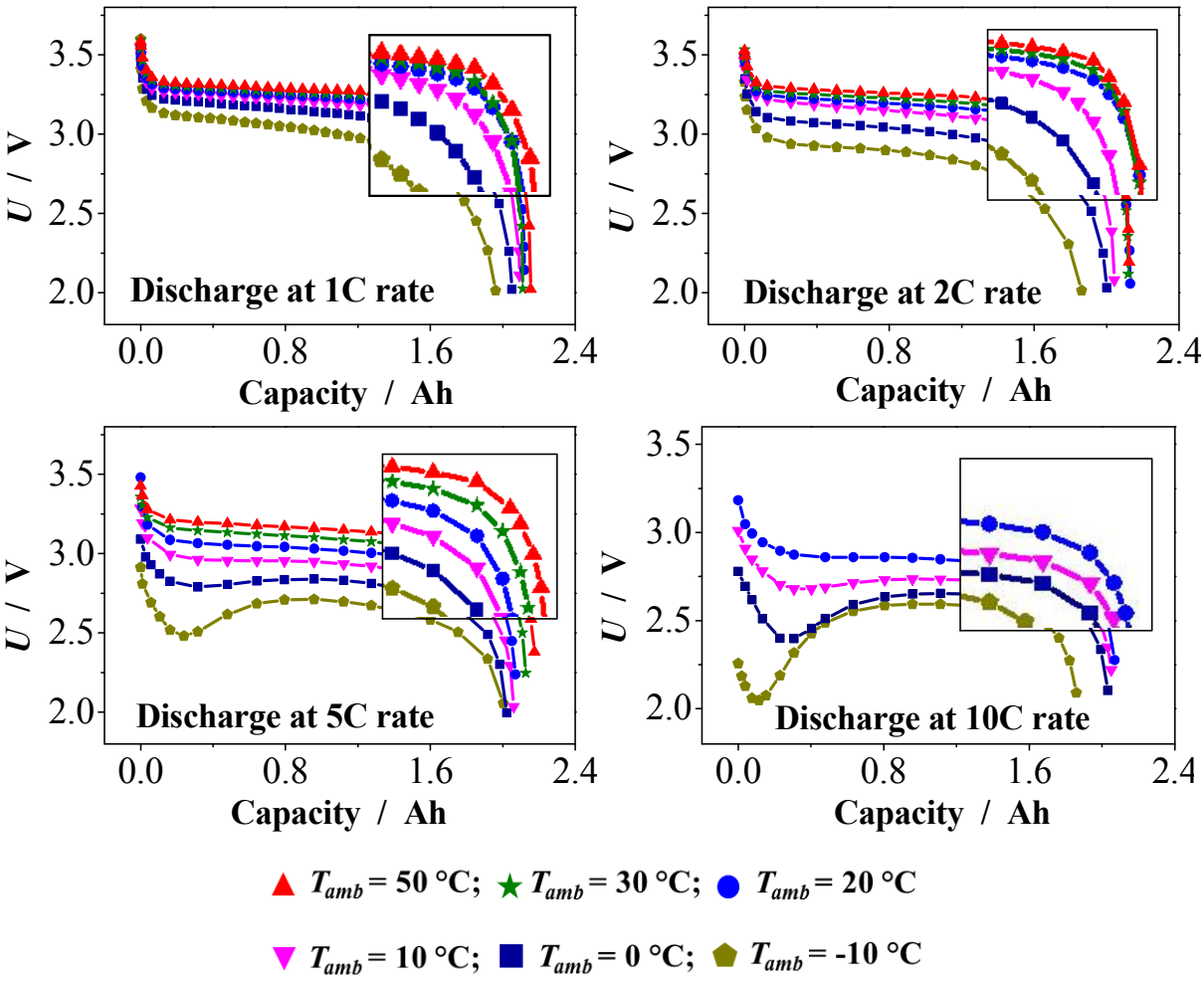

Figure 5.8: Cell discharge capacity at different ambient temperatures and at: a) 1C; b) 2C; c) 5C; and d) 10C.

Figure 5.8 shows that at lower T_{amb}, cell capacity tends to decrease while voltage drop tends to increase. It can also be seen that cell capacity is reduced if the cell is subjected to very high discharge currents. In other words high discharge current and lower operating temperature favours the loss in the cell capacity and hence the power deliverance capability. But in this particular case, we can see that almost all the discharge curves are quite flat except for that at 0 °C and -10 °C. In the plots of Figure 5.8, no significant loss in capacity was observed at T_{amb} >

0 °C. Even at T_{amb} < 0 °C, discharge curve does not drop too short indicating only a slight deterioration in capacity.

At lower operating temperatures (< 10 °C) and higher currents (5C or higher) significant loss in capacity has been observed. Especially operating the cell repeatedly at lower temperatures under high loads badly erodes cell capacity as discussed in section 5.2.1-II. It is safe to conclude that at lower to moderate loads (< 3C), 26650 cell is capable of delivering a sustained high power over a wide operating temperature window ranging from -10 °C to 50 °C. Discharge curves shown in Figure 5.8 have been derived from continuous discharge. In EVs and HEVs, on the other hand, battery discharges in short steps rather in continuous mode for longer time. It would help the battery to recover during the regenerative braking or while in idle improving the capacity profile of the battery.

5.2.3 Effect of applied current on T_{sur}

Apart from the operating temperature, applied current is also an important parameter that influences cell performance and safety. Both T_{amb} and current control the thermal behavior of the cell. In this section, variations in the cell surface temperature under the influence of applied current at different values of T_{amb} have been discussed.

Cell surface temperature (T_{sur}) plots presented in Figure 5.4 and Figure 5.5 have been reproduced in Figure 5.9 using normalized time along *y* axis instead of actual cycle time. Normalized time is the ratio of actual time of cycle to the theoretical time (t/t_{th}). Since applied current multiplied by time equals cell capacity (section 2.4.1), t_{th} is obtained by dividing cell capacity by applied current. For example, if cell capacity is 2.3 Ah, t_{th} for 2.3 A of applied load will be one hour and half an hour for 4.6 A of load. It should be noted here that normalized time can be considered analogous to the cell capacity.

Looking at the plots presented in Figure 5.9, cell capacity can be estimated from the extent of the T_{sur} curves along the normalized time axis. The farther the T_{sur} curve extends, higher is the capacity of the cell at that particular load and/or operating temperature.

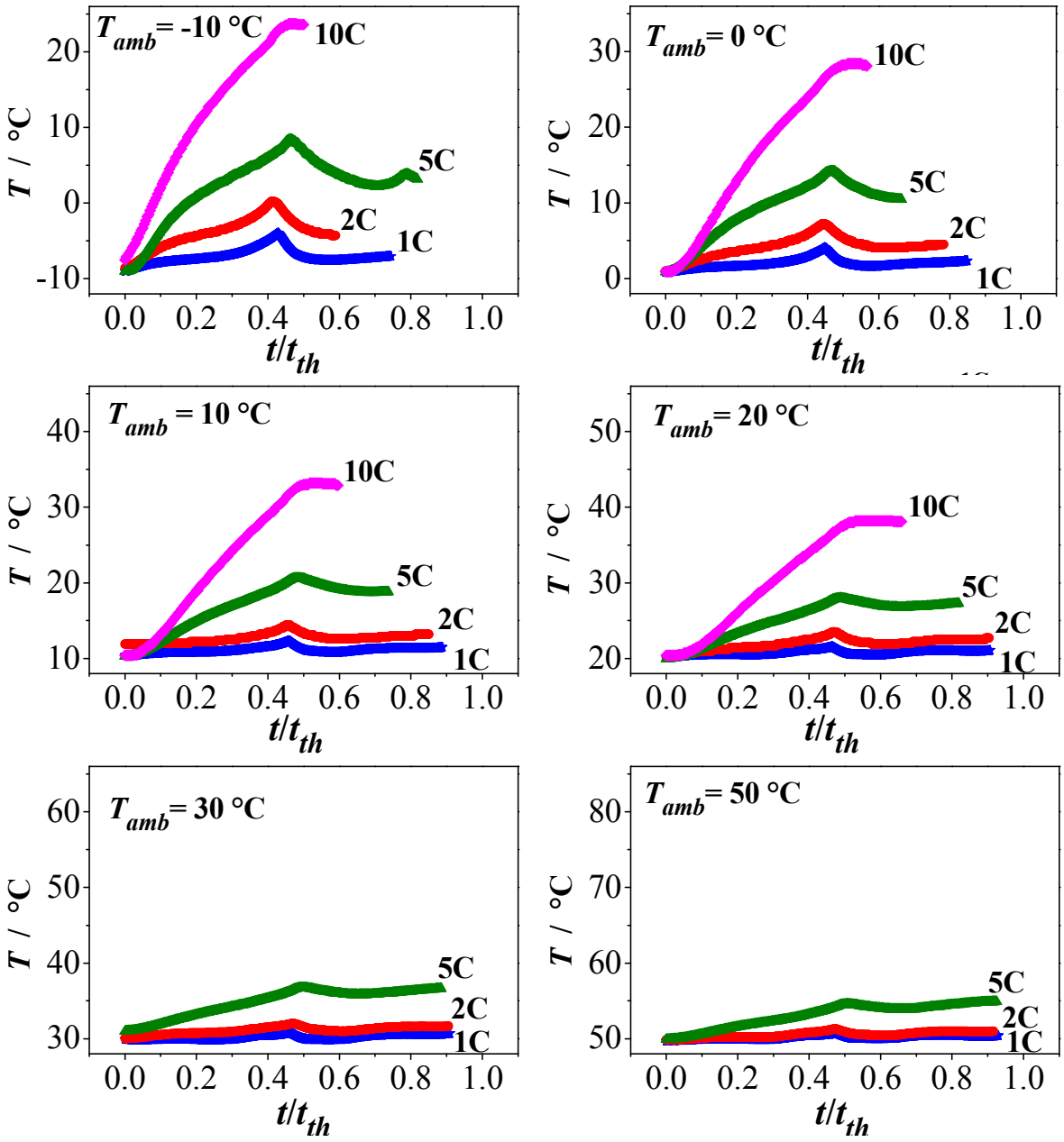

Figure 5.9: Effect of applied current on the T_{sur} for T_{amb} = -10 °C; 0 °C; 10 °C; 20 °C; 30 °C; and 50 °C.

Plots in Figure 5.9 elucidate that as we move from lower to the higher T_{amb}, slope of T_{sur} curve decreases. On the other hand, as we move from lower to higher currents, T_{sur} curve gets shortened and steep. This behaviour is attributed to the increased reaction rate at higher currents which makes the electrolyte and the SEI teeming with charged particles. As the number of charged

particles increased, they start to accumulate at the SEI due to lack of enough reaction sites to accommodate all the particles. That creates a rush of particles at the SEI waiting for the reaction to take place. Accumulated particles resist the close approach of the following particles bearing the similar charge due to their repulsive action thus creating a resistance at the interface. Due to particle accumulation, a concentration gradient is also created. Moreover particle interaction in the electrolyte increases thereby increasing the solution ohmic resistance.

All these phenomena contribute to a strong polarization which is clear from the potential curves in Figure 5.8 especially at low temperatures and higher currents. This strong polarization gives rise to higher heat generation thus making the cell temperature to rise. Thus higher current and lower operating temperatures favor the loss in cell capacity. At higher T_{amb} and lower current, the T_{sur} curve smoothens out and stretched almost to its fullest ($t/t_{th} \sim 1$) indicating a sustained capacity.

5.2.4 Open circuit voltage (OCV)

The next parameter studied in this work was the open circuit voltage (OCV). OCV is the voltage of a battery when no current is put into or drawn from it. It is an important parameter to assess the cell performance. Variations in OCV of a particular cell as a function of operating conditions (T_{amb}, SOC etc.) is a measure of its vulnerability to that particular condition. The procedure to measure OCV has already been described in section 5.1 of this chapter. Results obtained from the measurements are presented here.

In the first case where separate temperature steps with 30 minute relaxation time between each step were used, about 0.035 V drift in OCV had been observed (Figure 5.10*b*). In the second case where 60 minute relaxation time was used between the each temperature step over a period of 14 hours in a single run, OCV had been observed to drift only about 0.02 V (Figure 5.10*d*).

The term multi-run has been used for the first case while single-run for the second in the following discussion. The reason for lower divergence in OCV in case of single-run can be explained by the insufficient relaxation time of 60 minutes between the each temperature step especially at lower ambient temperatures. It can be seen from Figure 5.10*a* that OCV curves at

below 20 °C have still not reached the steady state showing again the insufficiency of 30 minutes relaxation time.

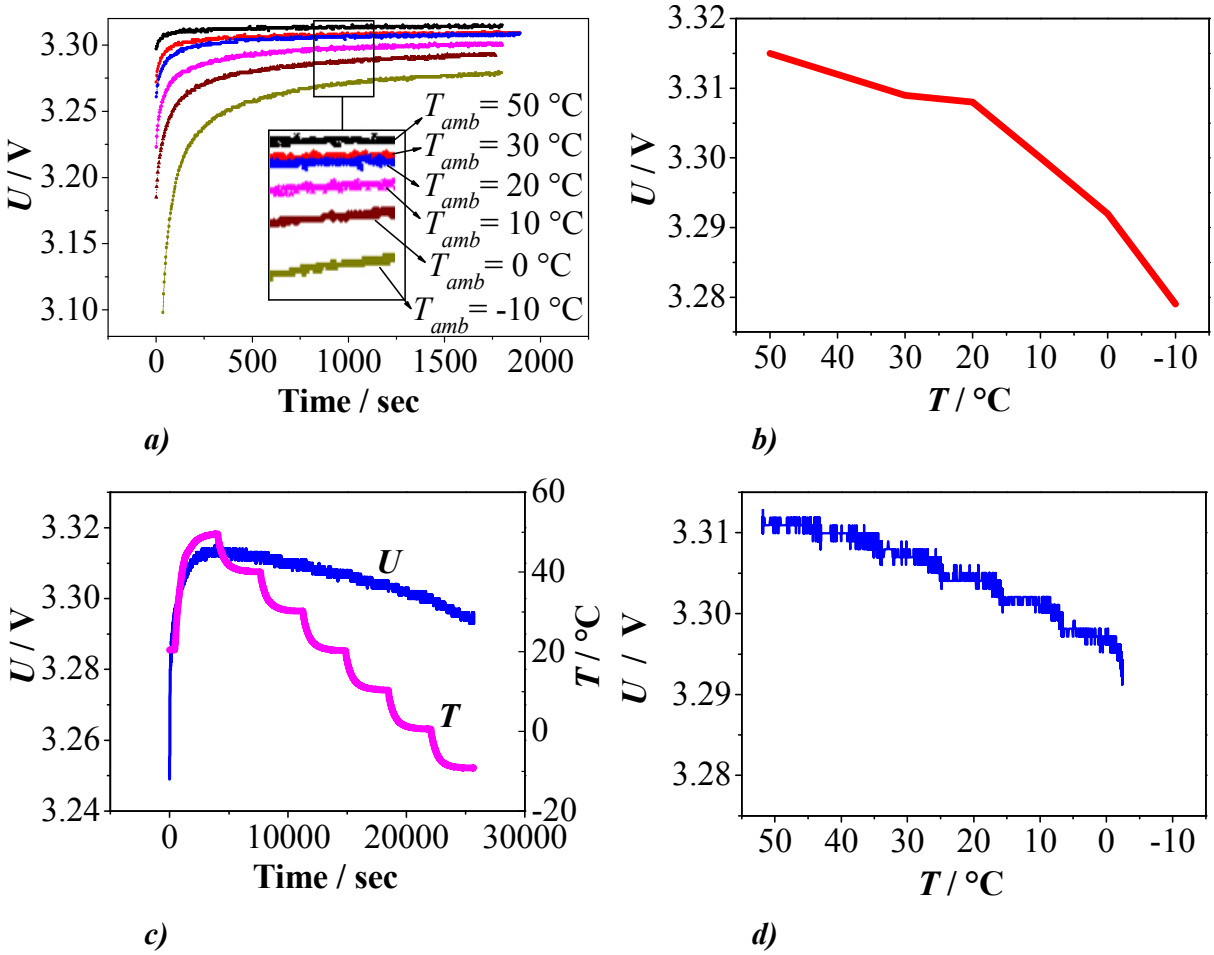

Figure 5.10: OCV versus time at different operating temperatures and 50 % SOC; *a)* and *b)* represent OCV measured in multi-run configuration with 30 minute relaxation; *c)* and *d)* represent OCV measured in single-run configuration with 60 minute relaxation interval between each step.

Michael A. Roscher et al. [118] suggest that at least five hour relaxation time is required for the OCV to reach steady state even if the SOC adjustment is made at lower C rates (1C rate in present case). They also suggest that the longer relaxation time is attributed to very slow intra-particle diffusion and other migration processes at lower operating temperatures making the low temperature relaxation even slower. Hence low temperature relaxation requires even more time to

reach steady state. In this view, it can be inferred that relaxation time used in this work seems way less than is required for the OCV to reach a complete steady state value and needs to be explored further.

In Figure 5.10*a*, larger voltage steps at the start at T_{amb} < 20 °C are attributed to increased resistance at lower operating temperatures as discussed in section 5.2.1. Nevertheless overall variation in OCV at 50 % SOC is very small in multi-run as well as single-run cases suggesting that 26650 cell is pretty stable at 50 % SOC over a temperature range of -10 °C to 50 °C.

In this chapter influence of operating temperature and applied current on thermal and discharge behaviour of 26650 cell has been discussed. In view of the experimental results presented in this chapter, some important conclusions have been drawn which are presented towards the end of chapter 7 (section 7.3). Experiments carried out to investigate the above mentioned parameters offer certain limitations in performing thorough thermal analysis of the cell. For example, temperature only at the cell exterior could be measured without having any clue of how temperature varies inside the cell under different loads and conditions. To remedy these shortcomings, the above experiments are simulated under similar conditions using the thermal model presented in chapter 4. Outcomes from the simulations are presented and discussed in the chapter 6 and chapter 7.

Chapter 6

Cell construction and cooling conditions

In EVs, size and volume of battery module is important. An ideal battery module for EV power delivery system should be compact and low weight. Cooling systems have to be designed in such a way not burden the module with extra weight and dimensions. Higher power demand in EVs puts an extra thermal load on batteries and requires an effective cooling strategy to avert thermal runaway. It is important to identify areas on the cell exterior where heat could effectively be rejected from. In addition, thermally efficient cell designs are required. Such designs should be aimed at dissipating the generated heat with minimum of external efforts and resources involved.

Battery size is affected by the geometrical design parameters like thickness of cell wall, current collectors etc. Cooling system comprises significant portion of battery module. Hence it is worthwhile to investigate the effect of geometrical design parameters and that of the cooling conditions on thermal behavior of the cell. A thorough investigation into the thermal response of VL 7P cell under the influence of changes in geometrical design parameters and cooling conditions has been performed.

6.1 Simulations

VL 7P cell has been selected to study the geometrical design parameters due to its comparatively complex internal construction and larger dimensions as compared to 26650 cell. Direct input method presented in section 4.6.1, I has been used ignoring spatial variations in heat generation

rate. A constant heat generation rate of about 8 Watts per cell has been applied to simulate transient thermal response of the cell. Model developed in section 4.4 has been employed for simulations using ANSYS APDL software package. VL 7P cell domain shown in Figure 6.1 has been discretized using FEM method. The FEM mesh on a bisected cell domain is shown in Figure 4.9*b*. Thermal model parameters presented in Table 4.2 have been used to run transient simulations for a time period of 10000 seconds. Radiation effects have been ignored in the analysis. Results obtained from the simulations are presented and discussed in the following sections.

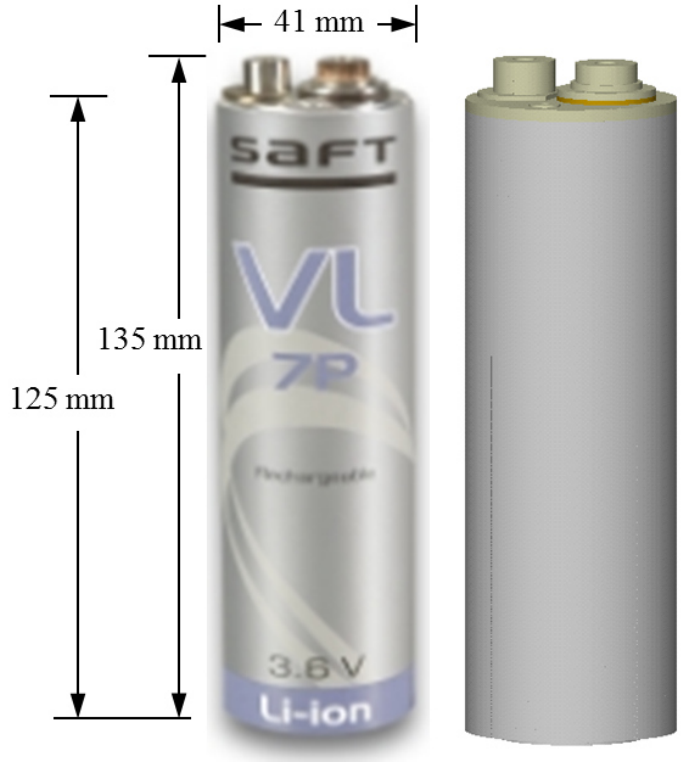

Figure 6.1: VL 7P, a 7 Ah high power NCA cell from SAFT Inc. (left) [93] with ANSYS CAD geometry model (right).

6.2 Geometrical design parameters

Cylindrical VL 7P cell is shown in Figure 6.1 along with CAD geometry model developed using ANSYS software package. Cell container wall thickness (CW) and that of the current collectors

(CC) thickness has been varied to study impact on overall temperature profiles and heat flow patterns in the cells. The aim is to find optimum locations on the cell exteriors where heat could more effectively be removed from. Owing to the higher k_z which is the axial (z-axis) component of thermal conductivity, heat flows conveniently along the length of the cell. In this direction, current collectors and cell wall offer lower resistance to the flow of heat. Higher thermal flux can be observed near the two current collectors and the cell wall in Figure 6.2 *b)*. Thus increasing thickness of these two low resistance points along the length of the cell could possibly further ease the flow of heat in that direction. As heat always takes the path of least thermal resistance, variations in these two geometrical parameters is expected to have pronounced effect on heat flowing out of the cell and ultimately on the overall cell temperature.

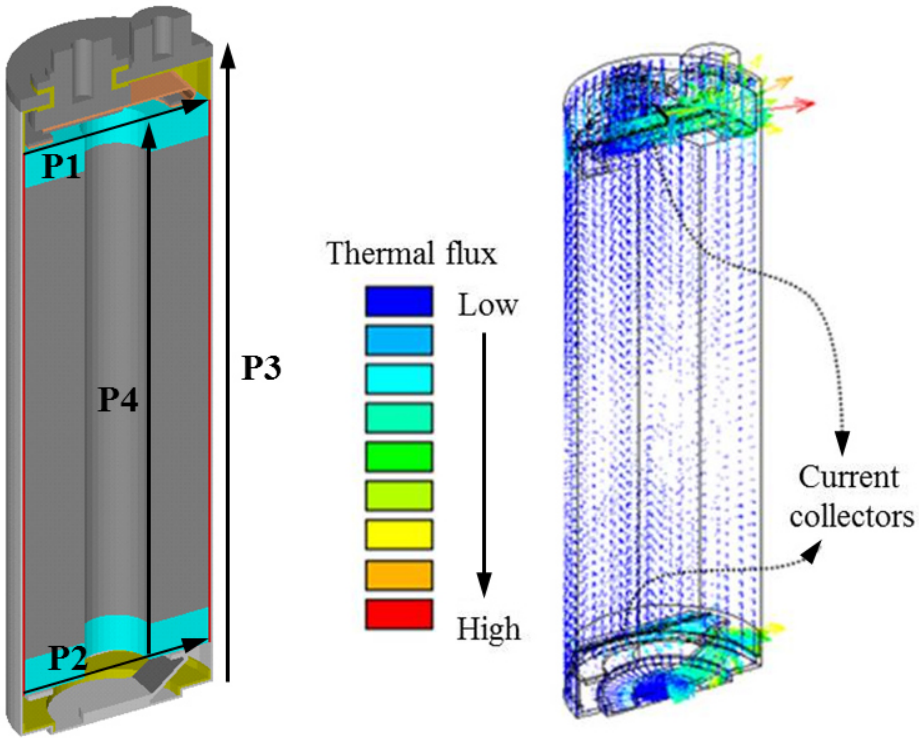

a) ***b)***

Figure 6.2: *a)* Map of path plot locations on the cell used to plot cell temperature; *b)* vector plot of thermal fluxes obtained from steady state simulations using constant heat generation rate in the jellyroll and uniform convection boundary conditions at the cell exteriors.

The possibility of easing the flow of heat through these two routes (through cell wall and current collectors) by increasing the dimensions as well as applying cooling has been explored in this study. Heat has been forced to flow out of the cell by simulating the cooling conditions. It has been done by applying boundary conditions with higher h_f and lower T_{amb} at different locations on the cell exterior e.g. top, bottom, and sides. In view of the result obtained from the simulations, some useful conclusions have been reached which along with certain recommendations are presented in chapter 7, section 7.3.

6.2.1 Effect of CW and CC thickness

Simulations have been carried out varying the cell container wall thickness and that of the current collectors to 0.5 mm, 1 mm, and 2 mm assuming steady state conditions. Original thicknesses of the cell container wall and current collectors are 0.5 mm and 1 mm respectively. For studying effect of cell container wall thickness, current collector thickness was kept at 1 mm while cell container wall thickness of 0.5 mm was used for investigating current collector thickness. Steady state has been assumed due to smaller expected variations in the output parameters e.g. cell temperature and heat flow due to small dimensions of cell wall and that of the current collectors. In order to draw reasonably accurate conclusions, fully developed gradients of output quantities are required which could only be obtained towards the end of transient solution. Results obtained from simulations are presented below. Locations of path along which temperature and thermal fluxes have been plotted are shown in Figure 6.2*a*.

Temperature contours resulted from FEM simulations are shown in Figure 6.3. It can be seen that the CW thickness has more pronounced effect on cell temperature than that of the CC thickness. Line plots of temperature profiles along paths P1 through P4 outlined in Figure 6.2*a* are presented in Figure 6.4. It can be seen that along paths P1 and P2 changing CW thickness from 0.5 mm to 2 mm produces a temperature change of about 2.5 °C whereas corresponding change observed in case of CC thickness is ~1 °C.

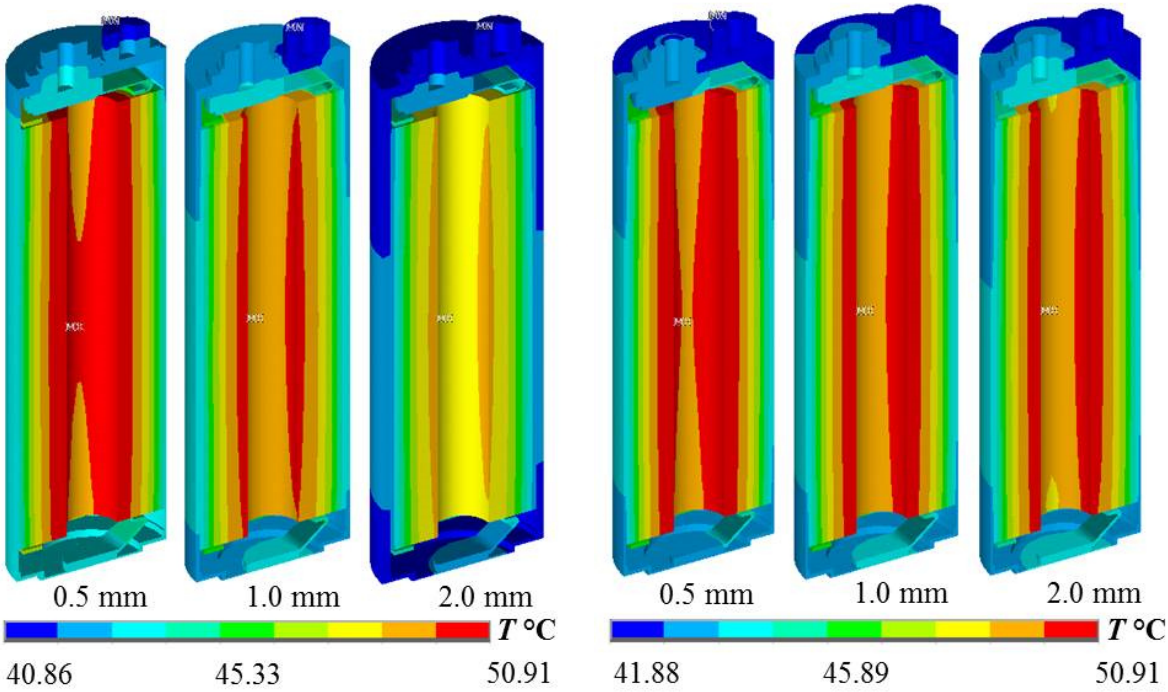

a) **Cell wall thickness** ***b)*** **Current collector thickness**

Figure 6.3: Temperature contours obtained from simulations carried out adjusting *a)* cell container wall thickness and *b)* current collector thickness to 0.5 mm, 1 mm, and 2 mm.

Fluctuation in temperature observed near 0.01 m and 0.03 m length in paths P1 and P2 is attributed to the welding joints connecting JR to the current collectors which are of the order of 1 mm in thick. Since these thin connectors are the only path for the heat to move out in axial direction, it produces an increased flow of heat which caused the temperature to drops sharply.

Along P3, variation in CW thickness from 0.5 mm to 2 mm produces about 2 °C decrease in temperature. The corresponding decrease in case of CC thickness is negligibly small. It can also be seen that as the CW thickness is increased, temperature distributes more uniformly suggesting that the gradient of temperature within the cell decreases at higher CW thickness. Changing CW thickness from 0.5 mm to 2 mm produces a temperature gradient of about 2 °C along path P4. Correspondingly temperature gradient in case of CC is less than 0.5 °C.

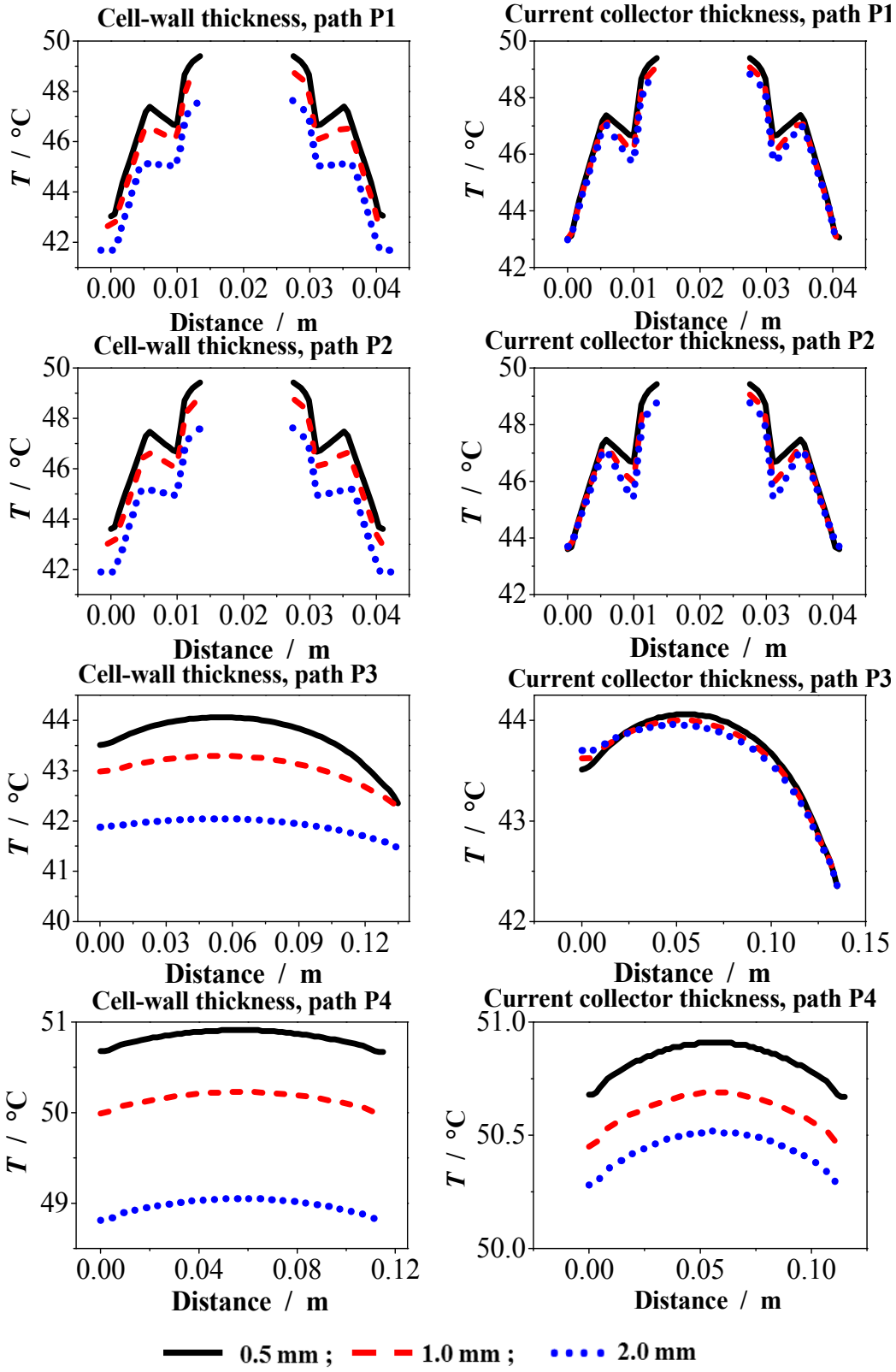

Figure 6.4: Line plots of temperature at path locations P1 – P4 (Figure 7.2*a*) at different thicknesses of cell container wall and current collectors.

Results suggest that a thicker CW slightly improve uniformity of temperature distribution whereas in case of CC no significant change is observed. In Figure 6.5 line plots of radial flux along path P3 at different values of CW and CC thickness are shown. It can be seen that in both the cases as thickness is increased, axial flux along the length of the cell gradually increases up and downwards from a point of zero flux and reaches its peak values near the edges of the cell where it abruptly falls again to its minimum.

This sharp decrease in thermal flux near the edges of the cell is caused by the dominance of axial component of flux over the radial one. It can also be observed that the gradual increase in radial flux is more profound in the upper part (> 0.05 m) of the cell which dominates even further at higher CW thickness. Figure 6.5 clearly shows that variation in CC thickness has only a negligible effect on thermal flux as compared to CW thickness.

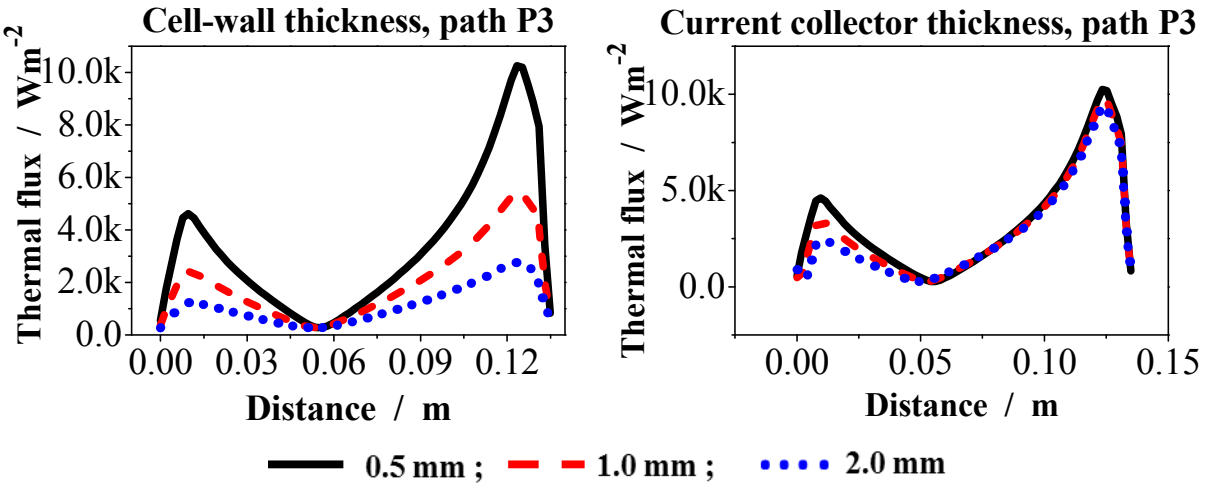

Figure 6.5: Radial component of thermal flux along P3 at different thicknesses of cell-wall (left) and current-collectors (right).

Since variations in circumferential (φ) direction are very small, thermal flux measured along P3 across length of the cell could provide enough information on heat dissipation rate across the side walls. Having known the external area of the cell container, the total amount of heat dissipated in radial direction (side walls) can easily be calculated.

From the above discussion it can be inferred that increasing CC thickness does not contribute to any improvement in thermal performance of the cell. Thermal performance is seen to be

improved slightly by increasing cell wall thickness. Nevertheless it adds to the weight and cost of the cell. For example, increasing CW thickness from 0.5 mm to 1 mm adds about 22 grams to the mass and about 0.03 USD to the cost. Similarly increasing CW thickness to 2 mm adds about 67 grams to the mass and ~ 0.10 USD to the cost. These calculations are made using aluminum price and physical properties data from [138] and [139] respectively. Above results give a clue on how the cell component dimensions can be used to further improve and optimize cell designs. A balance has to be traded amongst thermal performance as a function of geometrical design parameters and cost while designing a cell.

6.3 Cell configurations

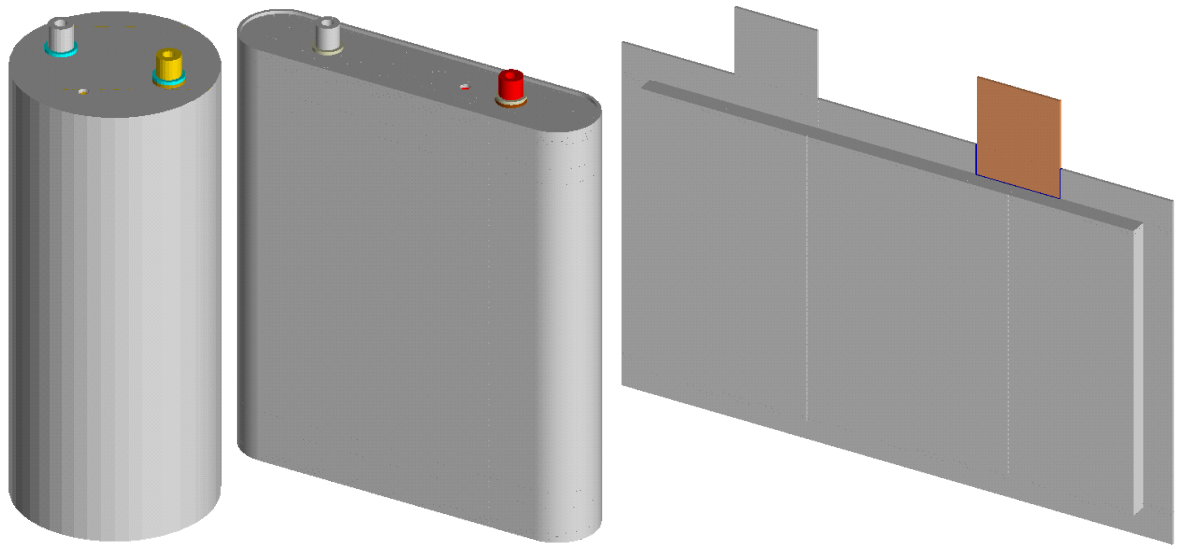

Figure 6.6: 3D CAD geometry models of three arbitrary lithium-ion cell configurations used for simulations: cylindrical (left); prismatic (center); and flat (right).

Three different configurations of lithium-ion cells i.e. cylindrical, prismatic and flat, shown in Figure 6.6, have been modeled using equivalent volume of JR. Volumetric heat generation rate and other parameters remains the same as used to study the geometry parameters in section 6.2 above. Natural convection boundary conditions were applied at the cell exteriors using h_f = 7 W/(m^2·K) and T_{amb} = 20 °C. Temporal evolution of T_{max} and T_{min} is shown in Figure 6.7 for all the three configurations. It can be seen that flat cell configuration produced the lowest overall

cell temperature and lower ΔT_{eff} whereas cylindrical cell produced the highest temperature and higher ΔT_{eff}. ΔT_{eff} is the effective temperature gradient which is the difference between limiting values of T_{max} and T_{min} obtained at the end of transient simulation time. It is indicative of how uniform cell temperature is distributed. Higher is ΔT_{eff}, less uniform is the distribution and vice versa.

Nonetheless cylindrical cell enjoys its own merits of being safe due to mechanical stability, pressure retention, and containment of possible hazards. Flat cell despite being more efficient in heat rejection is vulnerable to external shocks and stresses and internal gas pressure caused by electrochemical reactions during frequent charge-discharge cycles or in worst case scenarios like thermal runaway. Prismatic cell possess both the mechanical stability and safety features of cylindrical cell while thermal efficiency of flat cell. The choice has to be made depending on the individual application and needs.

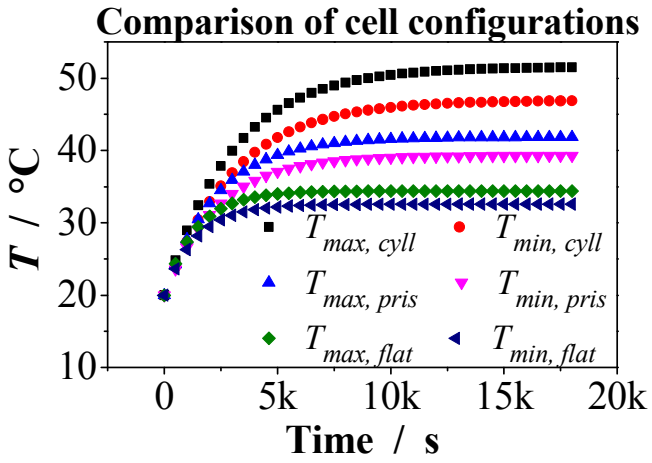

Figure 6.7: Transient T_{max} and T_{min} profiles obtained from FEM simulations of the three arbitrary cell configurations shown in Figure 6.6.

6.4 Effect of cooling conditions

Most of the heat generated in lithium-ion batteries dissipates through sides of the cell (normal to the wall of the cell container) due to larger surface area. Majority of the manufacturers of battery cooling systems adopt side-cooling, also called radial cooling, strategy thus utilizing larger surface area. But this utility comes at a cost of consuming more of space of the battery modules

which adds to the automotive volume and weight. In addition to occupy extra space, side-cooling has an inherent disadvantage which arises from significantly lower k_r (Table 4.3). Lower thermal conductivity restricts the flow of heat giving rise to an increased cell temperature. On the other hand, k_z being significantly higher (Table 4.3) makes the heat to flow unhindered.

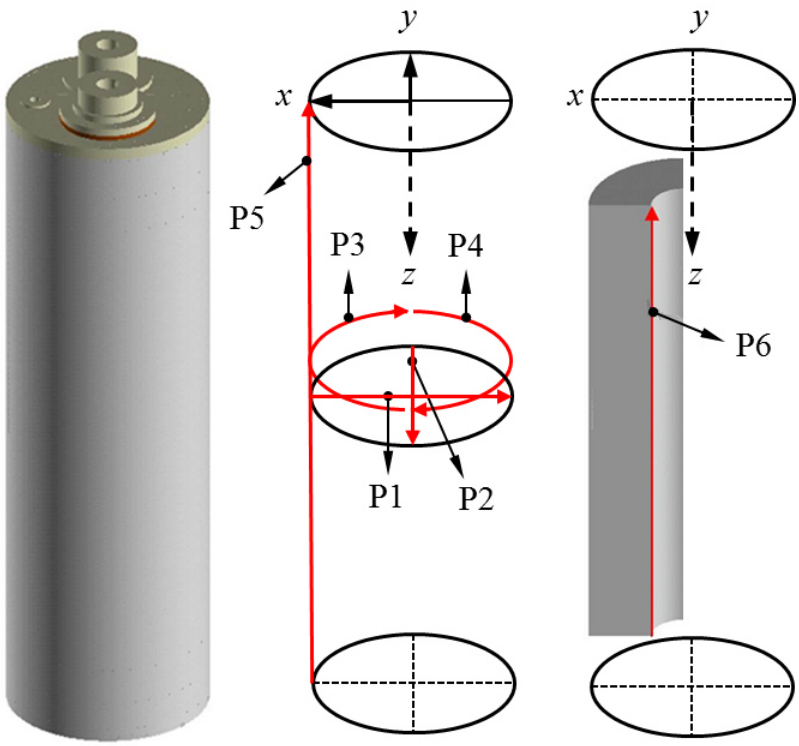

Figure 6.8: Path plot locations represented by red lines used for line plots along axial (z-axis), radial (x-axis), and circumferential (φ-axis) direction.

To make use of higher k_z, one possibility could be to use top or bottom cooling instead of side cooling thereby conserving module space. But the only possible channels for the heat to pass through in vertical direction are current collectors and the container wall. The two routes (cell wall and current collectors) have very small dimensions (~1 mm) as discussed in section 6.2 that resist the heat flow due to bottlenecking near the current collectors and the cell wall on top and bottom sides of the cell. In Figure 6.2*b*, higher thermal fluxes can be seen at the current collectors and near the ends of the cell wall which causes lower temperature at these locations as can be seen in Figure 6.4 and Figure 6.5. In this section, different heat removal strategies have been

explored for the purpose of identifying optimum heat removal surfaces on the exterior of VL 7P cell through FEM simulations.

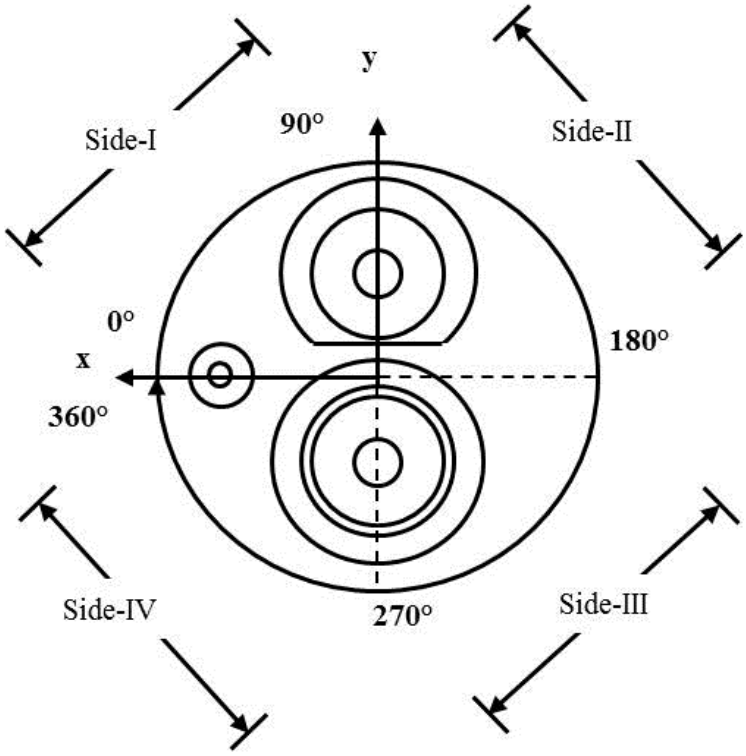

Figure 6.9: Coordinates and cell orientation used to apply cooling on cell container's side wall segments and to refer for the subsequent discussion.

6.4.1 Cooling cases

Different cooling scenarios have been investigated to study the impact of cooling conditions on temperature distribution and heat flow in VL 7P cell. Six different cooling cases have been explored by applying cooling on different parts of the cell exterior. Temperature distribution across the cell body and heat flow out of the cell have been computed as a function of ambient temperature (T_{amb}), coolant temperature (T_c), natural convection film coefficient (h_f), and forced convection film coefficient (h_c). Best cooling scenario is supposed to produce lower ΔT_{eff} across the cell.

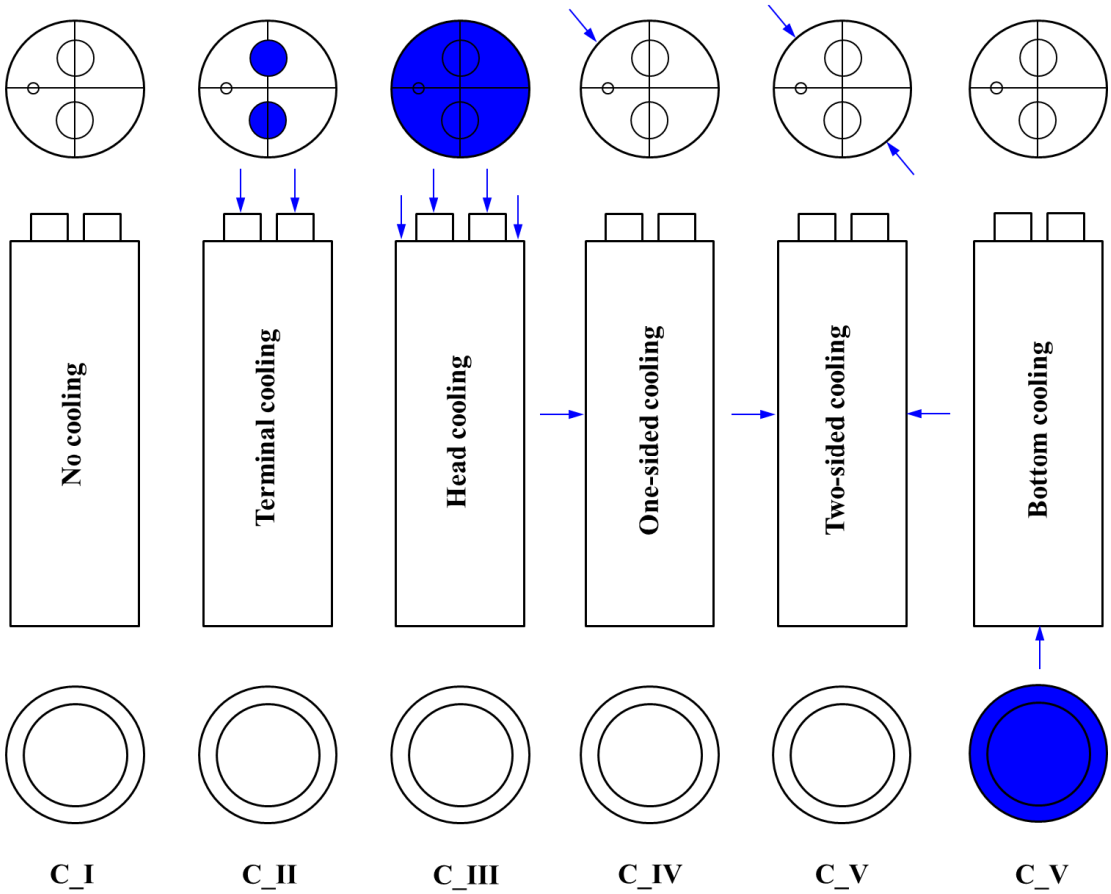

Figure 6.10: Cooling cases and cooling surfaces used in simulations; blue marks represent the location at which cooling has been applied.

Simulation results are presented in form of six path plots at different important locations on the cell body. Paths along which temperature have been plotted are shown in Figure 6.8. Line plots of transient T_{max} and T_{min} for each case are shown in Figure 6.11. Total simulation time of 10000 seconds has been used for each case. At the end of each transient simulation, nodes with maximum and minimum temperature (T_{max} and T_{min}) have been identified and temperature at these two nodes has been plotted versus time for each case. To apply cooling on cell side (radial cooling), cell container wall has been divided into four quarter sections as shown in Figure 6.9. Load cases and cooling surfaces (marked in blue) are elucidated in Figure 6.10 each of which is presented and discussed below. An overall heat generation rate of 76555 W/m^3 has been applied to the JR that amounts to about 8 watts. Two types of boundary conditions (BC) have been applied at the cell exterior: 1) natural convection and 2) forced convection or cooling conditions. Following parameters have been used for the two types of BC:

Natural convection: T_{amb} = 20 °C; h_f = 7 W/(m^2·K)
Forced convection: T_c = 10 °C; h_c = 100 W/(m^2·K)

I) Load case C_I (No cooling)

In load case C_I, no cooling has been applied to simulate natural convection conditions. Temperature profiles obtained from simulations are shown in Figure 6.11, Case I. It can be seen that, cell temperature evolves slowly over time and T_{max} reaches to 79.5 °C without attaining steady state even after 10000 seconds (total simulation time). At around 2500 seconds, T_{max} crosses 60 °C which normally is the limit for operating temperature for most of lithium-ion batteries. Effective temperature gradient ΔT_{eff} is found to be about 9.5 °C.

II) Load case C_II (Terminal cooling)

In this case cooling conditions have been applied at the electrical terminals of the cell as shown in Figure 6.10, C_II (marked in blue). Natural convection conditions have been used for rest of the surfaces. In axial direction, due to higher k_z, significant amount of heat is expected to be drawn through small cooling area for example, cell terminals.

It can be seen in Figure 6.11, Case II that cooling rate slightly increases with transient T_{max} and T_{min} curves end up in a lower limiting value as compared to that in C_I. Effective temperature gradient ΔT_{eff} is found to have increased to ~ 16 °C indicating a lesser uniform distribution of temperature as compared to C_I. Limiting value of T_{max} is around 74 °C in this case. 60 °C mark has again been crossed at around 2500 seconds. To overcome this problem of increased gradient and improve cooling time, higher h_c or lower T_c has to be used.

III) Load case C_III (Head cooling)

In this case cooling conditions have been applied on the cell head (full top part including terminals) as shown in Figure 6.10, C_III marked as blue. Natural convection conditions have been applied on rest of the surfaces. Resulting transient temperature curves are presented in Figure 6.11. It can be seen that in this case T_{max} is significantly reduced to about 52 °C and steady

state reached quicker than in the previous two cases (C_I and C_II) but ΔT_{eff} is increased to about 27 °C. Steady state is reached in about 5500 seconds which in the above two cases (C_I and C_II) not achieved even at the final simulation time i.e. 10000 seconds.

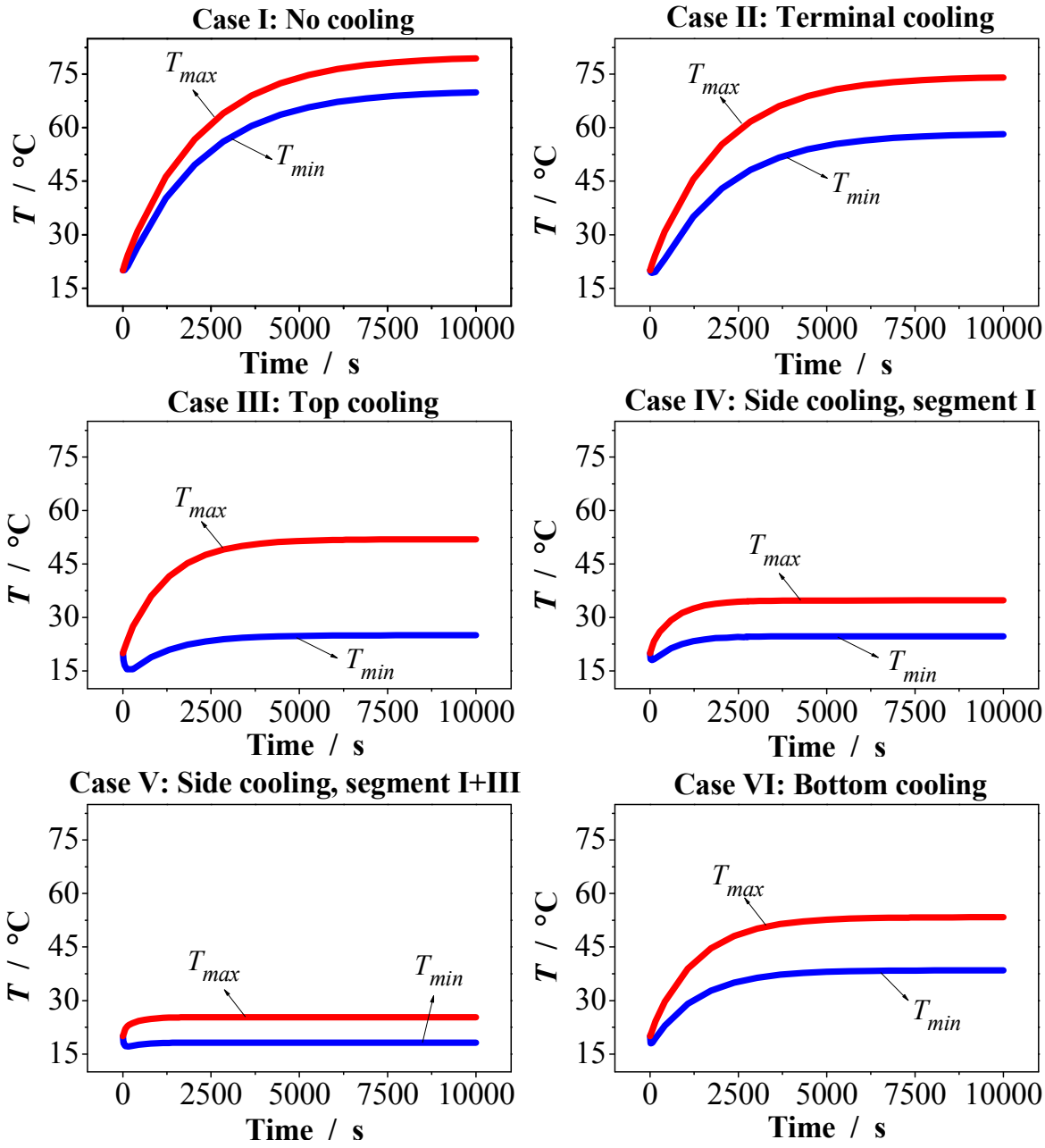

Figure 6.11: Transient T_{max} and T_{min} plots obtained from at different cooling case simulations.

IV) Load case C_IV (One-sided cooling)

In this cooling case, cooling conditions have been applied on a quarter section, indicated as Side-I, 0-90° in Figure 6.9, of the cell wall pointed by blue arrow in Figure 6.9, C_IV. It can be seen from Figure 6.11, Case IV that T_{max} decreases significantly to about 35 °C and steady state is reached in only about 3000 seconds. ΔT_{eff} again reduced to about 10 °C which is comparable to C_I while significantly lower than that in C_II and C_III.

These findings indicate that cooling on a quarter section of cell wall could help bringing temperature within safe operating range without investing much of cooling efforts primarily because of higher cooling area of the cell container wall. It is obvious from the plots that lower thermal conductivity in radial direction (k_r) has been compensated by the larger cooling area.

V) Load case C_V (Two-sided cooling)

In case C_V cooling conditions were applied on the two quarter sections of the cell wall on opposite sides to each other as in Figure 6.9 indicated by Side-I (0-90°) and Side-III (180-270°) and in Figure 6.10 by blue arrows. Resulting transient temperature plots are presented in Figure 6.11. It can be seen that steady state is reached in just about 1500 seconds. Steady state value of T_{max} is found to be 25.34 °C which is well lower than all the previous cases (C_I through C_IV). ΔT_{eff} is 7.1 °C which is also the lowest as compared to all the previous cases. Results indicate that as for now C_V appears to be the most promising regarding lower cell temperature, and uniform temperature distribution.

VI) Load case C_VI (Bottom cooling)

In the present cooling case, cooling conditions have only been applied at the bottom part of the cell as shown in Figure 6.10 by blue area. On all the remaining surfaces, natural convection conditions have been used. Transient temperature profile for this particular case is shown in Figure 6.10, Case VI which shows that T_{max} is about 53 °C with ΔT_{eff} is found to be ~ 15 °C.

6.4.2 Summary of results

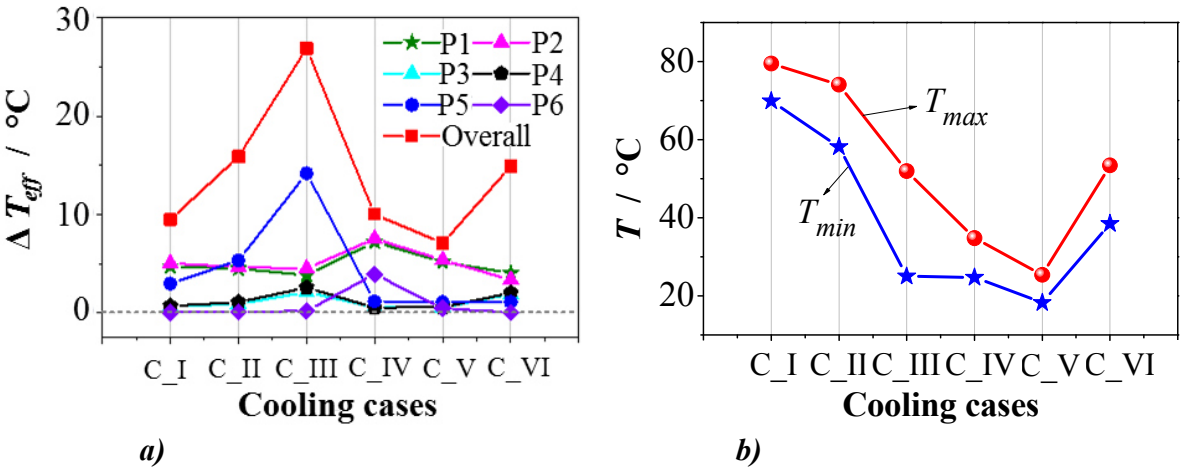

Figure 6.12: *a)* ΔT_{eff} calculated across each of path P1 through P6 and for the complete cell; and *b)* limiting values (final value at the end of transient simulation) of T_{max} and T_{min} plotted as a function of cooling case number.

An abstraction of the results obtained from simulations of different cooling cases is presented in Figure 6.12 and Figure 6.13. Temperature variation along each of the path (P1 – P6, Figure 6.8) has been obtained as ΔT_{eff} for each of the path and plotted as a function of cooling case number in Figure 6.12*a*. T_{max} and T_{min} for all the cooling cases have been plotted in Figure 6.12*b*. In addition an overall variation in the cell temperature for each case has also been computed represented by red curve in Figure 6.12*a*. It can clearly be seen in Figure 6.12*a* that the effective temperature gradient (ΔT_{eff}) of the cell and that measured at path P1 through P6 is minimum for cooling case C_V (Load case C_V). Moreover, Figure 6.12*b* shows that T_{max} and T_{min} for the cell are at their minimum again for cooling case C_V implying two-sided cooling produces more uniform temperature distribution.

In Figure 6.13, heat dissipation rate from top, bottom and sides of the cell along with overal heat dissipation rate is plotted as a function of cooling case number. It can be seen that heat disspation rate for cooling case C_V, presented by red curve with red spheres, is maximum. Thus it is strongly evident that load case C_V that is to apply cooling on two opposite quarter sections (side I, 0-90° and side III, 180-270° in Figure 6.9) of the cell container wall serves the purpose of

maintaining the cell temperature with in safe operating range with 50 % area of the cell container wall still to spare. That would conserve significant volume and weight of the module that would have otherwise been required, had the full wall cooling been used.

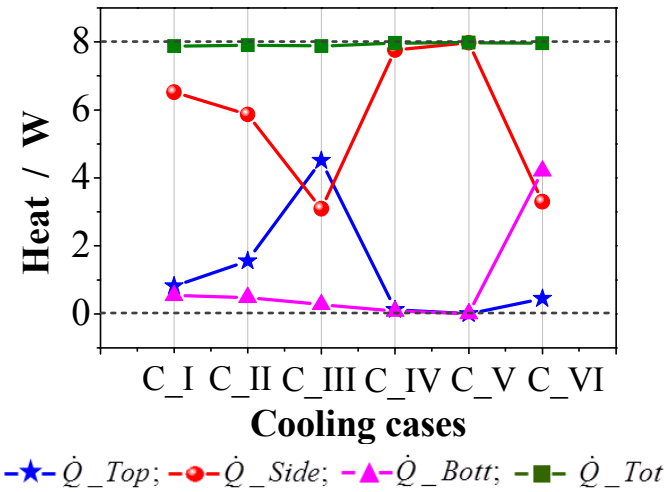

Figure 6.13: Heat dissipation rates from top, bottom, and sides of the cell along with overall heat dissipation rate as a function of cooling case number.

In this chapter thermal behaviour of lithium-ion cell in response to geometrical design parameter variations as well as cell shape and construction have been discussed. Optimum location to apply cooling on the cell exterior have been identified in view of results obtained from the simulations. Flat cell configuration has been found to be thermally more efficient but lacks mechanical stability. The choice therfore has to be made depending on the needs and specifics of application. Cell container wall thickness is found to have slightly better impact regarding improvement in thermal efficiency of cell than that of the current collectors. Nonetheless in both the cases impact is too small to be considered for commercial cell designs.

Due to comparative nature of the analysis presented in this chapter, simple 3D model with a constant rate of heat generation had been used which did not require a prior validation. To study the impact of applied loads and environmental conditions, a dynamic thermal model is required that considers both spatial as well as temporal variations in parameters. Such a model requires a prior validation. Next chapter deals with the validation of thermal coupled model developed in chapter 4 using experimental findings of chapter 5 followed by a detailed thermal analysis.

Chapter 7

Model validation and simulation results

As thermal model developed in chapter 4 was intended to be employed for a subsequent detailed thermal analysis of LFP 26650 cell, a prior validation of the model was required to prove authenticity of simulation results. Hence the model has been authenticated using experimental measurements, presented in chapter 5, corresponding to 1C, 2C, and 5C constant-current single discharge-charge cycle at T_{amb} ranging from -10 °C to 50 °C. Simulation results presented in the following section have been found to be in good agreement with the experimental findings.

Once validated, the model has then been used to carry out detailed simulations. Dynamic thermal behavior of 26650 cell has been studied under high current pulses for short intervals. Moreover, thermal response of the cell at high operating temperatures due to side reactions taking place at SEI has also been simulated. Following the model validation in section 7.1, simulation results are presented in section 7.2. Finally some important conclusions and recommendations have been made and presented in section 7.3.

7.1 Model validation

Thermal aspect of the model has been validated by comparing the simulated cell surface temperature (T_{sur}) to that experimentally measured. Whereas electrochemical aspect of the model has been validated by comparing simulated cell voltage (U) to the measured voltage. Equivalent

scales have been used for both temperature and voltage line plots for clarity and a better comparison.

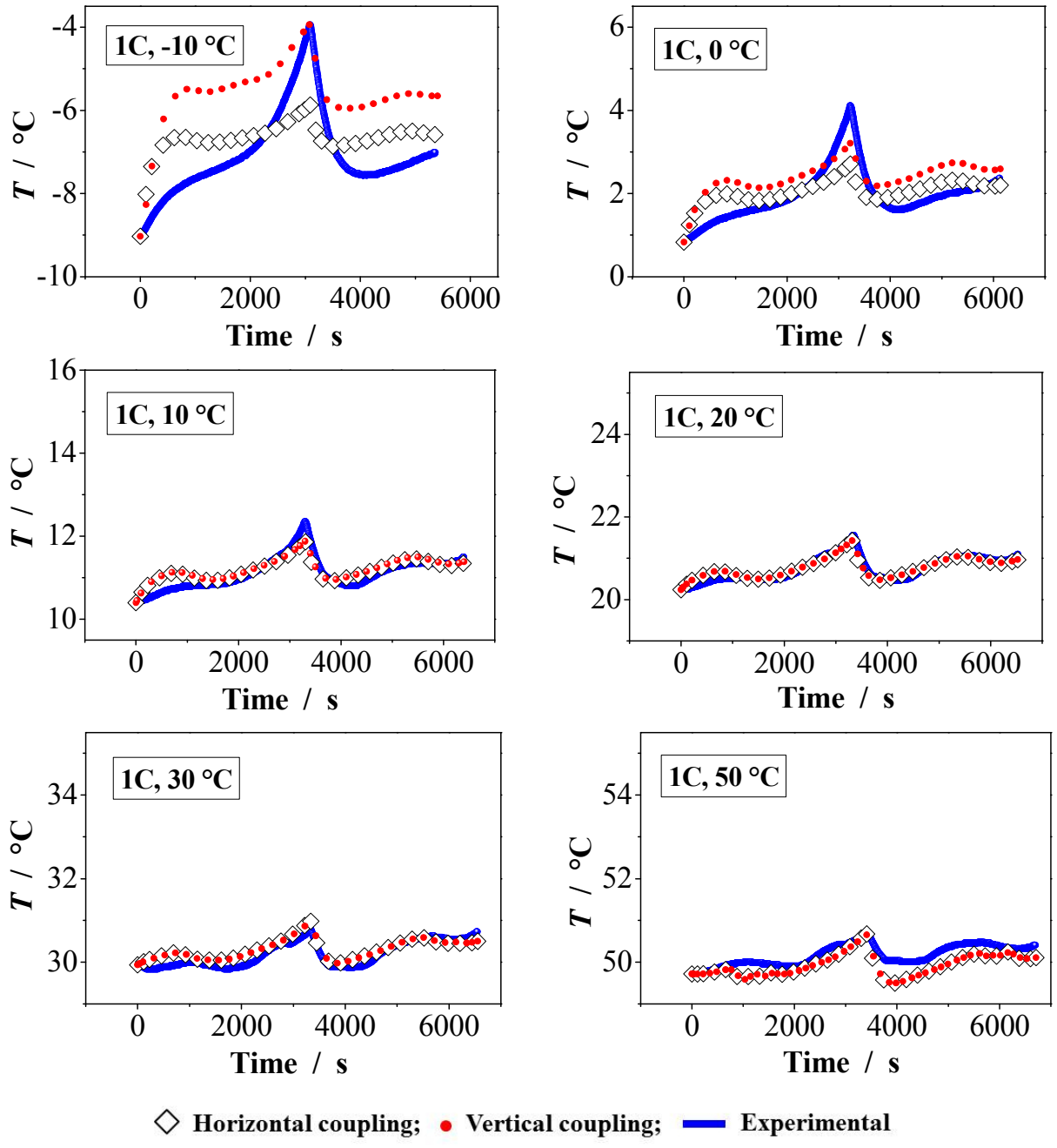

Figure 7.1: Simulated and measured cell surface temperature (T_{sur}) plotted as a function of time at 1C rate and different ambient temperatures (T_{amb}) for a single discharge-charge cycle.

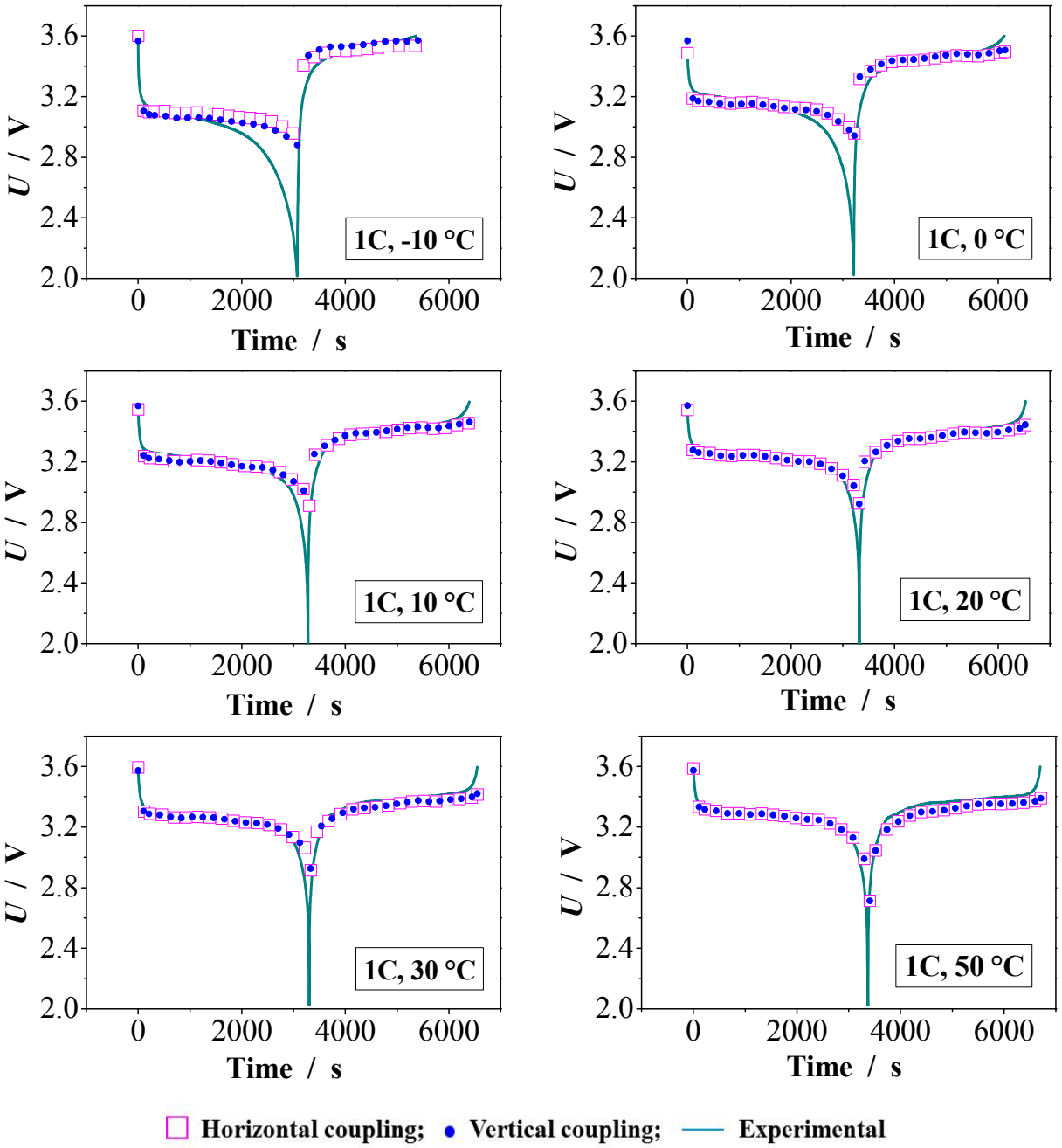

Figure 7.2: Simulated and measured cell potential (U) plotted as a function of time at 1C rate and different ambient temperatures (T_{amb}) for a single discharge-charge cycle.

Simulation results, obtained from horizontal (direct) coupling as well as vertical (indirect) coupling (section 4.6.1) between electrochemical heat generation and heat transfer models, have been validated against experimentally measured data. In vertical coupling, spatial variations in

heat generation rate have been ignored while in horizontal coupling heat generation rate has been dynamically updated as a function of temperature regarding spatial as well as temporal variations.

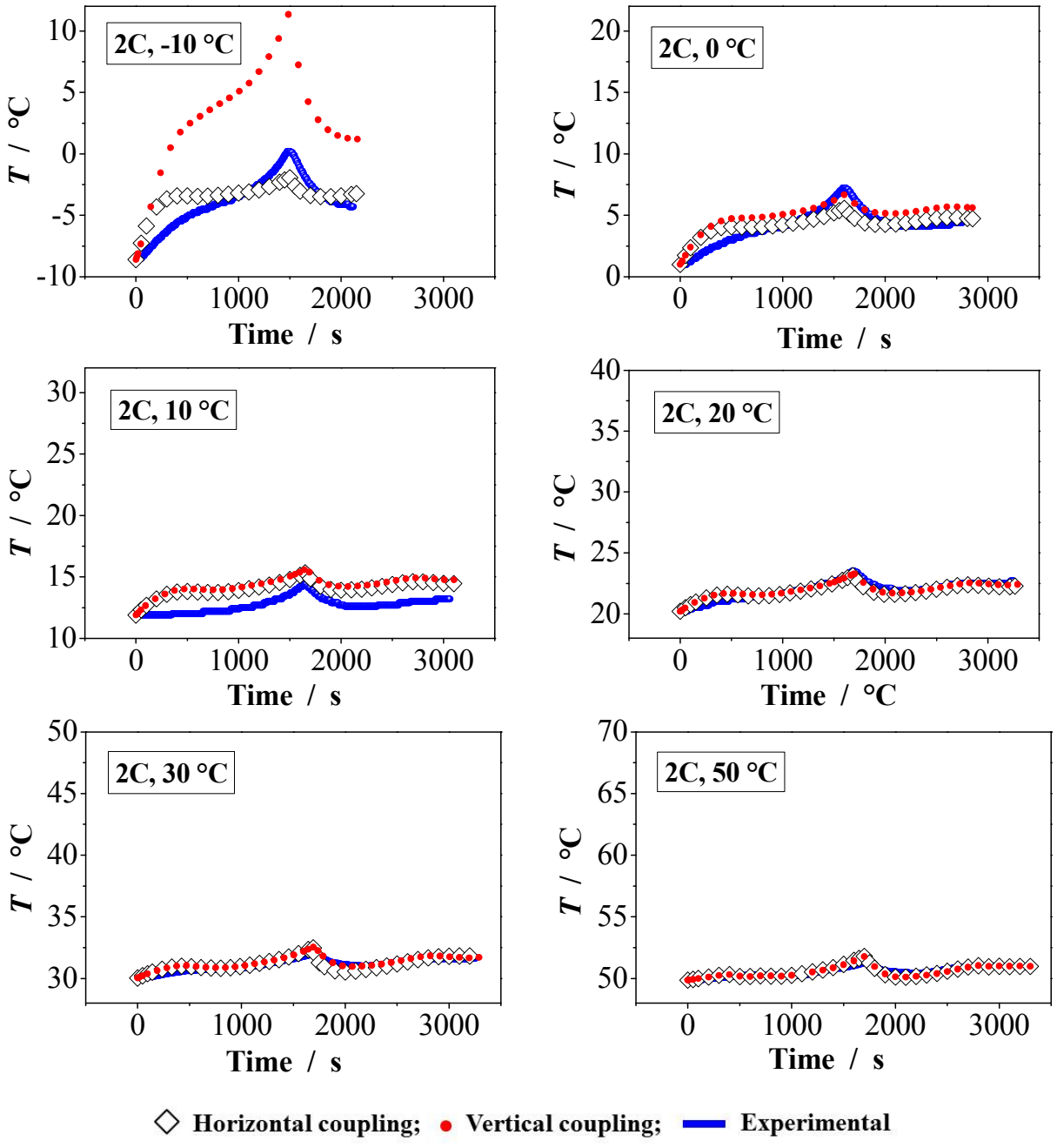

Figure 7.3: Simulated and measured cell surface temperature (T_{sur}) as function of time at 2C rate and different ambient temperatures (T_{amb}) for single discharge-charge cycle.

Figure 7.1, Figure 7.3, and Figure 7.5 represent measured and simulated cell surface temperature (T_{sur}) whereas Figure 7.2, Figure 7.4, and Figure 7.6 represent measured and simulated cell potential at 1C, 2C, and 5C rates respectively at different operating temperatures (T_{amb}).

Shorter temperature and potential curves along time axes indicate a loss in cell capacity. It can be seen from the Figure 7.1 through Figure 7.6 that at low temperatures and higher discharge currents, cell capacity tends to decrease. This reduction in capacity have already been explained in section 5.2.1. It can clearly be seen that at higher currents and lower operating temperatures, surface temperature and potential curves obtained through vertical coupling drift away from those obtained through horizontal coupling thereby exhibiting higher deviation from experimental data. This implies that at higher operating temperatures (> 10 °C) and lower applied currents (< 2C), spatial variations in heat generation can be ignored and less rigorous vertical coupling method can be employed with reasonable accuracy. Whereas at higher currents (> 2C) and lower operating temperatures (< 10 °C) a more rigorous horizontal coupling method needs to be employed but at the expense of higher computation time and resources.

Electrochemistry of porous electrodes is a complex phenomenon. Due to lack of accurate parameters, numerous assumptions and generalization of model parameters have to be made. At extreme conditions e.g. lower operating temperatures and higher currents, these assumptions give rise to increased discrepancies. For example, solid state diffusion has been ignored in the electrochemical heat generation model (section 4.5) which controls electrochemical reaction more dominantly at higher reaction rates (higher currents) and lower operating temperatures. Hence effect of such assumptions gets accumulated toward extreme conditions giving rise to higher deviations. Since vertical coupling method is further simplified by neglecting spatial variations in heat generation rate, even higher deviations from experimental data have been observed in case of vertical coupling.

Figure 7.1 through Figure 7.6 show that at operating temperatures ranging from 10 °C to 50 °C and 2C or lower currents, both the methods showed good agreement but in case an improved accuracy is required, horizontal coupling should be preferred. It can be concluded that the vertical coupling method (section 4.6.1, II) can be used at lower currents (≤ 1C) and temperatures ranging from 10 °C to 50 °C with reasonable accuracy. Whereas at low to moderate currents (up to 5C)

and wide temperature ranges (-10 °C – 50 °C), horizontal coupling method (section 4.6.1, III) produces results with higher accuracy.

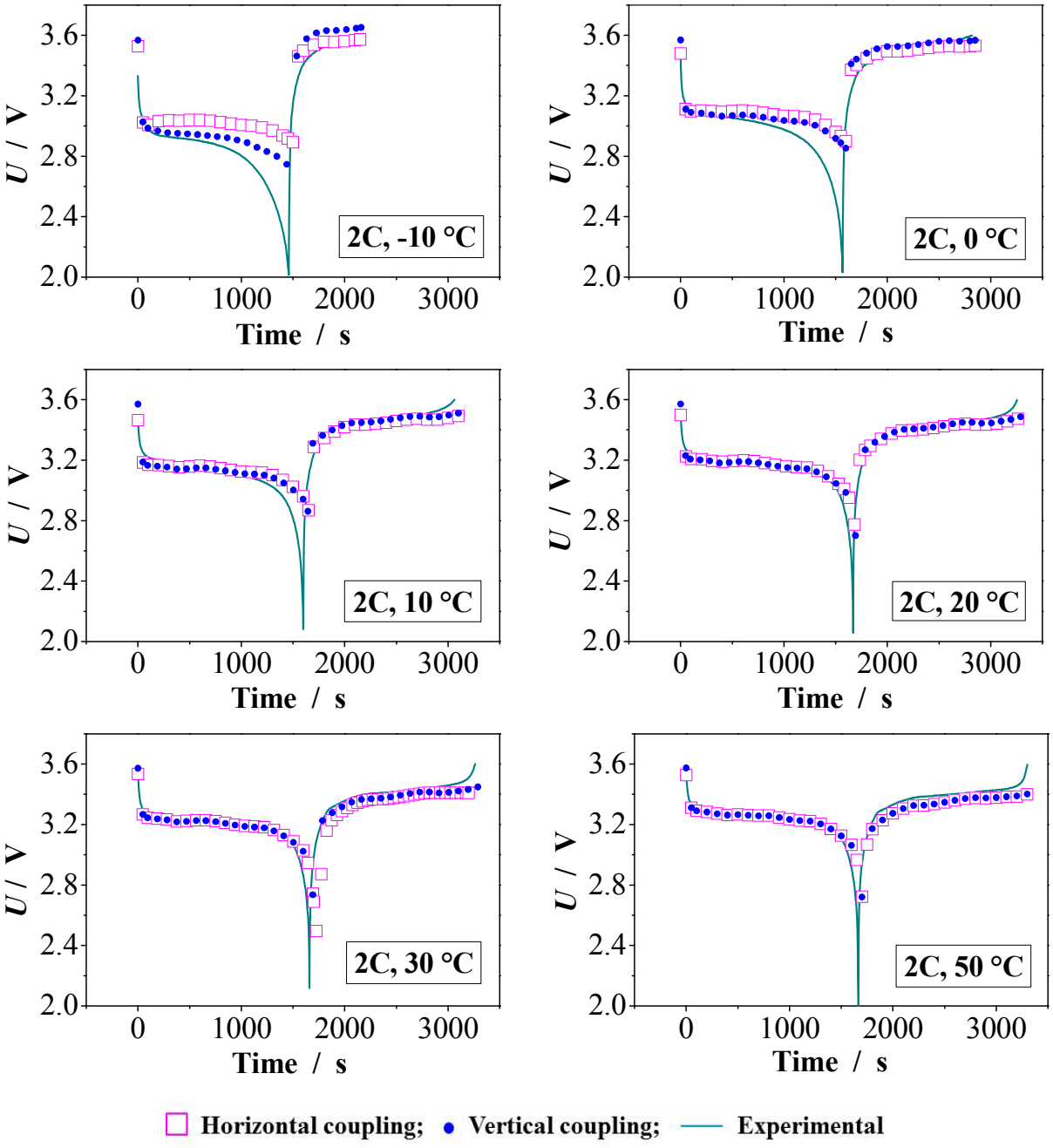

Figure 7.4: Simulated and measured cell potential (U) as a function of time at 2C rate and different ambient temperatures (T_{amb}) for a single discharge-charge cycle.

At very high currents (> 10C) and sub-zero temperatures, horizontal coupling method can be used with a decreased accuracy but within tolerable limit. Overall the simulated results show good agreement with experimental data with acceptable deviations which justifies employing the model for subsequent detailed simulations and thermal analysis of the cell.

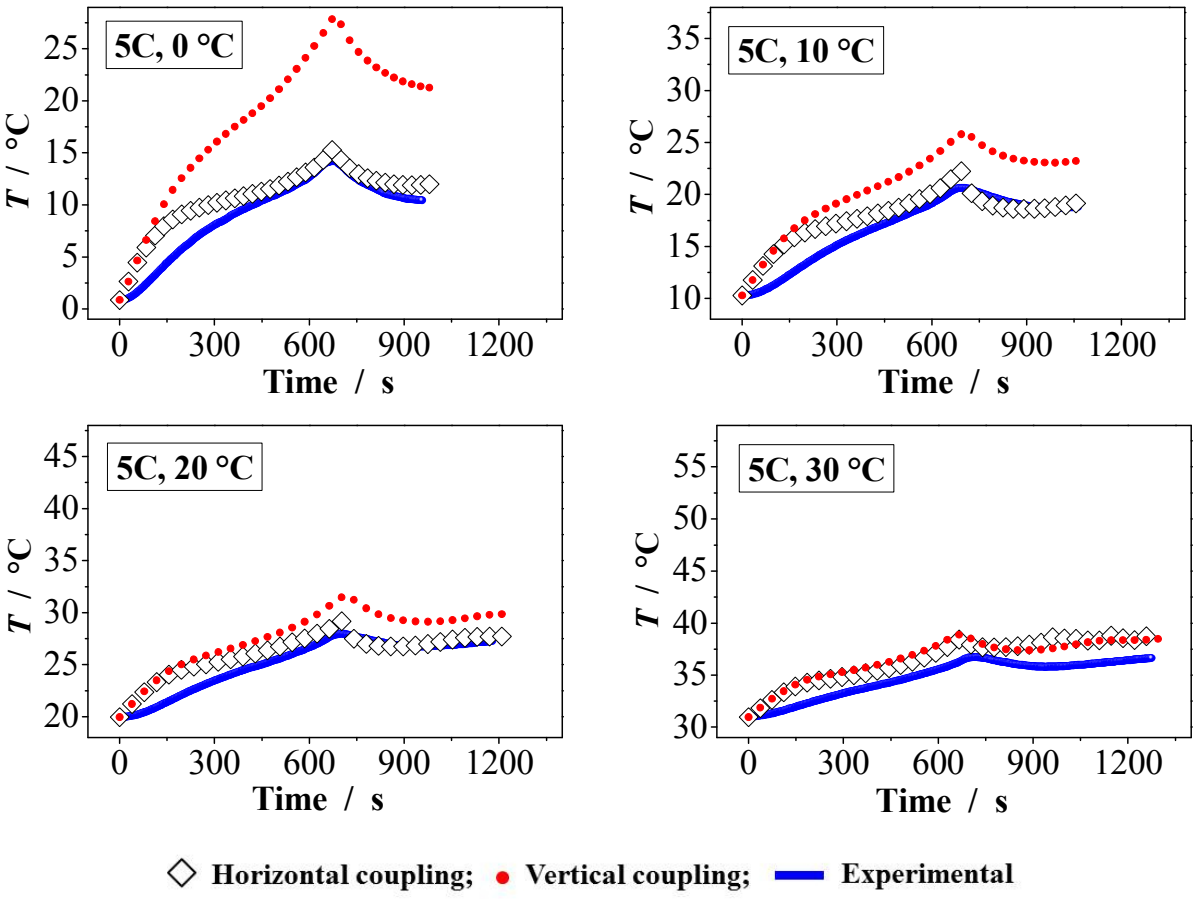

Figure 7.5: Simulated and measured cell surface temperature (T_{sur}) as a function of time at 5C rate and different ambient temperatures (T_{amb}) for a single discharge-charge cycle.

7.2 Simulation Results

In view of the validation results and discussion presented in section 7.1 above it has safely been concluded that horizontal coupling method showed promise in predicting dynamic thermal behavior of 26650 cell. Hence horizontal model has further been used for detailed thermal analysis of the cell. Vertical coupling method has also been used to make some useful predictions

regarding self-heating of the cell at elevated temperatures. Results obtained from the detailed simulations are presented below.

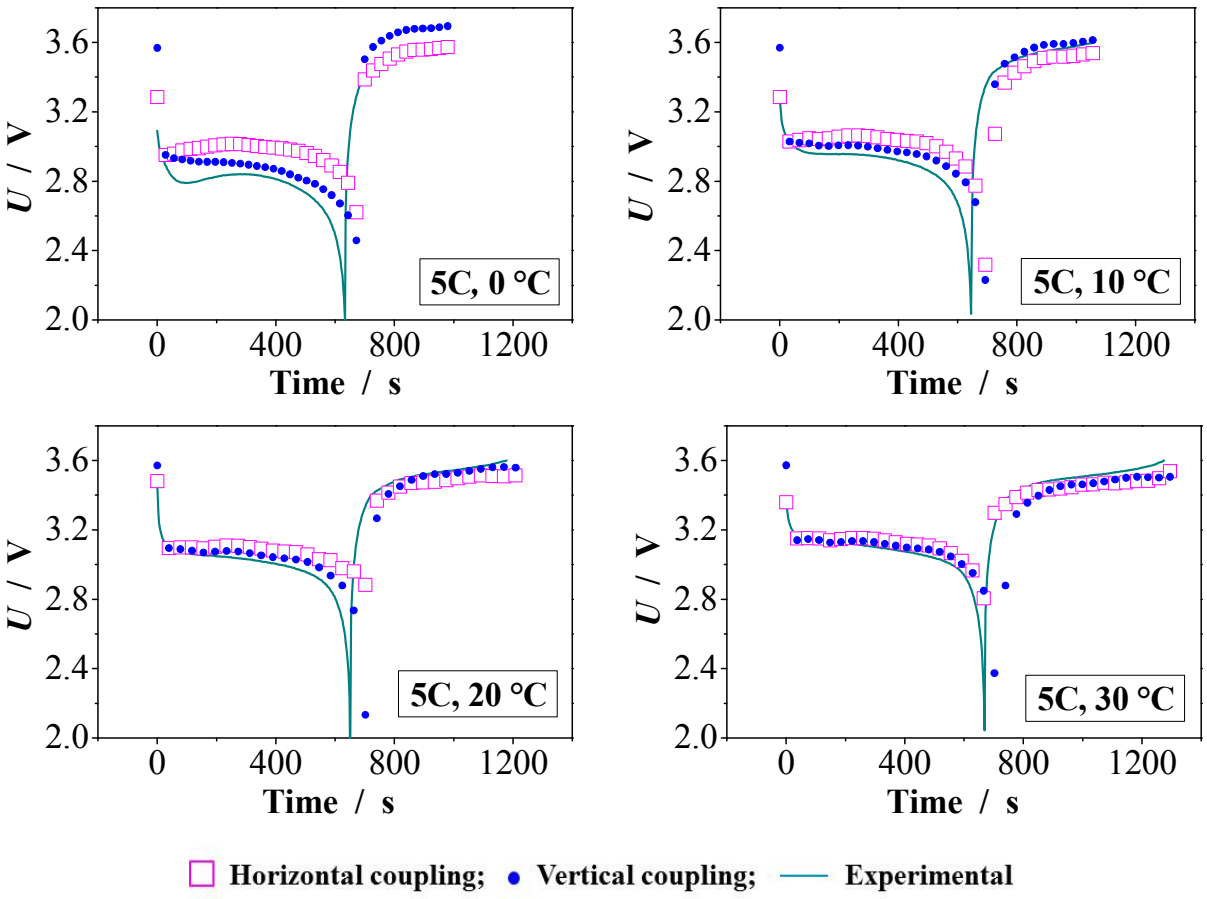

Figure 7.6: Simulated and measured cell potential (U) as a function of time at 5C rate and different ambient temperatures (T_{amb}) for a single discharge-charge cycle.

7.2.1 Effect of T_{amb} on T_{cell}

Effect of operating temperature amounting to -10 °C, 0 °C, 10 °C, 20 °C, 30 °C, and 50 °C on the cell temperature has been studied using horizontal coupling method and a constant current load amounting to 1C, 2C, and 5C rates. Dynamic simulation results are presented and discussed below.

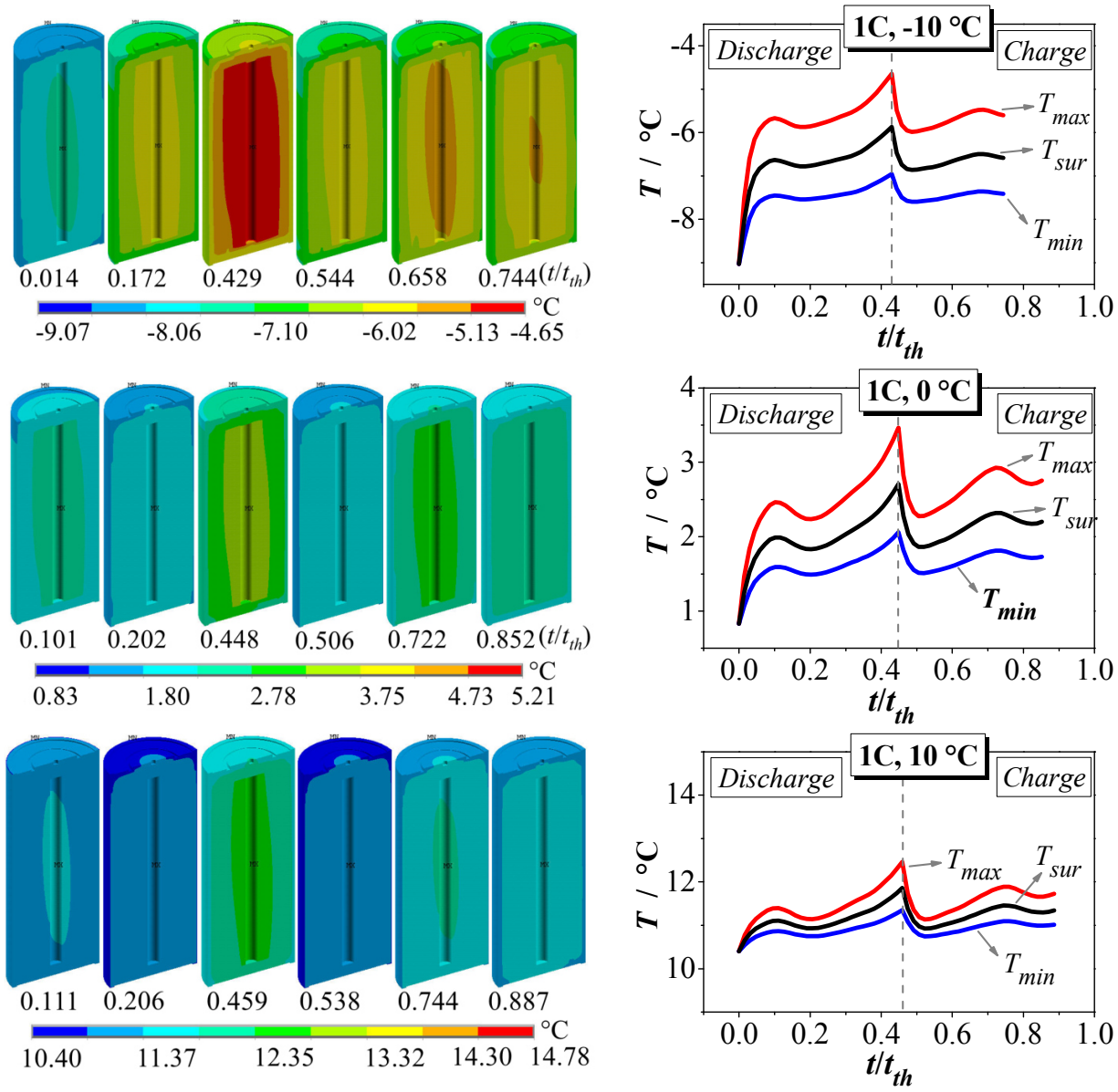

Figure 7.7*a*: Temperature contours on a bisection of 26650 cell (left) and line plots (right) for 1C current at T_{amb} = -10 °C, 0 °C, and 10 °C.

Maximum cell temperature (T_{max}), minimum cell temperature (T_{min}), and cell surface temperature (T_{sur}) are plotted as 2D line plots along with 3D contour plots on a bisection of 26650 cell. Along the *x*-axes in 2D line plots, normalized time obtained by dividing actual simulation time by theoretical simulation time (t/t_{th}) has been used. (t/t_{th}) is analogous to cell capacity i.e. farther the temperature curve extends to the right along *x*-axis, higher is the cell capacity and vice versa.

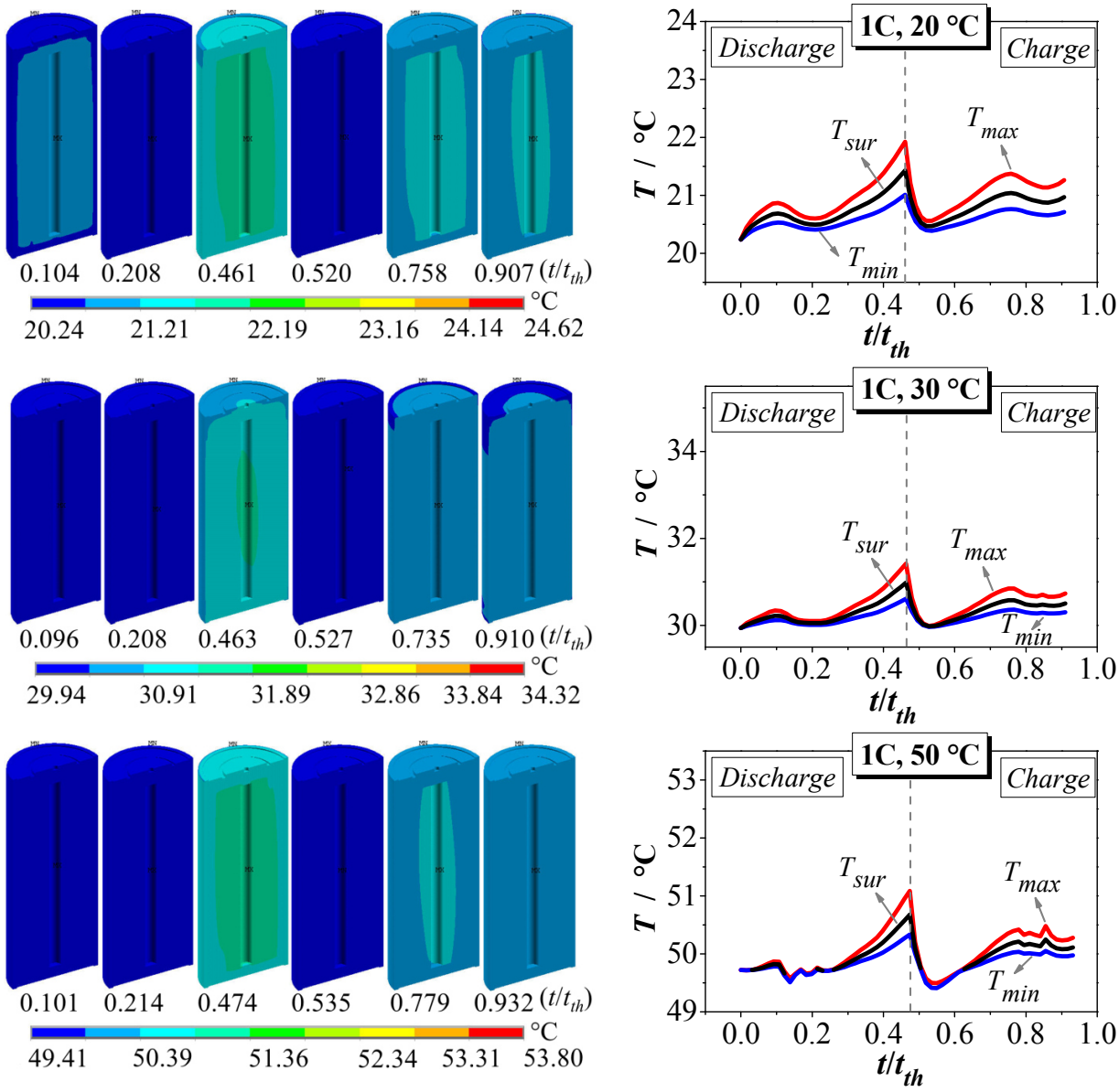

Figure 7.7*b*: Temperature contours on a bisection of 26650 cell (left) and line plots (right) for 1C current T_{amb} = 20 °C, 30 °C, and 50 °C ambient temperature.

Equivalent scales along *x*- and *y*-axes have been used for better comparison. Time intervals used in 3D contours correspond to the adjacent 2D line plots. Figure 7.7 [*a), b)*], Figure 7.8 [*a), b)*], and Figure 7.9 [*a), b)*] shows temporal as well as spatial variations in cell temperature at 1C, 2C, and 5C rates and at varying operating temperatures. Simulation results at 5C rate and T_{amb} = -10 °C and 50 °C have not been included due to bad convergence and quality of plots.

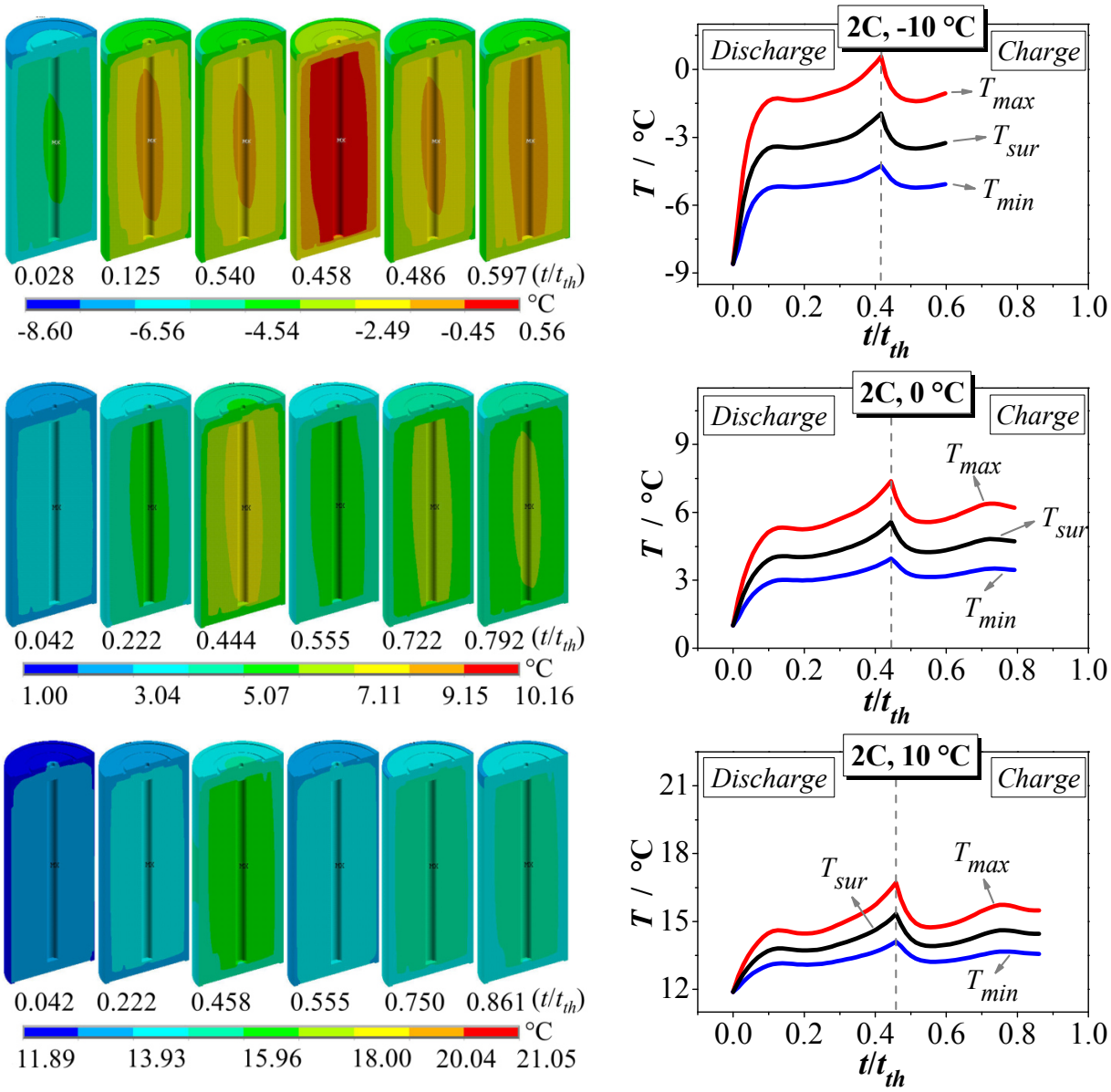

Figure 7.8*a*: Temperature contours on a bisection of 26650 cell (left) and line plots (right) for 2C current at T_{amb} = -10 °C, 0 °C, and 10 °C ambient temperature.

It can be seen that temporal as well as spatial variation in cell temperature is maximum at T_{amb} = -10 °C while minimum at T_{amb} = 50 °C. It can also be seen that effective gradient of cell temperature (ΔT_{eff}) decreases as T increases. Temperature curves tend to be flat at higher operating temperatures and lower currents. Section 5.2.1 and section 5.2.2 could be referred to for further details and discussion.

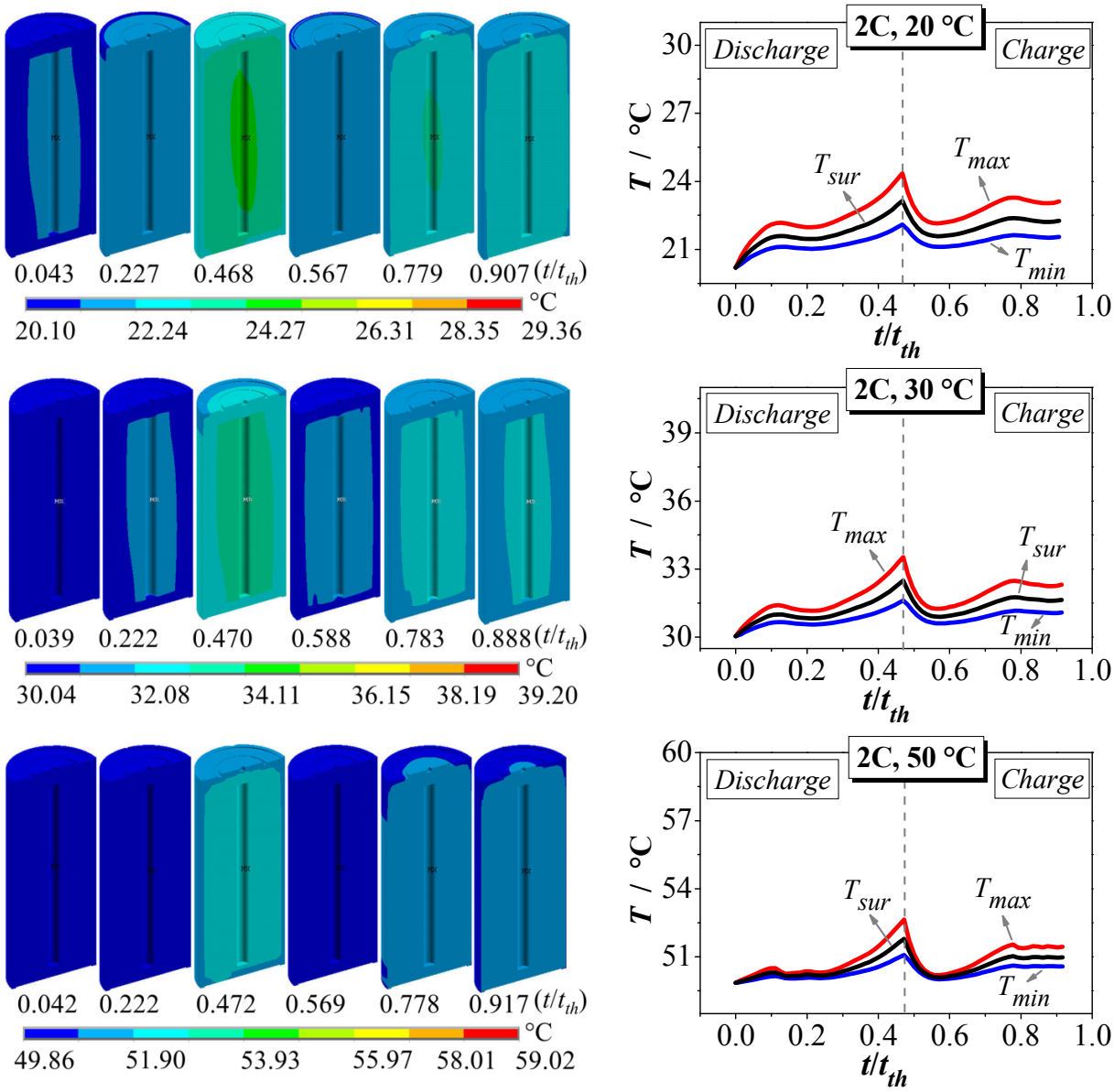

Figure 7.8*b*: Temperature contours on a bisection of 26650 cell (left) and line plots (right) for 2C current T_{amb} = 20 °C, 30 °C, and 50 °C ambient temperature.

7.2.2 Effect of T_{amb} on $\dot{Q}_{gen}$ and $\dot{Q}_{rej}$

As mentioned in section 3.4 [Equation (3.67)] that electrochemical energy storage systems generate heat contributed by different sources. Overall heat generation $\dot{Q}_{gen}$ and its constituent contributions i.e. reversible heat ($\dot{Q}_{rev}$), irreversible heat ($\dot{Q}_{irr}$), and Joule heat ($\dot{Q}_{joul}$) have been computed for 26650 cell using horizontal coupling method. In addition, overall heat dissipation rate ($\dot{Q}_{rej}$) along with constituting dissipations due to convection ($\dot{Q}_{rej,\ con}$) and radiation ($\dot{Q}_{rej,\ rad}$)

have also been computed. All the above mentioned quantities are plotted versus normalized time (t/t_{th}) for 1C, 2C, and 5C rates at different values of operating temperatures ranging from -10 °C to 50 °C. Again equivalent scales have been used for 2D line plots. Plots indicate how operating temperature and applied current influence different heat generation sources.

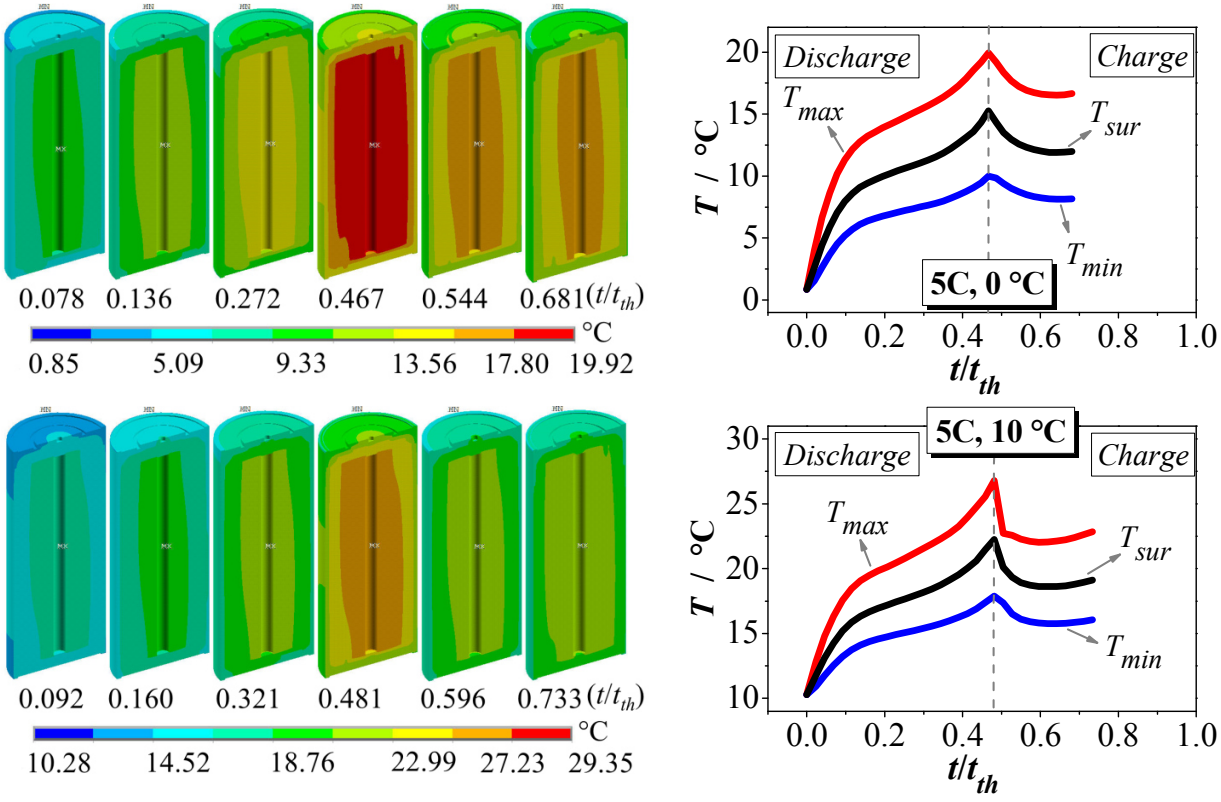

Figure 7.9*a*: Temperature contours on a bisection of 26650 cell (left) and line plots (right) for 5C current T_{amb} = 0 °C and 10 °C ambient temperature.

Since in horizontal coupling, overall heat generation ($\dot{Q}_{gen}$) varies spatially as can be seen in Figure 7.14, an average value of $\dot{Q}_{gen}$ has been used in the following line plots. Also heat dissipation rate $\dot{Q}_{rej}$ plotted as the sum of $\dot{Q}_{rej,\ con}$ and $\dot{Q}_{rej,\ rad}$. $\dot{Q}_{gen}$ along with individual contributions is plotted for 1C, 2C, and 5C rates in Figure 7.10, Figure 7.11, and Figure 7.12 respectively with T_{amb} ranging from -10 °C to 50 °C. Additionally heat dissipation rate ($\dot{Q}_{rej}$) for each case has also been plotted.

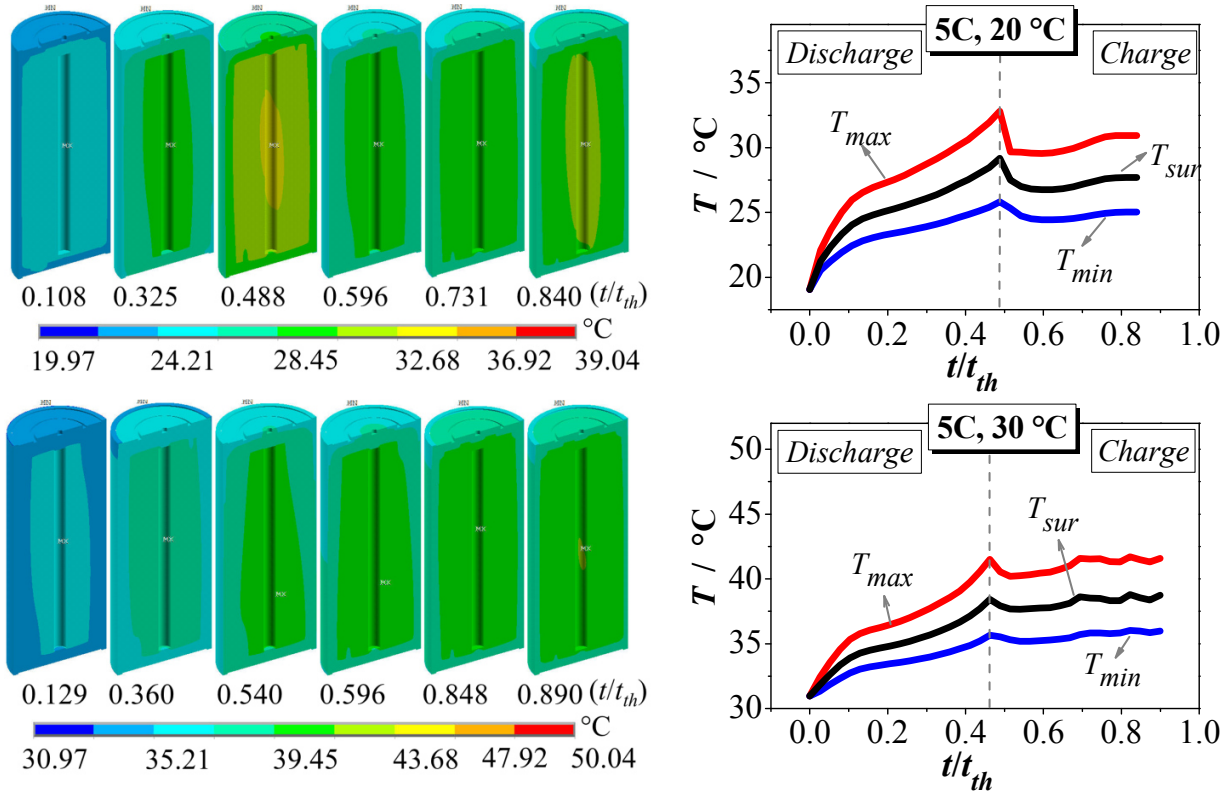

Figure 7.9*b*: Temperature contours on a bisection of 26650 cell (left) and line plots (right) for 5C current T_{amb} = 20 °C and 30 °C.

Plots show that $\dot{Q}_{gen}$ curve appears steeper at the start of discharge and charge processes. This can be explained by the fact that while the cell is in idle mode, concentration gradients within the electrolyte and the electrode active material are in a state of equilibrium and correspond to open circuit voltage (OCV) of the cell. When initially current is applied during discharge or charge, sharp concentration gradients develop immediately due mainly to ohmic resistances across the electrolyte and electrode active materials as well as across the solid circuitry causing the cell voltage to deviate steeply from OCV. $\dot{Q}_{joul}$ is the main contributor to $\dot{Q}_{gen}$ at this stage.

As resistances are higher at lower T_{amb} and higher currents, $\dot{Q}_{joul}$ is more dominant at low T_{amb} and higher C rates. This implies that combining higher currents with lower operating temperatures make things even worst regarding thermal efficiency and safer operation of the cell.

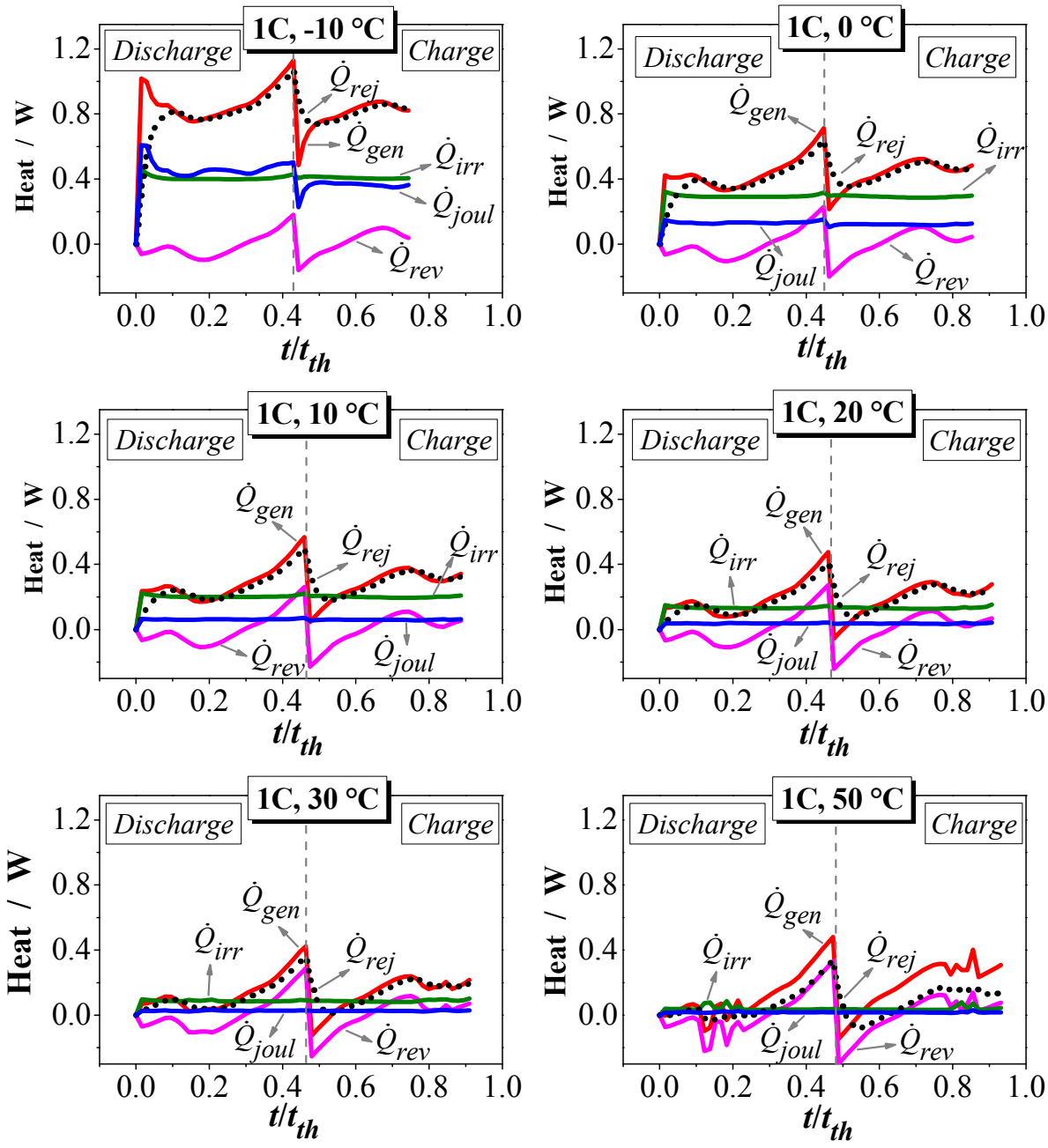

Figure 7.10: Different heat contributions in 26650 cell at 1C rate and T_{amb} = -10 °C, 0 °C, 10 °C, 20 °C, 30 °C, and 50 °C.

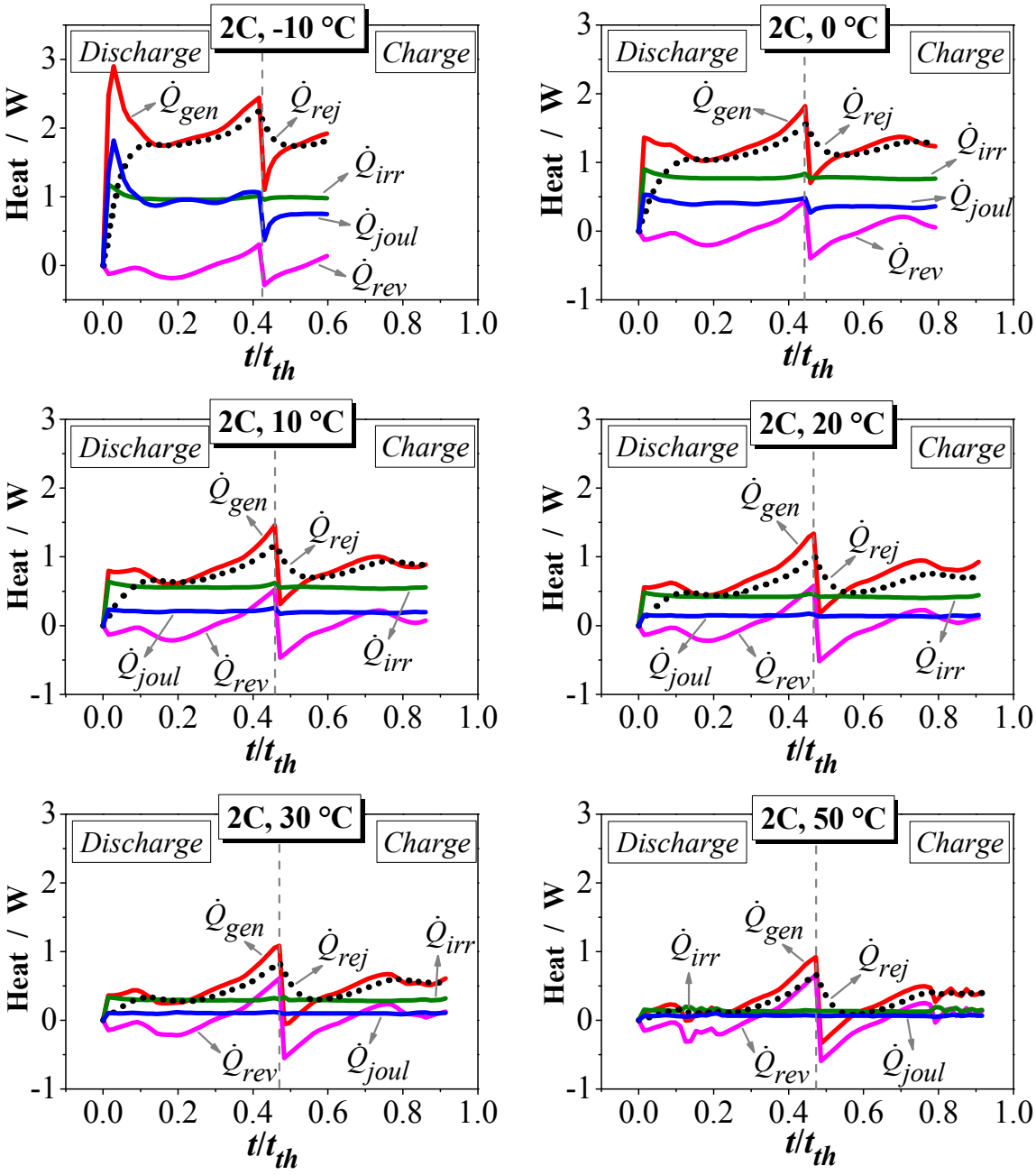

Figure 7.11: Different heat contributions in 26650 cell at 2C rate and T_{amb} = -10 °C, 0 °C, 10 °C, 20 °C, 30 °C, and 50 °C.

Abrupt rise in the $\dot{Q}_{gen}$ curve observed at the start of discharge and fall at the start of charge, caused by initial ohmic perturbations, disappears as current continues to flow. Concentration gradients across electrolyte and solid phases readjust causing the cell potential to stabilize and change more evenly making $\dot{Q}_{gen}$ curve to undergo a gradual change caused mainly by reversible

heating ($\dot{Q}_{rev}$). As seen in Figure 7.10 through Figure 7.12 that $\dot{Q}_{gen}$ curves evolve smoothly except for the end perturbations. As diffusion is controlling only at high currents, irreversible heating ($\dot{Q}_{irr}$), which depends on diffusion limitations, contribute little to the overall heat generation except for at high currents as can be seen in Figure 7.12 (at 5C). Due to higher diffusion at higher currents and lower ionic conductivity at lower operating temperatures, overall heat generation rate ($\dot{Q}_{gen}$) is higher at lower ambient temperatures and higher C rates (Figure 7.10 – Figure 7.12).

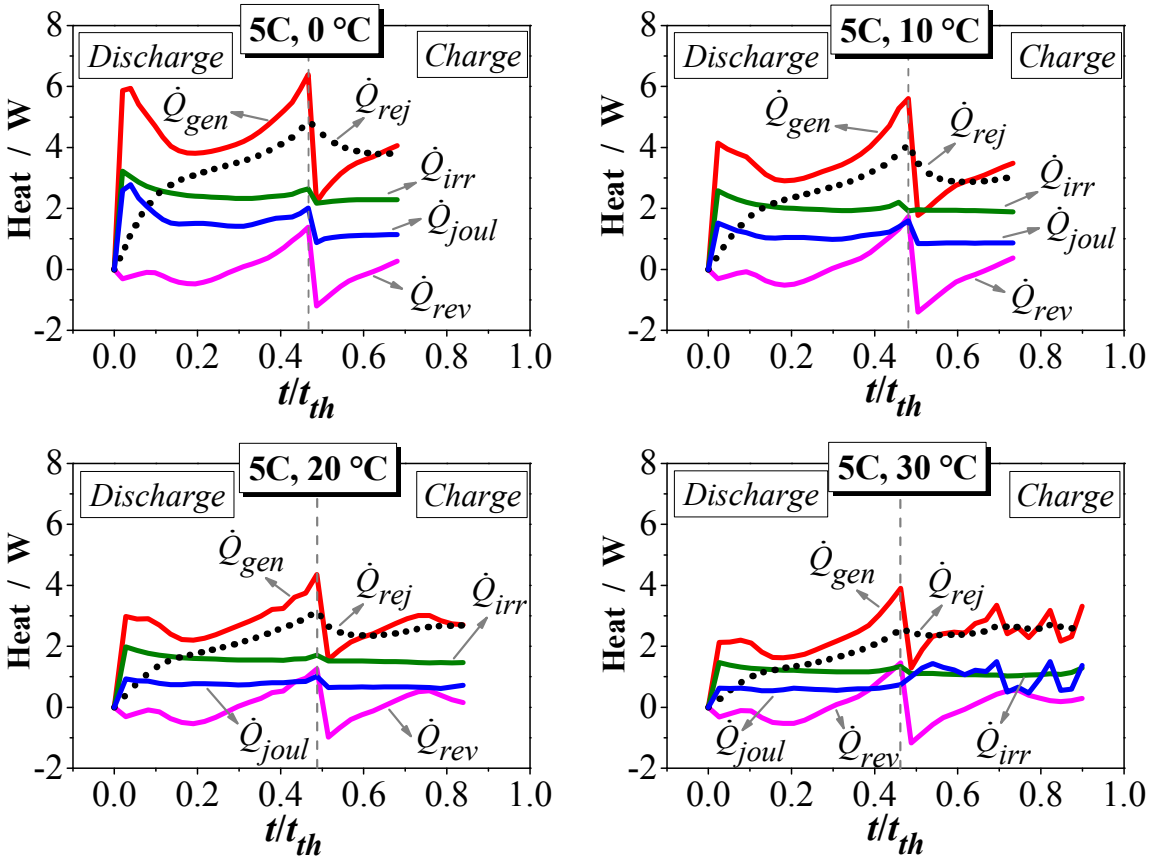

Figure 7.12: Different heat contributions in 26650 cell at 5C-rate and T_{amb} = 0 °C, 10 °C, 20 °C, and 30 °C.

Reversible or entropic heat ($\dot{Q}_{rev}$) reversibly causes heating and cooling during the course of discharge-charge cycle, as is apparent in Figures 7.10 through Figure 7.12, hence it appears to have small contribution to an abnormal or abrupt increase in the cell temperature. Within the

discharge zone, $\dot{Q}_{rev}$ is slightly higher than that within the charge zone giving rise to a slightly higher cell temperature during discharge as compared to that during charge.

At higher ambient temperatures, due to higher diffusion rate and ionic conductivity, $\dot{Q}_{joul}$ and $\dot{Q}_{irr}$ contribute negligibly to the overall heat generation leaving $\dot{Q}_{rev}$ the only dominating contributing source. But as mentioned above, due to reversible cooling effect, $\dot{Q}_{rev}$ does not have significant influence on the overall heat generation rate and hence on the cell temperature. That is the reason for a small increase in cell temperature at higher operating temperatures as compared to that at the lower operating temperatures.

In Figure 7.10 – Figure 7.12, crests in $\dot{Q}_{gen}$ curves at the beginning and end of discharge while a trough in the middle can be observed especially at lower ambient temperatures and higher C rates. This trend is imparted to $\dot{Q}_{gen}$ curve mainly by $\dot{Q}_{joul}$ and can be explained by the fact that at the beginning of discharge, lithium ion concentration in the electrolyte is lower. That means lower ionic conductivity and higher resistance give rise to higher $\dot{Q}_{joul}$ at the beginning of discharge. As Li^+ concentration in the electrolyte increases, electrolyte conductivity increases thus decreasing resistance thus minimizing $\dot{Q}_{joul}$ and hence stabilizing $\dot{Q}_{gen}$. After certain concentration of Li^+ (typically ~ 1 mol/l) is reached, conductivity starts decreasing again thus causing $\dot{Q}_{joul}$ and thus $\dot{Q}_{gen}$ to rise. That causes a dominant rise in the cell temperature curves (Figure 7.7 through Figure 7.9) at the beginning and end of discharge.

Moreover, as can be seen in Figure 7.10 – Figure 7.12 that at the beginning of discharge, $\dot{Q}_{rej}$ is significantly lower than that of $\dot{Q}_{gen}$ contributing to the sharp increase in cell temperature. On the other hand at the beginning of charge, $\dot{Q}_{rej}$ is higher than $\dot{Q}_{gen}$ that contributes to an abrupt decrease in the cell temperature. Other than these two locations, heat dissipates steadily stabilizing the temperature curves. $\dot{Q}_{rej}$ is almost equal to $\dot{Q}_{gen}$ at 1C rate except for the beginning of discharge. At 2C rate, it drops slightly below $\dot{Q}_{gen}$ curve whereas at 5C rate the drop is quite significant. That means at lower to moderate currents ($\leq$ 2C) natural convection sufficiently removes the generated heat under normal operation but at higher currents which are especially encountered in EVs and HEVs proper heat removal mechanism should be in place. Temperature surges are expected in electrically propelled vehicles during acceleration. Moreover possibility of some abuse event makes efficient heat removal even more essential.

7.2.3 Hybrid pulse power characterization (HPPC) test

HPPC test procedure is adopted from *FreedomCAR Battery Test Manual for Power-Assist Hybrid Electric Vehicles* [126] and used to run simulations with recommended current pulse profile (Table 7.1, Figure 7.13).

Table 7.1: Hybrid pulse power characterization profile [126]

Time increment (s)	Cumulative time (s)	Relative currents
10	10	1
40	50	0
10	60	− 0.75

HPPC test is aimed at determining dynamic power capabilities of the powering device (battery) within its designed load ranges. Present simulation test involves 10 second pulses of each discharge and regen (charge) separated by a 40 second relaxation interval applied as input load to horizontally coupled EC-T model (section 4.6.1-III). Regen is the charge interval of a device e.g. battery that corresponds to returning kinetic energy of the vehicle to the device typically from braking. Regen can only persist for small intervals at a time because of certain physical limitations [126].

Variations in the cell temperature, power, heat generation, and heat dissipation rates have been studied in response to a 20C discharge and 15C regen pulses. The original test adopted in [126] is used to demonstrate pulse power capabilities of the device for different DODs. But this simulation test is modified to be used for a single discharge-regen pulse at 100 % SOC and T_{amb} = 0 °C, 10 °C, 20 °C, and 30 °C. A value of 7 W/(m^2·K) has been used for heat transfer coefficient (h_f). Results obtained from the simulations are presented below.

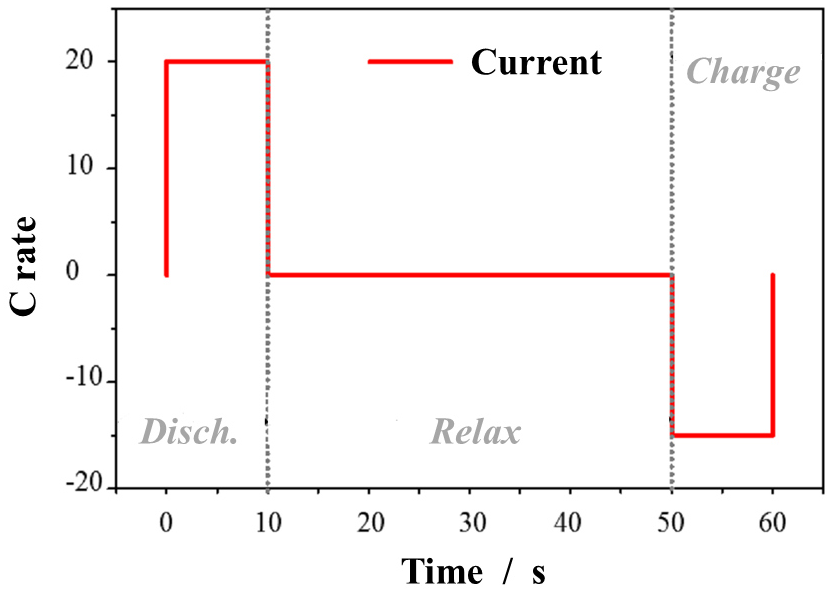

Figure 7.13: HPPC profile for 20C (269 A/m^2) discharge pulse and 15C (201.75 A/m^2) regen pulse, 10 seconds each with 40 seconds relaxation [126].

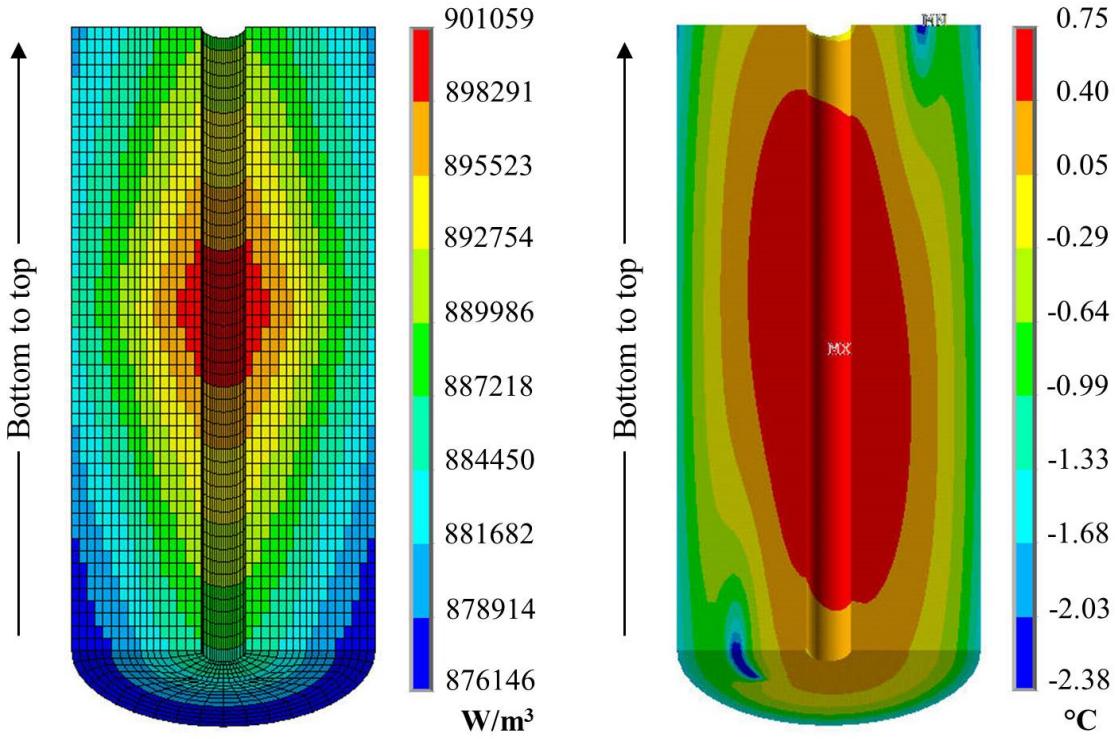

Figure 7.14: Linearly interpolated heat generation contours on a bisection of JR (left) obtained through horizontal coupling of EC-T model with resulting temperature contours (right) computed at the end of regen phase at T_{amb} = -10 °C.

Selected heat generation contours obtained through horizontal coupling at the six representative points on the JR (Figure 4.12) and subsequent linear interpolation are shown in Figure 7.14 along with resulting temperature contours. Line plots of cell temperature versus time are presented in Figure 7.15. Plots exhibit a similar trend as was seen in Figure 7.7 – Figure 7.9 and discussed in section 7.2.1, hence require little further elaboration. Figure 7.15 shows that T_{max} increases steeply during discharge phase and gradually drops during relaxation phase till it reaches regen phase where it starts increasing again. T_{min} does not change significantly during discharge and regen phases but gradually increases during relaxation phase. Whereas T_{sur} smoothly rises during discharge and regen phases but stands almost flat during relaxation phase.

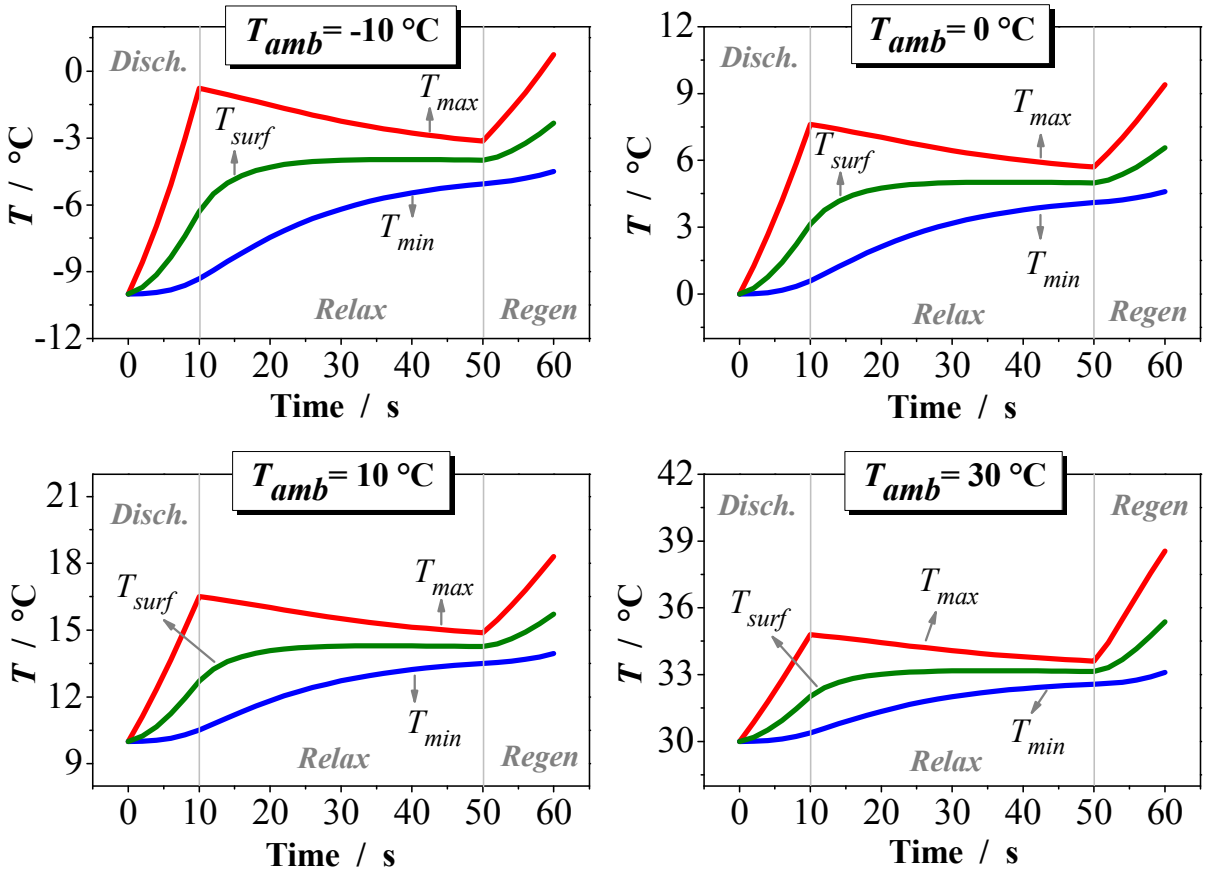

Figure 7.15: Cell temperature profiles resulted from simulations carried out using HPPC test profile and horizontal coupling method.

This can be explained by the fact that during discharge and regen phases, due to very high currents, the amount of generated heat greatly exceeds that dissipated making the cell temperature to rise sharply. During relaxation phase, the accumulated heat slowly dissipates from within the cell to the cell surface through conduction and from the cell surface to the environment it through convection and radiation. That makes the cell interior hotter than that of the cell surface. Hence during relaxation phase with no further heat being generated within the cell, the accumulated heat dissipates slowly thus making T_{max} to drops steadily. Since heat reaching the cell surface immediately dissipates to the surroundings, T_{sur} remains almost constant during relaxation phase. T_{sur} remains constant until no further heat is produced by discharge or regen. Since T_{min} is still lower than T_{max} and T_{sur}, heat still flows from comparatively hot surroundings to the point of lowest temperature (T_{min}), hence T_{min} keeps increasing even during the relaxation phase.

I) Cell potential

Figure 7.16*a* shows variation in cell voltage as a function of time during discharge, relax, and regen phases at different operating temperatures. A higher drop in potential with a steeper profile at lower ambient temperature during discharge phase is observed as compared to that at higher ambient temperature. That is due to higher polarization caused by lower diffusion and ionic conductivity at lower operating temperatures as discussed in section 7.2.2 and section 5.2.2.

In simulation test a start SOC of 100 % has been used that drops to about 94 % and remains intact during relaxation phase. During constant current simulations (section 7.2.1) upper CoV limit was set to 3.8 V but in order to analyze complete pulse cycle (till end of regen phase), a value of 4.2 V for upper CoV was used in HPPC test simulations. 3.8 V CoV limit is indicated in Figure 7.16*a* by a grey line. It can be seen that only at T_{amb} = 30 °C, regen phase is completed within 3.8 V limit. In all other cases, regen potential exceeds 3.8 V. Hence it seems more appropriate to start with rather a lower SOC. A more detailed study with different starting SOCs is planned for future.

II) Power deliverance

Power output of a battery is of prime importance in electrically powered vehicle systems. Conventionally lithium-ion batteries have higher energy but offer low power. Contrarily nanophosphate technology (section 4.2.1, Figure 4.2) adopted in 26650 cell is claimed to offer consistent power over an extended range of SOC [84]. Since most lithium-ion batteries compromise power output at low ambient temperatures and SOCs, it is important to study the power deliverance capabilities of 26650 cell at different operating temperatures and SOCs especially under high current demands as recommended in HPPC test.

Figure 7.16*b* includes power deliverance profile of 26650 cell during a high current pulse as per the HPPC test profile (Figure 7.13). It can be seen that at T_{amb} = -10 °C, lower power is delivered that drops sharply whereas at higher T_{amb}, delivered power is higher with a stable profile. It can also be seen that at higher T_{amb} (30 °C), higher power is delivered during discharge phase and lower power has to be added to the system during the regen phase. This implies that higher operating temperature (between 10 °C – 50 °C) favor the efficient power deliverance during high discharge pulses as encountered during acceleration in electric propulsion systems. Higher power deliverance during high current pulses at higher operating temperatures can be explained by the fact that due to lower polarization at higher T_{amb}, a flatter discharge curve results implying minimum loss in capacity. Hence, a stable voltage during a high current pulse gives rise to a stable power deliverance profile.

Pulse power profiles presented in Figure 7.16*b* correspond to simulations carried out at 100 % starting SOC (fully charged state). As SOC significantly influence power output of a battery, HPPC test has also been simulated using different starting SOCs at two different ambient temperatures (-10 °C and 20 °C). Resulting discharge and regen power deliverance profiles are presented in Figure 7.17. In Figure 7.17*a* and Figure 7.17*b*, cell power is plotted as function of time, for different starting SOCs, at T_{amb} = -10 °C and T_{amb} =20 °C respectively.

It is obvious that at T_{amb} = -10 °C, discharge power is lower than the regen power whereas it is slightly higher at T_{amb} = 20 °C. This implies that more power is delivered at higher operating temperatures. It can also be noticed that power curves appear steeper at T_{amb} = -10 °C and flatter at T_{amb} = 20 °C implying a more consistent power deliverance at higher operating temperatures. This is because of higher potential change (polarization) at lower operating temperatures. Except

for ending up in different slopes, discharge power profiles, at T_{amb} = -10 °C and 20 °C, vary in a similar way in response to change in starting SOC (from 100 % to 20 %). That means starting SOC influence the power profiles more or less regardless of operating temperature.

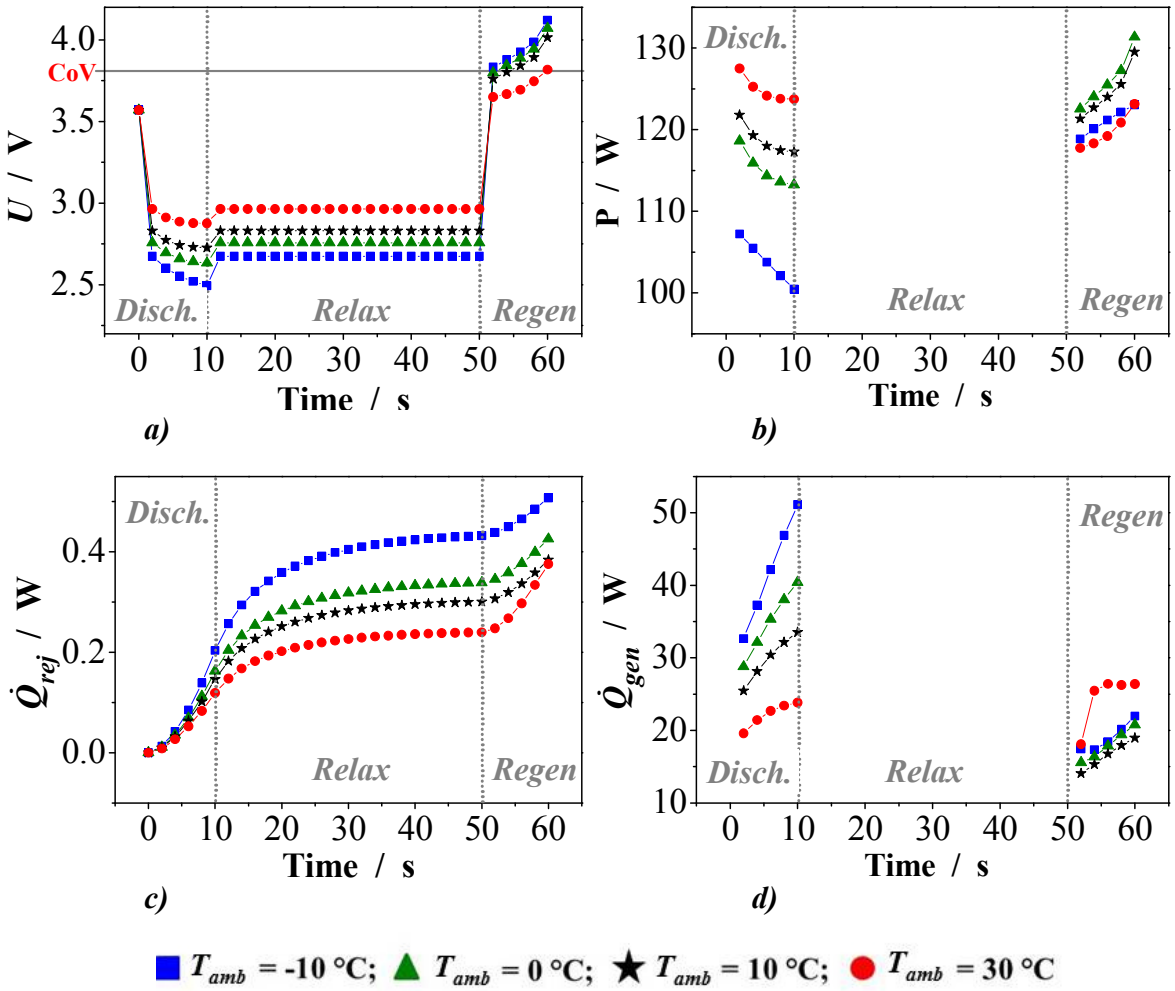

Figure 7.16: Derived quantities from HPPC test simulations using horizontal coupling method. Variation in ***a)*** cell potential; ***b)*** power deliverance; ***c)*** heat generation rate; and ***d)*** heat dissipation rate as a function of time during discharge, relaxation, and regen phases.

Upper CoV set by A123 Systems Inc., the manufacturer of 26650 cell is 3.8 V [91]. But in HPPC test simulations, the upper CoV limit has artificially been increased to 4.2 V. Because in most cases during the regen phase, 3.8 V upper limit is reached well before 10 seconds pulse

completion time producing incomplete profiles. In Figure 7.17, 3.8 V limit is marked by red line and it can be seen that at T_{amb}= -10 °C almost all regen power profiles exceeds 3.8 V limit. It can also be seen that increasing the upper CoV limit increases power output of the regen phase.

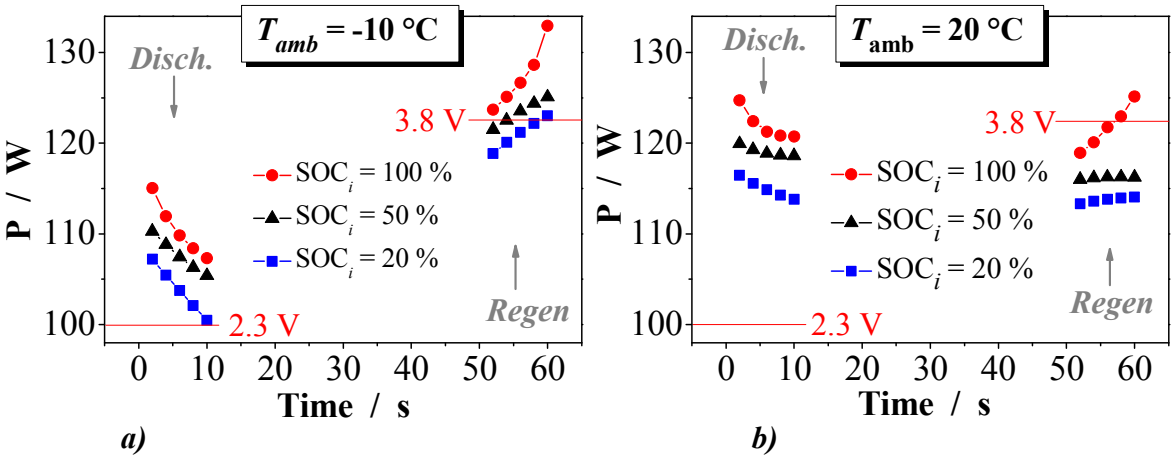

Figure 7.17: Power deliverance profiles during discharge and regen phases as function of time at different starting SOCs and operating temperatures obtained from simulations carried out as per HPPC test criteria.

From above discussion it can be concluded that in all the cases, cell power capabilities compromised at lower operating temperature and lower starting SOCs but effect of T_{amb} is more pronounced as compared to starting SOC. Though T_{amb} and starting SOC affect power deliverance capabilities of 26650 cell but it remains reasonably within acceptable limits. That suggests that 26650 cell can function efficiently at wider useable energy (SOC) and operating temperature windows without significantly compromising power deliverance capabilities which is the most sought after characteristic in case of EVs and HEVs.

III) Heat generation rate

Heat generation and heat dissipation profiles at different operating temperatures are shown in Figure 7.16*c* and Figure 7.16*d* respectively. It is quite clear that at lower T_{amb}, more heat is generated and a steeper $\dot{Q}_{gen}$ profile is resulted, whereas, at higher T_{amb}, lesser heat is generated with a less steep $\dot{Q}_{gen}$ profile. Higher polarization at lower operating temperatures causes more

heat to be generated resulting in a higher cell temperature as has already been discussed in section 7.2.2.

IV) Heat dissipation rate

Higher is the heat generation rate, more the heat dissipates. This is because higher heat generation within the cell creates higher gradients between the cell interior and the cell outer surface. This makes more heat to flow from a point of higher temperature (within the cell) to that of the lower temperature (surroundings). Section 7.2.2 can be referred for further details and discussion. It has been observed that at as temperature increases, the percentage $\dot{Q}_{rej,\ con}$ of the dissipated heat decreases whereas that of $\dot{Q}_{rej,\ rad}$ increases as can be seen in Figure 7.17. This is because radiation has higher temperature dependence as compared to convection as discussed in sections 3.1.2 and section 3.1.3 (Equation 3.9 and Equation 3.11).

7.2.4 SEI characterization

As discussed in section 2.7.2 that when lithium-ion battery is initially charged, a passive protective layer is formed at the anode active material surface which acts as a barrier to prevent the transfer of electrons from anode active material surface to the bulk of electrolyte thus inhibiting the exothermic side reactions. Higher temperature significantly reduces the stability of SEI thus triggering exothermic side reactions.

N. Tanaka and W.G. Bessler [127] modeled exothermic reactions taking place at the SEI in 26650 cell while in idle mode (self-heating). They used 1D model to simulate exothermic reactions between SEI and ethylene carbonate (EC) solvent as well as between cathode material and gaseous decomposition products at T_{amb} = 127 °C. Heat generation data produced in the above mentioned model has been used to produce a multi-segmented fit (Appendix A). The fitted data have been then used as input volumetric heat generation rate for 3D heat transfer model developed in section 4.4 through vertical coupling method (section 4.6.1). Simulations have been carried out using three different values of heat transfer coefficient i.e. h_f = 7, 55, and 200 W/(m^2·K) to investigate the effect of cooling on cell temperature resulting from self-heating at elevated temperatures.

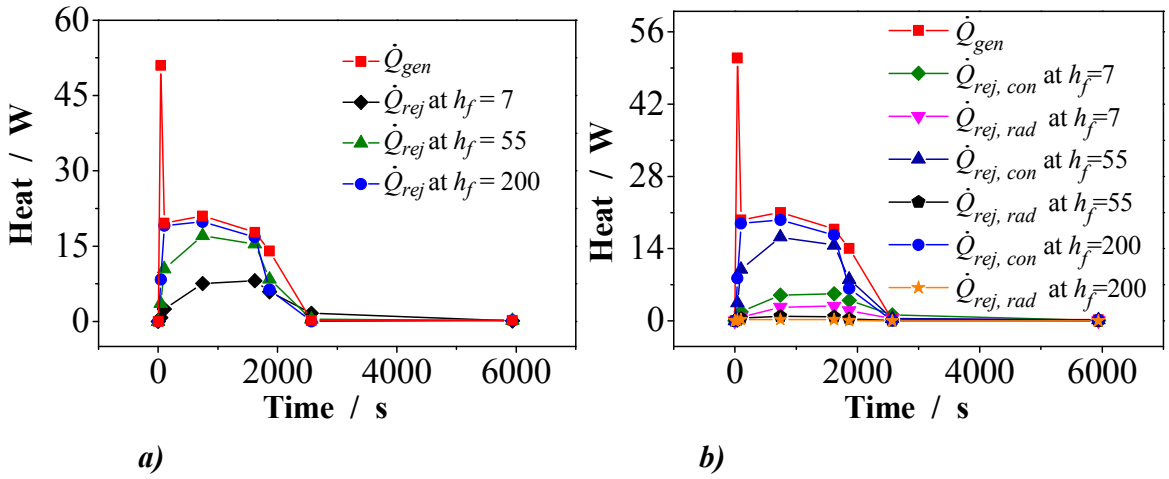

Figure 7.18: *a)* Transient profiles of overall heat generation rate ($\dot{Q}_{gen}$) and $\dot{Q}_{rej}$ at h_f = 7, 55, and 200 W/(m^2·K); and *b)* overall heat generation rate ($\dot{Q}_{gen}$) and heat rejected due to convection ($\dot{Q}_{rej, con}$) and radiation ($\dot{Q}_{rej, rad}$) at h_f = 7, 55, and 200 W/(m^2·K).

Simulation results are presented in Figure 7.18 and Figure 7.19. Fitted heat generation curve along with simulated heat dissipation profiles corresponding to different heat transfer coefficient values are presented in Figure 7.18. T_{max} and T_{min} as well as 3D temperature contours obtained from simulations at different heat transfer coefficients are presented in Figure 7.19.

N. Tanaka and W.G. Bessler [127] found that no self-heating has been observed at T_{amb} = 90 °C whereas at T_{amb} = 100 °C, heating is too slow to cause an onset to thermal runaway. A sharp peak in $\dot{Q}_{gen}$, shown in Figure 7.18, has been observed at T_{amb} = 127 °C. With T_{amb} between 137 °C and 252 °C, SEI alternately forms and decomposes giving rise to an almost constant rate of heat generation. At T_{amb}= 252 °C SEI gives away completely thereby stopping the exothermic reaction and thus heat generation. It has also been found that heat generation due to SEI exothermic reactions slowly dissipates bringing the cell temperature back to T_{amb} without causing any risk in itself. But it could indirectly contribute to the onset to thermal runaway by triggering other side reactions as mentioned in section 2.7.2.

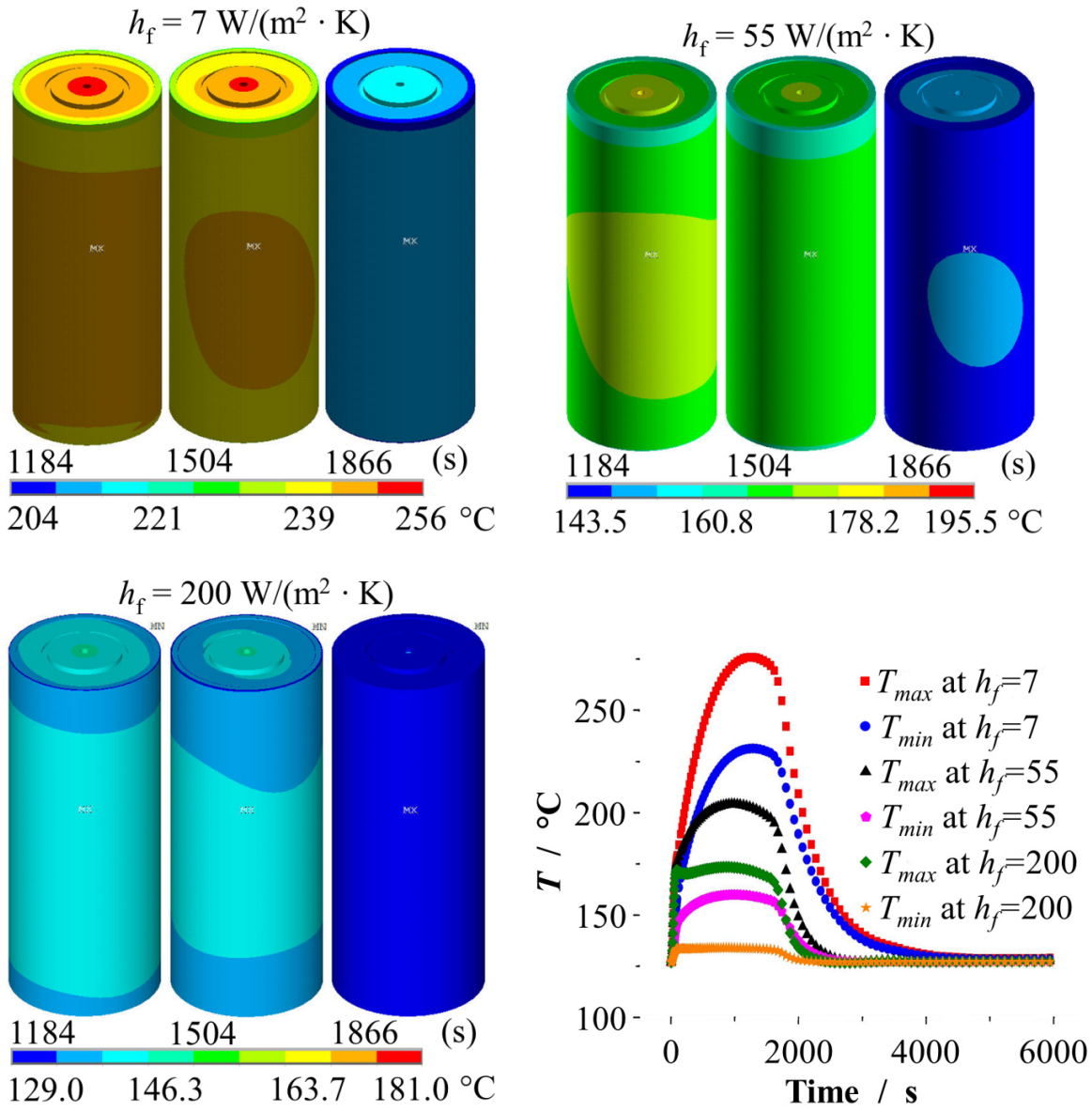

Figure 7.19: Transient 2D plots of T_{max} and T_{min} at different values of film coefficient (lower right) and 3D temperature contours on full cell model.

From Figure 7.19, it can be seen that under non-operating conditions and in the absence of abuse event, cell temperature drops back to T_{amb} = 127 °C spontaneously at all values of h_f. At h_f = 7 W/(m^2·K), it takes about 4500 seconds for the cell temperature to drop back to 127 °C (T_{amb}) as compared to about 2500 seconds at h_f = 200 W/(m^2·K). It can also be seen that except for h_f = 7 W/(m^2·K), at all other values of heat transfer coefficient, cell temperature stays well

below 252 ° C mark. Beyond 252 °C, exothermic side reactions could cause an exponential increase in heat generation rate that could trigger thermal runaway leading to fire or explosion. This is the main concern towards wide application of lithium-ion batteries in electric propulsion. Hence it is essential to keep the cell temperature well under control to avoid the worst case scenario by any possible means. This can be achieved thorough, for example, circulating cooling fluid (forced convection) at the cell exteriors or using phase change material (PCM) planned for future work.

7.3 Inference and outlook

In view of the results obtained from experimental measurements, detailed simulations, and discussion presented above and in the preceding chapters, some important conclusions have been drawn which are presented herein. In addition certain recommendations regarding the improvement of cell performance have also been made. Finally, a brief account of the planned future work regarding the extension of work carried out in this study has been given.

7.3.1 Conclusions

Experimental findings lead to the conclusions that at higher operating temperatures and lower C rates, cell temperature tends to be more uniform in distribution. Moreover lower operating temperature and higher applied currrents erode cell capacity causing reduction in power output efficiency of the cell. Discharge data showed that at T_{amb} < 0 °C, only a slight deterioration in capacity has been observed implying that 26650 cell is capable of delivering a sustained power over a wide operating temperature window ranging from -10 °C, 50 °C. Optimum operating temperature window for 26650 cell has been found to be between 10 °C and 50 °C. It should be noted that T_{amb} > 50 °C has not been investigated in this work. At 50 % SOC, 26650 cell exhibited a very small drop in OCV over an operating temperature window of -10 °C to 50 °C. 26650 cell demonstrated a good multiple cycling efficiency at $T_{amb} \geq$ 10 °C upto 5C load and at $T_{amb} \geq$ 20 °C till 10C load.

Overall simulation results have been found in good agreement with the experimental findings. Operating temperature is found to have more pronounced effect on spatial variations within the

cell than applied current. At 10 °C or higher operating temperatures and 1C or lower applied currents, spatial variations in heat generation rates within the jellyroll are too small to be ignored and less rigorous vertical coupling method that accounts only for temporal variations can be employed. Whereas at 2C or higher currents and lower than 10 °C operating temperature, a more rigorous horizontal coupling method needs to be employed costing higher computation time and resources. Higher currents combined with lower operating temperatures make spatial variations too dominant to be ignored thus making the horizontal coupling technique the best choice to predict accurate thermal behavior of the cell. Horizontal coupling method has shown promise in predicting dynamic thermal behavior of 26650 cell. For comperative analysis, direct input method sufficed and found to be swift and prompt carrying out stationary as well as transient simulations.

Geometrical design parameter variation results suggested that increasing CC thickness does not contribute to any improvement in thermal efficiency of the cell. Although increasing CW thickness from 0.5 mm to 2 mm does improve thermal efficiency of the cell to a certain extent but the impact is too small to compensate for the added weight and cost. A balance has to be traded amongst thermal efficiency as a function of geometrical design parameters and cost while designing a cell.

Cell design variation results revealed that flat cell configuration has been found to be thermally more efficient than cylindrical and prismatic cells. But despite this advantage flat cell lacks mechanical stability and can suffer swelling due to absence of proper venting mechanism. The choice therfore has to be made depending on the needs and specifics of application.

Power deliverance profiles of 26650 cell obtained from simulation tests carried out at different starting SOCs and operating temperatures as per HPPC set criteria [126] elucidated that power deliverance capabilities of 26650 cell compromised to some extent at lower operating temperatures and lower starting SOCs. But effect of T_{amb} is more pronounced as compared to that of the starting SOC. Nevertheless in both the cases the drop in power output remains well within the acceptable limits. This suggests that 26650 cell can function over a wider useable energy and operating temperature windows without significantly compromising power deliverance capabilities. This very characteristic makes 26650 cell well suited for electric propulsion systems.

SEI side reactions in 26650 cell while in idle mode at T_{amb} = 127 °C have been simulated and results showed that the cell temperature rises steeply reaching its peak value in about 1100

seconds. It then drops back to T_{amb} in a time depending on the value of film coefficient used (7 to 200 W/(m^2·K). This is because the heat generated due to SEI exothermic reactions slowly dissipates bringing the cell temperature back to T_{amb} without causing any risk in itself. But it could indirectly contribute to the onset to thermal runaway by triggering other side reactions. It has been found that under non-operating conditions and in the absence of abuse event, cell temperature spontaneously drops back to the surrounding temperature thus causing no harm to the cell.

7.3.2 Recommendations

Outcomes of this study can be used as a reference to optimize or further improve the cell design. While operating at elevated temperatures or in warm climates it is required to maintain the cell temperature within the safe operating limits. It is, therefore, essential to keep the cell temperature well under control to avoid the worst case scenario by any possible means. This can be achieved thorough, for example, circulating cooling fluid at the cell exteriors or using phase change material (PCM).

A thorough experimental and numerical investigation into 26650 cell's thermal performance showed that the cell performed well at temperatures simulating warm climates i.e. T_{amb} = 50 °C under moderate to high current loads i.e. 1C to 10C. But J. Dahn [89] showed that cycling a $LiFePO_4$/Graphite cell from A123 at 55 °C and C/56 current causes a catastrophic premature capacity loss amounting to ~ 60 % in just ~ 130 cycles. This possibly is caused by an increased rate of parasitic side reactions at higher temperature (55 °C) that get ample time to take place at slow cycling. These parasitic reactions get suppressed during fast cycling due mainly to not having enough time to occur. Hence this aspect needs require further investigation.

7.3.3 Future prospects

The model presented in chapter 4 has shown promise in predicting thermal performance of the selected cells by capturing complexities of electrochemical mechanisms taking place on micro level and details of the cell domain on a 3D level. The model is fully capable of handling spatial as well as temporal variations in parallel making it suitable to predict dynamic behavior of the

cells. Results suggested that at high currents and subzero temperatures, model has a room for further improvement. It is intended to improve electrochemical HG model by further refining the model parameters. Circumferential variations in heat generation that has been ignored in present work are be included next. For OCV measurements, longer relaxation periods need to be used between consecutive temperature steps (i.e. T_{amb} = -10 °C, 0 °C, 10 °C, 20 °C, 30°C, 40°C, and 50 °C) for the OCV to reach complete steady state values. It is planned to further investigate the SEI decomposition and parasitic side reactions under operating and non-operating modes and higher operating temperatures using a mixture of solvents.

Extension of 3D EC-T model to a module level using three-way coupling and include actual flow simulations using CFD tools is planned as well. Moreover module cooling simulations using phase change material (PCM) is also being considered.

Appendix A

Heat generation by SEI reactions

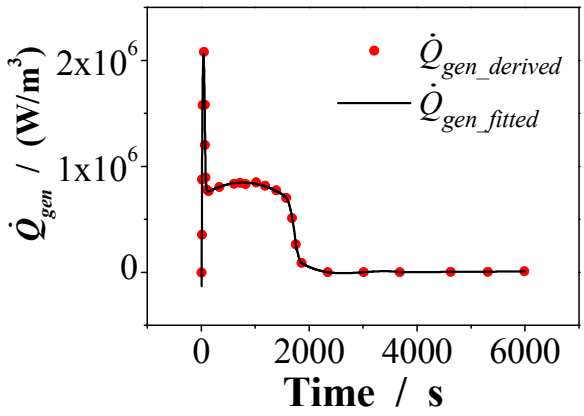

Figure A.1: Heat generation profile due to exothermic reactions taking place at the SEI derived from [127, 132] and a multi-segmented fit used as input in 3D heat transfer simulations of 26650 cell.

Appendix B

Thermal and physical parameterization

Accurate knowledge of model parameters forms the basis of any mathematical model. Thermal properties like anisotropic thermal conductivity and specific heat capacity and physical properties like density are the key parameters required for transient thermal simulations of lithium-ion batteries. These parameters can be measured experimentally, evaluated using modeling and simulation techniques, or using the information derived from authentic literature. The choice depends on the availability of experimental and simulation facilities and that of the primary data. In present work, experimental, simulation, and volume fractionation methods were used for parameter evaluation of different configurations of lithium-ion batteries (cylindrical or flat). Detailed procedures for these methods are described in this chapter. Experimental and simulation methods emphasize on describing the basic procedure rather than producing specific results owing to the confidentiality issues. Nevertheless the parameters evaluated using volume fractionation method are presented in this chapter and employed in the heat transfer model (section 4.4, Table 4.3).

B.1 Volume fractionation method

Generally thermal and physical properties of individual materials constituting lithium-ion batteries are comparatively easy to find in the published literature or to measure experimentally compared to properties of the cell or jellyroll as composite entities. Individual material properties

derived from literature are used to evaluate thermal and physical properties of jellyroll as a composite material. The primary data used for parameterization is presented in Table B.1. Each parameter presented in Table B.1 is multiplied by the volume fractions of corresponding component (material) constituting jellyroll. Multiples of all the material parameters are then summed up to give the overall value of that specific parameter. Thermal conductivity, specific heat, and density of the 26650 cell jellyroll used in the heat transfer model are calculated using volume fraction technique while that of the VL 7P cell are directly obtained from literature (see section 4.4, Table 4.3).

Table B.1: Thermal and physical parameters of individual components constituting 26650 battery

Component	k **(W/(m·K))**	c_P **(J/(kg·K))**	ρ **(kg/m^3)**	**Source**
Cu current collector	401		8900	[110]
		385		[108]
Al current collector	237		2700	[110]
		903		[108]
Cathode	1.48	800		[110]
Anode	1.04	800		[110]
Separator	1	800	1200	[110]
$LiFePO_4$			3580	[109]
LiC_6			2260	[109]
Electrolyte	0.6	2055	1130	[110]
Cell casing	14	460	7500	[110]

B.1.1 Thermal conductivity

Thermal conductivity values produced by this method represents the axial component (k_z) because in a direction parallel to the electrode layers (axial) thermal conductivity of each

component is independent of that of the other. This is because each individual component i.e. current collectors, electrodes, and separator do not cross each other's heat flow path as they do in a direction perpendicular (radial) to the layers. From section 4.2.1 (Figure 4.4) we know that thickness of one repeat unit of 26650 cell is 155 microns. Since the remaining dimensions of all the components i.e. anode, cathode, separator, and current collectors are the same, component thicknesses alone can used to calculate volumes fractions. Volume fraction of each component is obtained by dividing thickness by 155 microns which is the overall thickness of one repeat unit:

Volume fraction of copper current collector,	$V_{Cu} = 15/2/155$	$= 0.0484$
Volume fraction of aluminium current collector,	$V_{Al} = 25/2/155$	$= 0.0807$
Volume fraction of cathode active material,	$V_{ca} = 79.5/155$	$= 0.5129$
Volume fraction of anode active material,	$V_{an} = 35.5/155$	$= 0.2290$
Volume fraction of separator,	$V_{se} = 20/155$	$= 0.1290$

Using component thermal conductivities from Table B.1, we can find the contribution of each component to the jellyroll thermal conductivity by:

$$k_{mat,\,JR,} = k_{mat} \times V_{mat}$$

Where $k_{mat,\,JR}$ is thermal conductivity contribution of a specific component e.g. Cu, Al, k_{mat} is actual thermal conductivity of material, and V_{mat} is the volume fraction of individual material in the jellyroll. Hence;

Thermal conductivity of copper,	$k_{Cu} = 401 \times V_{Cu}$	$= 19.25$ W/(m·K)
Thermal conductivity of aluminium,	$k_{Al} = 237 \times V_{Al}$	$= 19.13$ W/(m·K)
Thermal conductivity of anode,	$k_{an} = 1.04 \times V_{an}$	$= 0.24$ W/(m·K)
Thermal conductivity of cathode,	$k_{ca} = 1.48 \times V_{ca}$	$= 0.76$ W/(m·K)
Thermal conductivity of anode,	$k_{an} = 1.04 \times V_{an}$	$= 0.24$ W/(m·K)
Thermal conductivity of separator,	$k_{se} = 1 \times V_{se}$	$= 0.13$ W/(m·K)

It should be noted that effect of voids present in the anode and cathode active materials is ignored while calculating k_{an} and k_{ca}. Now thermal conductivity of jellyroll in a direction parallel to the electrode layers can be obtained by taking the sum of individual contributions.

Thermal conductivity of the jellyroll, $k_{JR} = k_{Cu} + k_{Al} + k_{an} + k_{an} + k_{se}$

$k_{JR} = 39.66$ W/(m·K)

As mentioned above, this value is used in the heat transfer model of 26650 cell as axial component of thermal conductivity k_z. The radial component k_r was directly derived from literature [72].

$$\boldsymbol{k_{z,\,26650} = 39.66 \text{ W/(m·K)}}$$

$$\boldsymbol{k_{r,\,26650} = 1.02 \text{ W/(m·K)}}$$

Thermal conductivity of VL 7P cell was derived from literature [94].

$$\boldsymbol{k_{z,\,VL7P} = 27.00 \text{ W/(m·K)}}$$

$$\boldsymbol{k_{r,\,VL7P} = 0.80 \text{ W/(m·K)}}$$

B.1.2 Density

Density of the jellyroll of 26650 cell can be evaluated using data from Table B.1. Densities of individual components constituting jellyroll are calculated by multiplying the actual density of a component by its volume fraction in the jellyroll:

$$\rho_{\,mat,\,JR,} = \rho_{mat} \times V_{mat}$$

Where $\rho_{mat,\,JR}$ is density of a specific component e.g. Cu, Al, ρ_{mat} is actual density of material, and V_{mat} is the volume fraction of individual material in the jellyroll. Hence;

Density of copper in jellyroll, $\rho_{Cu} = 8900 \times V_{Cu} = 430.76$ kg/m^3

Density of aluminium in jellyroll, $\rho_{Al} = 2700 \times V_{Al} = 217.89$ kg/m^3

Electrode active materials ($LiFePO_4$, LiC_6) and separator contain empty voids or pores that can significantly impact the calculations. Hence the effect of pores has to be accounted for while calculating the density of jellyroll. As the porosity or void fraction of anode, separator, and cathode used in the electrochemical heat generation model is 0.33, 0.50, and 0.27 respectively (see Table 4.4), density of the jellyroll should be corrected for empty spaces. In the actual batteries during operation these voids are occupied by the electrolyte which also has influence on the parameters but for now the effect of electrolyte is ignored in these calculations due to non-

availability of authentic data on thermo-physical properties of the electrolyte. Hence component density corrected for porosity is calculated as follows:

$$\rho_{mat,JR,} = \rho_{mat} \times V_{mat} \times (1 - \varepsilon)$$

Density of anode (LiC_6) in JR, $\rho_{an} = 2260 \times V_{an} \times (1 - 0.33)$

$\rho_{an} = 346.75$ kg/m^3

Density of cathode ($LiFePO_4$) in JR, $\rho_{ca} = 3580 \times V_{ca} \times (1 - 0.27)$

$\rho_{ca} = 1340.41$ kg/m^3

Density of separator in JR, $\rho_{se} = 1200 \times V_{se} \times (1 - 0.50)$

$\rho_{se} = 77.40$ kg/m^3

Density of the jellyroll, $\rho_{JR} = \rho_{Cu} + \rho_{Al} + \rho_{an} + \rho_{an} + \rho_{se} = 2412.8$ kg/m^3

$$\boldsymbol{\rho_{26650} = 2412.8 \text{ kg/m}^3}$$

Density of VL 7P jellyroll is obtained from [94]:

$$\boldsymbol{\rho_{VL7P} = 1947 \text{ kg/m}^3}$$

B.1.3 Specific heat

Specific heat is calculated by dividing the volumetric heat capacities of the two cells by the corresponding densities. Volumetric heat capacities are obtained from literature [72, 94] whereas densities calculated in the previous section (section B.1.2) are used.

Volumetric heat capacity of VL 7P jellyroll, $c_{P,VL7P} = 2.04 \times 10^6$ J/(m^3·K)

Specific heat of VL 7P jellyroll, $c_{P,VL7P} = c_{VL7P} / \rho_{VL7P}$

$c_{P,VL7P} = 1047.77$ J/(kg·K)

$$\boldsymbol{c_{P,VL7P} = 1047.77 \text{ J/(kg·K)}}$$

Volumetric heat capacity of 26650 jellyroll, $c_{26650} = 1.85 \times 10^6$ J/(m^3·K)

Specific heat of 26650 jellyroll, $c_{P,26650} = c_{26650} / \rho_{26650}$

$c_{P,26650} = 766.74$ J/(kg·K)

$$\boldsymbol{c_{P,26650} = 766.74 \text{ J/(kg·K)}}$$

B.2 Experimental techniques

The method described in this section has originally been developed by C. Merten's group at the University of Stuttgart, Institute of Chemical Process Technology (ICVT), Department of Equipment Design and Construction, Stuttgart, Germany. This test method is based on the ASTM (Designation: E 1225-04) standard for the determination of thermal conductivity of homogeneous-opaque solids. This test method is suitable for materials with effective thermal conductivities in the approximate range $0.2 < k < 200$ W/(m·K) over the approximate temperature range of 90 K to 1300 K. It can be used outside these ranges with decreased accuracy [111]. Procedures for the determination of anisotropic thermal conductivity, specific heat, and density of flat and spirally wound jellyrolls are presented in this section.

B.2.1 Sample preparation

Because of safety reasons, this test method requires dry or electrolyte free electrodes for most of the electrolytes are toxic and inflammable. Dry electrodes can either be obtained directly from the manufacturer or by leaving the wet electrodes for drying. For that purpose the cell has to be opened to unpack the electrolyte laden electrodes. Proper care should be exercised while opening the cell. Electrodes should be expected to take four to six weeks until most of the electrolyte dries away. This work is restricted to flat cell configuration due to availability of dry electrodes. But the same procedure can be used for other configurations with some modifications.

This test method requires the specimen to be in cylindrical shape. In case of a cylindrical configuration, the specimen for measuring axial component of thermal conductivity k_z is prepared by cutting through a piece out of the jellyroll as shown in Figure B.1. For radial measurements, the basic assembly unit of the experimental setup shown in Figure B.10 has to be modified.

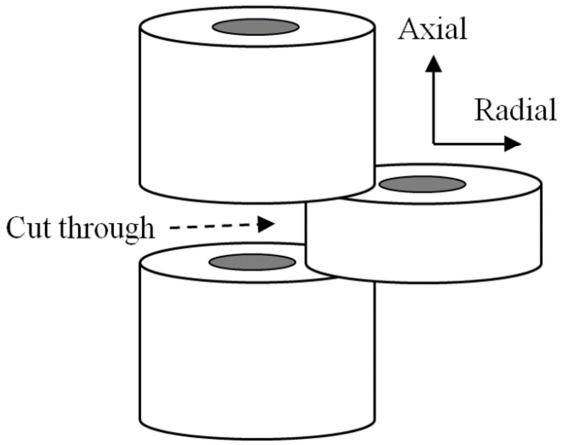

Figure B.1: Specimen preparation for a cylindrical cell for axial measurements.

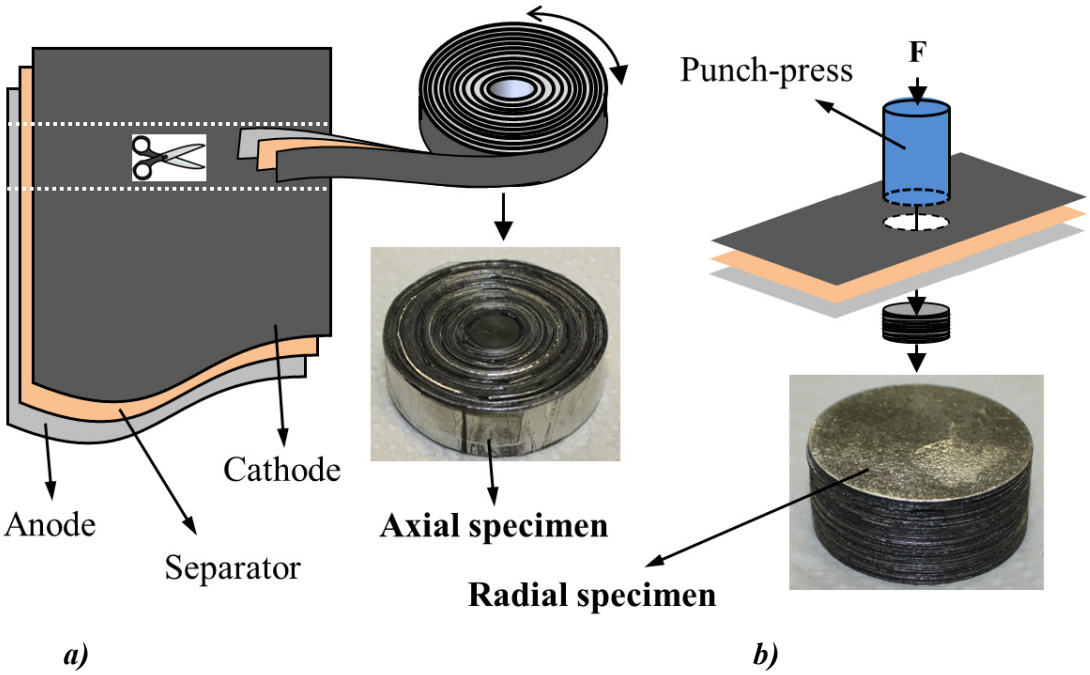

Figure B.2: Specimen preparation for flat cell axial and radial measurements of thermal conductivity.

In case of a flat cell, two different cylindrical specimens have to be prepared to measure thermal conductivity across the plane (axial) and across the electrode layers (radial). Any of the two specimens can be used for heat capacity and density measurements. Procedure used to prepare specimen is described below:

Specimen for axial measurements was prepared by cutting out an anode-separator-cathode repeat unit in the form of rectangular strips, end-to-end joining the strips, and then rolling them over each other in spiral order to make up the required diameter as shown in Figure B.2*a*. The outer and inner diameters of the specimen used was 40 mm and 10 mm respectively, while the thickness of the specimen was kept between 10 mm and 15 mm. Specimen to measure radial component of thermal conductivity was prepared using a hollow cylindrical punch-press of 40 mm diameter to blank out circular sheets of anode-separator-cathode sequences and stacking them together to make up the optimum thickness of 10 – 15 mm as elucidated in Figure B.2*b*.

B.2.2 Standard reference material

Stainless steel AISI 304L was used as standard reference material for which thermal conductivity versus temperature data was employed instead of using a constant value as normally practiced. Thermal conductivity data in Table B.2 was derived from [112]. Standard reference probes used to measure axial and radial components of thermal conductivity are shown in Figure B.3.

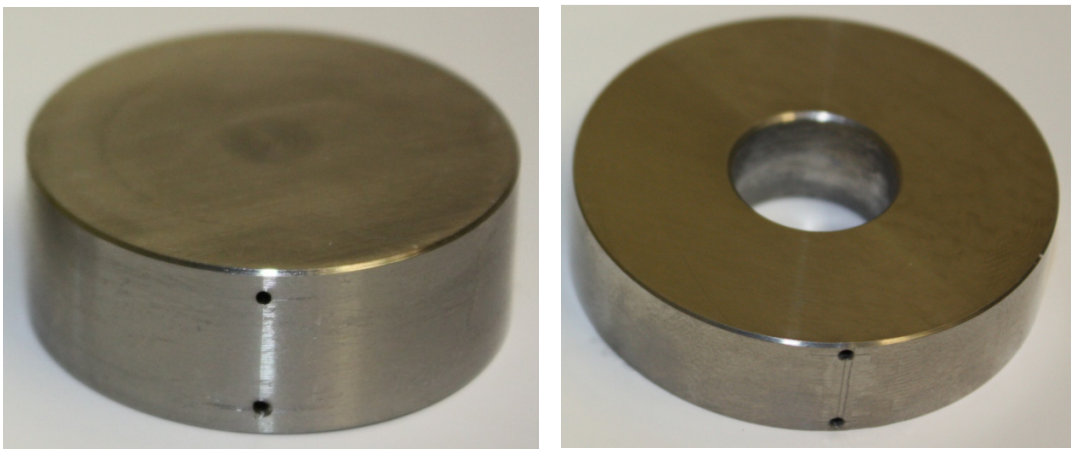

Figure B.3: AISI 304L stainless steel reference probes used for axial (right) and radial (left) measurements.

Average of the two temperatures recorded at the specimen sensor locations i.e. *T4* and *T5* (Figure B.9) was used as reference for the temperature locations. $\boldsymbol{T_{ref}}$ *and* $\boldsymbol{k_{Ref}}$ were calculated using equation (B.1) and equation (B.2) respectively. Equation (B.2) was obtained from a linear fit (Figure B.4) to the thermal conductivity versus temperature data presented in Table B.2.

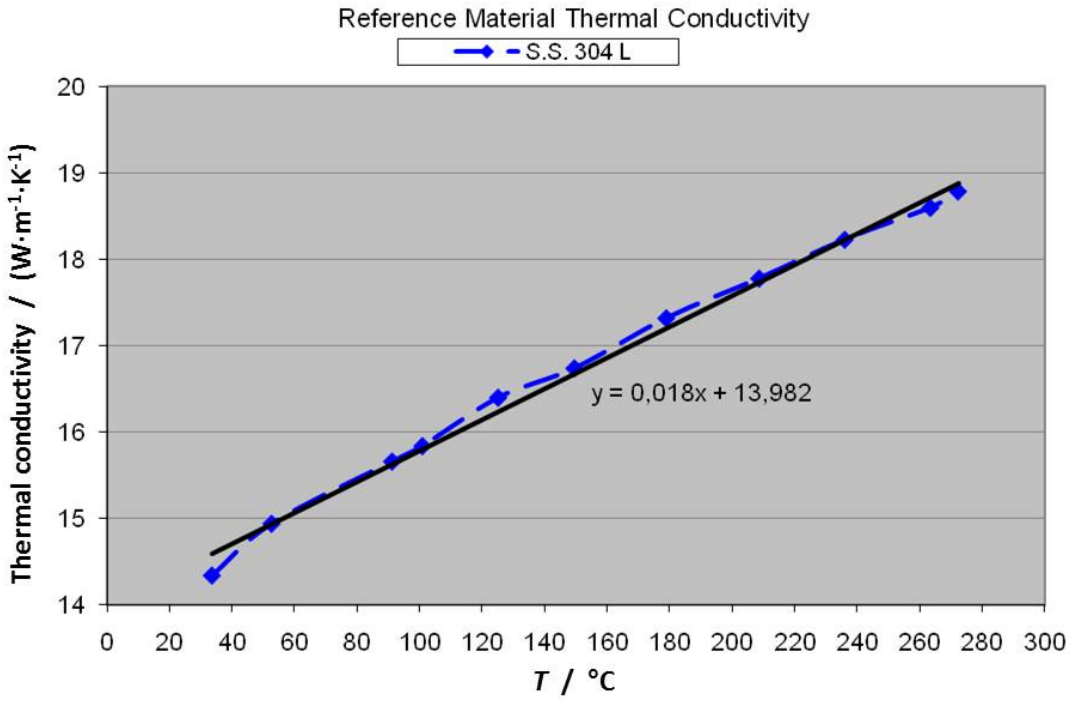

Figure B.4: Linear fit of stainless steel 304 L thermal conductivity data.

Table B.2: Thermal conductivity of stainless steel 304 L as a function of temperature [112]

Temperature (K)	**Temperature (°C)**	**Thermal Conductivity (W/(m·K))**
306.83	33.68	14.34
325.90	79.75	14.94
364.49	91.34	15.66
374.19	101.04	15.84

$$T_{ref} = (T4+T5)/2 \quad °C \quad (B.1)$$

$$k_{Ref} = 0.018\ T_{ref} + 13.982 \quad W/(m·K) \quad (B.2)$$

B.2.3 Wetting of specimens

Electrodes used in lithium-ion batteries contain micro pores that occupy significant part of the electrode volume. Dry electrodes in the absence of electrolyte trap air within the voids which could lead to erroneous results especially in case of radial specimen where trapped air crosses the heat flow path.

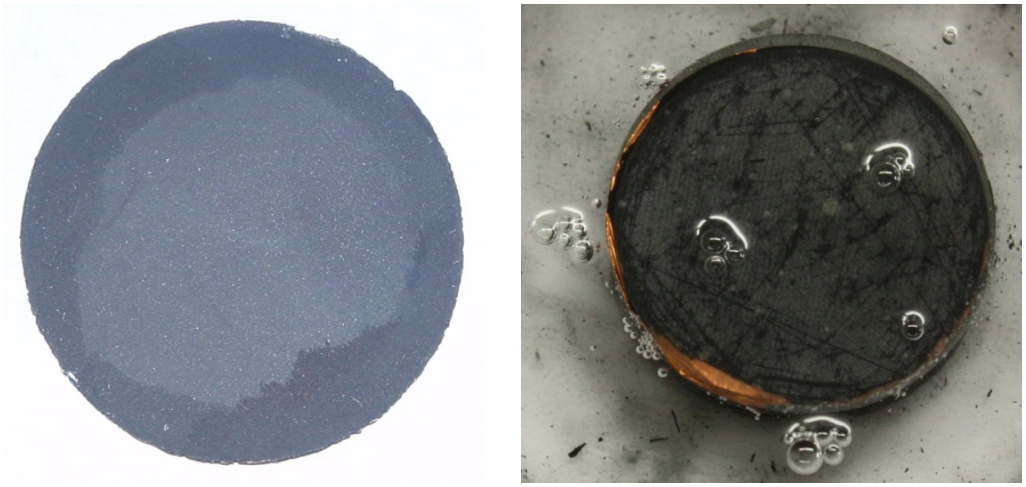

a) ***b)***

Figure B.5: *a)* Positive electrode after wetting under vacuum; *b)* Specimen immersed in low viscosity liquid paraffin to remove air and to simulate electrolyte.

To solve this problem low viscosity liquid paraffin was used to mirror the thermal effects of electrolyte. Liquid paraffin was used, firstly, because it is inert and safe to handle and secondly, its thermal properties are quite analogous to most of the organic solvents [113, 114, 115] used in lithium-ion batteries. Also as the thickness of electrode layers and separator is on the scale of micro-meters, effect of difference in thermal characteristics of actual electrolyte and liquid paraffin can justifiably be ignored. The main purpose of wetting is to expel the trapped air in electrode voids which can be done by partial or full wetting technique.

I) Partial wetting

Partial wetting was carried out by pressing the radial specimen using screw-press to remove part of the trapped air. Pressed specimen was then put under vacuum at about 50 °C. Small amount of paraffin oil was applied on the sides of the specimen so that it could fill the voids as air is removed under vacuum. Specimen was kept under negative pressure until no bubbles were seen originating from the sides of the specimen where paraffin oil was applied. This method was found to be lacking in fully expelling the trapped air. Wetting was found to be achieved only near the radial boundaries leaving most of the inner part dry as shown in Figure B.5*a*.

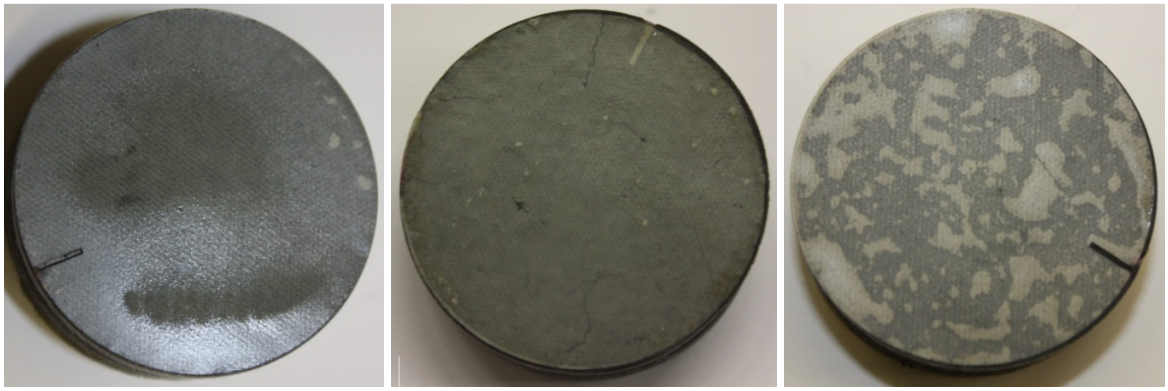

a) ***b)*** ***c)***

Figure B.6: Radial specimen in three different wetting states: *a)* over-wetted or excess oil state; *b)* properly wetted state; *c)* partially dried state.

II) Full wetting

Alternately the specimen was kept immersed in low viscosity paraffin oil until no bubbles were seen originating from the specimen indicating that all the air had been removed from the electrode sheets (Figure B.5*b*). The specimen was then carefully removed from the bath and pressed gently to remove the excess oil. It was then kept under pressure slightly higher than atmospheric pressure for 24 hours so that the oil gets absorbed in the pours. Immersion as well as drying time should be carefully adjusted so as to remove excess oil between the electrode sheets but to avoid drying of the specimen. Figure B.6 shows different states of oil penetration into the electrode-separator stack. Thermal conductivity as function of wetting time and amount of wetting agent remains open to further investigation.

Since air does not directly crosses the heat flow path air resistance in case of axial specimen shown in Figure B.7*a)* is not as significant as in case of radial specimen (Figure B.7*b*). It can be seen that the contact surface in case of axial specimen is not smooth enough to make good contact with the reference probes. To solve this problem thermally conductive silicon paste OMEGATHERM "201" was applied between the specimen and reference probes which effectively fills the voids and improves thermal contact [116].

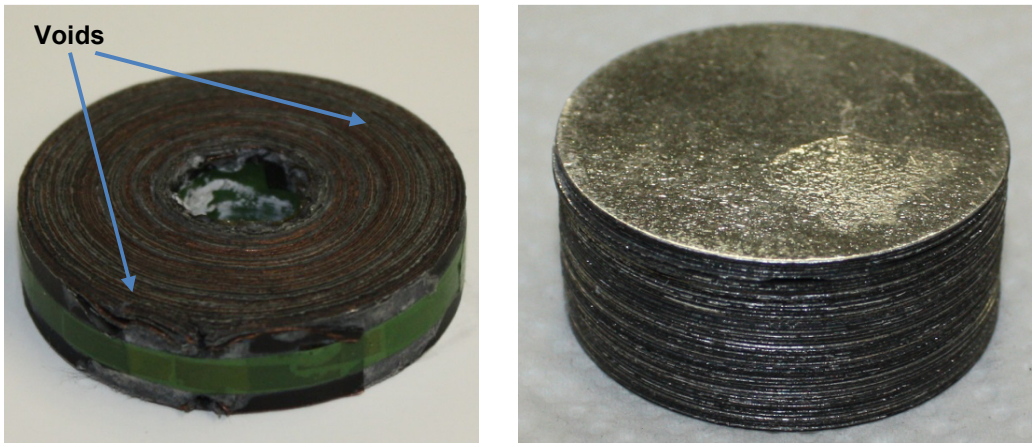

Figure B.7: Specimens used to measure *a)* axial and *b)* radial components of thermal conductivity.

B.2.4 Experimental setup and procedure

Experimental setup used for the measurements is shown in Figure B.8. It consists of a basic assembly unit attached to heating and cooling units, thermal sensor bank, and data acquisition system. Schematic of the basic assembly unit along with sensor locations is shown in the Figure B.9. Basic assembly unit with reference probes and the specimen is shown in Figure B.10.

The convention used in Figure B.9 is used in the subsequent calculations of thermal conductivity k_S. $T1$ through $T8$ represent the temperatures measured at different locations using fine wire T-type sensors from Omega Engineering Ltd. $X1$, $X2$, and $X3$ represent the distances between the corresponding sensor locations. k_{Ref} is the thermal conductivity of standard reference probes. Equation (B.3) is the basic equation used for the calculation of thermal conductivity (k_S) of the samples.

Experiment started by setting the thermocouples in place at the given locations (Figure B.9). Assembly unit was then insulated and heater and cooler temperature set points were adjusted at the required temperature values. Data continuously recorded in the data acquisition system until steady state is reached.

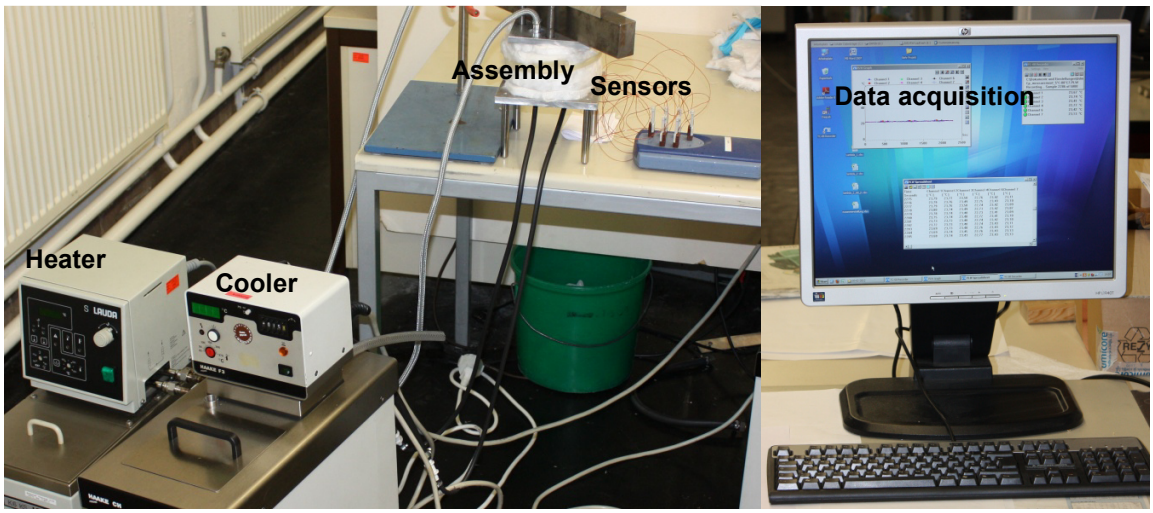

Figure B.8: Experimental setup used to measure thermal conductivity of cylindrical specimens.

B.2.5 Thermal conductivity

Steady state values of temperatures from sensor locations T2 through T7 (Figure B.9) along with separation between the sensors $X1$, $X2$, and $X3$ (Figure B.9) were plugged into Equation (B.3) below to find thermal conductivity k_S of the specimen.

$$k_S = \frac{X2}{T5-T4} \cdot \frac{k_{\mathrm{Re}f}}{2} \cdot \left(\frac{T3-T2}{X1} + \frac{T7-T6}{X3} \right) \qquad \text{(B.3)}$$

k_{Ref} was calculated using Equation B.2. Experiment was repeated by setting the heater and cooler at different temperatures. The range used for the heater and cooler set temperatures was from -20 °C to 80 °C. An inherent deviation exists in the results which was calculated using equation (B.4) through equation (B.8).

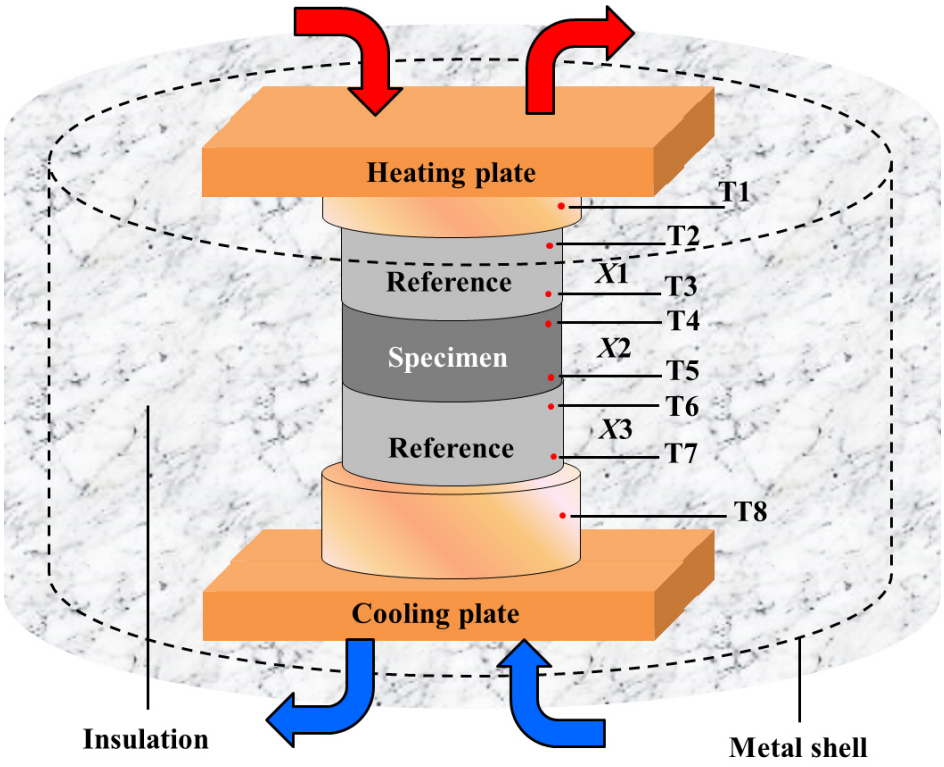

Figure B.9: Schematic of Comparative-Guarded-Longitudinal heat flow system showing locations of temperature sensors.

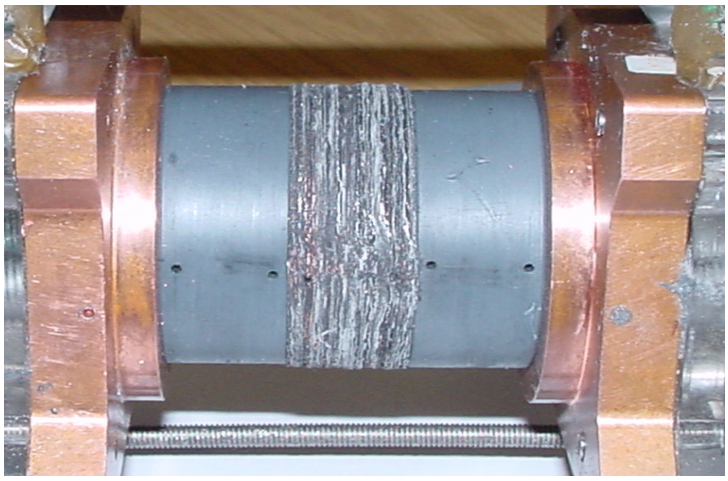

Figure B.10: Basic assembly unit used for thermal conductivity measurement.

Error estimation

$\boldsymbol{T_{ref}}$ [equation (B.1)], used to find $\boldsymbol{k_{Ref}}$ [equation (B.2)], was calculated by taking average of *T*4 and *T*5 whereas the representative temperatures for the two reference probes are *T*2, *T*3, *T*6 and *T*7. Hence an error is expected to be incorporated in the final value of thermal conductivity. This error was calculated using the following equation:

$$E_1 = \frac{k_{Ref,T_{Top}} - k_{Ref,T_{Bott}}}{k_{Ref,T_{Top}} + k_{Ref,T_{Bott}}} \cdot 100 \qquad [\%] \qquad \text{(B.4)}$$

Where, $T_{Top} = \frac{(T2+T3)}{2}$ and $T_{Bott} = \frac{(T6+T7)}{2}$ (B.5)

$k_{Ref,T_{Top}}$ and $k_{Ref,T_{Bott}}$ are the thermal conductivities of the reference material calculated at temperatures T_{Top} and T_{Bott} using equation (B.5).

The second source of error could be the fluctuation in sensor output temperatures which was calculated as:

$$E_2 = \frac{\frac{(k_{Sp,max} - k_{Sp,min})}{2}}{k_{Sp,Avg}} \cdot 100 \qquad [\%] \qquad \text{(B.6)}$$

Where,

$$k_{Sp,Avg} = \frac{(k_1 + k_2 + k_3)}{3} \qquad \text{(B.7)}$$

Maximum cumulative error is given by:

$$E = (E_1 + E_2) \qquad [\%] \qquad \text{(B.8)}$$

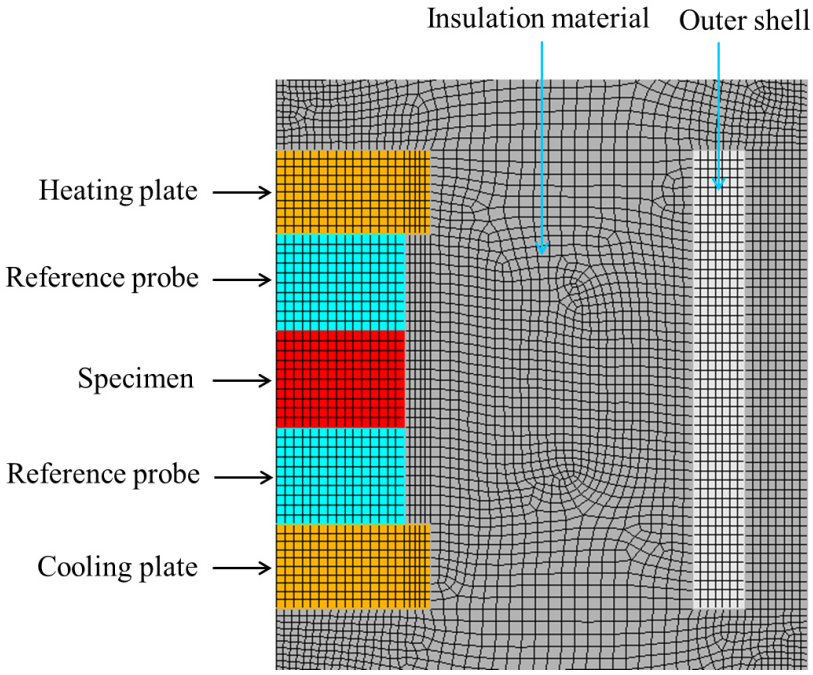

Figure B.11: 2-D axisymmetric FE model used to evaluate specific heat c_P of the given specimen of lithium-ion jellyroll. FE discretization of the domain is shown above; different colors represent different materials [117].

B.2.6 Specific heat

Specific heat denoted by c_P is defined as the amount of heat required to change the temperature of given mass of a material by 1 Kelvin and is given by:

$$c_P = \frac{Q}{m\Delta T} \tag{B.9}$$

In the SI system c_p has the units J/(kg·K). The method used to evaluate c_P of the above specimens was developed by C. Löw, A. Freund, C. Merten [117].

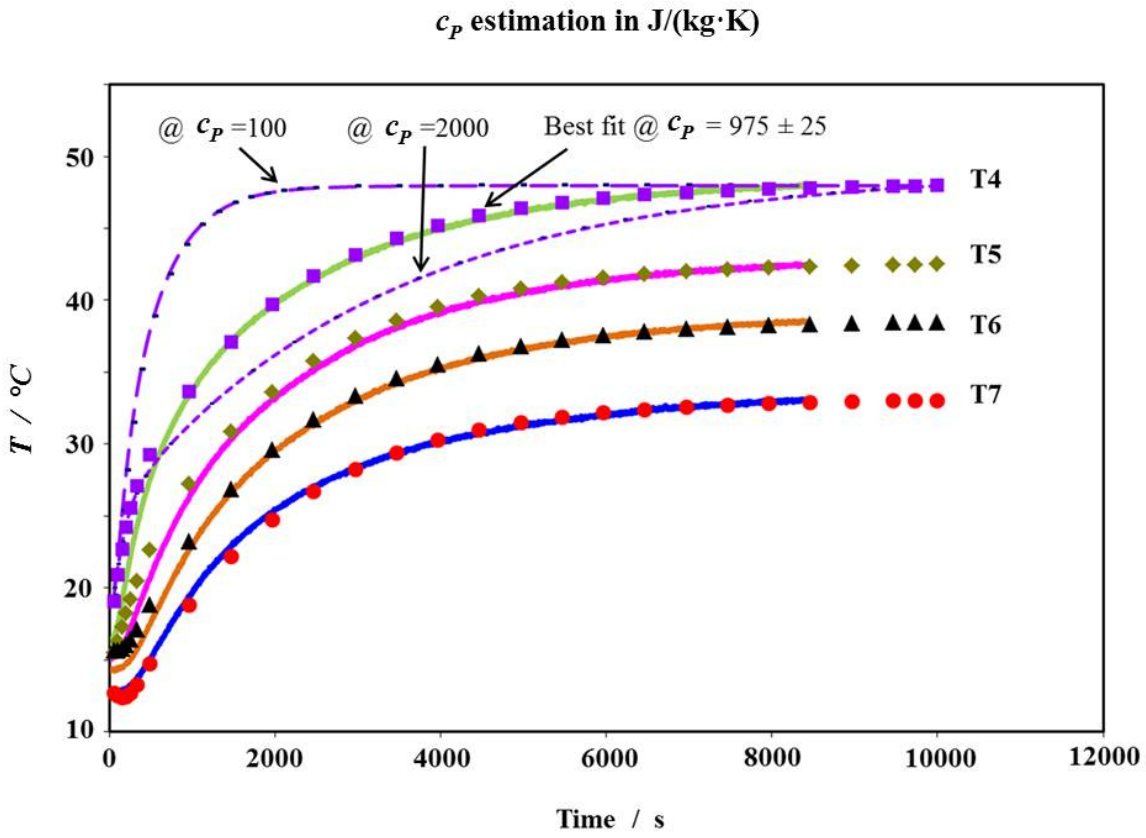

Figure B.12: c_P estimation by fitting FE simulation data to the experimentally determined transient temperature curves at *T*4, *T*5, *T*6, and *T*7 locations corresponding to Figure B.9. Solid lines represent measured data while those with markers represent simulation data.

Any one of the specimen used to measure axial and radial components of thermal conductivity could be used to evaluate specific heat. In this work the specimen used to measure radial thermal conductivity (Figure B.7*b*) was used. A 2D axisymmetric FE model of the basic assembly unit shown in Figure B.9 was used to evaluate specific heat of the given specimen. The geometry construction of the model is shown in Figure B.11. The whole system, shown in Figure B.11 has been brought to equilibrium at some lower value of temperature; let us say 20 °C, using the cooler section of the set up. When the system was reached the steady state, a preheated stream, at higher temperature e.g. 80 °C was introduced abruptly into the top part of the set up. The system was again allowed to reach steady state [117].

Temperature was continuously measured at all the sensor locations i.e. *T*1 through *T*8. The idea was to obtain the transient temperature curves and fit to these curves the FE simulation data. Simulations were carried out with different heat capacity values of the specimen. The heat capacity of the specimen was adjusted in a manner to obtain the best fit of the curves. An example of the fitted data is shown in Figure B.12.

B.2.7 Density

The third quantity to be determined in this work is the physical quantity density. It is denoted by the symbol ρ having the units of kg/m^3 in the SI system.

Density of the jellyroll was measured using the specimen prepared for the measurements of radial component of thermal conductivity shown in Figure 5.2*b)*. As density is the mass per unit volume of the given material:

$$\rho = m / V \tag{B.10}$$

$$V = 2\pi r^2 L \tag{B.11}$$

Where, V is the volume of specimen in m^3, m the mass in kg, r the radius in m and L the thickness in m. Knowing mass and volume, density of the specimen could easily be calculated using Equation (B.10).

B.3 Simulation technique

Certain parts of batteries owing to their complex geometry do not allow the thermal and physical properties to be measured in a straight forward manner using ordinary experimental techniques. Properties of such complex geometries have to be determined tactically. This section includes determination of thermal and physical properties of top and bottom parts of VL 7P cell shown in Figure 4.9*b)*. The basic procedure adopted is the same as presented in section 4.4. FE simulations were used to solve the basic energy balance equation, Equation (4.4), using ANSYS software package.

Geometry model

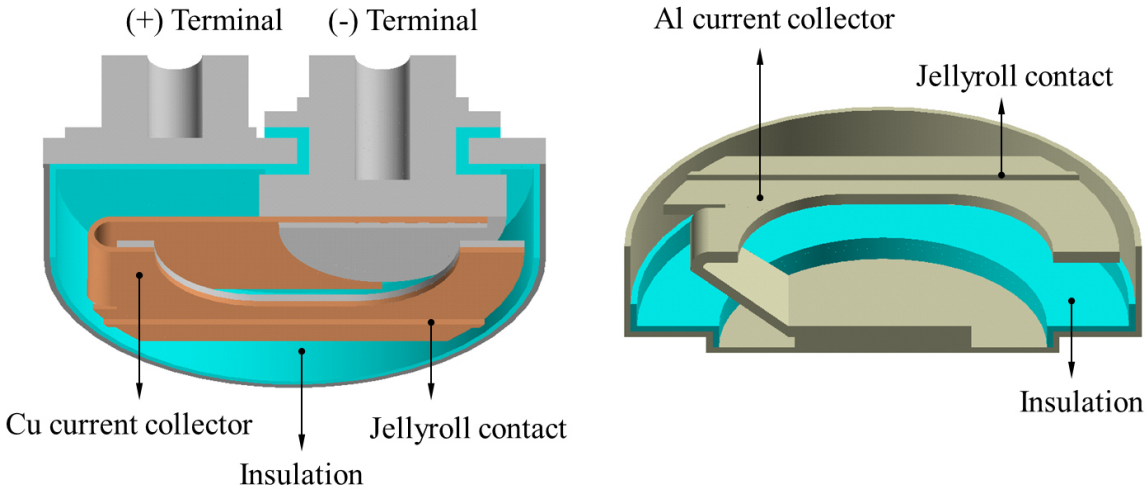

Figure B.13: Geometry models of complex shaped top and bottom parts of VL 7P battery.

Two types of boundary conditions were used in this analysis:

1. ***Constant temperature*** at the area in contact with the jellyroll (contact area) as shown in Figure B.13 (jellyroll contact).

2. ***Surface convection*** with bulk temperature and heat transfer coefficient at the exterior of the cell top (Figure B.14). Since this is a comparative study, an assumed value of heat transfer coefficient was used i.e. 10 W/(m^2·K).

Methodology

The simulation technique adopted in the present analysis is based on the idea to find the amount of heat dissipating to the environment from the actual geometry model consisting of different materials. Then develop a simple geometry consisting of a single material and having dimensions same as that of the actual geometry. Then adjust the parameters e.g. thermal conductivity to get the same amount of heat dissipating from the actual geometry under the same boundary

conditions. Actual and simplified geometries of the cell top and bottom parts are shown in Figure B.14.

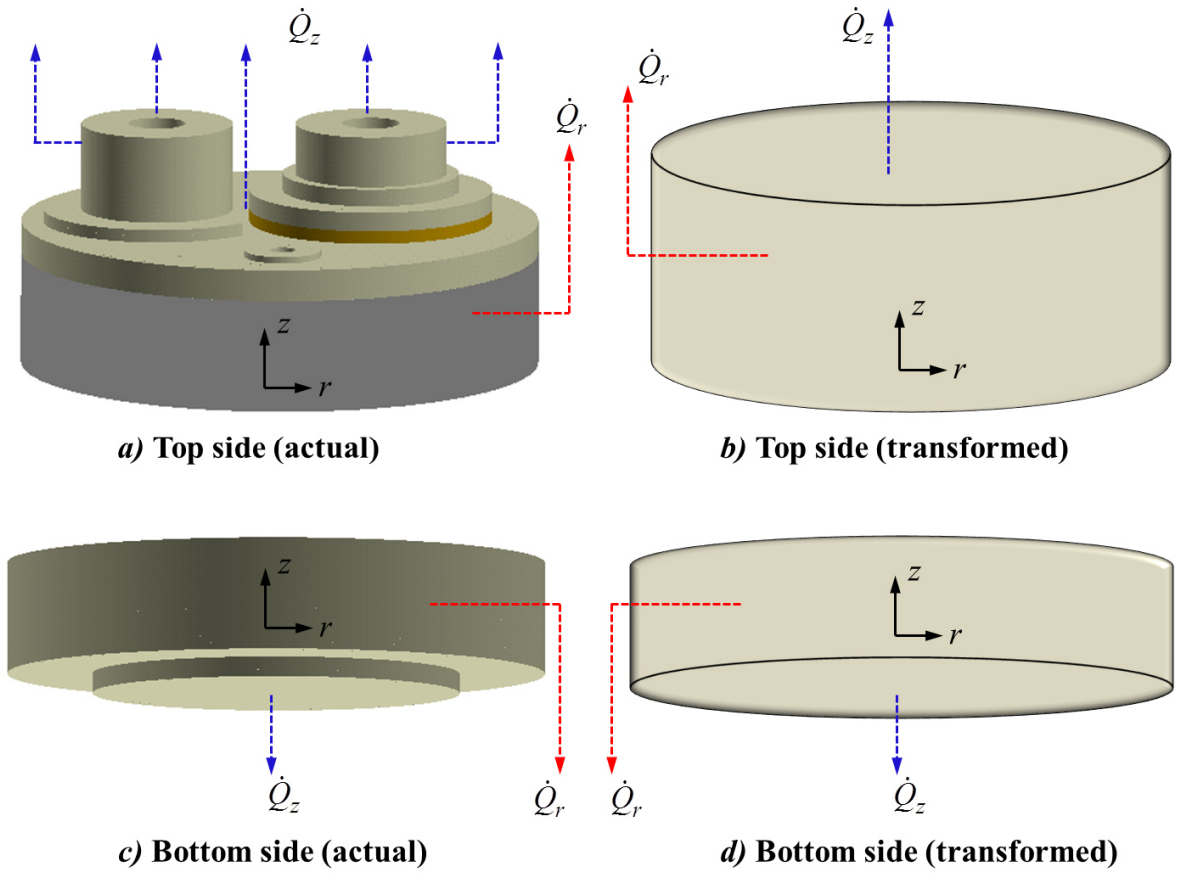

Figure B.14: *a)* Actual geometry of cell top; *b)* transformed geometry of cell top and *c)* actual geometry of cell bottom; *d)* transformed geometry cell bottom.

Such a technique can be used to model complex shaped structures or batteries in this case using much simpler domains comprising of a single material making the discretization process fast and easier resulting in a model that could directly be used in real time or on a system level.

Simulations were carried out at first with the actual geometries of the top and bottom parts of the VL 7P battery shown in Figure B.13. Constant temperature boundary conditions were applied at long and thin joints that are used for direct thermal contact with the jellyroll. These connecting joints can be seen in Figure B.13 as JR contacts. In a first step, adiabatic conditions were assumed in radial direction and all the heat was made to flow in z-direction calculated as $\dot{Q}_z$. Then in a next

step, adiabatic conditions were assumed in *z*-direction and all the heat was made to flow in *r*-direction calculated as $\dot{Q}_r$.

Next the equivalent symmetric volumes shown in Figure B.14*b)* and B.14*d)* were selected. Adiabatic conditions were set in radial direction and thermal conductivity in the *z*-direction ($\boldsymbol{k}_z$) was adjusted to get axial heat flow equal to $\dot{Q}_z$. Then all the heat was made to flow in radial direction by setting adiabatic conditions in the *z*-direction and *z*- and *r*- components of thermal conductivity ($\boldsymbol{k}_z$ and $\boldsymbol{k}_r$) were adjusted to get the amount of heat flowing in the *r*-direction equal to $\dot{Q}_r$.

Since almost all of the materials constituting top and bottom parts of VL 7P battery with corresponding thermal and physical properties are known, volume fraction technique presented in section B.1 was used to evaluate specific heat and density of the top and bottom parts of the battery. Volumes of the materials constituting top and bottom parts were obtained from ANSYS geometry model.

References

[1] B. COX, *Can We Make Star on Earth*, Documentary by BBC Horizon, A BBC / Discovery channel coproduction, February 2009.

[2] http://en.wikipedia.org/wiki/Peak_oil cited June 26, 2013.

[3] D. JAMAIL, *The Scourge of peak oil*, Features, Al Jazeera English, July 25, 2011.

[4] K. ZAGHIB, A. MAUGER, and C. M. JULIEN, *Oliven-Based Cathode Materials*, Rechargeable Batteries, Green Energy and Technology, Springer International Publishing, Switzerland, 2015.

[5] K. SOMASUNDARAM, E. BIRGERSSON, A. S. MUJUMDAR, *Thermal-electrochemical model for passive thermal management of a spiral-wound lithium-ion battery*, Journal of Power Sources 203 (84-96), 2012.

[6] Y. YE, Y. SHI, N. CAI, J. LEE, X. HE, *Electro-thermal modeling and experimental validation for lithium ion battery*, Journal of Power Sources 199 (227-238), 2012.

[7] U. SEONG, J. YI, C. B. SHIN, T. HAN, S. PARK, *Modeling the thermal behavior of a lithium-ion battery during charge*, Journal of Power Sources 196 (5115-5121), 2011.

[8] D. H. JEON, S. M. BAEK, *Thermal modeling of cylindrical lithium ion battery during discharge cycle*, Energy Conversion and Management 52 (2973-2981), 2011.

[9] W. B. GU, C. Y. WANG, *Thermal-electrochemical coupled modeling of a lithium-ion cell*, ECS Proceedings, Vol. 99-25 (1) (748-762), 2000.

References

[10] W. FANG, O. J. KWON, AND C. Y. WANG, *Electrochemical-thermal modeling of automobile Li-ion batteries and experimental validation using a three-electrode cell*, International Journal of Energy Research 34 (107-115), 2010.

[11] W. B. GU, C. Y. WANG, *Thermal-Electrochemical Modeling of Battery Systems*, Journal of The Electrochemical Society 147 (8) (2910-2922), 2000.

[12] K. KUMARESAN, G. SIKHA, AND R. E. WHITE, *Thermal Model for a Li-Ion Cell*, Journal of The Electrochemical Society 155 (2) (A164-A171), 2008.

[13] R. BENGER, H. WENZEL, H. P. BECK, M. JIANG, D. OHMS, G. SCHAEDLICH, *Electrochemical and Thermal Modeling of lithium-ion cells for use in HEV or EV application*, World Electric Vehicle Journal 3 (1-10), 2009.

[14] Y. HU, S. YURKOVICH, Y. GUEZENNEC, B. J. YURKOVICH, *Electro-thermal battery model identification for automotive applications*, Journal of Power Sources 196 (449-457), 2011.

[15] C. FORGEZ, D. V. DO, G. FRIEDRICH, M. MORCRETTE, C. DELACOURT, *Thermal modeling of cylindrical $LiFePO_4$/graphite lithium-ion battery*, Journal of Power Sources 195 (2961-2968), 2010.

[16] D. LINZEN, *Impedance-Based Loss Calculations and Thermal Modeling of Electrochemical Energy Storage Devices for Design Considerations of Automotive Power Systems*, Ph.D. Thesis, RWTH Aachen University, Germany, December 2006.

[17] M. W. TAHIR, C. HELLWIG, C. MERTEN, W. G. BESSLER, *A multi-scale thermal model of a high-power $LiFePO_4$ lithium-ion cell*, 8th Symposium on Fuel Cell Modeling and Experimental Validation, Bonn, Germany, March 8-9, 2011.

[18] http://www.silverbearcafe.com/private/02.11/silvershield.html; http://www.explainingthefuture.com/peak_oil.html cited August 2, 2013.

[19] H. A. KIEHNE, *Battery Technology Handbook*, second edition, Expert Verlag GmbH, Germany, 2003.

[20] *Impacts of Electric Vehicles, Deliverable 3, Assessment of the future electricity sector*, DELFT Report, April 2011.

[21] *Environmental Assessment of Plug-in Hybrid Electric Vehicles*, Electric Power Research Institute (EPRI), Final Report, Vol. 1: Nationwide Greenhouse Gas Emissions, July 2007.

[22] M. H. WESTBROOK, *The Electric Car: Development and Future of battery, hybrid and fuel-cell cars*, IEE Power and Energy Series 38, UK, 2005.

[23] http://en.wikipedia.org/wiki/History_of_the_electric_vehicle cited January 5, 2013.

[24] J. LARMINIE, J. LOWERY, *Electric Vehicle Technology Explained,* John Wiley & Sons, Ltd., UK, 2003.

[25] *History of Hybrid Cars,* http://www.historyofhybridcars.com/ cited January 5, 2013.

[26] C. TREJBAL, *The return of the electric car*, Roanoke.com editorial, January 9, 2011. http://ww2.roanoke.com/editorials/trejbal/wb/273241 cited January 5, 2013.

[27] *An expert panel report on Plug-in Electric Vehicles: A Practical Plan for Progress*, School of Public and Environmental Affairs at Indiana University, USA, February 2011.

[28] http://www.cartell.ie/car_check/wp-content/uploads/2010/06/2008_Tesla_Roadster.jpg cited January 5, 2013.

[29] http://www.autoweek.com/article/20110111/carnews/110119984 cited January 5, 2013.

[30] *The Revival of the Electric Car*, Worldwatch Institute, USA, May 3, 2012.

[31] *Electric Vehicle Charging Infrastructure Deployment Guidelines for the Oregon I-5 Metro Areas of Portland, Salem, Corvallis, and Eugene*, Electric Transportation Engineering Corporation (ETEC), Final version 3.1, April 2010.

[32] *The electric car – a green transport revolution in making?*, article, European Environment Agency, October 12, 2012.

http://www.eea.europa.eu/articles/the-electric-car-2014-a-green-transport-revolution-in-the-making cited January 5, 2013.

[33] A. BROWN JR., *Market Factors and Technology Trends in the global HEV/EV Segment*, The 2010 International Forum on Electric Vehicle, Seoul, South Korea, June 17, 2010.

[34] *The future is electric, clean and quite*, SIEMENS. http://cn.siemens.com/cms/cn/English/it-solutions/Documents/eCar_Byliner_EN.pdf cited 2011.

[35] M. MILLIKIN, *Gartner study finds BEVs face market adoption challenge in Germany; recommendations for the government*, Green Car Congress, article, August 7, 2011. http://www.greencarcongress.com/2011/08/gartner-20110807.html cited 2014.

[36] F. ZHANG, P. COOKE, *The Green Vehicle Trend, Electric, Plug-in hybrid or hydrogen fuel cell?*, Centre for Advanced Studies, Cardiff University, UK.

[37] *A market study on Hybrid Vehicles and the concept of V2G*, Dolcera Public Wiki, last modified on August 21, 2009. https://www.dolcera.com/wiki/index.php?title=A_market_study_on_Hybrid_vehicles_and_the_concept_of_V2G cited 2015.

[38] *Electric Powertrains*, MIT Electric Vehicle Team, USA, April 2008.

[39] B. GANJI, A. Z. KOUZANI, *A Study on Look-ahead Control and Energy Management Strategies in Hybrid Electric Vehicles*, 8th IEEE international conference on control and automation, Xiamen, China, June 9-11, 2010.

[40] Y. CUI, *Energy Tutorial: Battery Storage 101*, GCEP Research Symposium, Stanford, USA, 2010. http://www.youtube.com/watch?v=LftnyYFcP5s cited July 03, 2013.

[41] *Battery Performance Characteristics*, Battery and Energy Technologies, Electropaedia. http://www.mpoweruk.com/performance.htm cited January 5, 2013.

[42] J. K. PARK, *Principals and Applications of Lithium Secondary Batteries*, WILEY-VCH Verlag GmbH & Co. KGA, Germany, 2012.

[43] http://glossary.periodni.com/glossary.php?en=lead-acid+battery cited July 2, 2013.

[44] B. CANIS, *Battery Manufacturing for Hybrid and Electric Vehicles: Policy Issues*, Congressional Research Service, USA, March 22, 2011. http://digital.library.unt.edu/ark:/67531/metadc99028/ cited 2015.

[45] *Nickel Metal Hydride (section 3)*, Quest Batteries, Harding Battery Handbook for Quest, 2004.

[46] http://www.gbattery.com/images/english/technical/nimh_img01.gif cited July 3, 2013.

[47] *Technical information, NiMH*, NI-MH Handbook, Panasonic, Germany, 2011.

[48] J. MOLENDA, M. MOLENDA, *Composite Cathode Material for Li-ion Batteries Based on $LiFePO_4$ System*, *Metal, Ceramic and Polymeric Composites for Various Uses*, InTech Publisher, Poland, 2011.

[49] W. MIELKE, *Modellierung von Kennlinien, Impedanzspektren und thermischem Verhalten einer Lithium-Eisenphosphat-Batterie*, Masterarbeit, Deutsches Luft und Raumfahrtzentrum (DLR), Institut für Thermodynamik und Wärmetechnik (ITW), Universität Stuttgart, 2011.

[50] *A123 Batteries – $LiPO_4$ Battery Technology*, http://www.hooked-on-rc-airplanes.com/a123-batteries.html cited January 7, 2013.

[51] THE BOSTON CONSULTING GROUP (BCG), Focus, *Batteries for Electric Cars Challenges, Opportunities, and the Outlook to 2020*, 2010.

[52] E. RODA, *EV battery comparison*, Australian EV association (AEVA) meeting, February 23, 2010.

[53] *Batteries*, Ohio Aerospace Institute, DAS, Glenn Research Center at Lewis Field, NASA, November 17, 2004.

[54] M. MILLIKIN, *BCG Report Expects Battery Costs Will Constrain Widespread Market Adoption of Fully Electric Vehicles, Absent a Technology Breakthrough; Forecasts 26 % of Major Market New Cars in 2020 To be Hybrid or Electric*, article, Green Car Congress, January 8, 2010. http://www.greencarcongress.com/2010/01/bcg-20100108.html cited December 2, 2014.

[55] M. MASTRAGOSTINO, *Lithium ion batteries and supercapacitors for HEV*, International Workshop on Distributed Energy Systems, Milano, Italy, 2009.

[56] M. W. TAHIR, C. HELLWIG, C. MERTEN, W. G. BESSLER, *A multi-scale thermal model of a high-power $LiFePO_4$ lithium-ion cell*, yet to be published.

[57] P. VERMA, P. MAIRE, P. NOVAK, *A review of the features and analyses of the solid electrolyte interphase in Li-ion batteries*, Electrochimica Acta 55 (6332-6341), 2010.

[58] T. M. BANDHAUER, S. GARIMELLA, AND T. F. FULLER, *A Critical Review of Thermal Issues in Lithium-Ion Batteries*, Journal of the Electrochemical Society 158 (3) (R1-R25), 2011.

[59] S. DEARBORN, *Charging Lithium-Ion Batteries: Not All Charging Systems Are Created Equal*, Microchip Technology Inc., USA.

[60] *Aviation Incidents Involving Smoke, Fire, Extreme Heat or Explosion, Batteries & Battery-Powered Devices*, Report, Federal Aviation Agency, USA, March 20, 1991.

[61] http://www.bbc.co.uk/news/business-21054089 cited June 22, 2013.

[62] Q. WANG, PING, X. ZHAO, G. CHU, C. CHEN, *Thermal runaway caused fire and explosion of lithium ion battery*, Journal of Power Sources 208 (210-224), 2012.

[63] V. SRINIVASAN, *Batteries for Vehicular Application*, Presentation, Lawrence Berkeley National Laboratory, USA, March 10, 2008.

[64] R. B. BIRD, W. E. STEWART, E. N. LIGHTFOOT, *Transport Phenomena*, 2nd edition, John Wiley & Sons, Inc., USA, 2002.

[65] F. P. INCORPERA, DEWITT, BERGMAN, LAVINE, *Fundamentals of Heat and Mass Transfer*, 6th edition, John Willey & Sons. Inc., USA, 2007.

[66] W. H. MCADAMS, *Heat Transmission*, 3rd edition, McGraw-Hill Book Company Inc., 1954.

[67] Y. JALURIA, K. E. TORRANCE, *Computational Heat Transfer*, Hemisphere Publishing Corporation. Berlin, Germany, 1986.

[68] *Heat Flow, Theory Reference*, ANSYS version 12.1, ANSYS Inc., 2009.

[69] R. SIEGAL AND J. HOWELL, *Thermal Radiation Heat Transfer*, 4th edition, Tayler & Francis, New York, USA, 2002.

[70] H. A. KIEHNE, *Battery Technology Handbook*, 2nd edition, Expert Verlag GmbH, Germany, 2003.

[71] M. W. TAHIR, *Modeling of Cathodic Protection System for Buried Structures*, M.Sc. thesis, Chemical Engineering Department, KSU, Saudi Arabia, 2005.

[72] M. HEDWIG, *Skalenübergreifende Modellierung und Simulation des thermischen Verhaltens einer Lithium-Ionen-Batterie*, Master Thesis, Institut für Thermodynamik und Wärmetechnik (ITW), Universität Stuttgart, Germany, 2012.

[73] C. ENGELHARD, T. MEIER, C. ROCKSTROH, A. RZANY, *Electrodes for Bioelectric Signals Sensing and Stimulation*, Max Schaldach-Stiftungsprofessur für Biomedizinische Technik (MSTB), MB-JASS, 2009.

[74] W. G. BESSLER, S. GEWIES, M. VOGLER, *A new framework for physically based modeling of solid oxide fuel cells*, Electrochimica Acta 53 (1782-1800), 2007.

[75] A. J. BARD, G. INZELT, F. SCHOLZ, *Electrochemical Dictionary*, 2nd edition, Springer-Verlag, Germany, 2012.

[76] E. BERDAL, *Corrosion and protection, Engineering Materials and Processes*, Springer-Verlag, London, 2003.

[77] D. LINDEN, *Handbook of Batteries*, 2nd edition. McGraw-Hill INC., USA, 1994.

[78] J. NEWMAN, W. TIEDMANN, *Porous-Electrode Theory with Battery Applications*, AIChE Journal 21 (1) (25-41), January 1975.

[79] W. A. V. SCHALKWIJK AND B. SCROSATI, *Advances in Lithium-Ion Batteries*, Kulwer Academic/Plenum Publishers, New York, 2002.

[80] http://battery.berkeley.edu/Unprotected/02Feb10_echemIII.pdf cited July 10, 2013.

[81] G. KARIMI AND X. LI, *Thermal management of lithium-ion batteries for electric vehicles*, International Journal of Energy Research 37 (13-24), 2013.

[82] G. WANG, H. LIU, J. LIU, S. QIAO, GAOQING, M. LU, P. MUNROE, H. AHN, *Mesoporous $LiFePO_4$/C Nanocomposite Cathode Materials for High Power Lithium Ion Batteries with Superior Performance*, Advanced Materials 22 (4944-4948), 2010.

[83] O. TOPRAKCI, H. A. K. TOPRAKCI, L. JI, AND X. ZHANG, *Fabrication and Electrochemical Characteristics of LiFePO4 Powders for Lithium-Ion Batteries,* KONA Powder and Particle Journal No. 28, 2010.

[84] *Nanophosphate® Basics: An Overview of the Structure, Properties and Benefits of A123 Systems' Proprietary Lithium Ion Battery Technology*, A123 Systems, Inc.

[85] S. CHACKO, Y. M. CHUNG, *Thermal modeling of Li-ion polymer battery for electric vehicle drive cycles*, Journal of Power Sources 213 **(**296-303), 2012.

[86] L. KOSTETZER, S. NALLABOLU, E. RUDNYI, L. KRÜGER, M. GEPPERT, D. QUINGER, *Electro-thermal simulation of Lithium Ion battery for EV/HEV applications***,** CADFEM GmbH & LION Smart GmbH, Germany.

[87] K. J. LEE, K. SMITH, A. PESARAN, G. H. KIM, *Three dimensional thermal-, electrical-, and electrochemical-coupled model for cylindrical wound large format lithium-ion batteries*, Journal of Power Sources 241 (20-32), 2013.

[88] J. DAUBENSCHMID, Studienarbeit**,** *Thermische Modellierung einer Lithium-Batterie*, Institut für Verbrennungsmotoren und Kraftfahrwesen (IVK) Universität Stuttgart, Germany, May 31, 2010.

[89] J. DAHN, *Why do Li-ion batteries die? – and how to improve the situation?*, Waterloo Institute for Nanotechnology (WIN) Seminar July 30, 2013. https://www.youtube.com/watch?v=9qi03QawZEk cited December 2, 2014.

[90] M. HEDWIG, *Model description of Heat Macromodel LIB*, Internal Report, Institut für Technische Thermodynamik (ITT) Deutsches Zentrum für Luft- und Raumfahrt (DLR), Stuttgart, Germany, 2010.

[91] *High Power Lithium Ion ANR26650M1A cell*, Technical data sheet, A123 SYSTEMS, 2007.

[92] M. S, WHITTINGHAM, *Lithium Batteries and Cathode Materials***,** Chemical Reviews 104 (4271-4301), 2004.

[93] *High power Lithium-ion cells, VLP cells*, Technical information, SAFT, 2005.

[94] G. H. KIM, K. SMITH, K. J. LEE, S. SANTHANAGOPALAN, A. PESARAN, *Multi-Domain Modeling of Lithium-ion Batteries Encompassing Multi-physics in Varied Length Scales*, Journal of the Electrochemical Society, 158 (8) (A955-A969), 2011.

[95] H. LEE, *Finite Element Analysis Simulations with ANSYS Workbench*, *Theory, Application, and Case Studies*, SDC Publications, 2014.

[96] E. MADENCI, I. GUVEN, *The Finite Element Method Analysis and Applications in Engineering using ANSYS*, Springer, USA, 2006.

[97] C. HELLWIG, W. G. BESSLER, *A Multi-scale Electrochemical and Thermal model of a $LiFePO_4$ Battery*, ECS Transactions, 2010.

[98] M. SAFARI, C. DELACOURT, *Modeling of a Commercial Graphite/LiFePO4 Cell*, Journal of the Electrochemical Society, 158 (5) (A562-A571), 2011.

[99] Y. REYNIER, R. YAZAMI, B. FULTZ, *The entropy and enthalpy of lithium intercalation into graphite*, Journal of Power Sources 199-121 (850-855), 2003.

[100] J. L. DODD, *Phase Composition and Dynamical Studies of Lithium Iron Phosphate*, PhD thesis, California Institute of Technology, USA, 2007.

[101] J. P.NEIDHARDT, D. N. FRONCZEK, T. JAHNKE, T. DANNER, B. HORSTMANN, W. G. BESSLER, *A Flexible Framework for Modeling Multiple Solid, Liquid and Gaseous Phases in Batteries and Fuel Cells*, Journal of the Electrochemical Society, 159 (9) (A1528-1542), 2012.

[102] L.O. VALOEN, J. N. REIMERS, *Transport Properties of $LiPF_6$-Based Li-Ion Battery Electrolytes*, Journal of The Electrochemical Society 152 (5) (A882-891), 2005.

[103] W. G. BESSLER, S. GEWIES, M. VOLGER, *A new framework for detailed electro-chemical modeling of solid oxide fuel cells*, Electrochimica Acta 53 (1782-1800), 2007.

[104] C. FEHRENBACHER, through personal communications by C. HELLWIG, W. G. BESSLER, 2011.

[105] J. OGDEN, L. ANDERSON, *Sustainable transportation energy pathways,* Institute of Transportation Studies*,* Research summary, University of California, Davis, USA, 2011.

[106] B. METZ, O. DAVIDSON, P. BOSCH, R. DAVE, L. MEYER, Climate Change 2007 Mitigation of Climate Change, assessment report, Cambridge University Press, USA, 2007

[107] D. BROWN, R. G. LANDERS, *Control Oriented Thermal Modeling of Lithium Ion Batteries by the Global Arnoldi Algorithm from a First Principle Model via Model Reduction***,** Journal of The Electrochemical Society 159 (12) (A2043-A2052), 2012.

[108] R. E. GERVER AND J. P. MEYERS, *Three-Dimensional Modeling of Electrochemical Performance and Heat Generation of Lithium-Ion Batteries in Tabbed Planar Configurations*, Journal of The Electrochemical Society 158 (7) (A835-A843), 2011.

[109] W. DU, N. XUE, A. M. SASTRY, J. R. R. A. MARTINS, AND W. SHYY, *Energy Density Comparison of Li-ion Cathode Materials Using Dimensional Analysis,* Journal of The Electrochemical Society 160 (8) (A1187-A1193), 2013.

[110] Y. YE, Y. SHI, A. A. O. TAY, *Electro-thermal Cycle Life Model for Lithium Iron Phosphate Battery*, Journal of Power Sources 217 (509-518), 2012.

[111] *Standard Test Method for Thermal Conductivity of Solids by Means of The Guarded-Comparative-Longitudinal Heat Flow Technique*, ASTM DESIGNATION: E 1225– 04, USA, 2004.

[112] M. J. ASSAEL, K. GIALOU, K. KAKOSIMOS, I. METAXA, *Thermal Conductivity of Reference Solid Materials*, International Journal of Thermophysics 25 (397-408), 2004.

[113] L. O. OYEKUNLE, A. A. SUSU, *High Temperature Thermal Stability Investigation of Paraffin Oil*, Petroleum Science and Technology 23 (199-207), 2005.

[114] X. JIN, J. WU, Z. LIU, J. PAN, *The thermal conductivity of dimethyl carbonate in the liquid phase*, Fluid Phase Equilibria 220 (37-40), 2004.

[115] G. W. KAUFFMAN AND P. C. JURS, *Prediction of Surface Tension, Viscosity, and Thermal Conductivity for Common Organic Solvents Using Quantitative Structure-Property Relationship*, J. Chemical Information and Computer Science 41 (408-418), 2001.

[116] http://www.omega.com/pptst/OT-201.html cited January 7, 2013.

[117] C. LÖW, C. MERTEN, *Messung wärmetechnischer Parameter und Simulation des Wärmetransportverhaltens einer Lithium-Ionen-Zelle*, Internal Report, ICVT, University of Stuttgart, Germany, 2006.

[118] M. A. ROSCHER, O. BOHLEN, AND J. VETTER, *OCV Hysteresis in Li-Ion Batteries including Two-Phase Transition Materials*, International Journal of Electrochemistry 2011 (1-6) , 2011.

[119] http://www.azom.com/images/Article_Images/ImageForArticle_5813%282%29.jpg cited July 21, 2014.

[120] M. EBNER, D. W. CHUNG, R. E. GARCIA, AND V. WOOD, *Tortuosity Anisotropy in Lithium-Ion Battery Electrodes*, Advanced Energy Materials (1-6), 2013.

[121] I. V. THORAT, D. E. STEPHENSON, N. A. ZACHARIAS, K. ZAGHIB, J. N. HARB, D. R. WHEELER, *Quantifying tortuosity in porous Li-ion battery materials*, Journal of Power Sources 188 (592-600), 2009.

[122] M. BARRANDE, R. BOUCHET, AND R. DENOYEL, *Tortuosity of Porous Particles*, Analytical Chemistry 79 (9115-9121), 2007.

[123] D. W. CHUNG, M. EBNER, D. R. ELY, V. WOOD, AND R. E. GARCIA, *Validity of the Bruggeman relation for porous electrodes,* Modelling and Simulation in Materials Science and Engineering 21 (1-16), 2013.

[124] D. KEHRWALD, P. R. SHEARING, N. P. BRANDON, P. K. SINHA, AND S. J. HARRISD, *Local Tortuosity Inhomogeneities in a Lithium Battery Composite Electrode*, Journal of The Electrochemical Society 158 (12) (A1393-A1399), 2011.

[125] C. TRIONOIDE, B. CLIATH, *Molecular Thermodynamics and Kinetics*, lecture notes, Module JS CH3304, Trinity College Dublin, University of Dublin, 2014 https://chemistry.tcd.ie/undergraduate/chemistry/js/CH3304/index.php cited 2015.

[126] *FreedomCAR Battery Test Manual for Power-Assist Hybrid Electric Vehicles*, Idaho National Engineering & Environmental Laboratory, Idaho, USA, 2003.

[127] N. TANAKA, W. G. BESSLER, *Numerical investigation of kinetic mechanism for runaway thermo-electrochemistry in lithium-ion cells*, Solid State Ionics 262 (70-73), 2014.

[128] *Theory Reference for the Mechanical APDL and Mechanical Applications*, Chapter 6, section 6.1.2 and section 6.5, ANSYS version 12.1, ANSYS Inc., 2009.

[129] *Element Reference*, Chapter 4, ANSYS version 12.1, ANSYS INC., 2009.

[130] K. JALKANEN, T. AHO, K. VUORILEHTO, *Entropy change effects on the thermal behavior of a $LiFePO_4$/graphite lithium-ion cell at different states of charge*, Journal of Power Sources 243 (354-360), 2013.

[131] V. V. VISWANATHAN, D. CHOI, D. WANG,W. XU, S. TOWNE, R. E. WILLIFORD, J. G. ZHANG, J. LIU, Z. YANG, *Effect of entropy change of lithium intercalation in cathodes and anodes on Li-ion battery thermal management*, Journal of Power Sources 195 (3720-3729), 2010.

[132] N. TANAKA, P. BARTSCH, C. HELLWIG, A. LATZ, W. G. BESSLER, *Multi-scale Simulation of Thermo/Electrochemical Mechanism in Li-ion Cells at Elevated Temperature*, 224th ECS meeting, USA, October 27 – November 1, 2013.

[133] M. VOGLER, W. G. BESSLER, DENIS© User and Developer Manual, version 2, January 19, 2009.

[134] B. SMITH, Chevrolet Volt Battery Incident Overview Report, USA, January 20, 2012.

[135] W. G. BESSLER, *Electrochemistry and Transport in Solid Oxide Fuel Cells*, Habilitation (Postdoctoral), 2009.

[136] N. NITTA, F. WU, J. T. LEE, G. YUSHIN, *Li-ion battery materials; present and future*, Materials Today, November 2014.

[137] C. M. JULIEN, A. MAUGER, K. ZAGHIB, and H. GROULT, *Comparative Issues of Cathode Materials for Li-Ion Batteries*, Inorganics 2, 132-154, 2014.

[138] http://www.infomine.com/investment/metal-prices/aluminum/1-week/ cited November, 2015.

[139] https://en.wikipedia.org/wiki/Aluminium cited November, 2015.

[140] http://www.engineeringtoolbox.com/radiation-heat-emissivity-aluminum-d_433.html cited November, 2015.

[141] http://www.thermoworks.com/emissivity_table.html cited November, 2015.